

Acquisitions and Bibliographic Services Branch

395 Wellington Street Ottawa, Ontario K1A 0N4 Bibliothèque nationale du Canada

Direction des acquisitions et des services bibliographiques

395, rue Wellington Ottawa (Oritario) K1A 0N4

Year life. Velter interprise

Our file. Notice reference

NOTICE

The quality of this microform is heavily dependent upon the quality of the original thesis submitted for microfilming. Every effort has been made to ensure the highest quality of reproduction possible.

La qualité de cette microforme dépend grandement de la qualité de la thèse soumise au microfilmage. Nous avons tout fait pour assurer une qualité supérieure de reproduction.

AVIS

If pages are missing, contact the university which granted the degree.

S'il manque des pages, veuillez communiquer avec l'université qui a conféré le grade.

Some pages may have indistinct print especially if the original pages were typed with a poor typewriter ribbon or if the university sent us an inferior photocopy.

La qualité d'impression de certaines pages peut laisser à désirer, surtout si les pages originales ont été dactylographiées à l'aide d'un ruban usé ou si l'université nous a fait parvenir une photocopie de qualité inférieure.

Reproduction in full or in part of this microform is governed by the Canadian Copyright Act, R.S.C. 1970, c. C-30, and subsequent amendments.

La reproduction, même partielle, de cette microforme est soumise à la Loi canadienne sur le droit d'auteur, SRC 1970, c. C-30, et ses amendements subséquents.

Canadä

Nonlinear Dynamics of an Articulated Cylinder System Subjected to Confined Axial Flow

by

Ruxandra Mihaela Botez

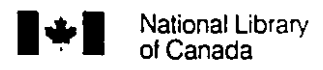
Department of Mechanical Engineering

McGill University

Montreal, Quebec, Canada

March, 1994

A Thesis submitted to the Faculty of Graduate Studies and Research in partial fulfillment of the requirements for the degree of Doctor of Philosophy



Acquisitions and Bibliographic Services Branch

395 Wellington Street Ottawa Ontario K1A 0N4 Biblioti:èque nationale du Canada

Direction des acquisitions et des services bibliographiques

395, rue Wellington Ottawa (Ontario) K1A 0N4

Your life - Votto reference

Our file - Notre reference

The author has granted an irrevocable non-exclusive licence allowing the National Library of Canada to reproduce, loan, distribute or sell copies of his/her thesis by any means and in any form or format, making this thesis available to interested persons.

L'auteur a accordé une licence irrévocable et non exclusive permettant à la Bibliothèque nationale du Canada reproduire, prêter, distribuer ou vendre des copies de sa thèse de quelque manière et sous quelque forme que ce soit pour mettre des exemplaires de cette thèse à la disposition personnes intéressées.

The author retains ownership of the copyright in his/her thesis. Neither the thesis nor substantial extracts from it may be printed or otherwise reproduced without his/her permission. L'auteur conserve la propriété du droit d'auteur qui protège sa thèse. Ni la thèse ni des extraits substantiels de celle-ci ne doivent être imprimés ou autrement reproduits sans son autorisation.

ISBN 0-315-94591-5



THANKS

This Thesis is dedicated to the following members of my family:

Alexandrina Botez, Prof. Mircea Ciurea, Thérèse Botez-Marquard, Prof. Mihai Ioan Botez, Prof. Vasilica Oprescu, Eugenia Oprescu, Nineta Rohat, Elena Botez, Prof. Alexandru Ciuca and Prof. Ion Juvara.

To some of my friends:

Bryan Halliday, Njuki Mureithi, Mary Fiorilli St-Germain, Karima Ben Souda, Anca Mateescu, Vinhson Nguyen, Guang Li, Hekmat Alighanbari, Victor Storm, Barbara Whiston, Olivier Marchand, Rafael Kouyoumdjian, Louis Lamarche, Luminita Sandu, Valerie Kern, Carole Forté, Suzanne Paquette, Christine Gedeon and Brigitte Picard.

To the following highschool, CEGEP and university professors:

Prof. Albu, Prof. Dumitrașcu, Prof. G. Rizescu, Prof. G. Călugărita, Prof. Popa, Prof. Meghea, Prof. Petre Augustin, Prof. I. Paraschivoiu and Prof. A. Misra.

ABSTRACT

This thesis deals with the nonlinear dynamics of an articulated system of cylinders in confined axial flow. The articulated cantilevered system is composed of rigid cylindrical segments, interconnected by rotational springs, and is hanging vertically in the centre of a cylindrical pipe, with fluid flowing downwards in the narrow annular passage.

The equations of motion were obtained by application of Lagrange's equations, for a system with an arbitrary number of articulations. The forces associated with the structure itself, i.e. the inertial, restoring and gravity forces acting on the structure, are taken into account in the kinetic and potential energies of the system. The hydrodynamic forces are incorporated partly in the kinetic energy and partly as generalized forces.

As the articulated system interacts with the outer pipe, this interaction or impact is modelled by a cubic or a trilinear spring, or by using the coefficient of restitution method.

The critical flow velocity for the onset of fluidelastic instabilities, such as divergence or flutter, is calculated by a linear eigenvalue analysis. Then, two models for the equations of motion are investigated, both analytically and numerically. Centre manifold and normal form theory are used to calculate the post-Hopf limit cycle amplitude, which will be compared with that obtained numerically.

Phase portraits, power spectral densities and bifurcation diagrams indicate in some cases a clear period-doubling cascade leading to chaos, while in others chaos arises via the quasiperiodic route or via type III intermittency. In addition, Poincaré maps and Lyapunov exponent calculations confirm the existence of quasiperiodicity or chaotic motion.

SOMMAIRE

Cette thèse traite de la dynamique nonlinéaire de cylindres articulés soumis à un écoulement annulaire axial. Le système articulé encastré libre est composé de segments rigides cylindriques, reliés par des ressorts rotationnels, et est suspendu verticalement au milieu d'un cylindre externe, l'écoulement coulant vers le bas dans un espace annulaire restreint.

Les équations du mouvement ont été obtenus par les équations de Lagrange, pour un nombre arbitraire d'articulations. Les forces associées à la structure, c'est à dire, les forces d'inertie, de raideur et de gravitation, sont incorporées dans l'énergie cinétique et dans l'énergie potentielle du système. Les forces hydrodynamiques sont incorporées en partie dans l'énergie cinétique et en partie dans les forces généralisées.

Lorsque le système articulé entre en contact avec le cylindre externe, cette interaction ou impact est modelisée par un ressort cubique ou un ressort trilinéaire, ou par la méthode du coefficient de restitution.

Les vitesses critiques de l'écoulement pour lesquelles des instabilités fluidelastiques apparaissent, comme la divergence ou le flottement, ont été calculées par l'analyse linéaire des valeurs propres. Ensuite, deux modèles d'équations de mouvement ont été analysés, analytiquement et numériquement. La théorie de la forme normale et celle des variétés centrales ont été utilisées pour le calcul de l'amplitude du cycle limite qui existe après la bifurcation de Hopf. Ces amplitudes ont été comparées avec celles obtenues numériquement.

Les portraits de phase, les analyses spectrales et les diagrammes de bifurcations indiquent que dans certains cas, le chaos provient d'un doublement de période, alors que dans d'autres cas, le chaos survient par quasipériodicité ou par une intermittence de troisième type. Les cartes de Poincaré et le calcul des exposants de Lyapunov confirment l'existence de mouvements quasiperiodiques ou chaotiques.

STATEMENT OF CONTRIBUTION TO ORIGINAL KNOWLEDGE

The nonlinear dynamics of a system of articulated cylinders subjected to external axial flow is the subject of this study. The contributions of this thesis to original knowledge are the modelling of the nonlinear equations and the analysis of different routes leading to chaos for this new model.

To the best of the author's knowledge, this is the first time this nonlinear model is constructed and its chaotic behaviour discussed. The contributions of this work are summarized as follows:

- Two new and original models for this system are constructed, the first linear
 and the second nonlinear. In both models, the impacting of the articulated
 system with the external cylinder is modelled by a cubic or a trilinear spring,
 or by the method of restitution coefficient.
- 2. An important number of significant conclusions concerning the nonlinear dynamical behaviour of the system are established in this thesis, for various physical and geometrical parameters.
- 3. Various dynamical tools, such as phase portraits, bifurcation diagrams, power spectral densities, Lyapunov exponents and Poincaré maps, are constructed and three routes leading to chaos are found: the classical period-doubling, the quasiperiodic route, and the type III intermittency route; this last route to chaos through intermittency is very original, and before to the author's knowledge this has not been encountered elsewhere.

ACKNOWLEDGEMENTS

The author wishes to express her gratitude to her supervisor, Prof. M. P. Païdoussis, for his attentive guidance and for his advice which he offered throughout this research.

I wish to thank to Mrs. Mary Fiorilli St-Germain and to Dr Njuki Mureithi for their special friendship for me.

The author is grateful to the Natural Sciences and Engineering Research Council of Canada for awarding her a postgraduate scholarship.

Acknowledgement is due again to the Natural Sciences and Engineering Research Council and Le Fonds FCAR of Québec for financing this thesis.

Contents

		Abstract	i
		Sommaire	ii
		Statement of Contribution to Original Knowledge	iii
		Acknowledgements	iv
		Contents	v
		List of Tables	хi
		Nomenclature	xii
1	INI	PRODUCTION	1
	1.1	MOTIVATION	1
	1.2	FROM PREVIOUS INVESTIGATIONS TO THE PRESENT ONE .	2
		1.2.1 Axial flow inside cylindrical structures	3
		1.2.2 Axial flow outside cylindrical structures	5
		1.2.3 Axial flow in annular regions between coaxial cylinders	7
		1.2.4 Articulated cylinders in axial flow	9
	1.3	MOTIVATION FOR AND OUTLINE OF THIS THESIS	11
2	тн	E FIRST THEORETICAL MODEL	14
	2.1	DESCRIPTION OF THE SYSTEM AND ASSUMPTIONS MADE .	14
	2.2	ENERGIES OF THE SYSTEM	16
		2.2.1 Kinetic and potential energies of the structure, T_s and V_s	17
		2.2.2 Kinetic energy of the fluid, T_t	18

	2.3	THE F	FLUID-DYNAMIC FORCES 2	
		2.3.1	Nonconservative inviscid force, F_{nc}	20
		2.3.2	The hydrostatic pressure forces, F_{px} and F_{py}	21
		2.3.3	Viscous Hydrodynamic Forces, F_N and F_L	23
	2.4	LAGR	ANGIAN EQUATIONS	23
	2.5	TRILI	NEAR AND CUBIC SPRING DESCRIPTION	25
	2.6	DERIV	VATION OF THE EQUATIONS OF MOTION	26
		2.6.1	The equations of motion for N=2 \dots	28
		2.6.2	The equations of motion for $N=3$	28
		2.6.3	The equations of motion for $N=4$	29
3	TH	EORE'	TICAL METHODS	31
	3.1	STAB	ILITY OF THE LINEARIZED SYSTEM	31
	3.2	ROUT	ES TO CHAOS	33
		3.2.1	Period-doubling route to chaos	33
		3.2.2	Quasiperiodic route to chaos	34
		3.2.3	Intermittence route to chaos	35
	3.3	NONL	LINEAR BEHAVIOUR OF THE SYSTEM	37
		3.3.1	Bifurcation and Phase-Plane diagrams	37
		3.3.2	Time traces and power spectra	38
		3.3.3	Poincaré maps	39
		3.3.4	Lyapunov exponents	40
		3.3.5	First and second return maps	42
		3.3.6	Number of laminar phases	42
4	NU	MERI	CAL RESULTS FOR THE FIRST MODEL WITH N=2	44
	4.1	CASE	E 1: $h = 0.5$, $f = 0.8$, $\kappa_c = 5 \times 10^3$ or $\kappa_t = 80$	4
	4.2	CASE	22: $h = 0.2$, $f = 0.8$ and $\kappa_c = 5 \times 10^3$	48
	12	CASE	$F > h = 0.5 f = 0$ and $\kappa = 5 \times 10^5$	r

	4.4	CASE	4: $h = 0.2$, $f = 0.4$ and $\kappa_c = 5 \times 10^5$	53
	4.5	SOME	GENERAL REMARKS ON THE N=2 RESULTS	55
5	AN	ALYT:	ICAL RESULTS: CENTRE MANIFOLD THEORY	56
	5.1	COMI	PUTATION OF THE UNFOLDING PARAMETERS	57
		5.1.1	Hopf Bifurcation	57
		5.1.2	Pitchfork bifurcation	58
	5.2	CENT	RE MANIFOLD CALCULATIONS	59
		5.2.1	Hopf Bifurcation	59
		5.2.2	Pitchfork bifurcation	61
6	NU	MERI	CAL RESULTS FOR THE FIRST MODEL WITH N=3	
	AN	D N=	4	62
	6.1	CASE	1: $h=0.5, f=0.8$ and $\kappa_c=5\times 10^3$	63
		6.1.1	Case 1 for the three-cylinder system, $N=3$	63
		6.1.2	Case 1 for the four-cylinder system, $N=4$	66
	6.2	CASE	2: $h = 0.2$, $f = 0.8$ and $\kappa_c = 5 \times 10^3$	69
		6.2.1	Case 2 for the three-cylinder system, $N=3$	69
		6.2.2	Case 2 for the four-cylinder system, $N=4$	72
	6.3	CASE	3: $h = 0.5$, $f = 0$ and $\kappa_c = 5 \times 10^5$	74
		6.3.1	Case 3 for the three-cylinder system, $N=3$	74
		6.3.2	Case 3 for the four-cylinder system, $N=4$	74
	6.4	CASE	4: $h = 0.2$, $f = 0.4$ and $\kappa_c = 5 \times 10^5$	75
		6.4.1	Case 4 for the three-cylinder system, $N=3$	78
		6.4.2	Case 4 for the four-cylinder system, $N=4$	76
	6.5	CASE	5: $h = 0.5$, $f = 0.4$, $\kappa_c = 5 \times 10^5$ and for $N = 3 \dots \dots$	77
7	GL	OBAL	COMPARISON OF THE RESULTS OBTAINED WITH	[
	тн	e eie	ST MODEL WITH N=2 AND N=3	81

	7.1	N=2, FIRST MODEL WITH CUBIC SPRING; $h=0.2$ 83
	7.2	N=2, FIRST MODEL WITH CUBIC SPRING; h=0.5 80
	7.3	N=3, FIRST MODEL WITH CUBIC SPRING; h=0.2 89
	7.4	N=3, FIRST MODEL WITH CUBIC SPRING; h=0.5 93
	7.5	N=2, FIRST MODEL WITH TRILINEAR SPRING; h=0.5 95
	7.6	COMMENTS
8	TH	E SECOND THEORETICAL MODEL 102
	8.1	ASSUMPTIONS MADE
	8.2	ENERGIES OF THE SYSTEM
		8.2.1 Kinetic and potential energies of the structure, T_s and V_s 103
		8.2.2 Kinetic energy of the fluid, T_f
	8.3	THE FLUID-DYNAMIC FORCES
		8.3.1 Nonconservative inviscid force, F_{nc}
		8.3.2 The hydrostatic pressure forces, F_{px} and F_{py} 100
		8.3.3 Viscous hydrodynamic forces F_N and F_L
	8.4	THE EQUATIONS OF MOTION
		8.4.1 The total kinetic and potential energies of the system 10
		8.4.2 The generalized forces
		8.4.3 Derivation of the equations of motion
9	NU	MERICAL RESULTS FOR THE SECOND MODEL WITH
	N=	2
	9.1	CASE 1: $h = 0.5$, $f = 0.8$ and $\kappa_c = 5 \times 10^3$
	9.2	CASE 2: $h = 0.2$, $f = 0.8$ and $\kappa_c = 5 \times 10^3$
	9.3	CASE 3: $h = 0.5$, $f = 0$ and $\kappa_c = 5 \times 10^5$
	0.4	CASE 4: $h = 0.2$ f = 0.4 and $r = 5 \times 10^5$

10	COI	MPARI!	SON BETWEEN MODELS 1 AND 2	119
	10.1	N=2, SI	ECOND MODEL WITH CUBIC SPRING; h = 0.2	120
	10.2	N=2, SI	ECOND MODEL WITH CUBIC SPRING; h = 0.5	123
	10.3	COMPA	ARISON BETWEEN MODELS 1 AND 2 FOR TWO	0
		DIFFER	RENT h	126
	10.4	MODEI	$_{2}$ WITH RESTITUTION COEFFICIENT AND $_{ m h}=0.5$. 128
11	COI	NCLUS	IONS	133
	11.1	SUMMA	ARY OF THIS THESIS WORK	133
	11.2	DESCR	IPTION OF THE MOST INTERESTING CASES	135
	11.3	SUMMA	ARY OF CONCLUSIONS	138
		11.3.1	Dynamics of the $N=2$ and $N=3$ systems via the first mo-	del 139
		11.3.2	Comparison of the dynamics of $N=2$ system as predicted by	y
		t	the first and second models	140
		11.3.3	The effect of varying f and h	140
		11.3.4	Analytical dynamics	141
		11.3.5	On the variety of nonlinear dynamical behaviour obtained	141
	11.4	SUGGE	ESTIONS FOR FUTURE WORK	142
В	BIBLIOGRAPHY 145			145
A)	PPE	NDICE	S	
A	Vis	cous Fo	rces — Laminar Boundary Layer	A-1
В	Vis	cous Fo	rces — Turbulent Boundary Layer	B-1
С	Lin	earizatio	on of Viscous Forces	C-1
D	Coı	nvergene	ce of the Solutions of the Equations of Motion	D-1
E	Det	ails for	the Centre Manifold Calculations	E-1

F	Estimation of the End-Form Coefficient f	F-1
G	Comments on the Signs of the Various Terms appearing in (F_N)	ز(
	and $(F_L)_j$	G-1
Н	Calculation of Base Drag Coefficient, C_b	H-1
I	Computer Programs Description	I-1

List of Tables

7.1	Explanation of symbols
7.2	Routes to chaos for $N=2$ and $N=3$ systems
7.3	Comparison between $N=2$ and $N=3$ systems
10.1	Routes to chaos for Model 1 and Model 2
10.2	Comparison between Model 1 and Model 2

NOMENCLATURE

Α	articulated cylinder area
A_f	annular flow area
a	coefficient used in centre manifold theory; focal distance
a_0, a_1, a_2, a_3	coefficients
[C]	damping matrix
C_b	base drag coefficient
C_d	drag coefficient in still fluid
C_{dp}	drag coefficient due to the normal component
C_{df}	drag coefficient due to the tangential component
C_f	uniform frictional coefficient
C_l	lift coefficient
c	nondimensional drag coefficient
c_b	nondimensional base drag coefficient
c_f	nondimensional frictional coefficient
c_{fb}	skin friction drag coefficient on the forebody
c_{τ}	coefficient of restitution
D	diameter of the articulated cylinder system
D_{ch}	internal diameter of the external pipe
D_{fore}	total drag acting on the forebody
D_h	hydraulic diameter
d_0	initial distance between two starting points
d(t)	distance between two starting points
EI	flexural rigidity
e	nondimensional parameter associated with the length
	of the last cylinder, $e = 1/2$
$F_c(\eta)$	force exerted by the cubic spring

Fei	ideal Feigenbaum number
Fei_p	Feigenbaum number associated with the pth bifurcation
F_d	force in the drag direction; Appendix B
F_l	force in the lift direction; Appendix B
F_L	viscous force in the longitudinal direction
F_N	viscous force in the normal direction
F_{nc}	nonconservative hydrodynamic force associated with
	the free end of the last cylinder
F_{px}	pressure force acting in x direction
F_{py}	pressure force acting in y direction
$F_t(\eta)$	force exerted by the trilinear spring
ſ	nondimensional free-end shape parameter
f_1/f_2	Winding number in which f_1 and f_2 are two incommensurate
	frequencies
g	gravitational acceleration
h	nondimensional hydraulic diameter coefficient
I_k	the kth maximum value of the displacement or velocity
	of one of the articulated cylinders (intermittency study)
[K]	stiffness matrix
k_c	cubic spring stiffness
k_{j}	rotational spring stiffness of the j th cylinder
k_t	trilinear spring stiffness
κ_c	nondimensional cubic spring stiffness
κ_t	nondimensional trilinear spring stiffness
l_j	length of the jth cylinder
L	Lagrangian term = $T - V$, equation (2.24)
[M]	mass matrix

M_c	moment associated with the cubic spring
M_t	moment associated with the trilinear spring
M_{i1}	virtual or added mass of fluid in the \mathbf{i}_1 direction
$M_{f j1}$	virtual or added mass of fluid in the j_1 direction
$M_c(\phi_1)$	moment associated with the cubic spring
$M_t(\phi_1)$	moment associated with the trilinear spring
$m_1,\!m_2$	integers used in calculation of frequencies
N	number of rigid articulated cylinders;
	number of laminar phases
n, n_1, n_2	integers used in calculation of frequencies
[<i>P</i>]	modal matrix
Q_{j}	generalized forces
r	limit-cycle amplitude, equation (5.17);
	radius of the articulated cylinder system;
	number of incommensurate frequencies, page 36
Re	Reynolds number
T	total kinetic energy; period of oscillation
T_f	kinetic energy of the fluid
$T_{fj}(\xi)$	kinetic energy of the fluid at point ξ of the structure
T_s	kinetic energy of the structure
T_{sj}	kinetic energy of the jth cylinder
t	time
U	dimensional external flow velocity
u	nondimensional external flow velocity, equations (2.34)
u_{ch}	flow velocity at which chaotic motion exists
u_{cr}	critical flow velocity
u_{div}	flow velocity at which a divergence instability occurs

u_{fl}	flow velocity at which a flutter instability occurs
u_{LC}	flow velocity at which a limit cycle occurs
u_p	flow velocity at which a pth bifurcation occurs
u_{pf}	flow velocity at which a pitchfork bifurcation occurs
V_{ai}	velocity of the structure after impact
V_{bi}	velocity of the structure before impact
V_{gj}	potential energy of the jth cylinder due to gravity
V_s	potential energy of the structure
V_{sj}	potential energy associated with the strain of the spring
	connecting the jth and the $(j-1)$ th cylinders
$v_{fj}(\xi)$	velocity of the fluid at point ξ of the jth cylinder
x, y	Cartesian coordinates
w	length of the noncylindrical part of the last cylinder
β	nondimensional mass coefficient, equations (2.34)
γ	nondimensional gravity parameter, equations (2.34)
ť	nondimensional slenderness parameter, equations (2.34)
η	displacement at the lower end of the first cylinder
η_g	maximum displacement at the lower end of the first cylinder
λ_{j}	eigenvalues of the system
μ	difference between u and u_{cr} ; dynamic viscosity
μ_1, μ_2, μ_3	unfolding parameters
ξ	local coordinate along the length of each cylinder
ρ	fluid density
σ	Lyapunov exponent, equation (3.10)
τ	nondimensional time
$ au_0$	nondimensional initial time (intermittency study)
ϕ_j	angular displacement of the j th cylinder

 $\dot{\phi}_{j}$ angular velocity of the jth cylinder χ apparent mass coefficient

xvi

Chapter 1

INTRODUCTION

1.1 MOTIVATION

In many engineering applications, flow-induced structural vibrations may arise and may cause problems. The subject of this Thesis is flow-induced vibration, including chaotic vibration, of cylindrical structures subjected to confined axial flow. The structures considered model various industrial components, such as components of valves, heat exchangers and nuclear reactor cores.

The vibration of the cylindrical structures subjected to external flow is a complex phenomenon, in which difficulties arise due to complex flow geometries and arbitrary, and changing, angles of incidence of the flow vis-à-vis the cylindrical structure. For this reason an idealization is often made that the flow is either purely axial with respect to the long axes of the cylinders, or purely normal to the axis. In this Thesis only the case of axial confined flow, i.e. annular flow, will be treated.

In most nuclear reactors, the nominal flow of the coolant past the fuel rods in the core is indeed axial. The vibrations induced by this flow are very small, but may still cause inter-cylinder impact, which in turn may produce wear and fretting damage. On the other hand, *confined* axial flow (i.e., annular flow or, as it is sometimes called, "leakage" flow) may induce instabilities, i.e., large amplitude

self-excited oscillations. Some case histories involving external-axial-flow-induced vibration problems in industry have been compiled by Païdoussis (1980); see also Païdoussis (1987, 1993). These problems may cause the stopping of a nuclear reactor operation for long periods of time, which is very costly, or equally serious problems in other applications.

Hence, the study of the problem and an understanding of the phenomena underlying annular flow problems are important. Such studies may lead, for example, to a better design of the annular flow passage between the control rod and the guide tube channel in certain reactors, thus minimizing the possibility of severe vibration and vibration-related breakdowns.

All the theoretical work on the topic of systems subjected to external axial flow has been done till now only with linear theory, and is thus applicable for flow velocities smaller than the critical ones. This is the first time when a system subjected to such flow is studied with nonlinear theory, which means that it can also be studied for flow velocities higher than the critical flow velocities where the system first loses stability.

Therefore, another motivation of this Thesis is the understanding of nonlinear dynamics of the system analyzed, by the use of modern nonlinear dynamics theory, currently being actively developed and used in applied mathematics, engineering and science (including medicine).

1.2 FROM PREVIOUS INVESTIGATIONS TO THE PRESENT ONE

In engineering, vibrations of cylindrical structures induced by unconfined or not tightly confined axial flow involve maximum amplitudes much smaller than those induced by cross flow: typically of the order of 10^{-3} or 10^{-1} cm. This is one

important reason why the study of axial-flow-induced vibrations began much later (around 1958) than that of cross-flow (around 1878).

In the axial flow case, there is (usually) no flow separation, and the fluid flows along the length of a given structure. The opposite is true in the cross-flow case, where there exists flow separation and, in the case of multiple cylinders, the fluid "encounters" structural elements sequentially. Therefore, the theoretical analysis of the axial flow case is much easier than that for cross-flow, and it is possible to develop analytical methods to a much higher level than those for the cross-flow case.

Three different classes of problems have been identified, depending on the disposition of the flow with respect to the long axis of the cylindrical structures (and will be discussed in the sections indicated): axial flow inside cylindrical structures (Section 1.2.1), axial flow outside cylindrical structures (Section 1.2.2), and axial flow in annular regions between coaxial cylinders (Section 1.2.3).

1.2.1 Axial flow inside cylindrical structures

Bourrières (1939) was perhaps the first to study the oscillatory instabilities of flexible pipes conveying fluid. Studies in the area of internal flow-induced vibrations were continued in the early '50s by Ashley and Haviland (1950), in connection with the study of vibration of the Trans-Arabian pipeline. Later, Feodos'ev (1951) and Housner (1952) found that for sufficiently high flow velocities a pipe supported at both ends may be subjected to divergence, i.e., it may buckle, essentially like a column subjected to axial loading. A subsequent study by Niordson (1953) led to the same equation of motion and to essentially the same conclusions regarding stability of pipes with simply-supported ends. In all the above studies, excepting Bourrières', the only form of instability discovered was divergence.

It was not until the '60s that Benjamin (1961a,b) predicted analytically the existence of oscillatory instability (of the single-mode flutter type) of articulated

cantilevered pipes conveying fluid. He found further that divergence was possible only in the case of vertical cantilevered articulated pipes (where gravity is operative) conveying a sufficiently heavy fluid (water, for example). If the fluid is air, only oscillatory instability can be observed. The occurrence or non-occurrence of divergence depending on the fluid conveyed was perplexing, and was clarified later by Païdoussis and Deksnis (1970).

Benjamin (1961a) also derived the equation of motion of a continuously flexible cantilever conveying fluid, by letting the number of degrees of freedom of the system approach infinity. This problem was further studied by Gregory and Païdoussis (1966a,b) for horizontal cantilevers. They have confirmed, by both theoretical and experimental work, the existence of oscillatory instability of horizontal cantilevers conveying fluid; divergence was found to be impossible. In this case, the behaviour of a continuously flexible cantilever conveying fluid was qualitatively identical to that of an articulated one; this is not surprising, considering that the articulated cantilever may be regarded as a lumped-parameter model of a continuously flexible one.

Later, Païdoussis (1970) found that vertical, continuously flexible pipes are never subject to divergence, irrespective of the fluid conveyed; they are subject only to oscillatory instability. It was assumed that a close analogy in the behaviour of the two systems (articulated and continuous) would be obtained in case of vertical cantilevers, as it was in the case of horizontal cantilevers. The transition from discrete to continuous system was studied in detail by Païdoussis and Deksnis (1970), who also clarified the aforementioned "anomaly" in dynamical behaviour concerning divergence, referred to in the foregoing.

More complex problems have been studied, such as the dynamics of curved pipes conveying fluid, the dynamics of straight pipes containing unsteady flow, and the dynamics of thin shell-like cylindrical pipes conveying fluid. In the latter case, it was found that the system is subject to shell-type instabilities due to the internal

axial flow; these have applications in the study of flutter and collapse of pulmonary passages due to high aspiration rates (Grotberg and Davis 1980; Webster et al. 1985).

The chaotic motions of a cantilevered pipe conveying fluid were observed for high flow velocities (Païdoussis and Moon 1988), and these motions were analyzed by Fast Fourier Transform, autocorrelation, Poincaré map and delay embedding techniques. A fractal dimension of 3.2 of the system in the chaotic regime was calculated, see also Païdoussis, Cusumano and Copeland (1992), suggesting that four-dimensional modelling (two degrees of freedom, N=2) may capture all essential features of the dynamics of this system. These studies were continued (Païdoussis, Li and Rand 1993) on higher-dimensional models (N>2) and a convergence of the results for N=4 or N=5 was shown in terms of the thresholds of Hopf and period-doubling bifurcations, and for the onset of chaos. In this paper, a quantitative comparison between theory and experiments was done, as well as with an analytical study involving centre manifold computations. The dynamics of a fluid-conveying cantilevered pipe with an intermediate spring support was further numerically investigated (Païdoussis and Semler 1993). A review of the topic of internal-flow-induced instabilities has recently appeared (Païdoussis and Li 1993).

1.2.2 Axial flow outside cylindrical structures

We shall now review some work related to the study of vibrations induced by external axial flow over cylindrical structures. The research in this area began almost twenty years later than the studies done on axial flow within cylindrical structures. Generally, it was found that there are similarities in the dynamical and stability behaviour of the two cases. For example, provided that the flow direction coincides with the axis of the cylindrical structures at rest, then, for small motions about the position of rest, the forces exerted by the fluid in the two cases of internal

and external flow are closely similar. This becomes evident on considering that the forces exerted by the fluid, excepting those due to fluid friction, in both cases arise from lateral acceleration of the flowing fluid, caused by lateral motion of the cylinder. In external flow, this acceleration is associated with the virtual or 'added' mass of fluid (Munk 1924), which is dynamically equivalent to the contained mass of fluid in internal flow.

Research into the vibration of cylindrical structures due to external axial flow has been done since 1958, beginning in the USA with Burgreen et al. (1958). Work was continued in the USA in this direction by Shields (1960), Quinn (1962, 1965) and Pavlica and Marshall (1966). Simultaneously, work was done in France at SOGREAH (1962), in Sweden by Roström and Andersson (1964a,b,c) and in Canada by Païdoussis (1965, 1966a). These studies, the first to appear in the open literature, had the following aims: (a) to measure the amplitude of vibration of particular cylindrical configurations which modelled nuclear reactor components and flow conditions; (b) to understand the nature and causes of the vibration, and (c) to develop means of predicting the vibration amplitudes in arbitrary cylindrical configurations, which is very important for design.

Later, the instabilities of cylindrical structures in axial flow were first studied theoretically and experimentally in the '60s by Païdoussis (1966a,b) for systems in unconfined flow. (These instabilities occur at flow velocities much higher than those in most applications; in the latter, only the low-amplitude vibration, studied as per the foregoing paragraph, is of concern.) In the theory, the inviscid forces were formulated by means of Lighthill's (1960) slender-body theory and viscous forces were adapted from formulations developed earlier for unconfined flows by Taylor (1952). It was found, both theoretically and experimentally, that cylinders with both ends supported lose stability by divergence, followed at higher flows by coupled-mode flutter. In contrast, cantilevered cylinders lose stability by one-degree-of-freedom flutter (Hopf bifurcation), and this only if the free end is streamlined (i.e., it is

terminated by an ogival end). Similar work was conducted for towed cylinders, displaying a more intricate dynamical behaviour (Hawthorne 1961; Païdoussis 1968). This theory was extended later (Païdoussis 1973), removing an inconsistency in the formulation of the viscous forces (which did not change the predicted dynamical behaviour substantially) and considering the effect of confinement of the flow by a duct. Both inviscid and viscous forces were developed from the earlier formulations. It was found that, as the flow becomes confined, the unsteady inviscid forces associated with lateral motions of the system become larger (effectively, the virtual mass of the fluid is increased) and the system loses stability much earlier.

In parallel to the foregoing, similar and notable research on the dynamics and flow-induced vibration of cylinders in axial flow was conducted by Chen and co-workers (Chen and Wambsganss 1971; Chen 1977; Yeh and Chen 1978) and by Païdoussis (1979), where the references cited are examples of an extensive set of publications.

Furthermore, Hannoyer and Païdoussis (1979) have studied the effect of nonuniformity of cantilevered axisymmetric beams on their stability in internal and external flows. Conical beams subjected to internal flow are less stable than cylindrical ones. In the external flow case, the opposite effect was observed; fully conical cantilevered beams do not become unstable, while for truncated conical cantilevers, instabilities are possible at higher flow velocities than for the cylindrical ones, if the free end is streamlined sufficiently.

1.2.3 Axial flow in annular regions between coaxial cylinders

Annular axial-flow over structures may be seen as an intermediate situation between external and internal axial flow in or around structures. Païdoussis and Ostroja-Starzewski (1981) studied the annular flow case and (i) derived the inviscid forces

for confined flow by the full (linear) potential-flow theory, rather than the slender-body approximation, so that the analysis would also be applicable to non-slender cylinders also, and (ii) considered compressibility effects. The inviscid forces in this case were formulated by means of the generalized force Fourier-transform method. It was found that the potential flow refinement effectively raised the critical flow velocities for instability, especially for non-slender cases, since slender-body theory overestimates the fluid-dynamic forces on cylinders. It was also shown that the effect of compressibility on the dynamics of the system is weak for slender cylinders, while being strong (significant) for non-slender ones.

Later, Hobson (1982) considered a rigid cylindrical body which was hinged at a point and coaxially positioned in a flow-carrying duct of nonuniform crosssectional area. Again he showed that the confinement of the narrow annular passage produced an increase in the negative fluid damping, which leads to oscillatory instabilities. This mathematical model explains the destabilizing effect of an upstream constriction and the stabilizing effect of a downstream end constriction of the annulus, on the system. Mateescu and Païdoussis (1985) represented a more rigorous, but more limited in its applicability, analytical inviscid model for the same physical system, hinged at some point along its length. It was shown that there exists a critical location of the hinge: if the hinge is situated upstream of that location, then the system remains stable at all velocities; on the other hand, oscillatory instabilities are possible if the hinge is moved downstream past that location. In addition, the critical location of the hinge is influenced by axial variations of the annular gap. Some improvement of the model was later made to account approximately for the unsteady viscous effects which were found to have a stabilizing influence on the system (Mateescu and Paidoussis 1987).

Experiments (Mateescu et al. 1988) validated the theory in these studies. For example, for different positions of the hinge, the unsteady pressures, frequencies of oscillation and flow velocities, were measured and then compared with the

corresponding theoretical ones. It was found that, except near the body extremities, good agreement was obtained.

Several other papers by Mateescu and co-workers on the same topic followed; see, e.g., Païdoussis et al. (1990).

1.2.4 Articulated cylinders in axial flow

1.2.4.1 Articulated cylinders with internal flow

The first nonlinear study on an articulated system of two rigid pipes flexibly interconnected, was done by Rousselet and Herrmann (1977). The equations of motion were a modified form of Benjamin's and Païdoussis and Deksnis', in which the flow velocity may vary with motions of the system through a frictional loss factor, but the upstream pressure remains constant (Roth 1964). The nonlinear form of the unstable-mode equation was then solved by the Krylov-Bogoliubov method.

Bajaj and Sethna (1982a,b) conducted an analysis of three-dimensional motions of the articulated cantilevered system in the neighbourhood of the critical flow velocity for Hopf bifurcation. The joints in this case do not have torsional rigidity, and they permit both motions transverse to the long axis of symmetry and rotary ones about it. Periodic solutions of the nonlinear equations are determined by the Method of Alternate Problems (Hale 1969; Bajaj 1982), which transforms a set of ordinary differential equations into a set of algebraic ones; then, two independent sets of periodic solutions to the algebraic equations were found to exist, corresponding to: clockwise or counterclockwise rotary motions, and planar transverse motions. Their stability was determined by the Floquet exponents of the corresponding variational equations.

The foregoing analysis was restricted to solutions in the neighbourhood of the straight, vertical equilibrium. The situation when this restriction is removed has been studied by Sethna and Gu (1985), where the 'limiting configurations' as $u \to \infty$

are examined. The authors examined five such generic shapes (configurations), all of the type in which the equations are invariant under rotation about the vertical axis. The stability of these generic shapes was studied either by a linear approach or by centre-manifold theory. They have found a second bifurcation (Hopf bifurcation) beyond the one that was found previously, for which some of the generic shapes become unstable. The analytical results were complemented by simulations.

Finally, Sethna and Shaw (1987) have studied codimension-three bifurcations of a two-segment articulated system vibrating in a plane, near a point of double degeneracy. A double degeneracy refers to the situation where a pitchfork and a Hopf bifurcation occur simultaneously for a special set of parameter values. Codimension-three refers to three parameters being used to 'unfold' the bifurcations in the vicinity of this double degeneracy — i.e., to develop gradually the evolution of the bifurcation as one or more parameters are varied. This is normally a codimension-two problem (Guckenheimer and Holmes 1983), but here a third parameter corresponding to imperfection-related asymmetries was added.

1.2.4.2 Articulated cylinders in external flow

Interest in the behaviour of articulated cylindrical systems in external axial flow is more recent than that of the continuous (distributed parameter) systems in external axial flow. Work was done (i) in conjunction with the dynamics of fuel "strings" or "stringers" of certain types of nuclear reactors (Païdoussis 1976), and (ii) underwater systems towed by a submarine (Hamy 1971; Païdoussis 1986). The fuel strings in question consist of fuel bundles held together by a central support tube; the string is mounted vertically within a pressure tube, and is held at the bottom end and free on top, with the flow upwards. The theoretical study by Païdoussis (1976) is of special interest here, since the physical system in that paper is quite similar to that considered in the present study and, hence, so are the equations of motion—although in the case of the fuel string they are considerably more complex.

Another example, item (ii) in the previous paragraph, is the concept of a "Sea Chain System", which was put forward in the early '70s (Hamy 1971). The "Sea Chain" is a submarine system consisting of a power module pulling a series of quasi-cylindrical freight modules, all connected by flexible couplings. This system is suited for operation in the Arctic as a transportation system for oil, gas and bulk cargo, its advantages being that: (i) it avoids the difficulties associated with surface transport in ice-infested waters; (ii) it is highly manoeuvrable; (iii) it is adaptable to transporting different cargos by simply changing modules. This system is similar to the Dracone, a semi-submerged, highly flexible, sausage-like container towed behind a small craft (Hawthorne 1961; Dunlop Dracones 1969), which is used for the transportation of oil and other lighter than sea-water cargo, including fresh water, to arid lands (e.g., to some of the Aegean islands from the Greek mainland).

Also of interest to the present study is the work on "pendular oscillations" of articulated systems modelling nuclear reactor reactivity-monitoring or -control systems, e.g., by Hennig et al. (1980) and Peterka (1991), where the cylindrical elements are hung in the form of simple or compound pendula within a tube and are cooled by annular flow.

The chaotic motions of an articulated cylinder system subjected to external axial flow have been studied by Païdoussis and Botez (1993); some of the results obtained will be presented in the first part of this Thesis.

1.3 MOTIVATION FOR AND OUTLINE OF THIS THESIS

It has been discovered quite recently that the motions of very simple dynamical systems cannot always be predicted far into the future. Such motions have been called *chaotic* and their study has prompted a discussion of some new mathematical

ideas in dynamics. The nonscientific concept of chaos is very old and often associated with a physical state or human behaviour without pattern and out of control. In the current literature, "chaotic" is a term assigned to a class of motions in deterministic physical and mathematical systems whose time history has a "sensitive dependence on initial conditions".

It is well known that an articulated system subjected to external axial flow loses its stability at high flow velocities by flutter or by divergence. All the early theoretical work on this topic has been done with linear theory. With the recent interest in chaotic motions of non-linear systems (Guckenheimer and Holmes 1983; Moon 1987), it seems appropriate to look into the possible existence of chaos in this particular system.

This Thesis deals with the dynamics of a system of articulated cylinders which are interconnected by rotational springs, within a pipe conveying fluid, with fluid flowing downward in the relatively narrow annular space. Analytical models for this system (of two, three and four degrees of freedom) are developed, and their dynamics, taking into account possible impacting with the outer pipe, are explored mainly numerically. It is shown, for the first time, that this system can develop chaotic oscillations.

The two models differ in the way the set of equations of motion is considered: in the first model, the dynamics of the system when no impact occurs with the confining pipe is described by a set of equations which are linearized; in the second case, the nonlinearities are taken into account approximately and are introduced mainly via Taylor expansions of the trigonometric functions of state variables; nonlinear terms are retained up to order three. In both models, impacting with the pipe is modelled by a trilinear or a cubic spring, presumed to exist between the pipe and the element of the articulated system contacting it.

This Thesis consists of eleven chapters. In Chapter 1 a brief review is given of previous studies related to the research work of the Thesis. The goals undertaken

by the Thesis have also been stated, and now the outline of the Thesis is being presented.

In Chapter 2, the development of the first analytical model for a system of cylinders subjected to a confined axial flow is given in detail. Presented are (a) the description of the system and assumptions made, (b) the energies of the system, (c) the fluid-dynamic forces, in which are included also the nonlinear forces due to the cubic spring or to the trilinear spring. In Chapter 3, the following are presented: (a) a theoretical stability analysis of the first model (no impacting with the channel), and (b) the methods used in subsequent chapters to study the nonlinear behaviour of this system, namely for bifurcation diagrams, phase-plane portraits, power spectra and time traces, Poincaré maps and Lyapunov exponents.

In Chapter 4, the numerical results are presented for the first model, in which the equations of motion are linearized, modelling impact with a cubic spring and for N=2 (two articulated cylinders), for four different cases. The analytical results, including those of centre manifold theory are presented in Chapter 5, for the same system (N=2). In Chapter 6, the numerical results for N=3 and 4 for the first model are presented, for the same cases as those in Chapter 4.

In Chapter 7, the results obtained for two- and three- degree-of-freedom systems are compared for different parameters, and additional results for the first model with impacting modelled by a trilinear spring are further presented.

In Chapter 8, the second model of a system of cylinders subject to a confined axial flow is described and the nonlinear equations of motion are derived. Chapter 9 gives the numerical results for the two-degree-of-freedom system, for the same four cases as those considered in Chapter 4.

In Chapter 10, the results obtained for the two models with N=2 (in Chapters 4 and 9) are compared to those obtained by restitution coefficient theory. Finally, Chapter 11 wraps up the Thesis with a summary of general conclusions and suggestions for future work.

Chapter 2

THE FIRST THEORETICAL MODEL

2.1 DESCRIPTION OF THE SYSTEM AND ASSUMPTIONS MADE

The articulated system here under consideration consists of a number, N, of rigid cylinders interconnected by rotational springs, with the lowest cylinder being terminated by a more or less streamlined, ogival end. The system is hung vertically in the centre of a pipe (Figure 2.1.(a)), and is supported at the upper end and free at the lower one. Fluid flows downward in the relatively narrow annular space.

To simplify the analytical model and, thus, to be able to carry out the analysis into the chaotic regime easily, a number of assumptions are made at the outset, as follows:

(a) The fluid is incompressible and of uniform density, and it is flowing with a uniform velocity U parallel to the x-axis, which coincides with the position of rest of the articulated cylinder system.

- (b) The diameter of the cylindrical elements is small compared to the length of the articulated system.
- (c) Since the system under consideration does not model any particular physical system, it may be considered to be so constructed that motions of the articulated system are indeed planar.
- (d) As the annular space between the articulated cylinder system and the external pipe is narrow (despite the diagrammatic spaciousness of Figure 2.1.(a)), the motions of the articulated system are considered to be of small amplitude, as constrained (contained) by the presence of the external pipe; that means that the dynamics of the system when no impact occurs with the confining pipe may be described by a linearized set of equations.
- (e) The presence of the external pipe (confining channel) becomes "felt" by the system quite apart from the effects on the fluid/flow-induced forces via the impact-related forces. A trilinear spring model for such impact is quite reasonable: there is no spring (zero stiffness) while the system oscillates without touching the wall; but once it does, then further movement is resisted by a very large stiffness associated with local deformation of the articulated system and of the constraining pipe wall. The cubic spring (to be discussed in Section 2.5) is a further idealization of the situation (cf. Païdoussis and Moon 1988; Païdoussis et al. 1992), and is introduced strictly for analytical convenience.
- (f) Another assumption made implicitly is that, despite the articulations and the rotational springs (which are presumed not to protrude into the fluid flow), there is no local separation of the flow as the articulated system oscillates, by virtue of the small angles of deflection involved. For the same reason, slender-body theory will be presumed to be applicable for the determination of the inviscid fluid forces.
- (g) The essence of this "first" model is that, apart from impact-related forces, the equations of motion will be linearized. Hence, the equations of motion will be correct to $O(\epsilon)$, where $\phi_j \simeq O(\epsilon)$. Accordingly, second order terms will be neglected

in the forces, and terms higher than second order will be neglected in the associated energies (Section 2.2).

Concerning the fluid forces, they could in principle be determined by an appropriate solution of the Navier-Stokes equations. This will not be attempted here, and the fluid forces will be determined essentially by superposition: inviscid and viscous forces will be determined separately. This has been shown to be quite acceptable (Païdoussis 1966a,b, 1973) for the continuously flexible counterpart of the present problem, as well as for more complex systems (Païdoussis 1979). Then, the forces associated with the structure itself, i.e., the restoring, inertial and gravity forces acting on the structure, are taken into account in the kinetic and potential energies of the system. The hydrodynamic forces are incorporated partly in the kinetic energy and partly as generalized forces.

The equations of motion will be obtained by application of Lagrange's equations, for a system with an arbitrary number of articulated cylinders, N, although the calculations to be presented will be confined to N=2, N=3 and N=4. The lengths of the cylinders in the system are l_j , the interconnecting rotational spring stiffnesses are k_j , and the generalized coordinates chosen are the angles of deformation ϕ_j , where j=1,...,N, as shown in Figure 2.1.(b).

2.2 ENERGIES OF THE SYSTEM

As the equations of motion will be derived by the Lagrangian method, in this section the kinetic and potential energies of the structure will be determined. The kinetic energy of the system will have two components, one due to the structure, and the other due to the fluid.

2.2.1 Kinetic and potential energies of the structure, T_* and V_*

In this section, the kinetic and potential energies of the structure, T_s and V_s , of the articulated system itself, are determined in terms of generalized coordinates, which are the angles of deformation, ϕ_j (Figure 2.1.(b)). Small deformations are assumed, so that $\sin \phi_j \simeq \phi_j$ and $\cos \phi_j \simeq 1$.

The local coordinate ξ is defined, along the length of each cylinder segment, $0 \le \xi \le l_j$ (Figure 2.1); then, for small deflections, the velocity at point ξ of the jth cylinder is

$$v_j(\xi) = \sum_{q=1}^{j-1} l_q \, \dot{\phi}_q + \xi \, \dot{\phi}_j \,, \tag{2.1}$$

where the dot denotes differentiation with respect to time, t. Hence, the kinetic energy of the jth cylinder is

$$T_{sj} = \frac{1}{2} \int_0^{l_j} m_j \left(\sum_{q=1}^{j-1} l_q \, \dot{\phi}_q + \xi \, \dot{\phi}_j \right)^2 d\xi \,, \tag{2.2}$$

where m_j is the mass per unit length and the subscript s stands for "structural". The total kinetic energy of the structure, neglecting the ogival part of the last cylinder, is

$$T_s = \frac{1}{2} \sum_{j=1}^{N} \left[\int_0^{l_j} m_j \left(\sum_{q=1}^{j-1} l_q \, \dot{\phi}_q + \xi \, \dot{\phi}_j \right)^2 \right] d\xi . \tag{2.3}$$

The potential energy of the structure V_s has two components, one due to gravity and another due to the strain of the intercylinder connecting springs. The potential energy of the jth cylinder due to gravity, V_{gj} , is given by

$$V_{gj} = \frac{1}{2} \left\{ \int_0^{l_j} m_j g \left(\sum_{q=1}^{j-1} l_q \, \phi_q^2 + \xi \, \phi_j^2 \right) d\xi \right\}, \tag{2.4}$$

where, by Taylor series expansion, $1 - \cos \phi_j \simeq \frac{1}{2} \phi_j^2$ has been used, and the subscript g stands for "gravity", such that the potential energy is correct to $O(\epsilon^2)$ if $\phi_j \simeq O(\epsilon)$, as it should.

The potential energy associated with the strain of the spring connecting the jth and the (j-1)th cylinders is

$$V_{sj} = \frac{1}{2} k_j (\phi_j - \phi_{j-1})^2 , \qquad (2.5)$$

where the subscript s stands for strain.

Finally, for small displacements, the total potential energy of the structure may easily be found to be

$$V_{s} = \frac{1}{2} \sum_{j=1}^{N} \left\{ \int_{0}^{l_{j}} m_{j} g \left(\sum_{q=1}^{j-1} l_{q} \phi_{q}^{2} + \xi \phi_{j}^{2} \right) d\xi \right\} + \frac{1}{2} \sum_{j=1}^{N} k_{j} (\phi_{j} - \phi_{j-1})^{2} . \tag{2.6}$$

2.2.2 Kinetic energy of the fluid, T_f

We adapt to this problem Lighthill's work (1960), which is essentially an application of slender body theory. By this theory, we shall calculate the normal flow velocity at any point ξ of the jth cylinder; with this flow velocity, we shall then calculate the kinetic energy of the fluid, T_f .

We describe the articulated cylinder system subjected to external axial flow as 'straight' when it is stationary in the vertical position (x direction), such that no resultant normal force acts on its cross-section. Then, we suppose that the articulated system has a displacement h(x,t) from the straight position in the y-direction (Figure 2.2.(a)); the x and y directions are defined in Figure 2.1.

Furthermore, in Figure 2.2(a) we introduce the new system of unit vectors (i_1, j_1) which corresponds to the (i,j) unit vector system rotated by an angle ϕ in the counterclockwise direction.

We isolate an element of a cylinder as in Figure 2.2(b), and then, by slender body theory, the flow may be regarded as composed of (a) the steady flow around the straight body, in which case the flow velocity is $v_a = U \cos \phi \mathbf{i}_1 \simeq U \mathbf{i}_1$, and (b) the flow due to the displacement h(x,t). In the latter case, the relative fluid-body velocity in the direction normal to the element, that means in the \mathbf{j}_1 direction,

is $v_b = (\partial h/\partial t)\cos\phi + U\sin\phi$. For small displacements $(\partial h/\partial x)$, $\cos\phi \simeq 1$, $\sin\phi \simeq \tan\phi = \partial h/\partial x$; therefore, in the \mathbf{j}_1 direction and for small displacements, $v_b(x,t) = [\partial h(x,t)/\partial t] + U[\partial h(x,t)/\partial x]$. In our case,

$$v_b(x,t) = \frac{\partial y}{\partial t} + U \frac{\partial y}{\partial x}$$
 (2.7)

in the j_1 direction. Then, the total velocity of the fluid at point ξ of the jth cylinder, $v_{fj}(\xi)$, is composed of two components in the i_1 and j_1 directions, and it can be written as follows:

$$v_{fj}(\xi) = U\mathbf{i}_1 + \left(\sum_{q=1}^{j-1} l_q \dot{\phi}_q + \xi \dot{\phi}_j + U\phi_j\right) \mathbf{j}_1.$$
 (2.8)

Therefore, the kinetic energy of the fluid at point ξ of the jth cylinder is

$$T_{fj}(\xi) = \frac{1}{2} \int_0^{l_j} M_{i1} U^2 d\xi + \frac{1}{2} \int_0^{l_j} M_{j1} \left(\sum_{q=1}^N l_q \dot{\phi}_q + \xi \dot{\phi}_j + U \phi_j \right)^2 d\xi, \tag{2.9}$$

where M_{i1} and M_{j1} are the corresponding virtual or added masses of fluid in the i_1 and j_1 directions. The first integral gives rise to a constant, i.e. to a term independent of ϕ or $\dot{\phi}$. Hence, when it is eventually substituted in the Lagrange equations, it will contribute nothing; it can therefore be neglected from here on.

 M_{j1} may be written as $\chi \rho A$ for confined flow, where ρ is the fluid density, and A is the cylinder constant cross-sectional area; thus, for unconfined flow we have $\chi = 1$, and $M_{j1} = \rho A$, as is well known. Generally, $\chi > 1$ for confined flow and it increases as the diameter of the confining flow-channel decreases. For axisymmetrically confined flow (i.e., annular flow between coaxial cylinders, which is our case), χ is found by potential flow theory to be (Chen et al. 1976):

$$\chi = [(1+h)^2 + 1]/[(1+h)^2 - 1], \tag{2.10}$$

where $h = D_h/D$, D being the cylinder diameter, and $D_h = D_{ch} - D$ is the hydraulic diameter of the annular flow passage, D_{ch} being the internal diameter of the external pipe (Figure 2.1(a)). It is implicitly assumed in arriving at equation (2.10) that the

displacement thickness of the boundary layer is small, as compared to the radius of a cylinder in the system, and viscous forces are not too large (i.e., the annular passage is not extremely narrow).

Then, the kinetic energy of the fluid associated with the inviscid component of fluid-dynamic forces will be

$$T_f = \frac{1}{2} \chi \rho A \sum_{j=1}^{N} \int_0^{l_j} \left(\sum_{q=1}^{N} l_q \dot{\phi}_q + \xi \dot{\phi}_j + U \phi_j \right)^2 d\xi.$$
 (2.11)

2.3 THE FLUID-DYNAMIC FORCES

As has already been mentioned, the fluid forces will be determined in several parts: inviscid unsteady forces, hydrostatic forces and viscous forces. They will generally be expressed as generalized forces for introduction into Lagrange's equations.

2.3.1 Nonconservative inviscid force, F_{nc}

If both ends of the articulated system were supported, expression (2.11) would represent the whole of the inviscid component of the fluid-dynamic forces. However, the cantilevered system is generally nonconservative, and hence there will generally be work done at the free end of the system by a nonconservative lateral inviscid force, F_{nc} (cf. Benjamin 1961a,b; Païdoussis 1966a). This force is associated with the non-cylindrical, ogival end of the last cylinder.

For a less than ideally streamlined end, this force will not develop fully because (i) the lateral flow will not be truly two-dimensional, (ii) boundary layer effects. This may be taken into account by introducing a parameter f, so that we obtain:

$$F_{nc} = (1 - f)\chi \int_{0}^{w} \left(\frac{\partial}{\partial t} + U \frac{\partial}{\partial x}\right) \rho S(x) v_{b} dx$$

$$= \chi (1 - f) \int_{0}^{w} \left(\frac{\partial}{\partial t} + U \frac{\partial}{\partial x}\right) \rho S(x) \left(\frac{\partial y}{\partial t} + U \frac{\partial y}{\partial x}\right) dx$$

$$\simeq \chi (1 - f) \rho \left(\frac{\partial y}{\partial t} + U \frac{\partial y}{\partial x}\right) U \int_{0}^{w} \frac{\partial S}{\partial x} dx.$$

where w is the length of the noncylindrical part of the last cylinder and v_b is the lateral velocity of the fluid, which is in fact the component in the j_1 direction of $v_{fj}(\xi)$, as defined by equation (2.7).

Thus, we can write the final form of F_{nc} , which is

$$F_{nc} = \chi(1 - f)MU\left(\frac{\partial y}{\partial t} + U\frac{\partial y}{\partial x}\right), \qquad (2.12)$$

in which f is a measure of departure from ideal slender body theory; as the end becomes progressively blunter, $f \to 0$.

For the articulated system, this expression may be written as follows:

$$F_{nc} = \chi(1 - f) MU \left(\sum_{j=1}^{N} l_j \dot{\phi}_j + U \phi_N \right) . \tag{2.13}$$

2.3.2 The hydrostatic pressure forces, F_{px} and F_{py}

The static pressure distribution, p(x), in the external channel flow is determined by the hydrostatic pressure distribution, modified by the skin-friction-related pressure drop; since the latter is approximately linear, p(x) is taken to be linear. The forces F_{px} and F_{py} acting on an element $\delta\xi$ of one of the cylinders (Figure 2.3) are determined by considering this element frozen and immersed in fluid on all sides.

Therefore, the resultant of the forces on the cylindrical surface of the jth cylinder (in terms of F_{px} and F_{py}) is equal to the total hydrostatic force on the element, which is the buoyancy force, minus the forces pA acting on the two cut, circular faces of the element; i.e.,

$$-F_{px}\delta\xi\mathbf{i} + F_{py}\delta\xi\mathbf{j} = -\frac{dp}{dx}A\delta\xi\mathbf{i} - \left(-\frac{d(pA)}{dx}\cos\phi_{j}\mathbf{i} - \frac{d(pA)}{dx}\sin\phi_{j}\mathbf{j}\right)\delta x, \quad (2.14)$$

where $A\delta\xi$ is the elemental volume. Since, for the inclined cylinder, $\partial\xi/\partial x = \cos\phi_j$, the forces on the element $\delta\xi$ of the jth cylinder are

$$(F_{px})_j = 0, \quad (F_{py})_j = A \frac{dp}{dx} \tan \phi_j \simeq A \frac{dp}{dx} \phi_j$$
 (2.15)

for small deformations ($\tan \phi_j \simeq \phi_j$). These results could have been obtained directly from adaptation of the equivalent results for a flexible cylinder (Païdoussis 1973): $F_{px} = 0$, $F_{py} = (\partial/\partial x)[pA(\partial y/\partial x)]$. From the latter, it is seen that there is also a change-of-angle (curvature term), which arises at the joints of the articulated cylinders. This, for the *j*th cylinder, gives rise to a contribution in the generalized force

$$-(dp/dx)Al_il_j\sin(\phi_i-\phi_j).$$

It is evident from equation (2.15) that $(F_{py})_j$ depends on the pressure drop (dp/dx). This will therefore be estimated. Consider the simplified diagram of Figure 2.4, in which it is assumed that the steady static pressure is uniform in any cross section. One can write

$$p_1 = p_2 + \frac{dp}{dx} A_f, (2.16)$$

where A_f is the annular flow area.

A uniform frictional coefficient C_f is assumed to apply throughout, so that the total frictional force is $\frac{1}{2}\rho(D+D_{ch})U^2C_f$, where D and D_{ch} were already defined in Section 2.2. Hence, a force balance will give the following equation:

$$A_f \frac{dp}{dx} = -\frac{1}{2}\rho(D + D_{ch})U^2C_f + \rho g A_f.$$
 (2.17)

By multiplication of the above equation by A/A_f , we obtain

$$A\frac{dp}{dx} = -\frac{1}{2}\rho(D+D_{ch})\frac{\pi D^2/4}{\pi(D_{ch}^2 - D^2)/4}U^2C_f + \rho gA.$$
 (2.18)

However, $(D+D_{ch})D^2/(D_{ch}^2-D^2)=D^2/(D_{ch}-D)=D^2/D_h$, where $D_h=D_{ch}-D$ is the hydraulic diameter. Hence, one obtains

$$A\frac{dp}{dx} = -\frac{1}{2}\rho DU^2 C_f \frac{D}{D_b} + \rho g A; \qquad (2.19)$$

if D_h is very large (unconfined flow), then $A(dp/dx) = \rho g A$.

Hence, for small deformations, i.e. $\tan \phi_j \simeq \phi_j$, one obtains

$$(F_{py})_j = \left(-\frac{1}{2}\rho DU^2 C_f \frac{D}{D_h} + \rho gA\right) \phi_j. \tag{2.20}$$

2.3.3 Viscous Hydrodynamic Forces, F_N and F_L

The viscous forces acting on long inclined cylinders have been discussed by Taylor (1952a). Taylor looked into cases where the boundary layer is either laminar (Appendix A) or turbulent (Appendix B). One can write these forces, as follows:

$$F_N = \frac{1}{2} \rho D U^2 \left(C_{dp} \sin^2 \theta + C_f \sin \theta \right), \quad F_L = \frac{1}{2} \rho D U^2 C_f \cos \theta , \qquad (2.21)$$

where $\theta = \tan^{-1} [(\partial y/\partial x)] + \tan^{-1} [(\partial y/\partial t)/U]$. For small $(\partial y/\partial x)$ and $(\partial y/\partial t)/U$, these equations reduce to

$$F_N = \frac{1}{2} \rho DU C_f \left(U \frac{\partial y}{\partial x} + \frac{\partial y}{\partial t} \right) + \frac{1}{2} \rho D C_d \frac{\partial y}{\partial t} , \qquad F_L = \frac{1}{2} \rho D U^2 C_f , \qquad (2.22)$$

where the second term in F_N represents a linearization of the quadratic viscous force at zero flow velocity (Appendix C), $\frac{1}{2}\rho DC_{dp}|\partial y/\partial t|(\partial y/\partial t)$, in which the drag coefficient represents $C_d = C_{dp}(\overline{\partial y/\partial t})$. For a point in the jth cylinder for the articulated system considered, these expressions may be written in the form

$$(F_N)_j = \frac{1}{2}\rho DU C_f \left(\sum_{q=0}^{j-1} l_q \dot{\phi}_q + \xi \dot{\phi}_j + U \phi_j \right) + \frac{1}{2}\rho DC_d \left(\sum_{q=0}^{j-1} l_q \dot{\phi}_q + \xi \dot{\phi}_j \right),$$

$$(F_L)_j = \frac{1}{2}\rho DU^2 C_f.$$
(2.23)

One could have used the more sophisticated but complex theory of Mateescu and Païdoussis (1987) to obtain more accurate expressions for the unsteady components of $(F_N)_j$ and $(F_L)_j$ —but, as shown by Païdoussis *et al.* (1990), the two sets of expressions give very similar results insofar as stability of the continuously flexible version of this system is concerned. Hence, the added complexity of that theory is not warranted for the purposes of this Thesis.

2.4 LAGRANGIAN EQUATIONS

The Lagrangian method is useful for finding the equations of motion when the number of degrees of freedom is large. Accordingly, if the generalized coordinates are the angles of deformation ϕ_j , then the equations of motion may be obtained by application of Lagrange's equations

$$\frac{d}{dt}\left(\frac{\partial L}{\partial \dot{\phi}_{i}}\right) - \frac{\partial L}{\partial \phi_{i}} = Q_{i}. \tag{2.24}$$

Here L = T - V, where T is the total kinetic energy of the system and is given by

$$T = T_{\bullet} + T_{f} \,, \tag{2.25}$$

where T_s and T_f are given by equations (2.3) and (2.11), respectively. The potential energy is exclusively associated with the articulated system, and so it is given by equation (2.6). Q_j are the generalized forces, which will be dealt with next.

It is recalled that since a linearized set of equations is sought in this chapter, whereas the energies are required to be correct to $O(\epsilon^2)$, the forces (and the generalized forces) must be correct only to $O(\epsilon)$, where $\phi_j \simeq O(\epsilon)$.

The generalized forces (actually moments) Q_j , $j=1,2,\ldots N$, will be determined by considering the virtual work δW_j associated with virtual displacements $\delta \phi_j$ in the generalized coordinates ϕ_j . Then the generalized force Q_j is defined via $\delta W_j = Q_j \, \delta \phi_j$. We proceed to determine the component of the generalized force Q_1 , associated with cylinder 1 and denoted by $Q_{1,1}$.

As shown in Figure 2.5(a), when the first cylinder is displaced by $\delta \phi_1$, the forces F_N and F_{py} do work, but F_L and the base pressure p_1A_1 do not. Hence, the virtual work $\delta W_{1,1}$ is given by

$$\delta W_{1,1} = -\int_0^{t_1} (F_N)_1 \, \xi \, \delta \phi_1 \, d\xi + \int_0^{t_1} (F_{py})_1 \, \xi \, \delta \phi_1 \cos \phi_1 \, d\xi \,; \tag{2.26}$$

then, $Q_{1,1} = \delta W_{1,1} / \delta \phi_1$.

Similarly, the virtual work associated with the forces acting on the second cylinder, $\delta W_{1,2}$, due to a virtual displacement associated with the generalized coordinate ϕ_1 , may be evaluated with the aid of Figure 2.5(b). Thus, $\delta W_{1,2}$ is given by

$$\delta W_{1,2} = -\int_0^{l_2} (F_N)_2 \, l_1 \, \delta \phi_1 \cos(\phi_2 - \phi_1) \, d\xi + \int_0^{l_2} (F_{py})_2 \, l_1 \, \delta \phi_1 \cos \phi_1 d\xi$$

+
$$\int_0^{l_2} (F_L)_2 \, l_1 \delta \phi_1 \sin(\phi_2 - \phi_1) \, d\xi - \left(\frac{\partial p}{\partial x}\right)_2 A_2 \, l_2 \, l_1 \, \delta \phi_1 \sin(\phi_2 - \phi_1),$$
 (2.27)

and so on for $\delta W_{1,k}$, $k=3,\ldots,N-1$, from which the $Q_{1,k}$ may be determined. The virtual work associated with the last cylinder, $\delta W_{1,N}$, will have the additional terms

$$\frac{1}{2} \rho D^2 U^2 C_b l_1 \delta \phi_1 \sin(\phi_N - \phi_1) + F_{nc} l_1 \delta \phi_1. \qquad (2.28)$$

The first of these two terms is associated with base drag at the free end, involving a base drag coefficient C_b , and the second term is associated with the nonconservative hydrodynamic forces F_{nc} , as discussed in Section 2.3.1. The total generalized force is simply given by

$$Q_1 = \sum_{j=1}^{N} Q_{1,j}. (2.29)$$

Proceeding in this manner and linearizing, the generalized force Q_j associated with the generalized coordinate ϕ_j is

$$Q_{j} = -\int_{0}^{l_{j}} (F_{N})_{j} \, \xi \, d\xi + \int_{0}^{l_{j}} (F_{py})_{j} \, \xi \, d\xi + \sum_{i=j+1}^{N} \left\{ -\int_{0}^{l_{i}} (F_{N})_{i} \, l_{j} \, d\xi + \int_{0}^{l_{i}} (F_{py})_{i} \, l_{j} \, d\xi + \int_{0}^{l_{i}} (F_{py})_{i} \, l_{j} \, d\xi + \int_{0}^{l_{i}} (F_{D})_{i} \, l_{j} \, (\phi_{i} - \phi_{j}) d\xi - (\partial p / \partial x)_{i} \, A_{i} \, l_{i} \, l_{j} \, (\phi_{i} - \phi_{j}) \right\} + \frac{1}{2} \rho D^{2} \, U^{2} \, C_{b} \, l_{j} (\phi_{N} - \phi_{j}) - F_{nc} \, l_{j} \,, \qquad (2.30)$$

where $(F_N)_j$ and $(F_L)_j$, $(F_{py})_j$, F_{nc} are given by linearized versions of equations (2.23), (2.20) and (2.13), respectively, for small ϕ_j (such that $\sin \phi_j \simeq \phi_j$, $\cos \phi_j \simeq 1$).

2.5 TRILINEAR AND CUBIC SPRING DESCRIPTION

Following the onset of flutter instability, the amplitude of oscillation will grow, resulting in impacting with the outer cylinder. The interaction with the outer cylinder is approximately trilinear, as shown in Figure 2.6. For contact at the

second articulation (lower end of the first cylinder)¹ and denoting the displacement at that point by $\eta = \ell_1 \phi_1$ and the contact stiffness by k_t , the force exerted by the trilinear spring may be expressed as

$$F_t(\eta) = k_t \left\{ \eta - \frac{1}{2} \left[|\eta + \eta_g| - |\eta - \eta_g| \right] \right\} ,$$

where $\eta_g = l_1 \phi_g$ is defined in Figure 2.6. Recalling that in the equations of motion we are dealing with moments and angles, rather than forces and displacements, the moment associated with the trilinear spring is

$$\mathcal{M}_{t}(\phi_{1}) = k_{t} l_{1}^{2} \left\{ \phi_{1} - \frac{1}{2} \left[|\phi_{1} + \phi_{g}| - |\phi_{1} - \phi_{g}| \right] \right\}. \tag{2.31}$$

For analytical convenience, an alternative, cubic-spring approximation may be utilized instead to model impacting with the outer cylinder. The force-displacement relationship in this case is

$$F_c(\eta) = k_c \, \eta^3 \,,$$

and the moment-displacement relationship is

$$\mathcal{M}_c(\phi_1) = k_c \, l_1^2 \, \phi_1^3 \,. \tag{2.32}$$

2.6 DERIVATION OF THE EQUATIONS OF MOTION

Equations (2.3), (2.11), (2.6), (2.30), (2.31) or (2.32) depending of the nonlinearity type, are substituted into Lagrange's equations,

$$\frac{d}{dt}\left(\frac{\partial T}{\partial \dot{\phi}_{i}}\right) - \frac{\partial T}{\partial \phi_{j}} + \frac{\partial V}{\partial \phi_{j}} = Q_{j}, \qquad j = 1, 2, \dots, N,$$
(2.33)

for a system of N articulated cylinders, yielding N equations of motion.

¹This, in fact, was later confirmed to represent the 'natural' actual motion.

We consider a "uniform" system, where all the cylinders have the same mass per unit length $(m_j = m, j = 1, ..., N)$ and physical dimensions $(A_j = A, D_j = D,$ etc., j = 1, ..., N), including length $l_j = l$, j = 1, ..., N - 1, except for the last cylinder, which is l_N long (see next paragraph). Similarly, the stiffnesses of all intercylinder springs are equal, $k_j = k$, j = 1, ..., N.

The equations of motion may now be rendered non-dimensional with the aid of the dimensionless parameters

$$\beta = \rho A/(\rho A + m), \qquad \gamma = (m - \rho A)gL^2 N/k, \qquad u = (\rho A L N/k)^{1/2} U,$$

$$\epsilon = L/D, \qquad l_N = el, \qquad c = (4/\pi)C_d [M L N/k]^{1/2}, \qquad c_f = (4/\pi)C_f, \quad (2.34)$$

$$c_b = (4/\pi)C_b, \qquad h = D_h/D, \qquad \tau = \left[(\rho A + m)L^3 N/k \right]^{-1/2} t,$$

$$\kappa_c = (k_c/k)L^4, \qquad \kappa_t = (k_t/k)L^2 N^2,$$

where L=Nl, and k is taken to be k=EI/l, EI being the flexural rigidity of a fictitious, continuously-flexible system to which the present system would converge as $N\to\infty$ (Païdoussis and Deksnis 1970). In a study of convergence of an articulated system of pipes conveying fluid (discrete N) to the equivalent continuously flexible one $(N=\infty)$ as N is increased, it was found (Païdoussis and Deksnis 1970) that optimum convergence is achieved with the length of the last cylinder $l_N=el$, $e=\frac{1}{2}$; this value is arbitrarily adopted here also.

We have also introduced in our equations the nonlinear moments associated, respectively, with the cubic spring, $\mathcal{M}_c = \kappa_c \phi_1^3$, or with the trilinear spring, $\mathcal{M}_t = \kappa_t \left\{ \phi_1 - \frac{1}{2} \left[|\phi_1 + \phi_g| - |\phi_1 - \phi_g| \right] \right\}$, where κ_c and κ_t have been already defined in equations (2.34).

The nondimensional equations of motion have been obtained for a system of N articulated cylinders, of course; however, the results to be discussed in this Thesis are confined to N=2, N=3 and N=4.

2.6.1 The equations of motion for N=2

The equations of motion for a two-degree-of-freedom articulated cylinder system (N=2) are the following:

$$[1 + (\chi - 1)\beta] \left[(\frac{1}{3} + e)\ddot{\phi}_1 + \frac{1}{2}e^2\ddot{\phi}_2 \right] + \frac{1}{6}(3e + 1) u \epsilon c_f \sqrt{\beta} \dot{\phi}_1 + \frac{1}{4} u \epsilon c_f \sqrt{\beta} e^2 \dot{\phi}_2 + \frac{1}{6}(3e + 1) \epsilon c\sqrt{\beta} \dot{\phi}_1 + \frac{1}{4} \epsilon c\sqrt{\beta} e^2 \dot{\phi}_2 + \chi (1 - f) u N \sqrt{\beta} \dot{\phi}_1 + \chi (2 - f) u N \sqrt{\beta} e \dot{\phi}_2 + \frac{1}{4}(1 + h^{-1})(2e + 1) u^2 N \epsilon c_f \phi_1 - \chi u^2 N^2 \phi_1 + \chi (1 - f) u^2 N^2 \phi_2 + \frac{1}{2} u^2 N^2 c_b (\phi_1 - \phi_2) + \frac{1}{2} (2e + 1) N \gamma \phi_1 - N^4 (-2\phi_1 + \phi_2) + \mathcal{M}_c(\mathcal{M}_t) = 0,$$

$$[1 + (\chi - 1)\beta] \left[\frac{1}{2} e^2 \ddot{\phi}_1 + \frac{1}{3} e^3 \ddot{\phi}_2 \right] + \frac{1}{4} u \epsilon c_f \sqrt{\beta} e^2 \dot{\phi}_1 + \frac{1}{6} u \epsilon c_f \sqrt{\beta} e^3 \dot{\phi}_2 + \frac{1}{4} \epsilon c \sqrt{\beta} e^2 \dot{\phi}_1 + \frac{1}{6} \epsilon c \sqrt{\beta} e^3 \dot{\phi}_2 - \chi u N \sqrt{\beta} e f \dot{\phi}_1 + \chi (1 - f) u N \sqrt{\beta} e^2 \dot{\phi}_2 + \frac{1}{4}(1 + h^{-1}) u^2 N \epsilon c_f e^2 \phi_2 - \chi u^2 N^2 e f \phi_2 + \frac{1}{2} N \gamma e^2 \phi_2 + \frac{1}{4}(1 + h^{-1}) u^2 N \epsilon c_f e^2 \phi_2 - \chi u^2 N^2 e f \phi_2 + \frac{1}{2} N \gamma e^2 \phi_2 + \frac{1}{4}(4\phi_2 - \phi_1) = 0.$$

$$(2.35)$$

In these and the equations that follow, the dots denote differentiation with respect to τ . (It is noted that the definition of h in the equations (2.35), (2.36) and (2.37) is the inverse of what it is in some previous work (e.g., Païdoussis 1973); hence, the terms $1 + h^{-1}$ here, instead of 1 + h therein. The present definition is physically more meaningful: a small h represents a narrow annulus).

2.6.2 The equations of motion for N=3

Similarly, the equations of motion for a three-degree-of-freedom articulated cylinder system (N=3) are the following:

$$\begin{split} & \left[1 + (\chi - 1)\beta\right] \left[\left(\frac{4}{3} + e\right) \ddot{\phi}_1 + \left(\frac{1}{2} + e\right) \ddot{\phi}_2 + \frac{1}{2} e^2 \ddot{\phi}_3 \right] + \frac{1}{6} (3e + 4) u \, \epsilon \, c_f \, \sqrt{\beta} \, \dot{\phi}_1 \\ & + \frac{1}{4} (2e + 1) u \, \epsilon \, c_f \, \sqrt{\beta} \, \dot{\phi}_2 + \frac{1}{4} u \, \epsilon \, c_f \, e^2 \, \sqrt{\beta} \, \dot{\phi}_3 + \frac{1}{6} (3e + 4) \, \epsilon \, c \, \sqrt{\beta} \, \dot{\phi}_1 \\ & + \frac{1}{4} (2e + 1) \, \epsilon \, c \, \sqrt{\beta} \, \dot{\phi}_2 + \frac{1}{4} \, \epsilon \, c \, \sqrt{\beta} \, e^2 \, \dot{\phi}_3 + \chi \, (1 - f) \, u \, N \, \sqrt{\beta} \, \dot{\phi}_1 + \chi \, (2 - f) \, u \, N \, \sqrt{\beta} \, \dot{\phi}_2 \\ & + \chi \, (2 - f) \, u \, N \, \sqrt{\beta} \, e \, \dot{\phi}_3 + \frac{1}{4} (1 + h^{-1}) (2e + 3) \, u^2 \, N \, \epsilon \, c_f \, \phi_1 - \chi \, u^2 \, N^2 \, \phi_1 \end{split}$$

$$+\chi (1-f) u^2 N^2 \phi_3 + \frac{1}{2} u^2 N^2 c_b (\phi_1 - \phi_3) + \frac{1}{2} (2e+3) N \gamma \phi_1 + N^4 (2 \phi_1 - \phi_2)$$

+ $\mathcal{M}_c(\mathcal{M}_t) = 0$,

$$\begin{split} &[1+(\chi-1)\beta] \left[(\frac{1}{2}+e)\ddot{\phi}_1 + (\frac{1}{3}+e)\ddot{\phi}_2 + \frac{1}{2}\,e^2\,\ddot{\phi}_3 \right] + \frac{1}{4}\,(2e+1)\,u\,\epsilon\,c_f\,\sqrt{\beta}\,\dot{\phi}_1 \\ &+ \frac{1}{6}\,(3e+1)\,u\,\epsilon\,c_f\,\sqrt{\beta}\,\dot{\phi}_2 + \frac{1}{4}\,u\,\epsilon\,c_f\,\sqrt{\beta}\,e^2\,\dot{\phi}_3 + \frac{1}{4}\,(2e+1)\,\epsilon\,c\,\sqrt{\beta}\,\dot{\phi}_1 \\ &+ \frac{1}{6}\,(3e+1)\,\epsilon\,c\sqrt{\beta}\,\dot{\phi}_2 + \frac{1}{4}\,\epsilon\,c\sqrt{\beta}\,e^2\,\dot{\phi}_3 - \chi\,u\,N\,\sqrt{\beta}\,f\,\dot{\phi}_1 + \chi\,(1-f)\,u\,N\,\sqrt{\beta}\,\dot{\phi}_2 \\ &+ \chi\,(2-f)\,u\,N\,\sqrt{\beta}\,e\,\dot{\phi}_3 + \frac{1}{4}(1+h^{-1})(2e+1)\,u^2\,N\,\epsilon\,c_f\,\phi_2 - \chi\,u^2\,N^2\,\phi_2 \\ &+ \chi\,(1-f)\,u^2\,N^2\,\phi_3 + \frac{1}{2}\,u^2\,N^2\,c_b\,(\phi_2-\phi_3) + \frac{1}{2}(2e+1)\,N\,\gamma\,\phi_2 \\ &- N^4(\phi_1-2\phi_2+\phi_3) = 0, \end{split}$$

$$[1 + (\chi - 1)\beta] \left[\frac{1}{2} e^{2} \ddot{\phi}_{1} + \frac{1}{2} e^{2} \ddot{\phi}_{2} + \frac{1}{3} e^{3} \ddot{\phi}_{3} \right] + \frac{1}{4} u \epsilon c_{f} \sqrt{\beta} e^{2} \dot{\phi}_{1} + \frac{1}{4} u \epsilon c_{f} \sqrt{\beta} e^{2} \dot{\phi}_{2}$$

$$+ \frac{1}{6} u \epsilon c_{f} \sqrt{\beta} e^{3} \dot{\phi}_{3} + \frac{1}{4} \epsilon c \sqrt{\beta} e^{2} \dot{\phi}_{1} + \frac{1}{4} \epsilon c \sqrt{\beta} e^{2} \dot{\phi}_{2} + \frac{1}{6} \epsilon c \sqrt{\beta} e^{3} \dot{\phi}_{3}$$

$$- \chi u N \sqrt{\beta} e f \dot{\phi}_{1} - \chi u N \sqrt{\beta} e f \dot{\phi}_{2} + \chi (1 - f) u N \sqrt{\beta} e^{2} \dot{\phi}_{3}$$

$$+ \frac{1}{4} (h^{-1} + 1) u^{2} N \epsilon c_{f} e^{2} \phi_{3} - \chi u^{2} N^{2} e f \phi_{3} + \frac{1}{2} N \gamma e^{2} \phi_{3}$$

$$+ N^{4} (\phi_{3} - \phi_{2}) = 0. \tag{2.36}$$

2.6.3 The equations of motion for N=4

Finally, the equations of motion for a four-degree-of-freedom articulated cylinder system (N = 4) are the following:

$$\begin{split} &[1+(\chi-1)\beta] \left[(\frac{7}{3}+e) \, \ddot{\phi}_1 + (\frac{3}{2}+e) \, \ddot{\phi}_2 + (\frac{1}{2}+e) \, \ddot{\phi}_3 + \frac{1}{2} \, e^2 \, \ddot{\phi}_4 \right] \\ &+ \frac{1}{6} \left(3e+7 \right) u \, \epsilon \, c_f \, \sqrt{\beta} \, \dot{\phi}_1 + \, \frac{1}{4} (2e+3) \, u \, \epsilon \, c_f \, \sqrt{\beta} \, \dot{\phi}_2 + \, \frac{1}{4} (2e+1) \, u \, \epsilon \, c_f \, \sqrt{\beta} \, \dot{\phi}_3 \\ &+ \frac{1}{4} \, e^2 \, u \, \epsilon \, c_f \, \sqrt{\beta} \, \dot{\phi}_4 + \, \frac{1}{6} \left(3e+7 \right) \epsilon \, c \, \sqrt{\beta} \, \dot{\phi}_1 + \, \frac{1}{4} \left(2e+3 \right) \epsilon \, c \, \sqrt{\beta} \, \dot{\phi}_2 \\ &+ \frac{1}{4} \left(2e+1 \right) \epsilon \, c \, \sqrt{\beta} \, \dot{\phi}_3 + + \, \frac{1}{4} \, e^2 \epsilon \, c \, \sqrt{\beta} \, \dot{\phi}_4 + \chi (1-f) \, u \, N \, \sqrt{\beta} \, \dot{\phi}_1 \\ &+ \chi (2-f) \, u \, N \, \sqrt{\beta} \, \dot{\phi}_2 + \chi (2-f) \, u \, N \, \sqrt{\beta} \, \dot{\phi}_3 + \chi (2-f) \, u \, N \, \sqrt{\beta} \, e \, \dot{\phi}_4 \\ &+ \frac{1}{4} (1+h^{-1}) \left(2e+5 \right) u^2 \, N \, \epsilon \, c_f \, \phi_1 + \chi u^2 N^2 \left[-\phi_1 + (1-f)\phi_4 \right] \end{split}$$

$$\begin{split} &+\frac{1}{2}\,u^2\,N^2\,c_b\,(\phi_1-\phi_4)+\frac{1}{2}(2e+5)\,N\,\gamma\,\phi_1++N^4\,(2\,\phi_1-\phi_2)+\mathcal{M}_c(\mathcal{M}_t)=0\,,\\ &[1+(\chi-1)\beta]\,\left[(\frac{3}{2}+e)\,\ddot{\phi}_1+(\frac{4}{3}+e)\,\ddot{\phi}_2+(\frac{1}{2}+e)\,\ddot{\phi}_3+\frac{1}{2}\,e^2\,\ddot{\phi}_4\right]\\ &+\frac{1}{4}\,(2e+3)\,u\,\epsilon\,c_f\,\sqrt{\beta}\,\dot{\phi}_1+\frac{1}{6}\,(3e+4)\,u\,\epsilon\,c_f\,\sqrt{\beta}\,\dot{\phi}_2+\frac{1}{4}(2e+1)\,u\,\epsilon\,c_f\,\sqrt{\beta}\,\dot{\phi}_3\\ &+\frac{1}{4}\,u\,\epsilon\,c_f\,\sqrt{\beta}\,e^2\,\dot{\phi}_4+\frac{1}{4}\,(2e+3)\,\epsilon\,c\,\sqrt{\beta}\,\dot{\phi}_1+\frac{1}{6}(3e+4)\,\epsilon\,c\,\sqrt{\beta}\,\dot{\phi}_2\\ &+\frac{1}{4}(2e+1)\epsilon\,c\,\sqrt{\beta}\,\dot{\phi}_3+\frac{1}{4}\,\epsilon\,c\,\sqrt{\beta}\,e^2\,\dot{\phi}_4-\chi\,u\,N\,\sqrt{\beta}\,f\,\dot{\phi}_1+\chi\,(1-f)u\,N\,\sqrt{\beta}\,\dot{\phi}_2\\ &+\chi\,(2-f)\,u\,N\,\sqrt{\beta}\,\dot{\phi}_3+\chi\,(2-f)\,u\,N\,\sqrt{\beta}\,e\,\dot{\phi}_4\\ &+\frac{1}{4}\,(1+h^{-1})\,(2e+3)\,u^2\,N\,\epsilon\,c_f\,\phi_2-\chi\,u^2\,N^2\,[\phi_2-(1-f)\phi_4]\\ &+\frac{1}{4}\,u^2\,N^2c_b(\phi_2-\phi_1)+\frac{1}{2}(2e+3)\,N\,\gamma\,\phi_2+N^4(-\phi_1+2\,\phi_2-\phi_3)=0\,,\\ &[1+(\chi-1)\beta]\,\left[(\frac{1}{2}+e)\ddot{\phi}_1+(\frac{1}{2}+e)\ddot{\phi}_2+(\frac{1}{3}+e)\ddot{\phi}_3+\frac{1}{2}e^2\,\ddot{\phi}_4\right]\\ &+\frac{1}{4}\,(2e+1)\,u\,\epsilon\,c_f\,\sqrt{\beta}\,\dot{\phi}_1+\frac{1}{4}\,(2e+1)\,u\,\epsilon\,c_f\,\sqrt{\beta}\,\dot{\phi}_2\\ &+\frac{1}{6}\,(3e+1)\,\epsilon\,c\,\sqrt{\beta}\,\dot{\phi}_3+\frac{1}{4}\,\epsilon\,c\,\sqrt{\beta}\,e^2\,\dot{\phi}_4-\chi\,u\,N\,\sqrt{\beta}\,f\,\dot{\phi}_1-\chi\,u\,N\,\sqrt{\beta}\,f\,\dot{\phi}_2\\ &+\chi\,(1-f)\,u\,N\,\sqrt{\beta}\,\dot{\phi}_3+\chi\,(2-f)\,u\,N\,\sqrt{\beta}\,e\,\dot{\phi}_4+\frac{1}{4}\,(1+h^{-1})(2e+1)u^2\,N\,\epsilon\,c_f\,\phi_3\\ &-\chi\,u^2\,N^2\,\phi_3+\chi(1-f)\,u^2\,N^2\,\phi_4+\frac{1}{2}u^2\,N^2\,c_b\,(\phi_3-\phi_4)+\frac{1}{2}\,(2e+1)\,N\,\gamma\,\phi_3\\ &-N^4\,(\phi_2-2\phi_3+\phi_4)=0\,,\\ &[1+(\chi-1)\beta]\,\left[\frac{1}{2}e^2\ddot{\phi}_1+\frac{1}{2}\,e^2\,\ddot{\phi}_2+\frac{1}{2}\,e^2\,\ddot{\phi}_3+\frac{1}{6}\,u\,\epsilon\,c_f\,\sqrt{\beta}\,e^3\,\dot{\phi}_4+\frac{1}{4}\,u\,\epsilon\,c_f\,\sqrt{\beta}\,e^2\,\dot{\phi}_1\\ &+\frac{1}{4}\,u\,\epsilon\,c_f\,\sqrt{\beta}\,e^2\dot{\phi}_2+\frac{1}{4}\,u\,\epsilon\,c_f\,\sqrt{\beta}\,e^2\dot{\phi}_3+\frac{1}{6}\,u\,\epsilon\,c_f\,\sqrt{\beta}\,e^3\,\dot{\phi}_4+\frac{1}{4}\,u\,\epsilon\,c_f\,\sqrt{\beta}\,e^2\dot{\phi}_1\\ &+\frac{1}{4}\,u\,\epsilon\,c_f\,\sqrt{\beta}\,e^2\dot{\phi}_2+\frac{1}{4}\,u\,\epsilon\,c_f\,\sqrt{\beta}\,e^2\dot{\phi}_3+\frac{1}{6}\,u\,\epsilon\,c_f\,\sqrt{\beta}\,e^3\dot{\phi}_4-\chi\,u\,N\,\sqrt{\beta}\,e\,f\,\dot{\phi}_1\\ &-\chi\,u\,N\,\sqrt{\beta}\,e\,f\,\dot{\phi}_2-\chi\,u\,N\,\sqrt{\beta}\,e\,f\,\dot{\phi}_3+\chi(1-f)\,u\,N\,\sqrt{\beta}\,e^2\,\dot{\phi}_4\\ &+\frac{1}{4}(h^{-1}+1)u^2\,N\,\epsilon\,c_f\,e^2\phi_4-\chi\,u^2\,N^2\,e\,f\,\phi_4+\frac{1}{2}\,N\,\gamma\,e^2\phi_4\\ &+\frac{1}{4}(h^{-1}+1)u^2\,N\,\epsilon\,c_f\,e^2\phi_4-\chi\,u^2\,N^2\,e\,f\,\phi_4+\frac{1}{2}\,N\,\gamma\,e^2\phi_4\\ &+N^4\,(\phi_4-\phi_3)=0\,. \end{split}{\begin{tabular}{l}}$$

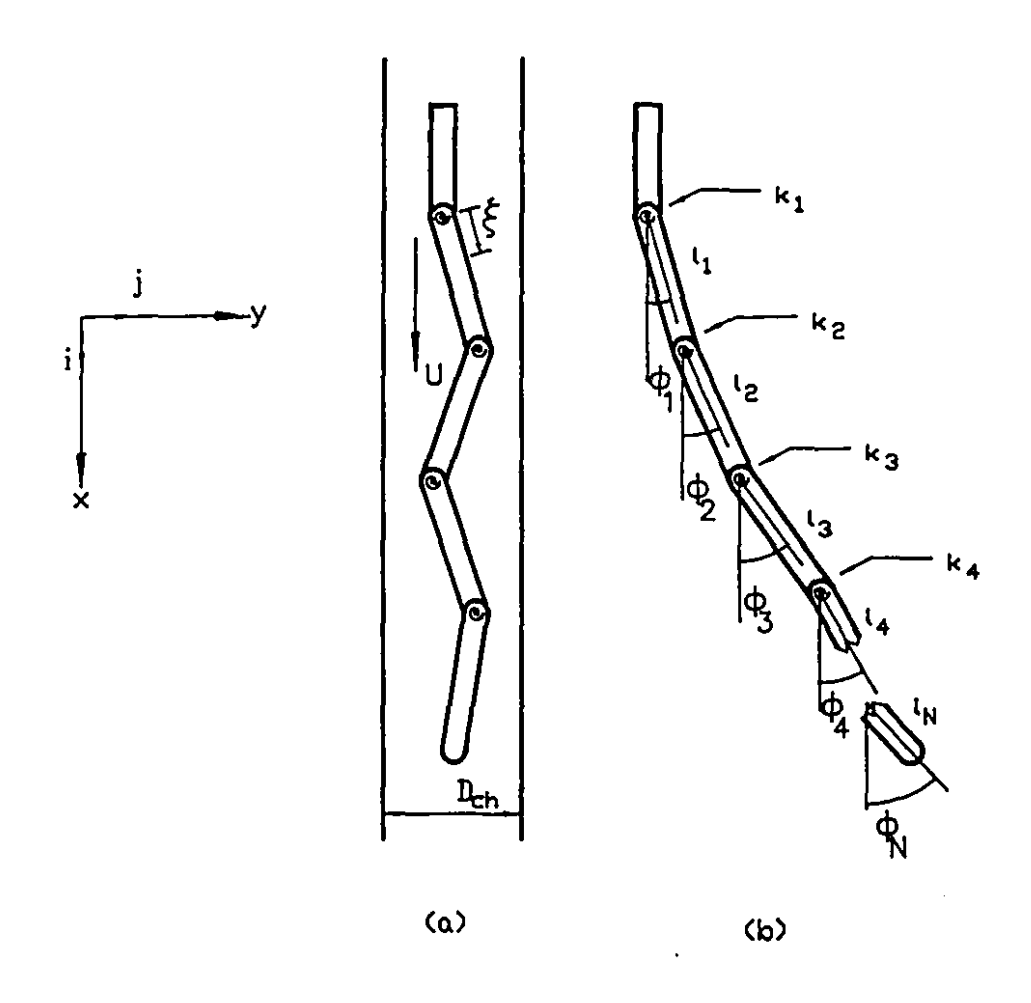


Figure 2.1. (a) Diagram of the articulated cylindrical system in confining channel, subjected to a mean annular flow of velocity U; (b) definition diagram for the generalized coordinates ϕ_j , $j=1,\ldots,N$, showing the cylinder lengths ℓ_j and interconnecting springs of stiffnesses k_j .

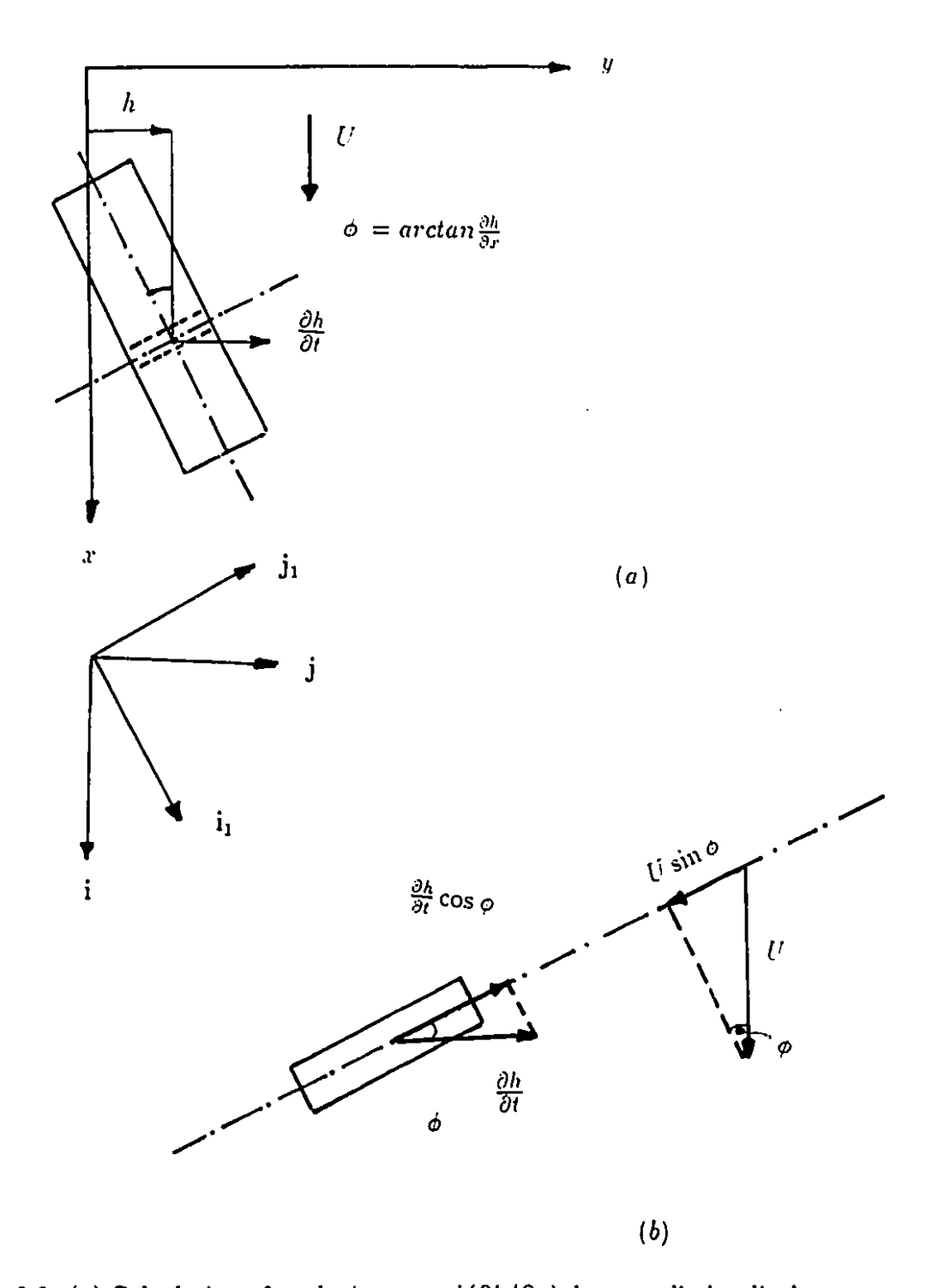


Figure 2.2. (a) Calculation of angle $\phi = \arctan(\partial h/\partial x)$ due to cylinder displacement h(x,t) in the y direction; (b) calculation of the relative fluid-body velocity in the \mathbf{j}_1 direction.

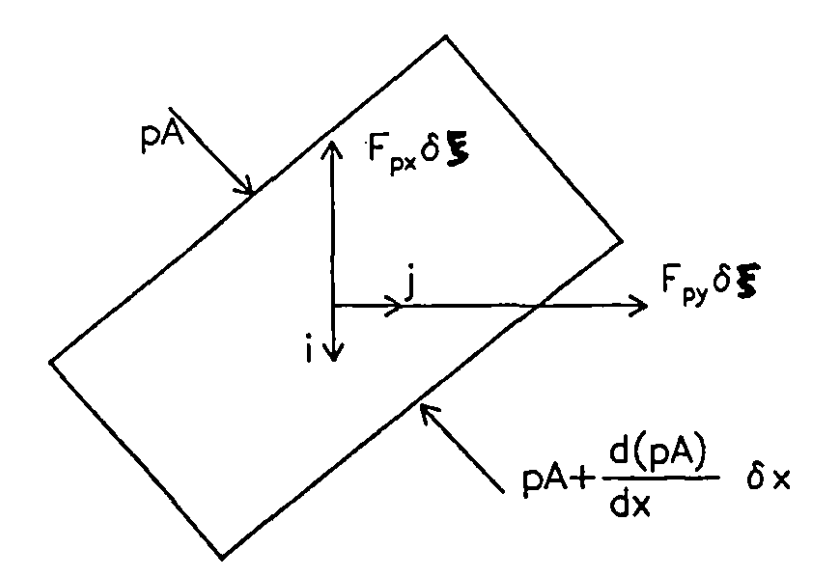


Figure 2.3. Pressure forces acting on an element δx of one of the rigid cylinders of the articulated system.

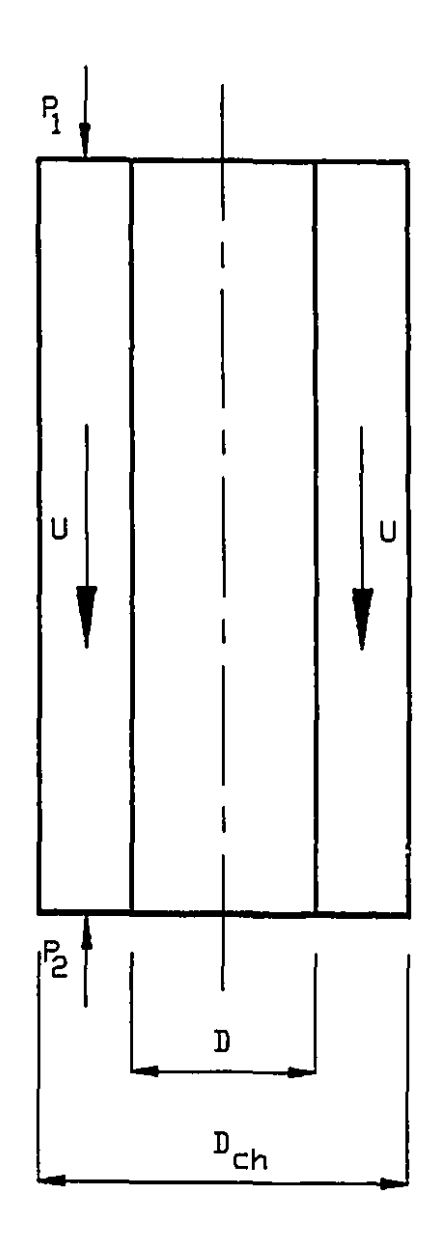


Figure 2.4. Calculation of the steady-state A(dp/dx) from the momentum equation.

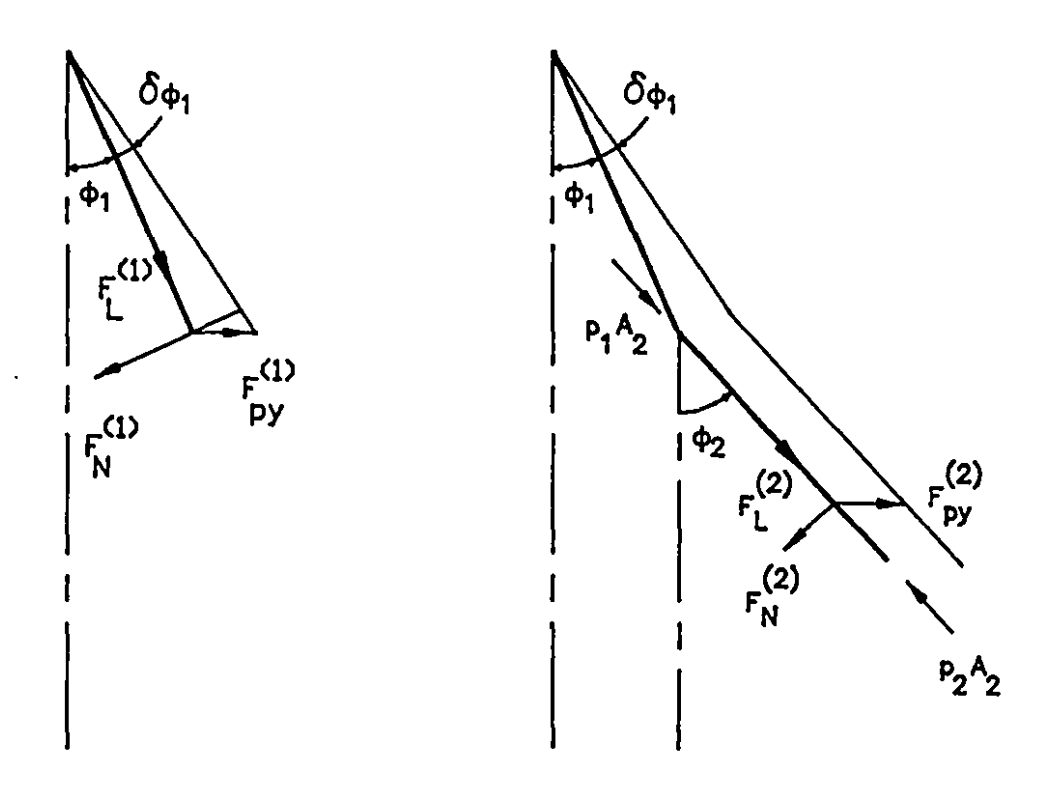


Figure 2.5. Diagrams for the calculation of the generalized forces for (a) the first cylinder and (b) the second cylinder.

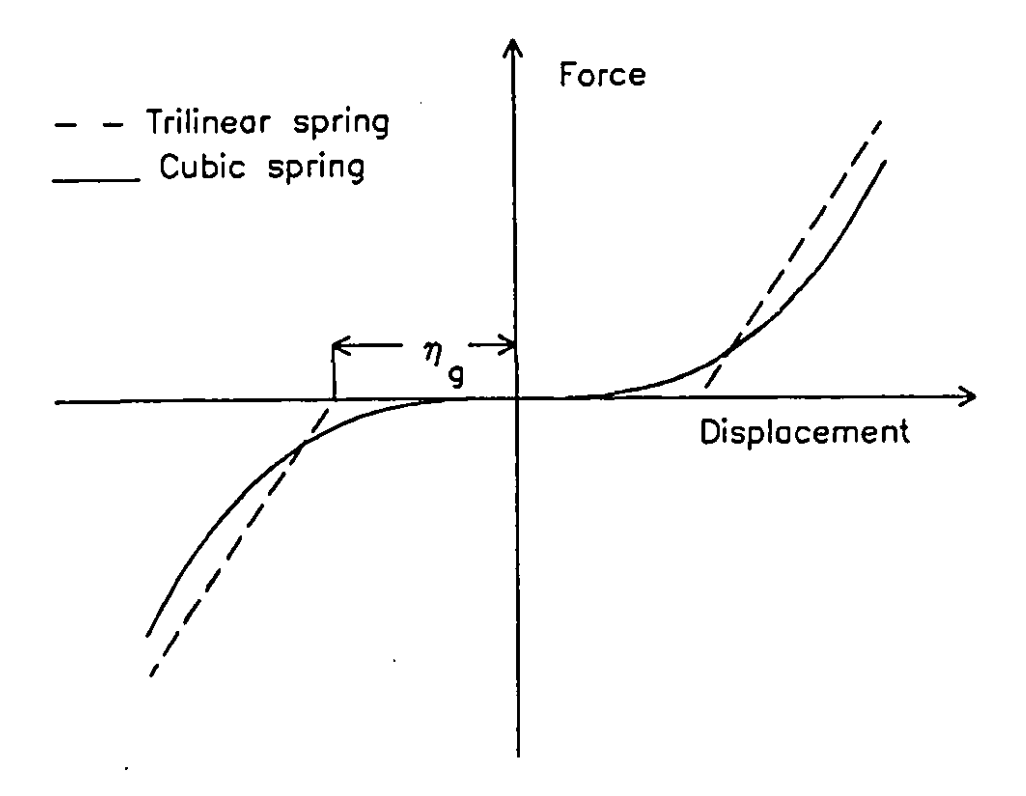


Figure 2.6. Force-displacement curves for the realistic trilinear-spring model for impacting of the articulated system on the confining channel, and the cubic-spring idealization.

Chapter 3

THEORETICAL METHODS

3.1 STABILITY OF THE LINEARIZED SYSTEM

Before proceeding to nonlinear analysis, it is necessary to first understand the linear behaviour of the system.

Therefore, the dimensionless linearized equations of motion are rewritten in matrix form, such that

$$[M]\{\ddot{\phi}\} + [C]\{\dot{\phi}\} + [K]\{\phi\} = \{0\},\tag{3.1}$$

where [M] is the mass, [C] is the damping, and [K] the stiffness matrix; $\{\phi\}$ is the vector of the generalized coordinates.

Let the following square partitioned matrices be defined as

$$[B] = \begin{bmatrix} [0] & [M] \\ [M] & [C] \end{bmatrix}, \quad [E] = \begin{bmatrix} -[M] & [0] \\ [0] & [K] \end{bmatrix}, \tag{3.2}$$

each matrix being of order 2N, and the vector $\{z\}$ as

$$\{z\} = \left\{ \begin{array}{c} \{\dot{\phi}\} \\ \{\phi\} \end{array} \right\} . \tag{3.3}$$

It may now be verified that the linearized equations of motion (3.1) may be written in the form

$$[B] \{\dot{z}\} + [E] \{z\} = \{0\}. \tag{3.4}$$

Pre-multiplying the equation (3.4) by $[B]^{-1}$ and defining $[B]^{-1}$ [E] = -[Y], where

$$[B]^{-1} = \begin{bmatrix} -[M]^{-1} [C] [M]^{-1} & [M]^{-1} \\ [M]^{-1} & [0] \end{bmatrix},$$
(3.5)

equation (3.4) becomes

$$\{\dot{z}\} - [Y]\{z\} = \{0\}.$$
 (3.6)

Solutions of equation (3.6) are then sought of the form

$$\{z\} = \{\overline{\phi}\} \exp(i\omega\tau), \qquad (3.7)$$

and by replacing these solutions into the previous equation we obtain

$$(\lambda[I] - [Y])\{\overline{\phi}_i\} = \{0\},$$
 (3.8)

in which $\lambda=i\omega$; non-trivial solutions are obtained when det $(\lambda\,[I]-[Y])=0$, which gives 2N eigenvalues of the matrix [Y], λ_j .

The eigenvalues λ_j of the system, which are generally complex, permit the assessment of (linear) stability for each set of system parameters. For a stable system, the λ_j are either real and negative or complex conjugate with negative real parts. The corresponding eigenvectors are $\{\overline{\phi}_j\}$.

Critical values of a parameter, in our case the flow velocity u, are needed in order to determine where the eigenvalues of the linearized system contain a purely imaginary pair (Hopf bifurcation) or a single zero value (pitchfork bifurcation).

In the following sections, the Argand diagrams are presented for the real and imaginary parts of the eigenvalues of the system, $Re(\lambda_j)$ and $Im(\lambda_j)$, as functions of the flow velocity u, for the corresponding modes of the articulated system (N=2,3,4). The Argand diagrams will show the behaviour of the system from

the point of view of linear stability about the original (straight) configuration of the system.

3.2 ROUTES TO CHAOS

Chaotic phenomena may be found in a wide class of natural events in the physical world. Chaos can be thought of as a new regime of nonlinear oscillations, as a compromise between competing periodicities, as accumulation of many instabilities, or (in fluid mechanics) as the prelude to turbulence.

Some "routes" or "scenarios" towards chaos have been proposed which are, in fact, series of a limited number of bifurcations. They are classified mainly into three routes, according to the way in which the periodic regime loses its stability: (i) the Period-doubling route, (ii) the Quasi-periodic route and (iii) the Intermittency route.

In analyzing one of these three routes to chaos, one should vary one or more of the control parameters in the system. In our dynamical system case, we shall choose the dimensionless flow velocity u as the control parameter. Short descriptions of these routes to chaos are given in the following subsections.

3.2.1 Period-doubling route to chaos

In the period-doubling phenomenon, one starts with a system which has a fundamentally periodic motion. Then, as the control parameter u is varied, the motion undergoes a bifurcation, or change in its periodic motion to twice the period of the original oscillation. As u is changed further, the system bifurcates to periodic motions with twice the period T or half the frequency f of the previous oscillation, and this will entail:

multiplication by two of the number of points of a Poincaré map

• the appearance in the Fourier spectrum of the frequency f/2 and its odd subharmonics 3f/2, 5f/2, 7f/2, and so on.

The study of period-doubling bifurcations has revealed a new universal constant, the "ideal" Feigenbaum number, Fei = 4.6692016, defined as the ratio of successive differences in values of the control parameter between period-doubling bifurcations. In our case, if u_p is the control parameter at which the pth bifurcation occurs, then we may define its corresponding Feigenbaum number Feip as follows:

$$Fei_{p} = \lim_{p \to \infty} \frac{u_{p} - u_{p-1}}{u_{p+1} - u_{p}}.$$
 (3.9)

In practice, as well as for the articulated system considered in this Thesis, the limit approaches Fei by the third or fourth bifurcation, i.e., when p = 3 or 4.

This period-doubling bifurcation process will start at a critical value of the control parameter (identified in equation (3.9) as u_{p-1}), after which the motion becomes chaotic, and remains so for a range of the control parameter; however, it may happen that, as the control parameter is increased, periodic windows may develop which, in turn, may undergo period-doubling bifurcations leading once more to chaotic motions.

3.2.2 Quasiperiodic route to chaos

Before explaining this route to chaos, we shall define the difference between a periodic and a quasiperiodic motion, by taking our two-degree-of-freedom system as an example. The state of the system may be characterized by the angular displacements ϕ_1 and ϕ_2 , and by their corresponding velocities, $\dot{\phi}_1$ and $\dot{\phi}_2$. If the system has two frequencies f_1 and f_2 , its displacements may be written as $\phi_1 = \sin f_1 t$ and $\phi_2 = \sin f_2 t$, with $|\dot{\phi}_1| = f_1$ and $|\dot{\phi}_2| = f_2$. The ratio f_1/f_2 will represent the number of rotations in the ϕ_1 direction per rotation in the ϕ_2 direction.

If $f_1/f_2 = n_1/n_2$ is rational, the motion of the system is periodic with period n_2 and completes n_1 cycles per period.

If f_1/f_2 is irrational, the two frequencies are incommensurate, and the motion is quasiperiodic-two (Bergé et al. 1984). Finally, a system containing r incommensurate frequencies, is said to be quasiperiodic-r.

The route to chaos associated with quasiperiodicity has been proposed by Newhouse et al. (1978). Suppose that when the control parameter is increased, the system loses its stability (fixed point) and begins to oscillate with frequency f_1 which corresponds to the first Hopf bifurcation. Now suppose that the same process is repeated two more times, so that a total of three successive Hopf bifurcations have occurred, producing three frequencies f_1 , f_2 and f_3 .

This can be explained as follows: The second Hopf bifurcation transforms the periodic regime (frequency f_1) into a quasiperiodic-two regime (frequencies f_1 and f_2). Furthermore, the third Hopf bifurcation causes the transition from the quasiperiodic regime with two frequencies to a quasiperiodic one with three frequencies (f_1 , f_2 and f_3).

As the control parameter is changed further, the time-dependent behaviour of the system is no longer quasiperiodic with three frequencies, and it becomes chaotic. Thus, the precursor to such chaotic motion is the presence of two simultaneous periodic oscillations of incommensurate frequencies f_1 and f_2 . The winding number (rotation number) has been defined as a measure of the quasiperiodic motion, and represents in fact the ratio between f_1 and f_2 , f_1/f_2 .

3.2.3 Intermittence route to chaos

In this last route to chaos, one observes long periods of periodic motion with bursts of chaos. As one varies a parameter, the chaotic bursts become more frequent and longer (Manneville and Pomeau 1980). Some models for intermittency predict that the average time of the regular or "laminar" phase of the motion $<\tau>$ will scale

in a precise way as some parameter is varied; for example, $<\tau>\simeq (u-u_{cr})^{-1/2}$, where u_{cr} is always the critical flow velocity.

Furthermore, the theory of intermittent transitions may be divided into two parts [as explained by Bergé, Pomeau and Vidal (1984)]. The first part, associated with Floquet theory, deals with the linear instability of a limit cycle, explaining the "spontaneous" growth of fluctuations, starting from a regime close to the periodic regime. Classification of intermittency into types I, II and III is based on the three types of linear instabilities of periodic trajectories: crossing of the unit circle by the Floquet multiplier at +1 (type I), -1 (type III), or at two complex conjugate eigenvalues (type II).

The second is the process of "relaminarization" via which the intermittent fluctuation ceases, to be replaced by another phase of regular oscillations (laminar phase). The idea of laminar phase makes sense only if, while it lasts, we may observe a large number of these oscillations. If these laminar phases are represented through "regular" limit cycles, then the intermittency is of type I, as already observed in the Lorenz model. The shapes and the slopes for the first return map I_{k+1} versus I_k (in type I intermittency), or for the second return map I_{k+2} versus I_k (in type III intermittency), where I_k is the kth maximum value for the velocity or the displacement of one articulated cylinder in time (for our system) are studied, and then the type of intermittency which occurs in the system may be easily identified. Furthermore, by drawing the distribution of the lengths of laminar phases $P(\tau)$ in time τ , as well as the number of laminar phases $N(\tau > \tau_0)$ lasting longer than τ_0 versus τ_0 , one may distinguish between type I and type III intermittency.

3.3 NONLINEAR BEHAVIOUR OF THE SYSTEM

3.3.1 Bifurcation and Phase-Plane diagrams

In this system, the number of degrees of freedom has been defined as the number of pairs of displacement-velocity which, more physically speaking, is in fact equal to the number of articulated cylinders in the system.

Whenever the solution to an equation or system of equations changes qualitatively at a given value – called a critical value – of a parameter, this will be called a bifurcation. The point in parameter space where such an event occurs is defined as a bifurcation point. From this bifurcation point emerge several (two or more) solution branches, either stable or unstable. The representation of any characteristic property of the solutions as a function of the bifurcation parameter constitutes a bifurcation diagram.

In this Thesis, graphing a typical property of the solution, e.g. the maximum displacement ϕ_{max} , as a function of the flow velocity u, we construct the bifurcation diagram for flow velocities u higher than u_{cr} ; u_{cr} being the critical flow velocity for which the system becomes unstable, either by flutter or by divergence, which in nonlinear analysis correspond to a Hopf and a pitchfork bifurcation, respectively. In the results to be shown, ϕ_{max} corresponds to the maximum value of first cylinder angular displacement $\phi_1(t)$, which is $\phi_{1max}(t)$, so that the bifurcation diagram represents $\phi_{1max}(t)$ versus u.

To clarify the meaning of the dynamics depicted in a bifurcation diagram, phase-plane portraits are also presented. The phase-plane portraits present in a compact way the evolution of the system with time, for example showing the velocity of the first cylinder $\dot{\phi}_1$ versus its displacement ϕ_1 .

In the end, it can be specified that if the system undergoes period—one motion, which is equivalent to a limit cycle, this motion may be represented on a bifurcation diagram by one point; if the system undergoes period—two, —four, —eight motion, these motions are represented in the bifurcation diagram by, respectively, two, four and eight points. Quasiperiodic and chaotic motions are represented by many points, and this is why it is very hard to distinguish between these two motions in bifurcation diagrams. In order to really differentiate these motions, we shall need more nonlinear dynamics tools, which will be described in the following sections.

3.3.2 Time traces and power spectra

The results obtained could be verified by plotting time traces, for example, the displacement of the first cylinder, i.e., ϕ_{1max} versus time τ , and computing their corresponding power spectra. These are very important for characterizing quasiperiodic motion and the intermittence route to chaos. Usually, the power spectrum gives the r.m.s. value of each frequency component, and the ordinate scale is logarithmic.

The emergence in the power spectrum of the subharmonics $f_1/2$, $f_1/4$, $f_1/8$, $f_1/16$, $f_1/32$ (and their odd subharmonics) is the signature of the period-doubling route to chaos. From these results we can evaluate the convergence ratio of the successive bifurcations which should be close to the Feigenbaum number predicted by theory.

One identifies a quasiperiodic-two motion by looking, generally, for the value of the ratio of the two fundamental frequencies, f_1 and f_2 , that is, f_1/f_2 .

If f_1/f_2 is irrational, then the frequencies of the high-amplitude peaks will be simple combinations $|m_1f_1 \pm m_2f_2|$, with m_1 and m_2 small integers: 0, ± 1 , ± 2 ,..., and the motion will be quasiperiodic-two of two incommensurate frequencies f_1 and f_2 .

If f_1/f_2 is rational, with $f_1/f_2 = n_1/n_2$ (n_1 and n_2 integers), the "quasiperiodic" motion is in fact periodic with period $T = n_1T_1 = n_2T_2$, and the frequencies of the high-amplitude peaks are harmonics of the lowest frequency $f = f_1 - f_2$: $f = 1/T = f_1/n_1 = f_2/n_2$. Then, consecutive peaks in the spectrum are always separated by the same distance of 1/T and one says that there is frequency locking of f_1 with f_2 . In the Section 3.3.3, we shall see the differences in Poincaré maps, depending of the value of f_1/f_2 .

The time traces are also one of the most useful tools for recognizing the intermittence route to chaos, for which the system changes its behaviour in time from periodic or laminar phases to chaotic and back again.

Finally, one cannot distinguish between chaotic and random motion by looking at power spectra. This limits the applicability of power spectra in this respect, and leads us to choose other methods, notably Poincaré maps.

3.3.3 Poincaré maps

In an N-state-variable problem, one can obtain a Poincaré map by measuring the N-1 variables when the Nth variable reaches some particular value or when the phase space trajectory crosses some arbitrary plane in phase space.

In the case of a two-degree-of-freedom articulated cylinders system, we shall have four variables: the angular displacements of the first and second cylinders, ϕ_1 and ϕ_2 , and the angular velocities of the first and second cylinders, $\dot{\phi}_1$ and $\dot{\phi}_2$. Then, when one of these four variables, ϕ_1 , for example, reaches zero ($\phi_1 = 0$), we plot $\dot{\phi}_2$ versus ϕ_2 , which presents the Poincaré map for our two-degree-of-freedom system. In the same way, we shall define the Poincaré map for a three-degree-of-freedom system, i.e., for $\phi_1 = 0$ we shall obtain two Poincaré maps, $\dot{\phi}_2$ versus ϕ_2 and $\dot{\phi}_3$ versus ϕ_3 , which should have the same geometrical form; similarly for a four-degree-of-freedom system.

The Poincaré map is very useful in differentiating the various types of motion for the articulated system. Thus, when the system is periodic (period—one), the phase—plane portrait is a limit cycle and the Poincaré map, which is a section through the limit cycle, is a single point. If the system undergoes a period—two,—four and—eight motion (period—doubling route to chaos), then the Poincaré map is represented through, respectively, two, four and eight points.

It has already been mentioned that the quasiperiodic motion of a dynamical system takes place in the presence of two simultaneous periodic oscillations of frequencies f_1 and f_2 , which are incommensurate, and for which the Winding number $(=f_1/f_2)$ has been calculated. The exact form of the Poincaré map depends on the ratio f_1/f_2 . If f_1/f_2 is irrational, the Poincaré map is a closed continuous curve. If f_1/f_2 is rational, the Poincaré map is composed of a finite set of points distributed along a curve, which is no longer continuous. In this case, a frequency locking between f_1 and f_2 is found to exist, so that the ratio f_1/f_2 is equal to that of two integers n_1 and n_2 . After having accomplished n_1 "circuits" and n_2 "rotations" per circuit, the trajectory closes upon itself, and (as remarked previously) we have in fact a periodic solution of period $T = (n_1/f_1) = (n_2/f_2)$, and the Poincaré map will contain only n_1 points. This is a useful method in distinguishing the various types of quasiperiodic motions and chaotic ones.

Finally, when the dynamics of the system is chaotic, the Poincaré map becomes more complex, but nevertheless should retain some definite structure, in contrast to that for a random process.

3.3.4 Lyapunov exponents

There are many tools in nonlinear dynamics utilized in order to recognize if a system is chaotic or not, and one of them, a quantitative one, is the Lyapunov exponents, named after the Russian mathematician Lyapunov (1857–1918).

Chaotic motion in a dynamical system implies a sensitive dependence on initial conditions. This means that if two trajectories start close to each other in phase space, they will move exponentially away from each other for small times on the average. Thus, if d_0 is a measure of the initial distance between the two starting points, a brief time later the distance is

$$d(t) = d_0 2^{\sigma t}, (3.10)$$

 σ being the Lyapunov exponent. The choice of base 2 in equation (3.10) is convenient but arbitrary. Good reviews of Lyapunov exponents and their use in experiments to characterize chaotic motion are given by Benettin et al. (1980) and by Wolf et al. (1985). The review by Wolf et al. contains also two computer programs for calculating Lyapunov exponents.

The divergence of chaotic orbits can only be locally experimental, since if the system is bounded, as most physical experiments are, d(t) cannot go to infinity. Thus, to define a measure of this divergence of orbits, we must average the exponential growth at many points along the trajectory, as shown in Figure 3.1.

One begins with a reference trajectory and a point on a nearby trajectory and measures $d(t)/d_0$. When d(t) becomes too large (i.e., the growth departs from exponential behaviour), one looks for a new "nearby" trajectory and defines a new d_0 . One can define the first Lyapunov exponent by

$$\sigma = \frac{1}{t_N - t_0} \sum_{k=1}^{N} \log_2 \frac{d(t_k)}{d_0(t_{k-1})}.$$
 (3.11)

Then, σ will be negative for stable systems with fixed points, zero for periodic or quasiperiodic motions, and positive for chaotic motion.

3.3.5 First and second return maps

Let I_k be the value of the kth maximum displacement of the first cylinder of the articulated system. The first return map would be the graph of $I_{k+1} = f(I_k)$, while the second return map would be of the form $I_{k+2} = f(I_k)$, for a sequence of values of k (Bergé at al. 1984).

The theory for type III intermittency predicts the following form for the second return map function: $I_{k+2} = (1+2\mu)I_k + aI_k^2 + bI_k^3$, where a and b are constants with a << b, near the intermittency threshold. An inflection point in the neighbourhood of the fixed point of $f(I_k)$ is found to exist. This corresponds to the vanishing of the quadratic term in the Taylor series of $f(I_k)$. By expanding the time scale in case of graph I_k versus time τ , the growth of the subharmonic (increasing displacements) and the correlated decay of the fundamental (decreasing displacements) might be observed.

Furthermore, one may differentiate between the two types of intermittency, type I and type III, by analyzing the first return map $I_{k+1} = f(I_k)$. Classification of intermittency into types I and III is based on the crossing of the unit circle by the Floquet multiplier at +1 (type I), and at -1 (type III). This corresponds to the value of the slope of $I_{k+1} = f(I_k)$ with the first diagonal, as follows: (i) when the slope of I_{k+1} is equal to 1, and the graph $I_{k+1} = f(I_k)$ is tangent to the first diagonal, the intermittency is of type I; (ii) if the slope of I_{k+1} is equal to -1, the intermittency is of type III.

3.3.6 Number of laminar phases

Another interesting nonlinear dynamics tool used in the study of the intermittency is the statistical distribution of the duration τ of the laminar phases, that is $P(\tau, \mu)$, where μ is the difference between u and $u_{c\tau}$. In a sample of N laminar phases, one expects $N \int_0^{\tau} P(\tau, \mu) d\tau$ phases which last less than τ .

The average duration of a laminar phase is $\int_0^\infty P(\tau,\mu)d\tau \simeq \mu^{-1/2}$. In type I intermittency, for μ fixed, the duration of laminar phases is bounded from above by a quantity of order $\mu^{-1/2}$, and the closer we get to the threshold, the less the duration fluctuates. The exact form of $P(\tau,\mu)$ depends upon the details of the problem, as the fluctuations of τ reflect the fluctuations of the process of reinjection into the laminar channel. The distribution of laminar phase duration $P(\tau,\mu)$ versus τ follows completely different laws for type I and for type III intermittency.

In the case of type III intermittency, the distribution law has a maximum for short times and decreases exponentially at large times, while in type I intermittency this distribution follows a different law: it depends on the details of the relaminarization process. The upper bound of order $\mu^{-1/2}$ close to $\mu=0_+$ is specific to type I intermittency, and corresponds to the maximum time for traversal of the channel.

In type III intermittency, if $P(\tau)d\tau$ is the fraction of laminar phases which last between τ and $\tau + d\tau$ ($d\tau$ small), then

$$P(\tau) \simeq \frac{\exp(-2\mu\tau)}{[1 - \exp(-4\mu\tau)]^{3/2}}$$
 (3.12)

For $\tau >> \mu^{-1}$ we have $P(\tau) \simeq e^{-2\mu\tau}$, while for $1 << \tau << \mu^{-1}$, we obtain $P(\tau) \simeq (4\mu\tau)^{-3/2}$.

By counting the number of laminar phases $N(\tau > \tau_0)$ lasting longer than τ_0 , one may obtain, for type III intermittency

$$N(\tau > \tau_0) \simeq \int_{\tau_0}^{\infty} P(\tau) d\tau \simeq \left[\frac{\exp(-4\mu\tau_0)}{1 - \exp(-4\mu\tau_0)} \right]^{1/2}.$$
 (3.13)

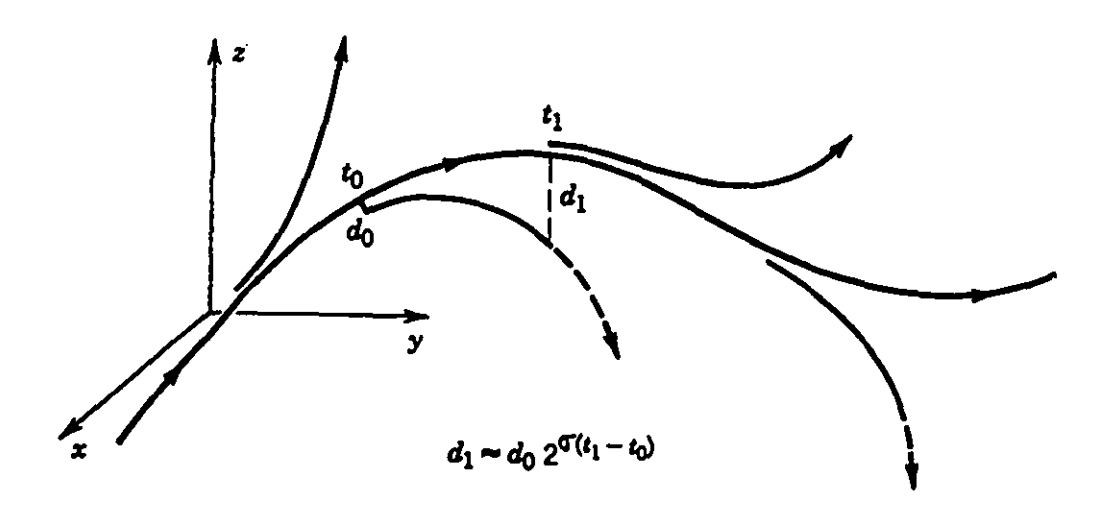


Figure 3.1. Change in distance between two nearby orbits used to define the largest Lyapunov exponent.

Chapter 4

NUMERICAL RESULTS FOR THE FIRST MODEL WITH

N = 2

The dynamical behaviour of the system of two articulated cylinders (N=2) is investigated for the following numerical values of dimensionless parameters given in Chapter 2 by equations (2.34):

$$\epsilon = 10, \quad e = 0.5, \quad f = 0.8, \quad \beta = 0.4, \quad \gamma = 10, \quad \epsilon c_f = 0.25, \quad c_b = 0.1.$$

Solutions of the equations of motion were obtained by using a fourth-order Runge-Kutta integration algorithm, with the time step $\delta\tau$ of 0.01. If this time step is changed to $\delta\tau = 0.001$, we have obtained the same results to the fourth significant figure. As the external flow velocity u increases (for u higher than the corresponding u for Hopf bifurcation), the convergence of the solutions is faster: we need fewer time steps for higher flow velocities than for lower flow velocities for the solution to converge. Details regarding the convergence of the solutions, with corresponding numerical examples, are given in Appendix D.

In the calculations of the bifurcation diagrams and phase-plane portraits, 100 time steps were used, while in the case of Poincaré maps and power spectra, between

10,000 and 30,000 time steps were used.

Furthermore, for the purpose of checking the convergence of the solution, the Runge-Kutta-Fehlberg algorithm was also used, but the same results were obtained.

We chose four cases by varying two parameters, h and f, h representing a measure of the annular gap between the articulated cylinder system and the external channel, and f the nondimensional parameter of the free-end shape. These cases are the following:

Case 1:
$$h = 0.5$$
, $c = 0.38$ ($C = 0.30$), $f = 0.8$, $\kappa_c = 5 \times 10^3$;
Case 2: $h = 0.2$, $c = 0.79$ ($C = 0.62$), $f = 0.8$, $\kappa_c = 5 \times 10^3$;
Case 3: $h = 0.5$, $c = 0.38$ ($C = 0.30$), $f = 0$, $\kappa_c = 5 \times 10^5$;
Case 4: $h = 0.2$, $c = 0.79$ ($C = 0.62$), $f = 0.4$, $\kappa_c = 5 \times 10^5$.

4.1 CASE 1:
$$h = 0.5, f = 0.8, \kappa_c = 5 \times 10^3$$
 or $\kappa_t = 80$

(i) Stability analysis of the linearized system

In concordance with Chapter 3.1, an eigenvalue analysis of the linearized equations (2.35) without considering the impacting of the articulated system with the outer channel (\mathcal{M}_t or $\mathcal{M}_c = 0$) is first carried out. Figure 4.1 shows, in the form of Argand diagrams, the real and imaginary parts of the eigenvalues of the system, $\operatorname{Re}(\lambda)$ and $\operatorname{Im}(\lambda)$, for (a) the first and (b) the second mode of the system, as functions of the flow velocity u.

As the flow velocity is increased in Figure 4.1(a), both the real and imaginary components of the first-mode eigenvalue approach zero; this corresponds to a divergence instability (pitchfork bifurcation), which occurs at u = 1.695. As u is increased further, the real part of the eigenvalues again becomes negative, so that the system is restabilized, at u = 2.53. Furthermore, at u = 2.74, in the second mode (Figure 4.1(b)), purely imaginary eigenvalues arise, which corresponds to a flutter instability (Hopf bifurcation). As u is increased beyond 2.74, the real part becomes positive and this corresponds to a linearly unstable system (amplified oscillations).

(ii) Bifurcation and Phase Plane diagrams

Figure 4.2 shows the bifurcation diagram with the trilinear spring representation ($\kappa_t = 80$) for the system, and Figure 4.3 the bifurcation diagram with the cubic-spring representation ($\kappa_c = 5 \times 10^3$) for the same case. The range of u shown covers the behaviour beyond the Hopf bifurcation. It is seen that, qualitatively, the dynamical behaviour in the two cases is similar, and attention will henceforth be diverted to the more idealized system involving the cubic spring. The reason for this is that direct comparison with analytical work to be presented in Chapter 5 then becomes possible, because \mathcal{M}_c (the cubic spring representation) is an analytical function whereas \mathcal{M}_t (for the trilinear spring) is not. Thus, concentrating on the cubic spring representation with $\kappa_c = 5 \times 10^3$, Figures 4.3 and 4.4 show bifurcation diagrams and phase-plane portraits for the first cylinder in the system, for flow velocities above the critical flow velocity (for the occurrence of the Hopf bifurcation (u > 2.74)).

The route to chaos for the bifurcation diagram of Figure 4.3 is clarified via the phase-plane portraits of Figure 4.4. For $u \simeq 2.74$, there exists a stable, symmetric limit cycle that develops after the Hopf bifurcation (not shown). The symmetry of the limit cycle is lost by a symmetry-breaking pitchfork bifurcation at u = 2.795, the first bifurcation shown in Figure 4.3, where the two branches are obtained with different-sign initial conditions. At higher u, a cascade of period-doubling

bifurcations occurs, and Figure 4.4(a,b) shows period-2 and period-4 motions. Figure 4.4(c) shows chaotic motion for u = 2.8295, corresponding to the first dense cloud of points in the bifurcation diagram. Figure 4.4(d) shows a periodic (akin to period-5) motion for u = 2.831, corresponding to the sparse patch (periodic window) in the bifurcation diagram. At higher u, the motion becomes strongly chaotic again.

The period-doubling bifurcations have been pin-pointed to occur at $u_{p-1} = 2.8195$ (period-2 motion), $u_p = 2.8234$ (period-4 motion), $u_{p+1} = 2.8243$ (period-8 motion) etc., where the interval in u between bifurcations becomes progressively smaller. From these values, the Feigenbaum number, $\text{Fei}_p = (u_{p+1} - u_p)/(u_{p+2} - u_{p+1})$, may be computed, giving $\text{Fei}_p = 4.33$, which is reasonably close to the "ideal" Fei = 4.6692 (Moon 1987).

(iii) Power Spectra and Time Traces

This case, involving a cascade of period-doubling bifurcations, is quite similar to that studied by Païdoussis and Moon (1988) and Païdoussis et al. (1991), for a similar problem. As it is the first case of period-doubling bifurcations route to chaos in this Thesis, the frequencies and periods for different flow velocities u are calculated from time traces and simultaneously from power spectra, and the results are presented as follows. For u = 2.80 (period-one motion), the nondimensional period from the time traces is calculated to be T = 0.68, while its dominant frequency, i.e., f = 1.47 = 1/0.68 with its related subharmonics 2f, 3f, 4f are found from the power spectra. Furthermore, for u = 2.82 (period-2 motion) and u = 2.824 (period-4 motion), it is found that the dominant frequency for u = 2.82 (f = 0.735) is half the frequency calculated for u = 2.82. Their corresponding subharmonics are 2f, 3f, 4f, 5f and so on. These results are summarized as $f_{u=2.8}$ (period-1 motion) = $2f_{u=2.82}$ (period-2 motion) = $4f_{u=2.824}$ (period-4 motion), so that they verify the period-doubling nature of the motion.

The chaotic character of the motion at u=2.8295 is self-evident in Figure 4.5(a), in both the time trace and the PSD. The motion depicted in Figure 4.5(b) for u=2.831 is periodic, with the dominant dimensionless frequency of f=2.245, modulated mainly by its fifth subharmonic of f=0.449; this gives rise to the period-5-like phase portrait of Figure 4.4(d). The second peak in the PSD corresponds to $f=\frac{3}{5}\times 2.245$ and, indeed, Figure 4.4(d) could be considered as a "modified" form of period-3 motion also!

(iv) Poincaré Maps and Lyapunov Exponents

Figure 4.6, for u = 2.84, shows a typical Poincaré map in the chaotic regime. A very definite structure is seen to exist, the map showing some similarity (in this cross-sectional form) to a Möbius strip (cf. Païdoussis *et al.* 1992).

The largest Lyapunov exponents shown in Figure 4.7 display basically similar behaviour: beyond a certain threshold (conform Figure 4.3), the motion is chaotic and remains so $(\sigma > 0)$, apart from one region of periodic (Figure 4.7) motion $(\sigma = 0)$, and for which the flow velocity u = 2.831 (periodicity seen also in Figure 4.4(d)).

4.2 CASE 2: h = 0.2, f = 0.8 and $\kappa_c = 5 \times 10^3$

This case corresponds to a narrower annulus than Case 1.

(i) Stability analysis of the linearized system

For the lower value of h (Figure 4.8(a)), the real and imaginary parts of the first-mode eigenvalue vanish for u = 1.16; this value of u corresponds to the pitchfork bifurcation. The system is restabilized between u = 1.71 and u = 1.95. Then, flutter (Hopf bifurcation) occurs at u = 1.95 in the first mode. In the second mode (Figure 4.8(b)), the real part of the eigenvalues is always negative; so, from the linear stability point of view, only the first-mode behaviour is of interest.

From the results presented here, it can be seen that for the larger gap (h = 0.5) larger critical flow velocities are obtained than for the smaller gap (h = 0.2): u = 1.695 and 2.74 versus u = 1.16 and 1.95. This can be further verified by studying the behaviour of a system in unconfined flow; in that case, much higher critical flow velocities than those for confined flow are obtained.

(ii) Bifurcation and Phase-Plane Diagrams

For the narrower annulus (h = 0.2), the dynamical behaviour is broadly similar, but quite different in detail, as seen in the bifurcation diagram (Figure 4.9) and phase-plane plots (Figure 4.10). The symmetry-breaking pitchfork bifurcation occurs at $u \simeq 2.023$ (Figure 4.9). This is followed by a "period-bubbling" event, where a period-doubling bifurcation occurs but is then reversed to period-1 motion, in the interval 2.0392 < u < 2.0498; period-2 and period-1 phase-plane portraits shown in Figure 4.10(a,b) for u = 2.045 and 2.050, respectively. At u = 2.05225 (Figure 4.9) the motion becomes quasiperiodic-2, but, if the calculation is carried out for sufficient nondimensional time steps (> 100), it develops into chaotic motion. This occurs in the neighbourhood of u = 2.052; for larger u the transition to chaos is much faster.

Although all period-bubbling bifurcations necessary for the Feigenbaum number calculation are not obtained (i.e. period-8; period-4; period-2), for the inverse cascade a number is calculated by the Feigenbaum theory, Fei₂, by taking $u_1 = 2.0392$ corresponding to the first period-2 motion; at $u_2 = 2.0498$ a period-1 occurs, followed by a quasiperiodic motion for $u_3 = 2.0518$ (cf. Figure 4.12 to be discussed under (iv)), which is very close to a chaotic motion. Then, Fei₂ = 5.3, which by definition is not the classical Feigenbaum number, is "reasonably close" to the ideal Feigenbaum number Fei, and this value verifies the definition of inverse cascade.

A typical chaotic phase portrait is shown in Figure 4.10(c) for u = 2.0535. The system will be shown to follow the quasiperiodic route to chaos (see Section

(iii)). Chaos persists to u = 2.058, with a quasiperiodic window at u = 2.0568 (Figure 4.10(d)), which locks like period-3 motion.

(iii) Power Spectra and Time Traces

Figure 4.11 depicts quasiperiodic-2 motion, for u=2.0568, where the power spectrum was obtained from a 100 time-step trace. The two fundamental frequencies are $f_1=0.377$ 5748 and $f_2=1.150$ 704, and all other peaks in the PSD may be confirmed to correspond to f=n $f_1\pm m$ f_2 , with n and m integers. For example, the third peak in the FFT is $2f_2-f_1$, while the fourth is $2f_2+f_1$. Thus, despite Figure 4.10(d) looking like period-3 motion, it represents more complex behaviour. The ratio f_1/f_2 , usually referred to as the winding (or rotation) number, is W=0.328 125 = 21/64, a rational number, as found by the continued fraction method by using Mathematica software. (Of course, whether f_1/f_2 is truly rational and equal to 21/64, and hence the Poincaré map would have a finite number of points, depends on the accuracy of determination of f_1 and f_2 as given above.)

(iv) Poincaré Maps and Lyapunov Exponents

Figure 4.12, for u = 2.052525, close to the onset of chaos, corresponds to quasiperiodic-2 motion that eventually becomes chaotic. In this figure, we see the closed curves characteristic of quasiperiodic motion, but with the beginnings of chaotic perturbations off the curves clearly visible. It is this figure that gives definite proof that chaos is obtained via the quasiperiodic route.

The largest Lyapunov exponents shown in Figure 4.13 display basically similar behaviour: beyond a certain threshold (cf. Figure 4.9), the motion is chaotic and remains so $(\sigma > 0)$, apart from one region of quasiperiodic (Figure 4.12) motion $(\sigma = 0)$.

¹Even if these frequencies are correct to a smaller number of significant figures than the one given here, this will not change the general conclusion regarding the quasiperiodic nature of the motion.

4.3 CASE 3: h = 0.5, f = 0 and $\kappa_c = 5 \times 10^5$

Physically, the system is similar to that of Case 1, but the free end is blunt in this case.

(i) Stability analysis of the linearized system

As the flow velocity u is increased in Figure 4.14(a), the first-mode eigenvalues become purely imaginary for $u_{cr} = 4.47$, which corresponds to a flutter instability (Hopf bifurcation). As u is increased beyond 4.47, the real part becomes positive and the system becomes unstable. In the second mode (Figure 4.14(b)), the real part of the eigenvalues is always negative; so, from the linear stability point of view, only the first-mode behaviour is of interest.

(ii) Bifurcation and Phase Plane diagrams

Figures 4.15 and 4.16-4.18 show bifurcation diagrams and phase-plane portraits for the first cylinder in the system, for flow velocities above the critical flow velocity for which a Hopf bifurcation occurs ($u_{cr} = 4.47$). The route to chaos for the bifurcation diagram of Figure 4.15 is clarified via the phase-plane portraits of Figures 4.16-4.18. For u = 5 (Figure 4.16(a)) there exists a period-one motion that develops after the Hopf bifurcation; its fundamental frequency is $f_1 = 1.08$, and it has odd subharmonics (as ascertained from power spectra). For 7 < u < 8.2 approximately, a period-two motion with two frequencies (with ratio 1/3) develops, which is shown in Figure 4.16(b), and it looks as if it was developing around two symmetrical points with respect to the origin. This motion is called period-2, because its period $T_2 = 1.85$ is twice the previous period (for u = 5), or, more exactly, its fundamental frequency $f_2 = 0.54$ is half the previous fundamental frequency $(f_2 = f_1/2)$. In the power spectra, one may observe odd subharmonics of the fundamental frequency. For u = 8.4 and u = 8.6, in Figure 4.16(c,d), and in accordance with the bifurcation diagram, a period-3 motion (of frequency $f_3 = f_1/3$) followed by a period-4 motion $(f_4 = f_1/4)$ may be observed around the two symmetrical points already mentioned. The previous motions for (b) u = 7.25, (c) u = 8.4 and (d) u = 8.6 may be considered to be periodic with two dominant frequencies, the ratio of which is rational and equal to 1/3. As the periods are two, three or four times higher than the previous periodone motion, they might also be considered period—two, period—three and period—four motions.

Small-scale chaotic motion in Figure 4.17(a,b) is observed for (a) u = 9.075 and (b) u = 9.085. Figure 4.17(b) shows the chaotic motion of the system around one of the two symmetrical points, and Figure 4.18(c) gives the chaotic motion of the system around the other point for the same flow velocity u = 9.085, but which is obtained with opposite-sign initial condition, $\dot{\phi_1} = -0.1$. For higher flow velocities, a period-bubbling event takes place, for which a period-four motion may be observed for u = 9.09 (not shown here, but for which $f_1 = 0.39$); a period-two motion is presented in Figure 4.17(c), for u = 9.1 ($f_2 = 0.78$), which is followed by an inversion, back to period-1, as seen in Figure 4.17(d) for u = 9.25 ($f_3 = 1.56$), and the motion reduces further to a fixed point, as illustrated in Figure 4.17(e) for u = 9.30. In the period-bubbling case, all the subharmonics of the predominant frequencies f_1 , f_2 or f_3 are multiples of n, so that they are of the form nf_1 , nf_2 or nf_3 , with n as positive integer or natural number.

In the end, this case has a very rich dynamical behaviour. Chaos arises through period-n motions with n=1 to n=4; then a period-bubbling phenomenon takes place, from period-four, to period-two and back to period-one motion, and then, the motion finally reduces to a fixed point.

(iii) Power Spectra, Time Traces and Poincaré maps

The power spectra and time traces were obtained for this case, for two flow velocities, for which we thought that we had chaotic behaviour of this system: (a) u = 9.075 and (b) u = 9.085. We can observe in Figure 4.19(a,b) that the time traces and the power spectra are indeed characteristic of chaotic motion.

In addition, Figure 4.19(a), showing the displacement of the first cylinder as a function of time for u = 9.075, looks "strange" because of its sudden reduction at $\tau \simeq 108.5$. This may be explained easily by the shape of phase-plane plots of Figure 4.17(a) or 4.18(a).

For the same flow velocities (u = 9.075 and 9.085), we have constructed Poincaré maps (Figure 4.20(a,b)) which, although uninteresting in shape, are characteristic of chaotic motion.

4.4 CASE 4: h = 0.2, f = 0.4 and $\kappa_c = 5 \times 10^5$

This system is similar to Case 2, but with an intermediately blunt free end—blunter than for Case 2, but not as blunt as Case 3.

(i) Stability analysis of the linearized system

As u is increased in Figure 4.21(a), the first mode eigenvalues become purely imaginary for u = 2.38, which corresponds to a flutter instability (Hopf bifurcation). Then, as u is increased beyond 2.38, the real part becomes positive and the system becomes unstable.

In the second mode, (Figure 4.21(b)), the real part of the eigenvalues is always negative; so, from the linear stability point of view, only the first mode behaviour is of interest (the same as for Case 3).

(ii) Bifurcation and Phase Plane diagrams

Figures 4.22 and 4.23 show the bifurcation diagram and the phase-plane plots for the first cylinder in this system, for flow velocities u higher than the critical flow velocity for which a Hopf bifurcation occurs ($u_{cr} = 2.38$). The route to chaos associated with the bifurcation diagram of Figure 4.22 is clarified via the phase-plane portraits of Figure 4.23.

There exists a symmetric stable limit cycle which develops after the Hopf bifurcation which occurred for $u_{cr} = 2.38$ (not shown). Then, the symmetry of the

limit cycle is lost by a symmetry-breaking pitchfork bifurcation at $u \simeq 2.75$, the first bifurcation shown in Figure 4.22, where the two branches are obtained with different sign initial conditions. At flow velocities u higher than 2.75, a cascade of period-doubling bifurcations occurs; Figure 4.23(b,c) shows period-two and period-four motions for (b) u = 2.965 and (c) u = 2.972. Figure 4.23(d) shows chaotic motion for u = 2.975. The Feigenbaum number is calculated for the period-doubling bifurcations shown in Figures 4.23(a) to 4.23(d), with thresholds at $u_1 = 2.952$ (period-2 motion), $u_2 = 2.97$ (period-4 motion) and $u_3 = 2.974$ (period-8 motion). They give Fei₂ = 4.5, which is very close to the ideal Feigenbaum number.

Periodic windows appear for u=2.9789 to u=2.9812, as shown in Figure 4.23(e) for u=2.98. By analyzing the time traces and the power spectra for $u_1=2.9789$, the fundamental frequency f=0.38 together with its subharmonics nf (where n is a positive integer) may be calculated. For $u_2=2.9807$, the frequency is half the previous frequency for u=2.9789 and is equal to 0.19, f=0.19, so that this motion is period-two with respect to the previous period-one motion. For $u_3=2.9811$ the motion becomes period-four and is followed by period-eight motion for $u_4=2.98121$; for higher flow velocities the motion of the system becomes chaotic. The Feigenbaum number corresponding to these period-two motions is Fei₃ $\simeq 3.64$, which is not too close to the ideal Feigenbaum number Fei = 4.6692.

For u = 3, a periodic window appears. Then, for u > 3, a new cascade (the third one) of period-two motions appears, which is qualitatively the same as the second one (u = 2.979 to u = 2.981). Finally, it has been observed that chaotic motions arise in this system through three period-doubling sequences as u is increased (Figure 4.22).

(iii) Power Spectra, Time Traces and Poincaré maps

The power spectra and time traces were obtained for this case, for two flow velocities, u = 2.975 and u = 3.2, for which we thought that we had chaotic behaviour of this system. The power spectra in Figure 4.24 confirm this fact.

For the same values of u, we have constructed the Poincaré map which has a chaotic shape for (a) u = 2.975 (Figure 4.25(a)) and (b) u = 3.2 (Figure 4.25(b)).

4.5 SOME GENERAL REMARKS ON THE N = 2 RESULTS

The four cases examined show a variety of interesting dynamical behaviour obtained by varying just two parameters: the width of the annulus, characterized by h (and c), and the bluntness of the free end, involving the parameter f.

Case 2 shows quasiperiodic motion, and chaos comes about via the quasiperiodic route. Case 3 is a more "special" case, for which chaos arises through period-n motions, which develop around two symmetrical points, as shown in Figures 4.16-4.18, and the motion eventually collapses to fixed points after a period-bubbling sequence (shown in Figures 4.17(c,d)).

Further discussion will be postponed until after the results with N>2 have been presented.

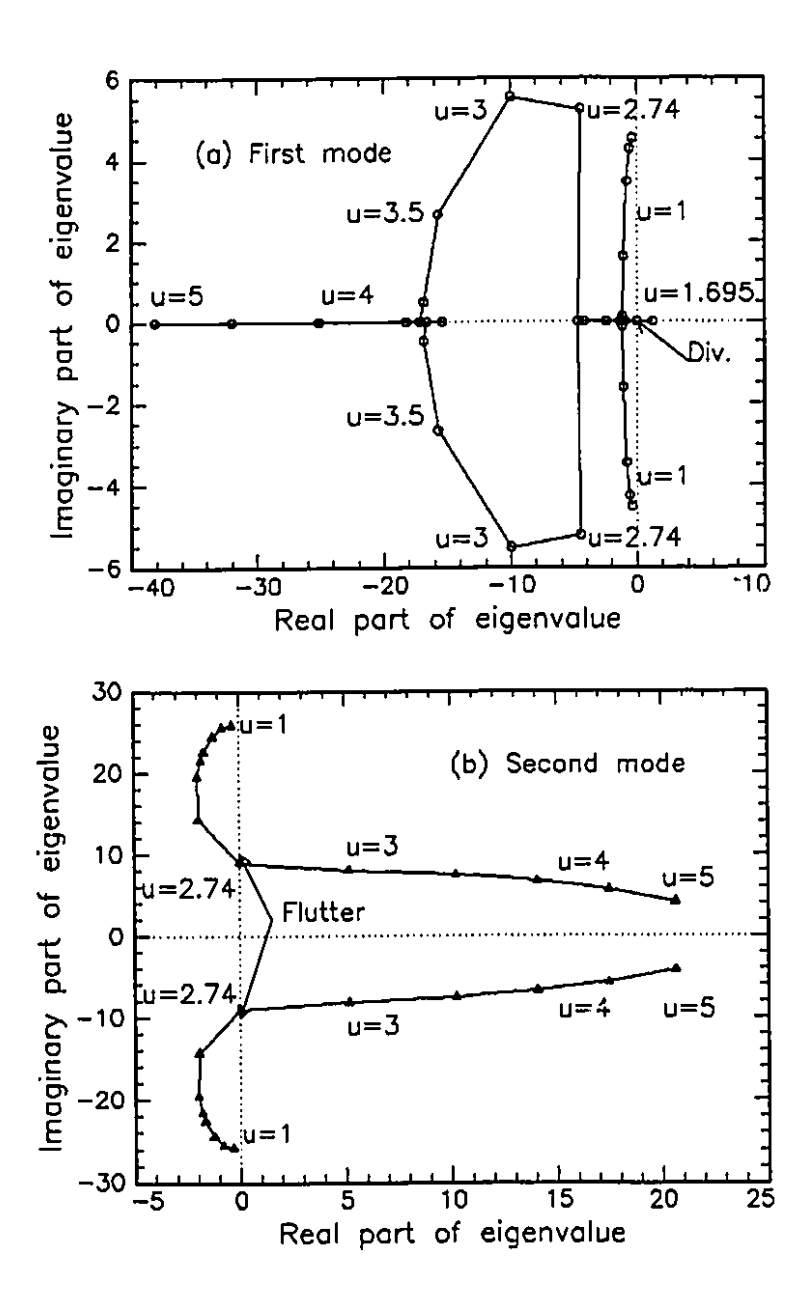


Figure 4.1. Argand diagrams for (a) the first mode and (b) the second mode of the system of Case 1: h = 0.5, c = 0.38, f = 0.8 and $\kappa_c = 5 \times 10^3$. The imaginary part of the eigenvalue, $\text{Im}(\lambda)$, is plotted versus the real part, $\text{Re}(\lambda)$, with the nondimensional flow velocity, u, as parameter.

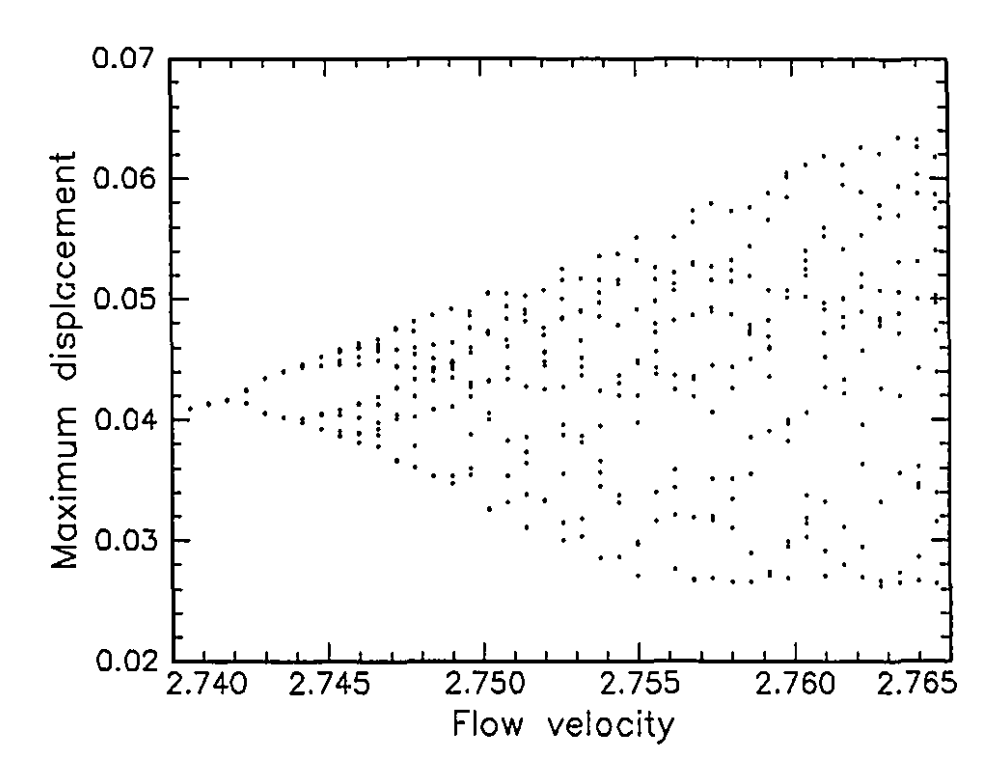


Figure 4.2. Bifurcation diagram for the system of Case 1: h = 0.5, c = 0.38, f = 0.8, with the trilinear spring model ($\kappa_t = 80$) for impacting with the channel; the maximum displacement $\phi_1(\tau)$ versus the dimensionless flow velocity, u.

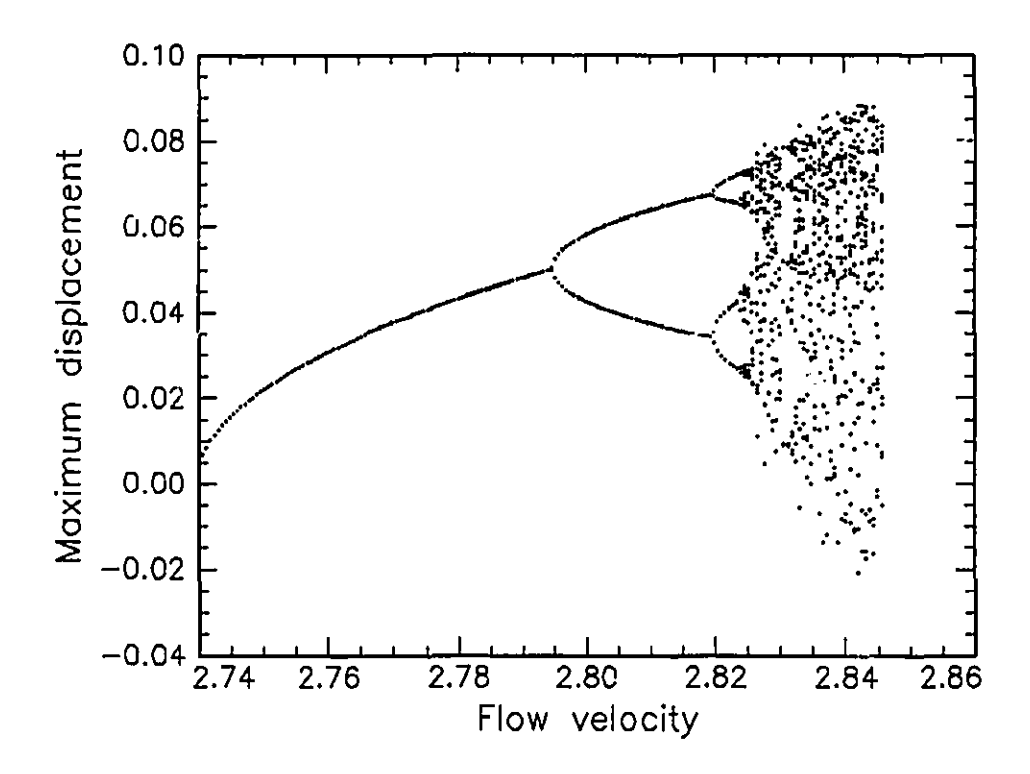


Figure 4.3. Bifurcation diagram for the system of Case 1: h = 0.5, c = 0.38, f = 0.8, with the cubic-spring model ($\kappa_c = 5 \times 10^3$) for impacting with the channel; the maximum displacement $\phi_1(\tau)$ very us the dimensionless flow velocity, u.

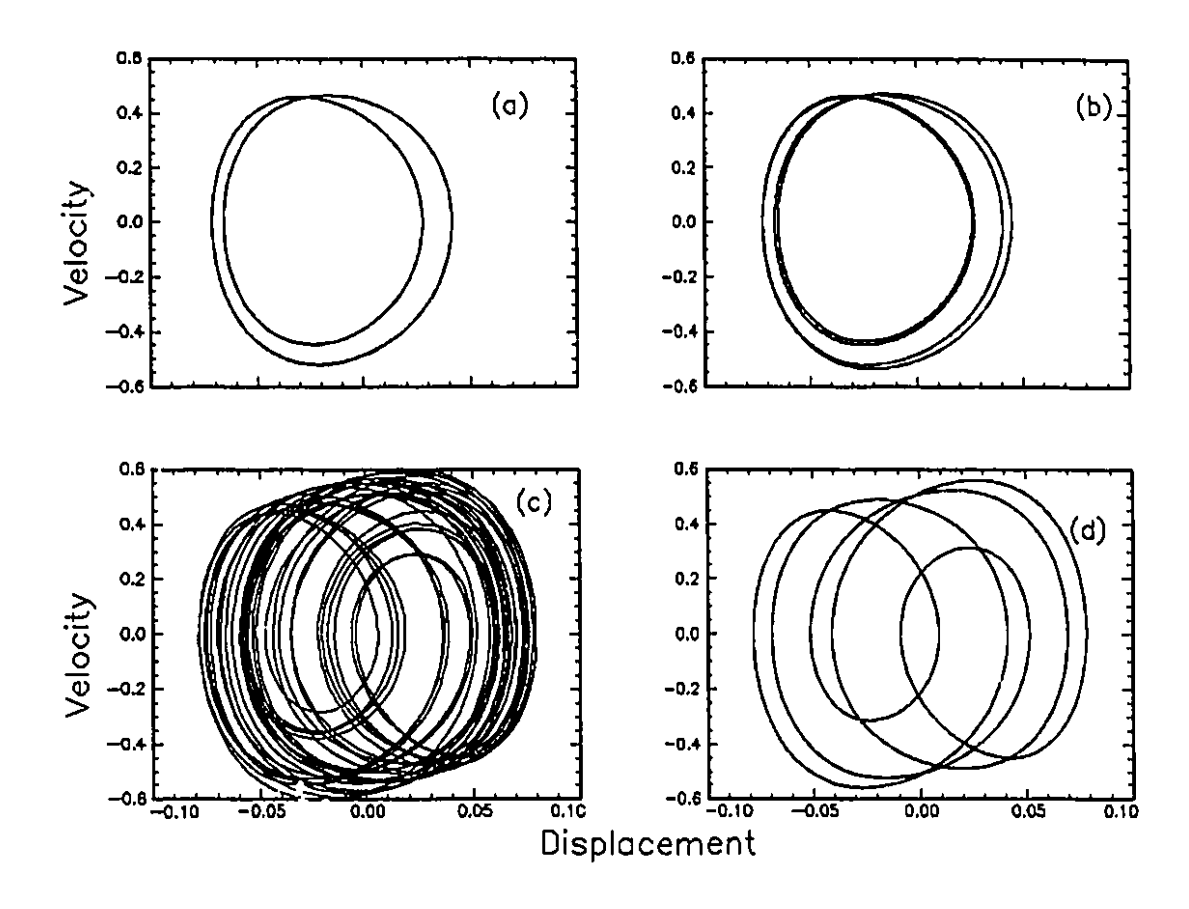


Figure 4.4 Phase-plane plots of $\dot{\phi}_1(\tau)$ versus $\phi_1(r)$ at (a) u=2.8225, (b) u=2.8240, (c) u=2.8295 and (d) u=2.8310, for the system of Case 1: h=0.5, c=0.38, f=0.8 and $\kappa_c=5\times10^3$.

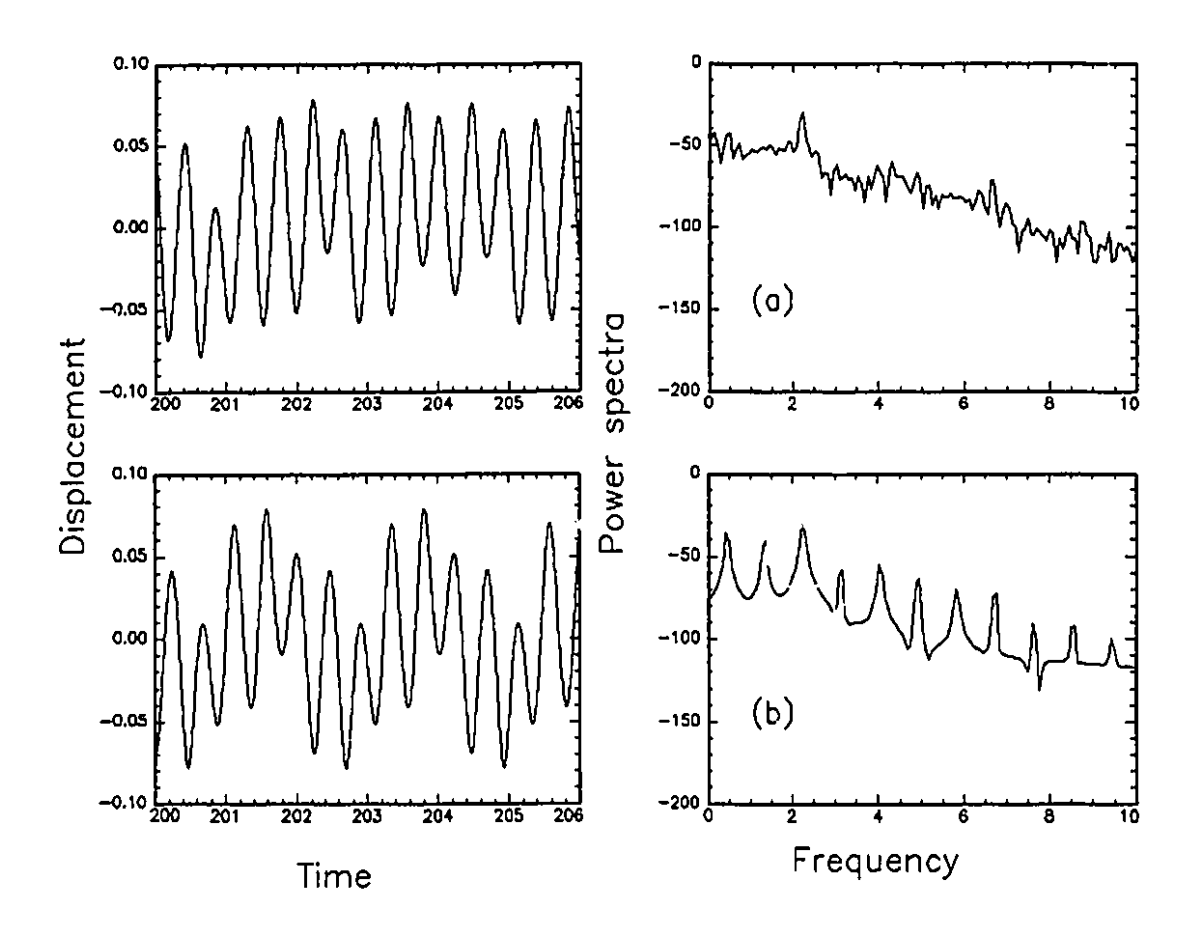


Figure 4.5. Time traces of $\phi_1(\tau)$ versus dimensionless time, τ , and the associated power spectra (dB) for the system of Case 1: $h=0.5, c=0.38, f=0.8, \kappa_c=5\times10^3$ for (a) u=2.8295 and (b) u=2.8310, showing chaotic and periodic motions, respectively.

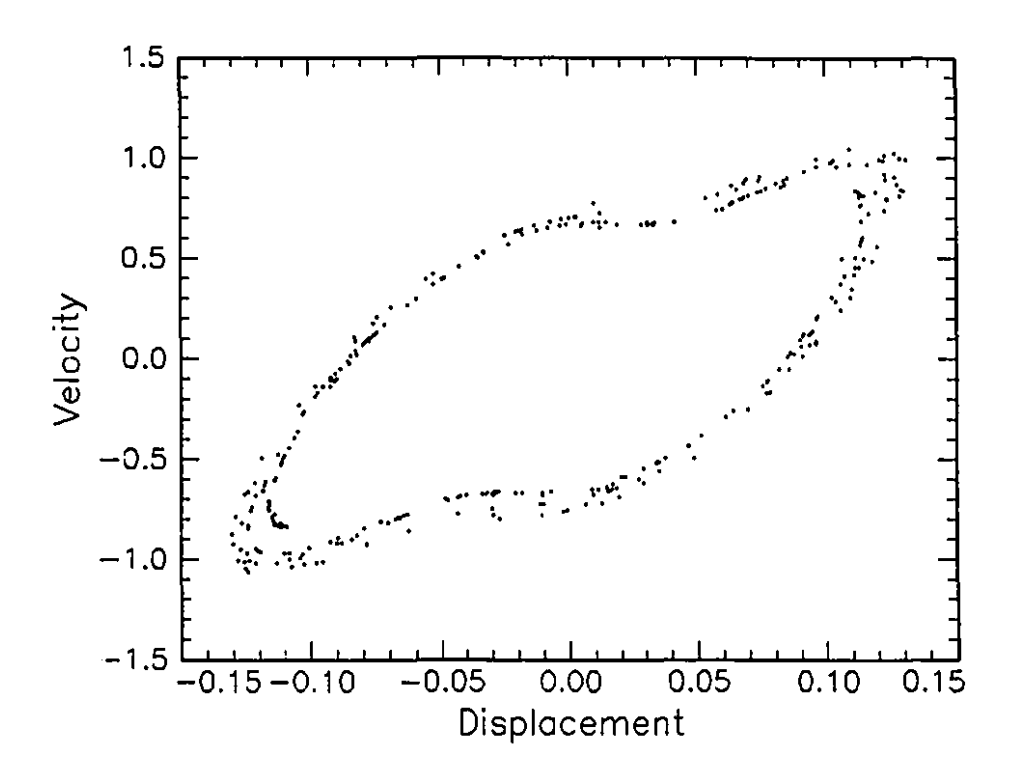


Figure 4.6. Poincaré map of $\dot{\phi}_2(\tau)$ versus $\phi_2(\tau)$ when $\phi_1(\tau)=0$ for Case 1: h=0.5, $c=0.38, f=0.8, \kappa_c=5\times 10^3$, and u=2.84, in the chaotic region.

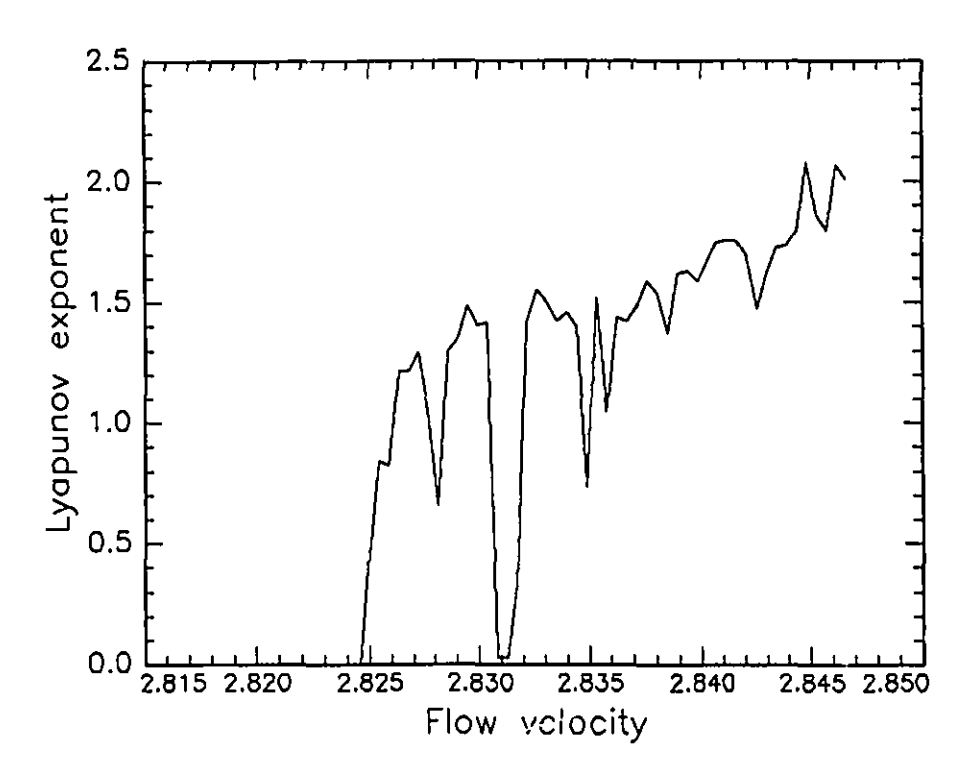


Figure 4.7. The largest Lyapunov exponent versus u for Case 1: h=0.5, c=0.38, f=0.8 and $\kappa_c=5\times 10^3.$

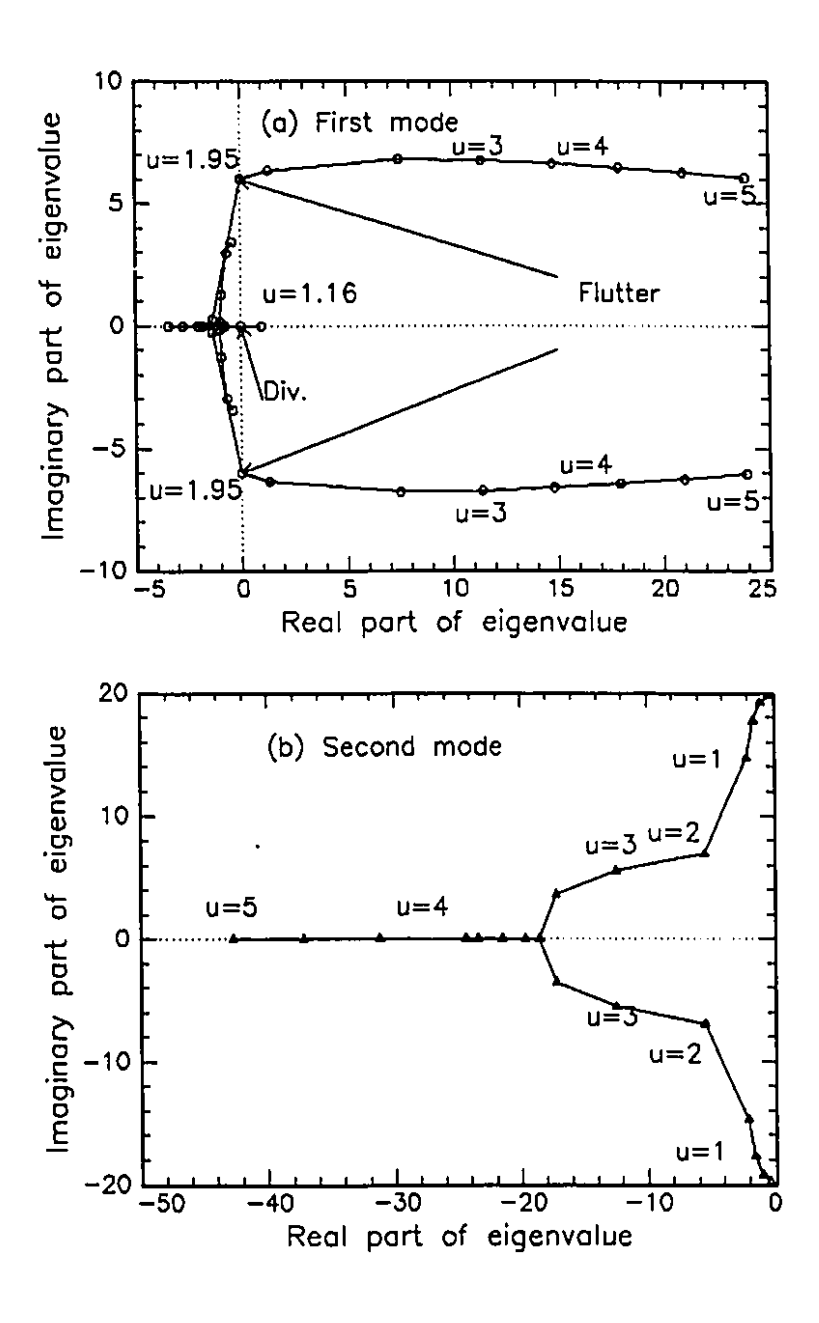


Figure 4.8. Argand diagrams for (a) the first mode and (b) the second mode of the system of Case 2: h = 0.2, c = 0.79, f = 0.8 and $\kappa_c = 5 \times 10^3$. The imaginary part of the eigenvalue, $\text{Im}(\lambda)$, is plotted versus the real part, $\text{Re}(\lambda)$, with the nondimensional flow velocity, u, as parameter.

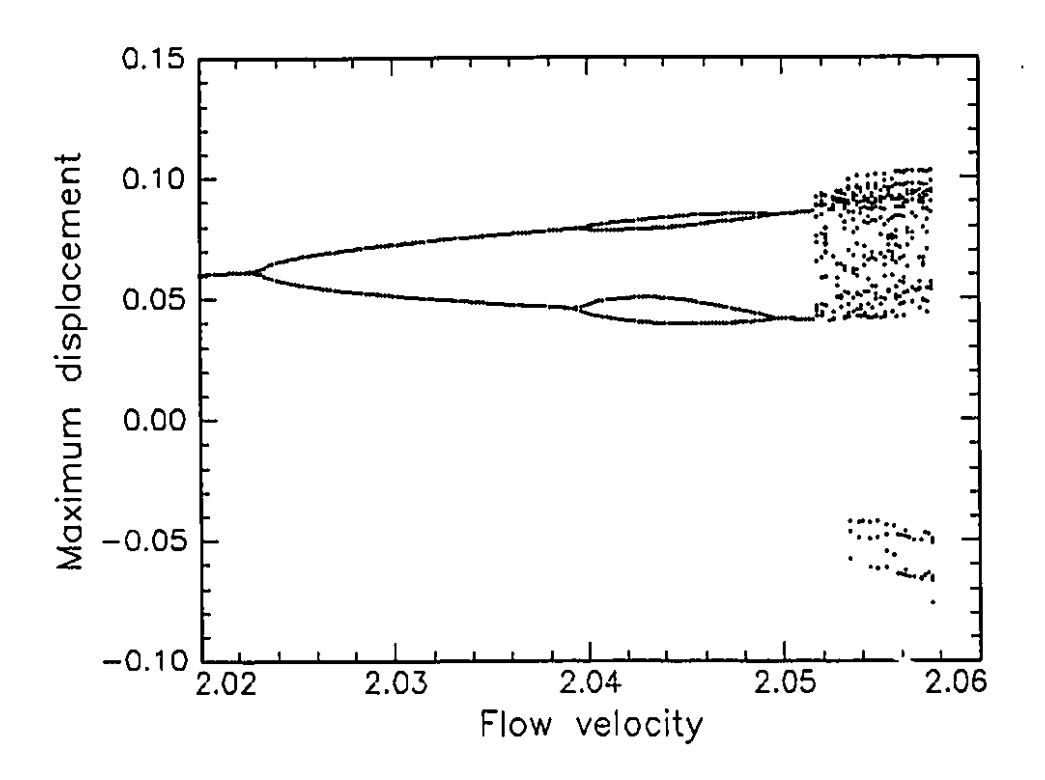


Figure 4.9. Bifurcation diagram for the system of Case 2: h = 0.2, c = 0.79, f = 0.8, with the cubic-spring model ($\kappa_c = 5 \times 10^3$) for impacting with the channel; the maximum displacement $\phi_1(\tau)$ versus the dimensionless flow velocity, u.

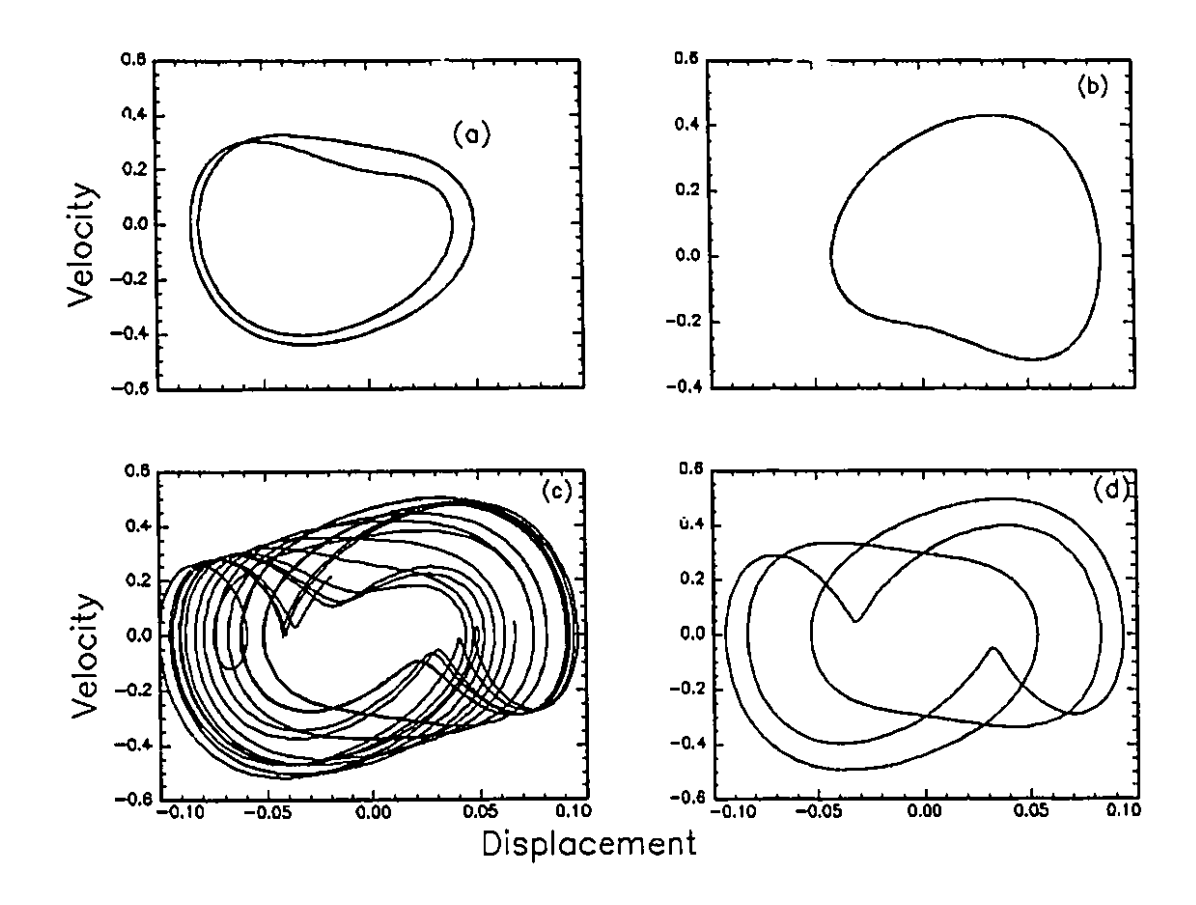


Figure 4.10. Phase-plane plots of $\dot{\phi}_1(\tau)$ versus $\phi_1(\tau)$ at (a) u=2.045, (b) u=2.050, (c) u=2.0535 and (d) u=2.0568 for the system of Case 2: h=0.2, c=0.79, f=0.8 and $\kappa_c=5\times 10^3$.

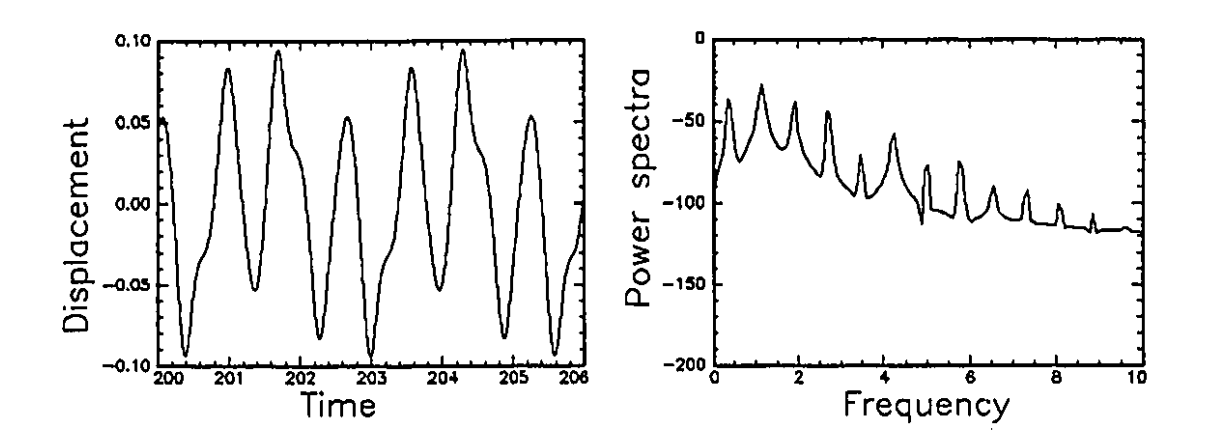


Figure 4.11. Time traces of $\phi_1(\tau)$ versus dimensionless time τ , and the associated power spectra (dB) for the system of Case 2: $h=0.2, c=0.79, f=0.8, \kappa_c=5\times10^3$ for u=2.0568, showing quasiperiodic-2 motion.

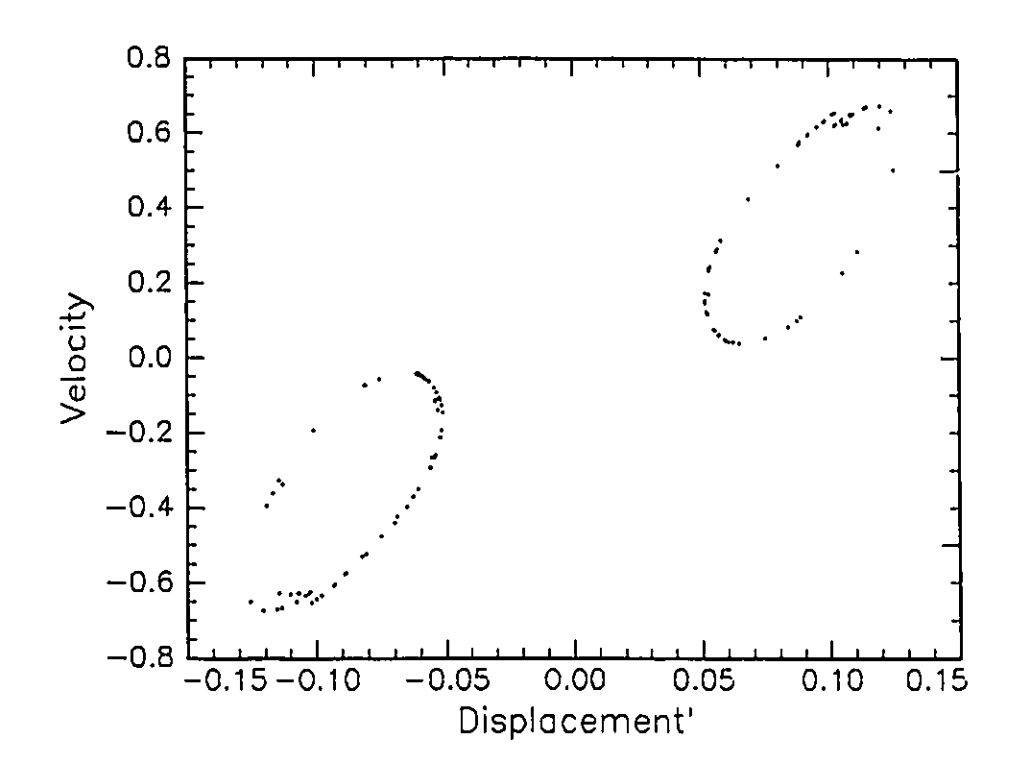


Figure 4.12. Poincaré map of $\dot{\phi}_2(\tau)$ versus $\phi_2(\tau)$ when $\phi_1(\tau)=0$ for Case 2: h=0.2, $c=0.79, f=0.8, \kappa_c=5\times 10^3$, and u=2.0525, in the quasiperiodic-2 region.

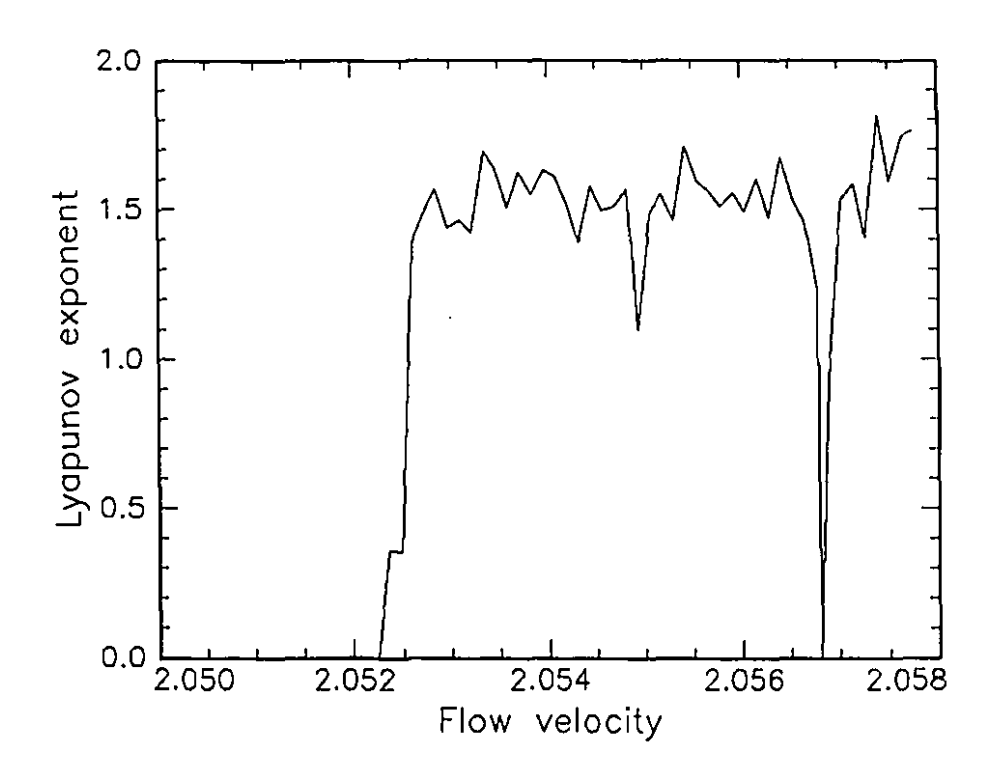


Figure 4.13. The largest Lyapunov exponent versus u for Case 2: h=0.2, c=0.79, f=0.8 and $\kappa_c=5\times 10^3.$

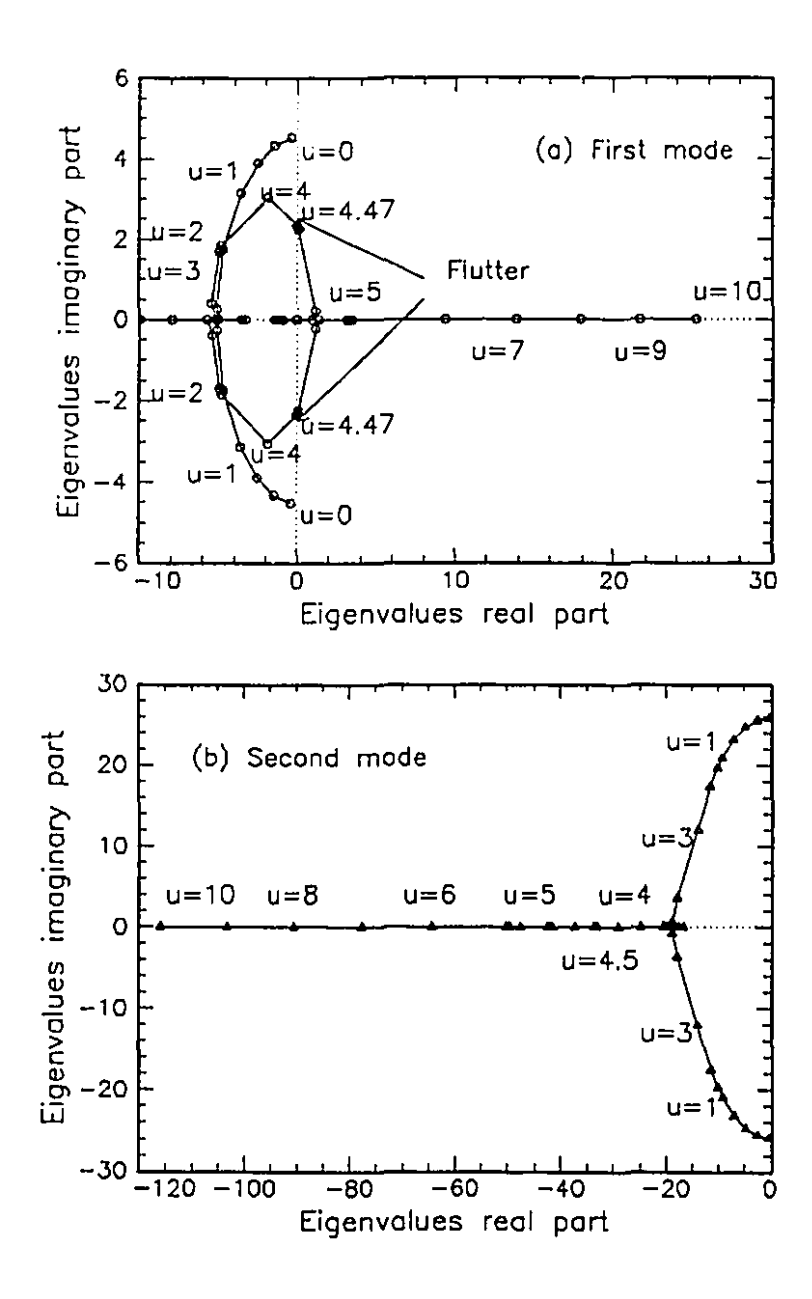


Figure 4.14. Argand diagrams for (a) the first mode and (b) the second mode of the system of Case 3: h = 0.5, c = 0.38, f = 0 and $\kappa_c = 5 \times 10^5$. The imaginary part of the eigenvalue, $\text{Im}(\lambda)$, is plotted versus the real part, $\text{Re}(\lambda)$, with the nondimensional flow velocity, u, as parameter.

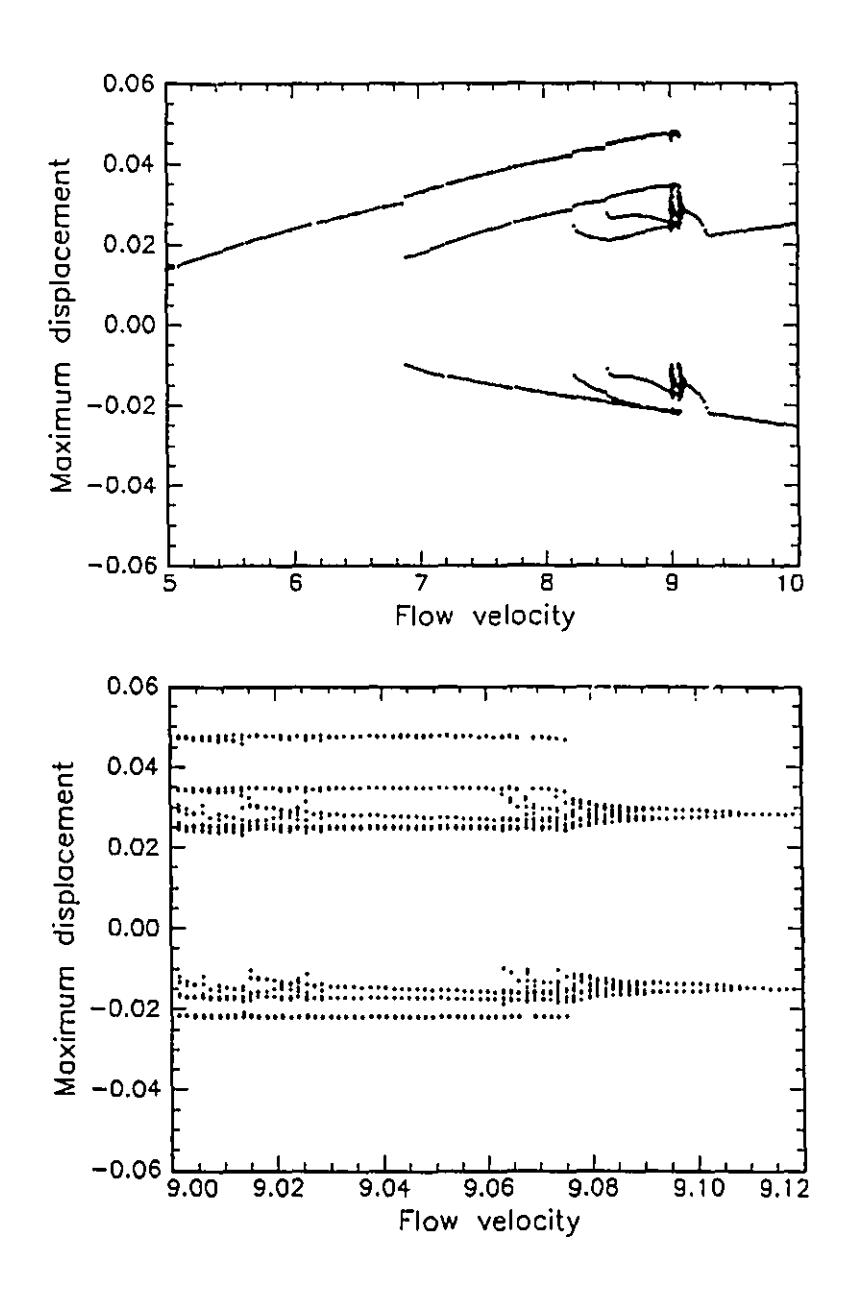


Figure 4.15. Bifurcation diagram for the system of Case 3: h=0.5, c=0.38, f=0, with the cubic spring model ($\kappa_c=5\times 10^5$) for impacting with the channel; the maximum displacement $\phi_1(\tau)$ versus the dimensionless flow velocity, u, for (a) 5 < u < 10 and (b) 9 < u < 9.12.

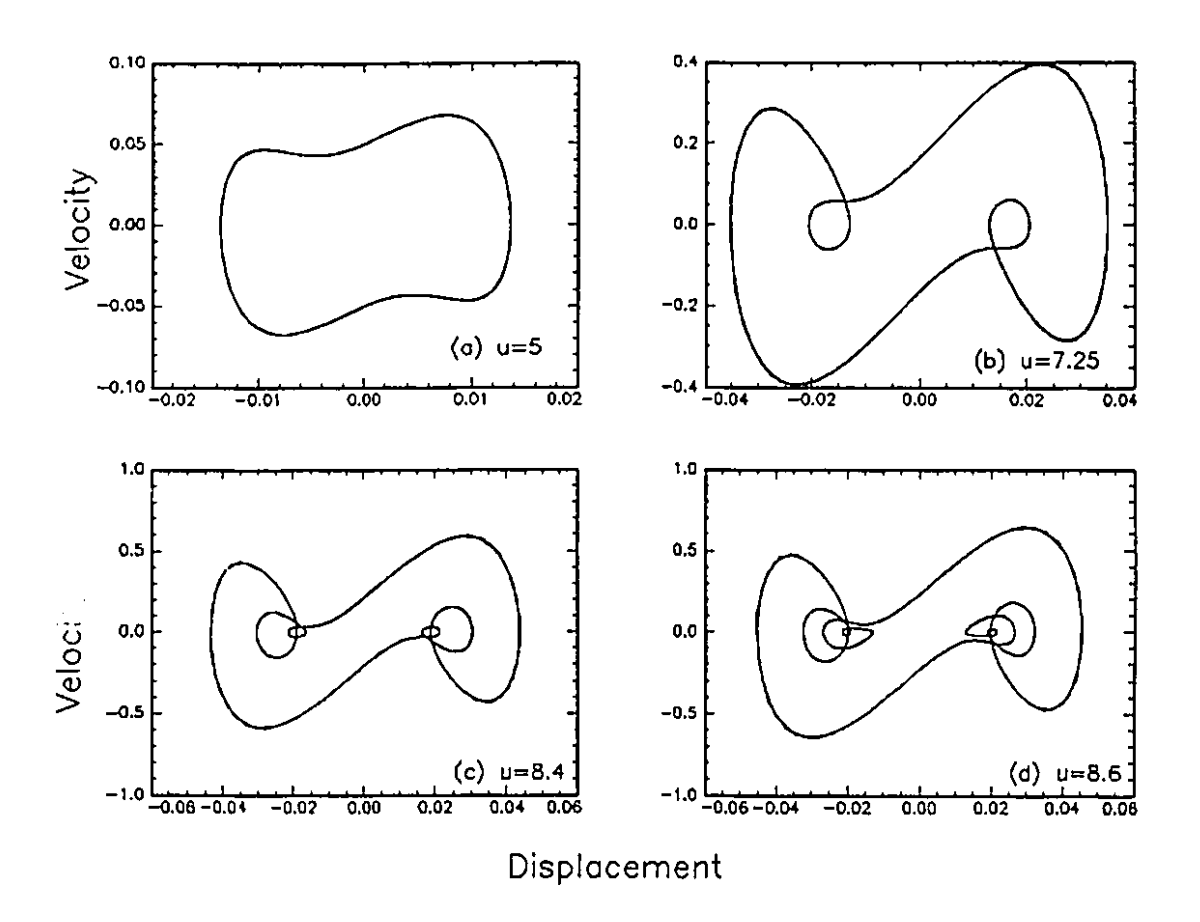


Figure 4.16. Phase-plane plots of $\dot{\phi}_1(\tau)$ versus $\phi_1(\tau)$ at (a) u=5, (b) u=7.25, (c) u=8.4 and (d) u=8.6 for the system of Case 3: h=0.5, c=0.38, f=0 and $\kappa_c=5\times 10^5$.

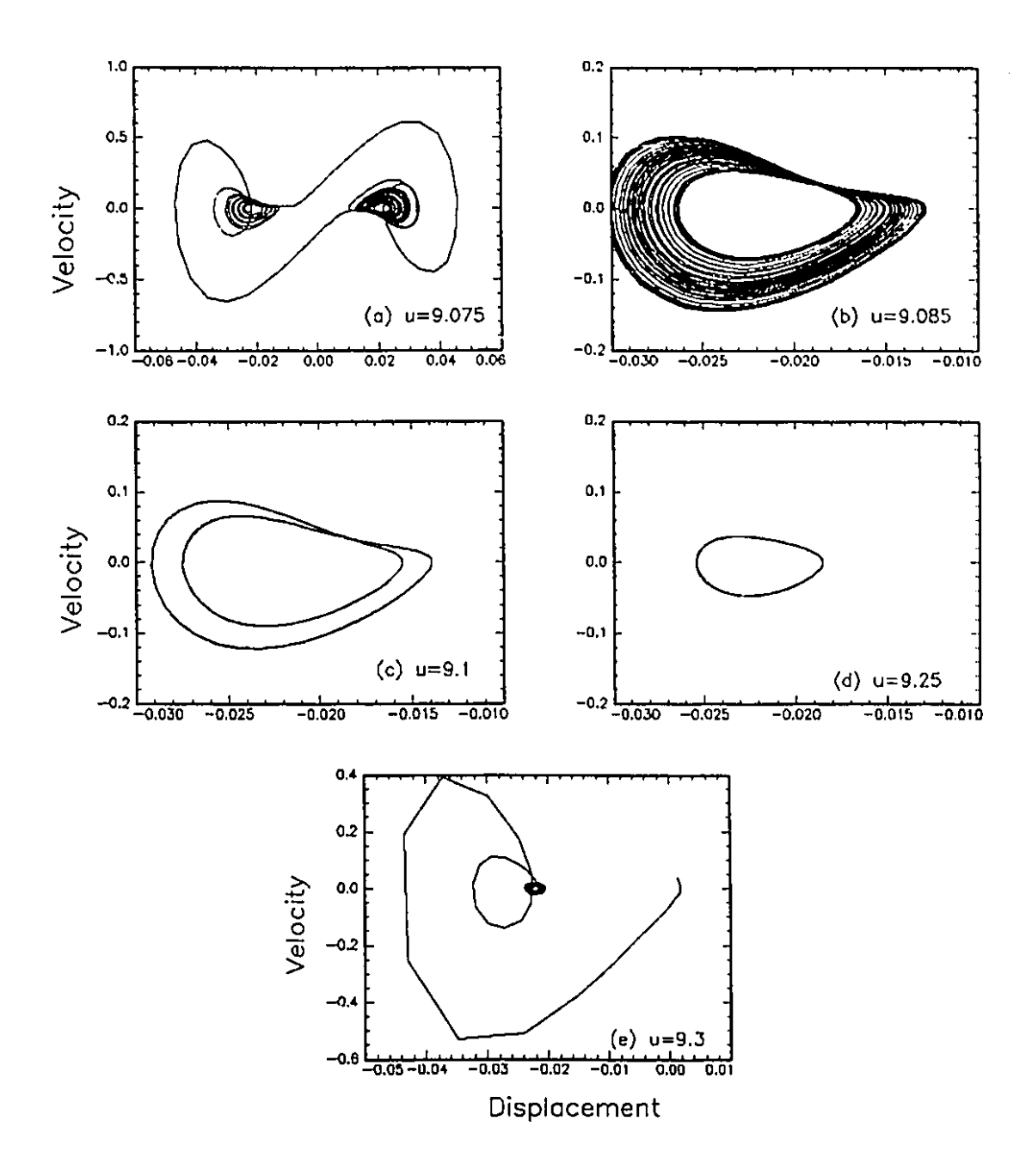


Figure 4.17. Phase-plane plots of $\dot{\phi}_1(\tau)$ versus $\phi_1(\tau)$ at (a) u = 9.075, (b) u = 9.085, (c) u = 9.10, (d) u = 9.25 and (e) u = 9.30 for the system of Case 3: h = 0.5, c = 0.38, f = 0 and $\kappa_c = 5 \times 10^5$.

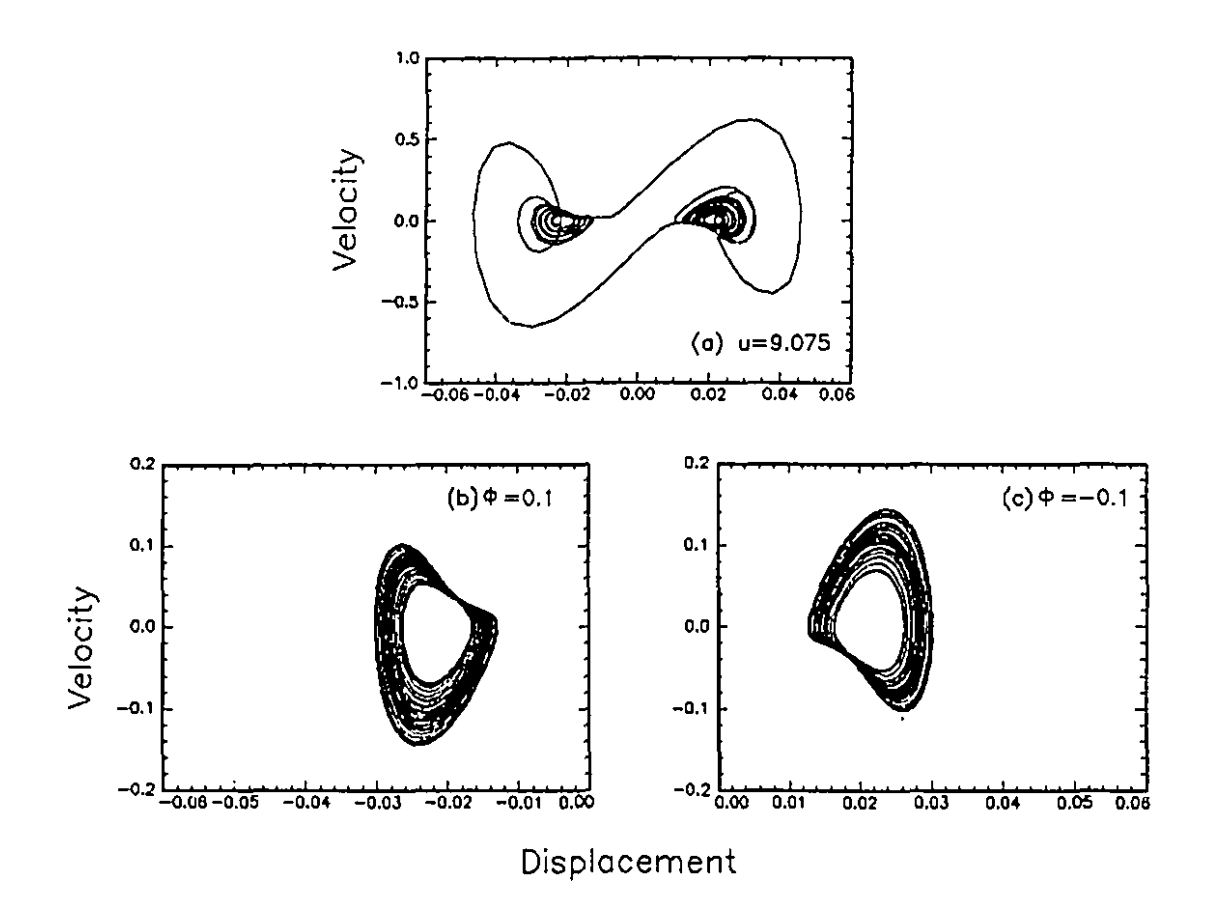


Figure 4.18. Phase-plane plots of $\dot{\phi}_1(\tau)$ versus $\phi_1(\tau)$ at (a) u = 9.075 for $\dot{\phi}_1(\tau) = 0.1$ or $\dot{\phi}_1(\tau) = -0.1$, at (b) u = 9.085 and $\dot{\phi}_1(\tau) = 0.1$, and (c) u = 9.085 and $\dot{\phi}_1(\tau) = -0.1$, for the system of Case 3: h = 0.5, c = 0.38, f = 0 and $\kappa_c = 5 \times 10^5$.

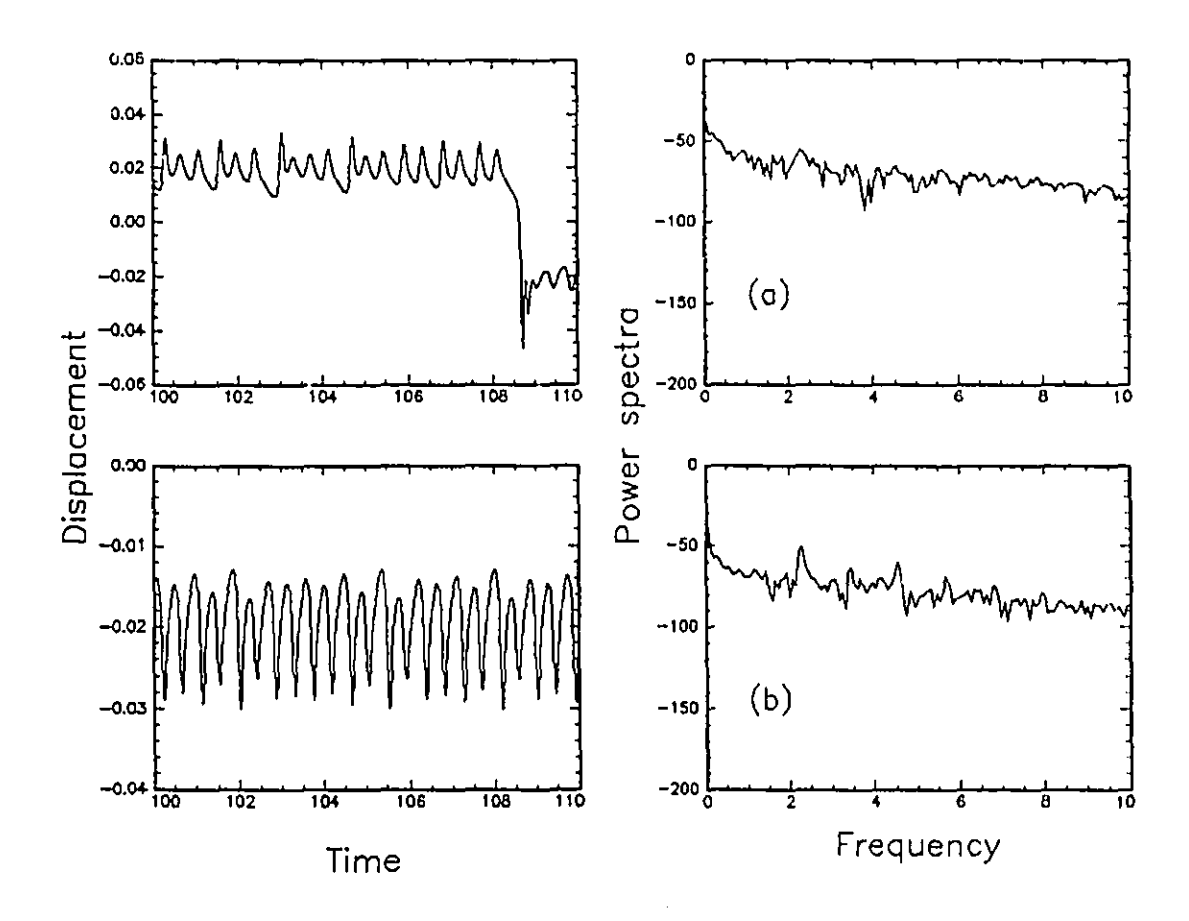


Figure 4.19. Time traces of $\phi_1(\tau)$ versus dimensionless time, τ , and the associated power spectra (dB) for the system of Case 3: $h=0.5, c=0.38, f=0, \kappa_c=5\times10^5$ for (a) u=9.075 and (b) u=9.085, showing chaotic motions.

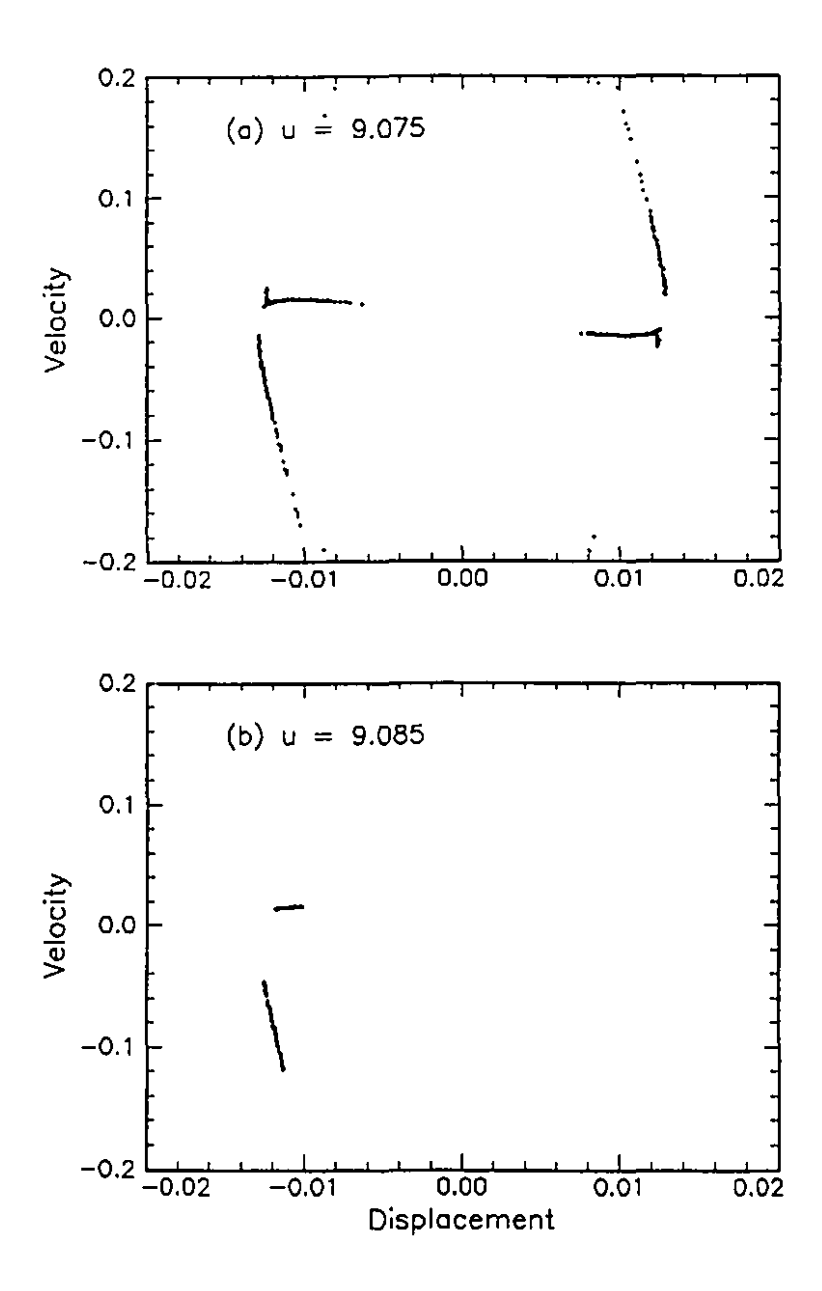


Figure 4.20. Poincaré maps of $\dot{\phi}_2(\tau)$ versus $\phi_2(\tau)$ when $\phi_1(\tau) = 0$ for Case 3: h = 0.5, c = 0.38, f = 0, with the cubic spring model ($\kappa_c = 5 \times 10^5$) for impacting with the channel; showing chaotic motions for (a) u = 9.075 and (b) u = 9.085.

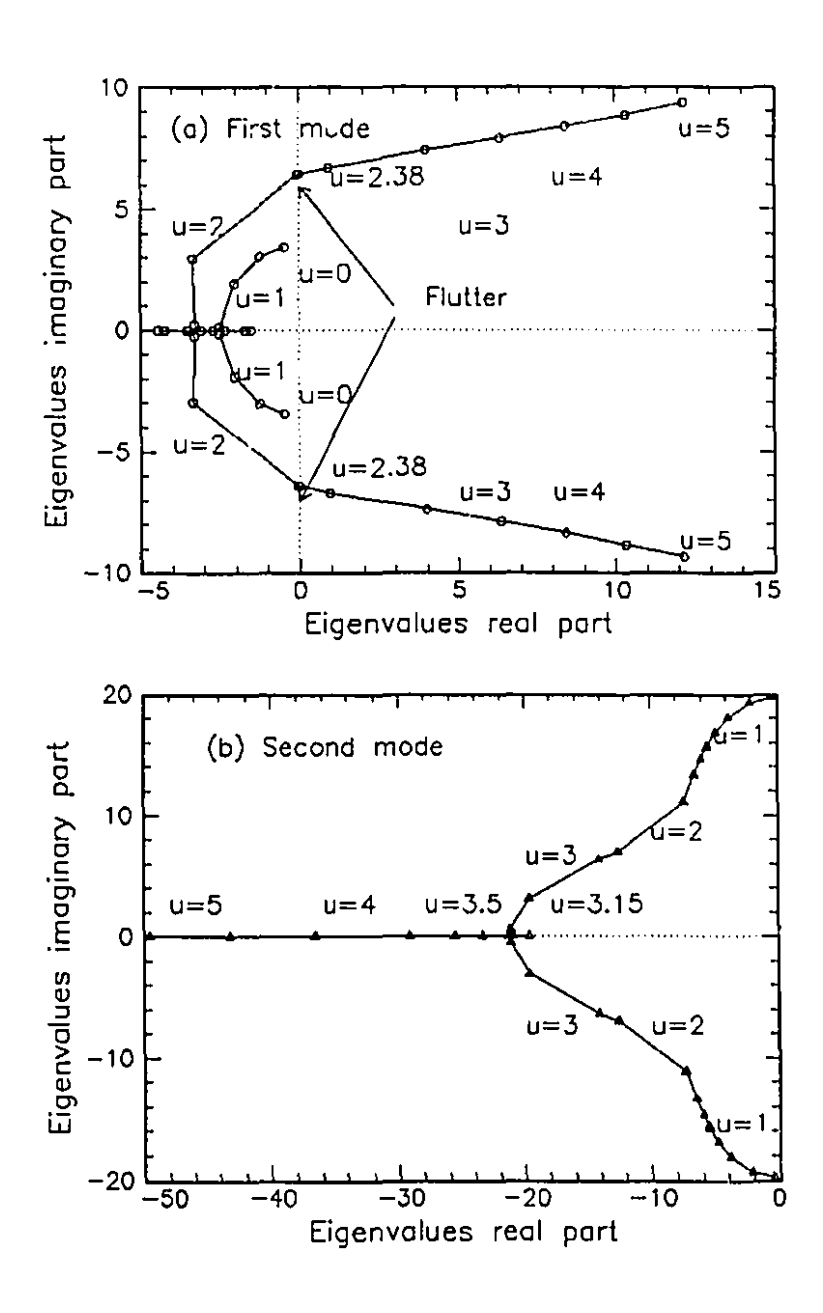


Figure 4.21. Argand diagrams for (a) the first mode and (b) the second mode of the system of Case 4: h = 0.2, c = 0.79, f = 0.4 and $\kappa_c = 5 \times 10^5$. The imaginary part of the eigenvalue, $\text{Im}(\lambda)$, is plotted versus the real part, $\text{Re}(\lambda)$, with the nondimensional flow velocity, u, as parameter.

Figure 4.22. Bifurcation diagram for the system of Case 4: h=0.2, c=0.79, f=0.4, with the cubic-spring model ($\kappa_c=5\times 10^5$) for impacting with the channel; the maximum displacement $\phi_1(\tau)$ versus the dimensionless flow velocity, u.

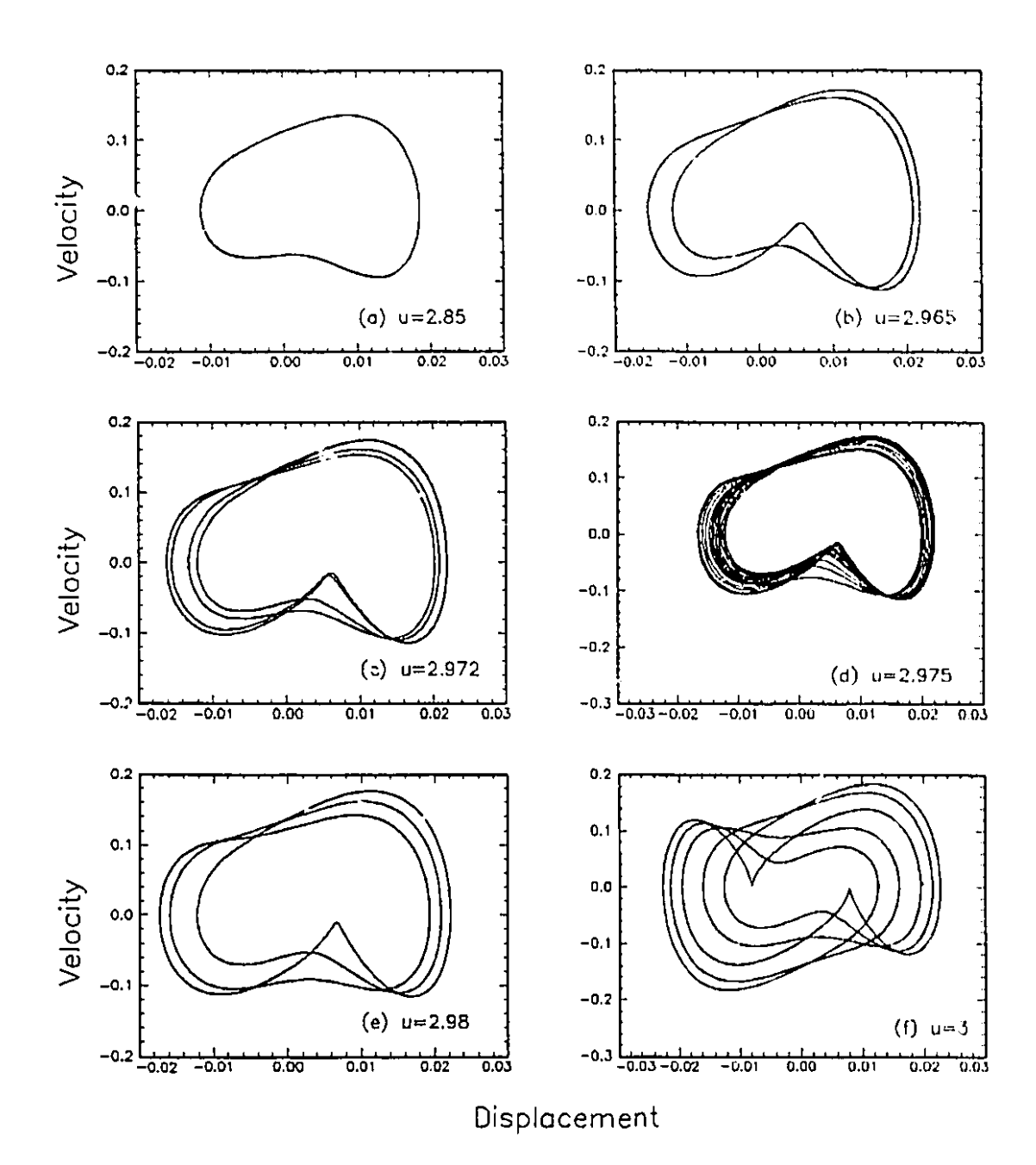


Figure 4.23. Phase-plane plots of $\dot{\phi}_1(\tau)$ versus $\phi_1(\tau)$ at (a) u=2.85, (b) u=2.965, (c) u=2.972, (d) u=2.975, (e) u=2.98 and (f) u=3 for the system of Case 4: h=0.2, c=0.79, f=0.4 and $\kappa_c=5\times10^5$.

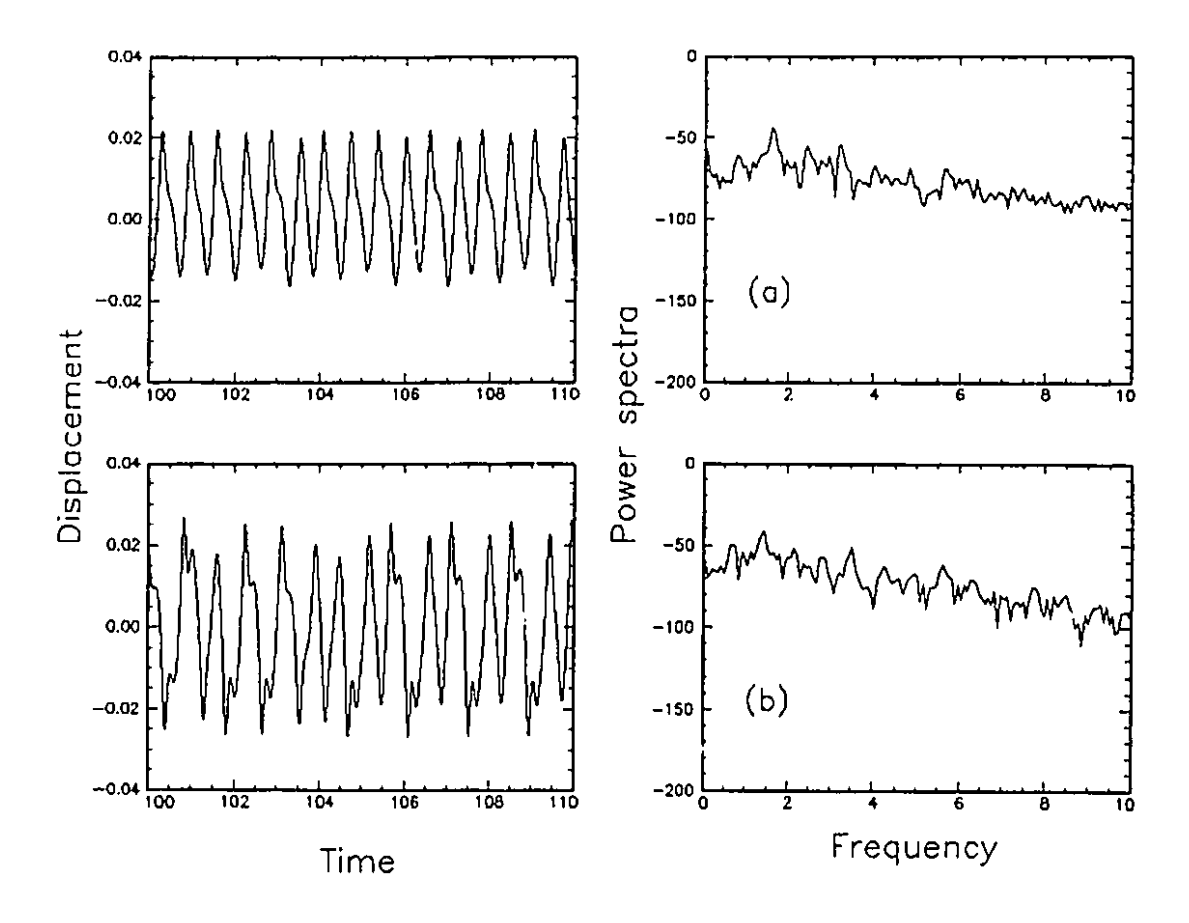


Figure 4.24. Time traces of $\phi_1(\tau)$ versus dimensionless time, τ , and the associated power spectra (dB) for the system of Case 4: $h=0.2, c=0.79, f=0.4, \kappa_c=5\times10^5$ for (a) u=2.975 and (b) u=3.2, showing chaotic motions.

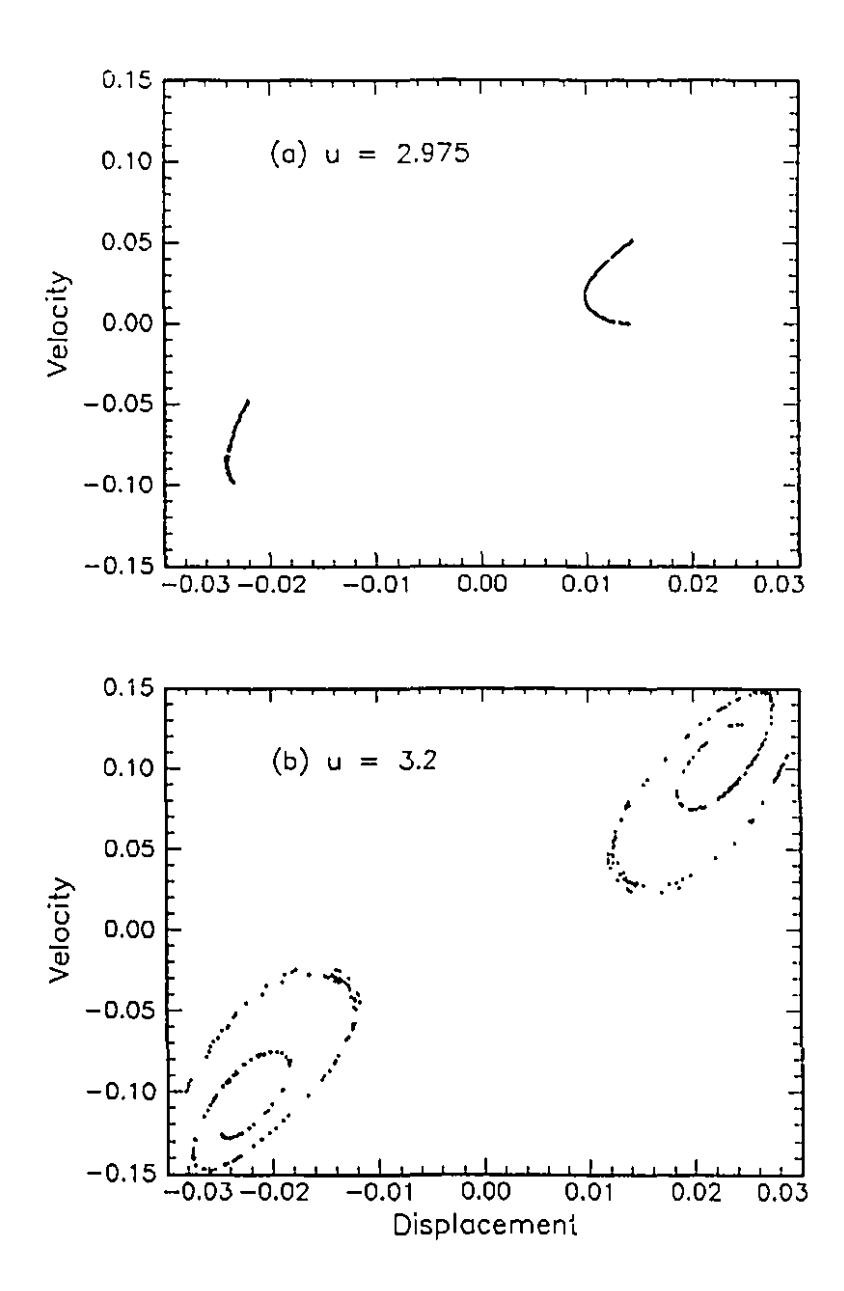


Figure 4.25. Poincaré maps of $\dot{\phi}_2(\tau)$ versus $\phi_2(\tau)$ when $\phi_1(\tau) = 0$ for Case 4: h = 0.2, c = 0.79, f = 0.4, $\kappa_c = 5 \times 10^5$, for (a) u = 2.975 and (b) u = 3.2.

Chapter 5

ANALYTICAL RESULTS: CENTRE MANIFOLD THEORY

Centre manifold theory (Li and Païdoussis 1994) is a method which uses power series expansions in the neighbourhood of an equilibrium point in order to reduce the dimension of a system of ordinary differential equations, thereby helping to understand the dynamical behaviour of an otherwise complex system.

At a degenerate point, which has at least some eigenvalues with zero real part, the space in which the system dynamics evolve can be divided into three subspaces: the stable, unstable and centre eigenspaces, spanned by the eigenvectors whose eigenvalues have negative, positive and zero real parts. At this degenerate point, there exist three invariant subspaces, similarly called stable, unstable and centre manifolds, tangent to the corresponding linear counterparts at the fixed point. Since the stability properties of the dynamical system along the stable and unstable manifolds are known, the system dynamics in the vicinity of the degenerate point is determined by the flow restricted to the centre manifold.

In this chapter, we compare the analytical and the numerical results for the system of Case 1: h = 0.5, f = 0.8, $\kappa_c = 5 \times 10^3$.

5.1 COMPUTATION OF THE UNFOLDING PARAMETERS

Our system of equations is written in the following form:

$$\dot{\mathbf{y}} = \mathbf{A}(\mathbf{u})\mathbf{y} + \epsilon \,\mathbf{f}(\mathbf{y})\,,\tag{5.1}$$

where $\mathbf{y} = \{\phi_1, \ \phi_2, \ \dot{\phi}_1, \ \dot{\phi}_2\}^T$. The coefficients in the nonlinear function $\mathbf{f}(\mathbf{y})$, which in our case is due to the cubic spring, are evaluated at critical values.

Considering u in an ϵ neighbourhood of u_{cr} as $u = u_{cr} + \epsilon \mu$, by assuming that the eigenvalues of A have the general form $\lambda_{1,2} = \sigma_1 \pm i\omega_1$ and $\lambda_{3,4} = \sigma_2 \pm i\omega_2$, one can construct a modal matrix P consisting of the real and imaginary parts of the eigenvectors; then, the system equations may be brought into the standard form

$$\dot{\mathbf{x}} = \mathbf{\Lambda} \, \mathbf{x} + \epsilon \, \mathbf{P}^{-1} \, \mathbf{f}(\mathbf{P} \mathbf{x}), \tag{5.2}$$

where

$$\mathbf{x} = \mathbf{P}^{-1} \mathbf{y}, \qquad \mathbf{\Lambda} = \mathbf{P}^{-1} \mathbf{A} \mathbf{P} = \begin{bmatrix} \sigma_1 & -\omega_1 & 0 & 0 \\ \omega_1 & \sigma_1 & 0 & 0 \\ 0 & 0 & \sigma_2 & -\omega_2 \\ 0 & 0 & \omega_2 & \sigma_2 \end{bmatrix}. \quad (5.3)$$

The matrix Λ is evaluated at the critical points, and [A] is the modal matrix of the system.

5.1.1 Hopf Bifurcation

At $u=u_{cr}$ the first pair of eigenvalues becomes purely imaginary, $\lambda_{1,2}=\pm i\,\omega_0$, with $\omega_0>0$, while $\lambda_{3,4}=-a\pm ib$, a>0, b>0. For ϵ sufficiently small, both σ_i and ω_i in (5.3) can be expanded in terms of ϵ :

$$\sigma_1 = 0 + \epsilon \mu_1 + \mathcal{O}(\epsilon^2), \qquad \omega_1 = \omega_0 + \epsilon \mu_3 + \mathcal{O}(\epsilon^2),$$

$$\sigma_2 = -a + \epsilon \mu_2 + \mathcal{O}(\epsilon^2), \qquad \omega_2 = b + \epsilon \mu_4 + \mathcal{O}(\epsilon^2).$$
(5.4)

The coefficients μ_i , i = 1, 2, 3, 4, are the unfolding parameters, and they represent the effect of the deviation of the control parameter u from the critical value.

Let $\lambda_{1,2} = \sigma_1 \pm i\omega_1$ be the first pair of eigenvalues of A, so that

$$\det \left[\mathbf{A} - (\sigma_1 \pm i\omega_1) \mathbf{I} \right] = \operatorname{Re}_1(\sigma_1, \, \omega_1, \, u) + i \operatorname{Im}_1(\sigma_1, \, \omega_1, \, u) = 0 \,; \tag{5.5}$$

then we obtain for $u = u_{cr} + \epsilon \mu$ the following equations:

$$\operatorname{Re}_{1}(\epsilon\mu_{1}, \,\omega_{0} + \epsilon\mu_{3}, \,u_{cr} + \epsilon\mu) = 0, \quad \operatorname{Im}_{1}(\epsilon\mu_{1}, \,\omega_{0} + \epsilon\mu_{3}, \,u_{cr} + \epsilon\mu) = 0. \quad (5.6)$$

Expanding Re₁ and Im₁ in terms of ϵ , and noting that Re₁(0, ω_0 , u_{cr}), Im₁(0, ω_0 , u_{cr}) = 0, results in

$$\epsilon \mu_1 \frac{\partial \operatorname{Re}_1}{\partial \sigma_1} + \epsilon \mu_3 \frac{\partial \operatorname{Re}_1}{\partial \omega_1} + \epsilon \mu \frac{\partial \operatorname{Re}_1}{\partial u} = 0, \qquad \epsilon \mu_1 \frac{\partial \operatorname{Im}_1}{\partial \sigma_1} + \epsilon \mu_3 \frac{\partial \operatorname{Im}_1}{\partial \omega_1} + \epsilon \mu \frac{\partial \operatorname{Im}_1}{\partial u} = 0, \tag{5.7}$$

where all derivatives are evaluated at the critical values. It is seen that μ_1 and μ_3 may be solved in terms of the variation $\epsilon \mu$ of u.

The flow velocity for the system of Case 1, for which we obtained a limit cycle, which emerges via a Hopf bifurcation, is $u=u_{cr}=2.7396$. Following the above calculation procedure, we obtained $\mu_1=31.0465\mu$ and $\mu_3=-19.3943\mu$. The details of this calculation are presented in Appendix E, Section E.1.

5.1.2 Pitchfork bifurcation

In the case of pitchfork bifurcation, that means for a case of a single zero eigenvalue, the calculation of the unfolding parameters may be carried out in a similar manner. For a single zero eigenvalue, we let $\lambda_3 = \sigma_2$ be the eigenvalue when $u = u_{cr} + \epsilon \mu$, and $\lambda = 0$ at $u = u_{cr} = 1.6946$; we thus have

$$\det(\mathbf{A} - \sigma_2 \mathbf{I}) = \operatorname{Re}_2(\sigma_2, u) = 0.$$
 (5.8)

For ϵ small, letting $\sigma_2 = \epsilon \mu_2$ at $u = 1.6946 + \epsilon \mu$, by expanding and evaluating $\text{Re}_2(\sigma_2, u)$ we obtain

$$\epsilon \mu_2 \frac{\partial \text{Re}_2}{\partial \sigma_2} (0, u_{cr}) + \epsilon \mu \frac{\partial \text{Re}_2}{\partial u} (0, u_{cr}) = 0,$$
 (5.9)

from which $\mu_2 = -4.919\mu$ (Appendix E, Section E.2).

5.2 CENTRE MANIFOLD CALCULATIONS

5.2.1 Hopf Bifurcation

The details for these calculations may be found in Appendix E, Section E.3.

For the critical flow velocity $u_{cr}=2.7396$, the eigenvalues are $\lambda_{1,2}=\pm 9.0176i$ (hence, $\sigma_1=0$, $\omega_1=9.0176$) and $\lambda_{3,4}=-4.4646\pm 5.2242i$ (hence, $\sigma_2=4.4646$, $\omega_2=5.2242$). The second of equations (5.3) may therefore be written as

$$\mathbf{\Lambda} = \begin{bmatrix} 0 & -9.0176 & 0 & 0 \\ 9.0176 & 0 & 0 & 0 \\ 0 & 0 & -4.4646 & -5.2242 \\ 0 & 0 & 5.2242 & -4.4646 \end{bmatrix}. \tag{5.10}$$

The system of equations (5.2) can be reduced to a two-dimensional system by centre manifold theory, involving the "centre space" of (5.10), i.e., the part associated with the purely imaginary eigenvalues; this leads to the reduced two-dimensional system

By replacing $\omega_0 = \omega_1 = 9.0176$ and by substituting $\mu_1 = 31.0465\mu$, $\mu_3 = -19.3943\mu$, as determined in Section 5.1.1, equation (5.11) gives

$$\left\{ \begin{array}{c} \dot{x}_1 \\ \dot{x}_2 \end{array} \right\} = \left[\begin{array}{ccc} 31.0465 \,\mu & -9.0176 + 19.3943 \,\mu \\ 9.0176 - 19.3943 \,\mu & 31.0465 \,\mu \end{array} \right] \left\{ \begin{array}{c} x_1 \\ x_2 \end{array} \right\} + \left\{ f(x_1, x_2) \right\} ,$$
 (5.12)

where

$$\{f(x_1, x_2)\} = \begin{cases} f_1 \\ f_2 \end{cases} = \begin{cases} 0.1968x_1^3 - 1.2342x_1^2x_2 + 2.5775x_1x_2^2 - 1.7943x_2^3 \\ 0.9246x_1^3 - 5.7989x_1^2x_2 + 12.1102x_1x_2^2 - 8.4301x_2^3 \end{cases}.$$
(5.13)

Either the method of normal forms or the method of averaging may be used to solve these equations. We shall use the latter and, accordingly, let

$$x_1 = r\cos\theta , \qquad x_2 = r\sin\theta . \qquad (5.14)$$

Then, after substituting into (5.13) and applying the method, the averaged equations

$$\dot{r} = \epsilon(\mu_1 + a r^2) + \mathcal{O}(\epsilon^2), \quad \dot{\theta} = \omega_0 + \epsilon \mu_2 + e b r^2 + \mathcal{O}(\epsilon^2)$$
 (5.15)

are obtained, where

$$a = [f_{1,12} + 3 f_{1,30} + 3 f_{2,03} + f_{2,21}]/8.$$
 (5.16)

The terms $f_{i,jk}$ are the coefficients of $f_i(i=1,2)$ in equation (5.13), in which jk is associated with $x_1^j x_2^k$ (Guckenheimer and Holmes 1983); for example, $f_{1,12} = 2.5775$.

In the case under consideration, it is found that a = -3.4902, i.e. a < 0, signifying that the Hopf bifurcation is supercritical (Guckenheimer and Holmes 1983). Limit-cycle motions are obtained when $\dot{r} = 0$, or from (5.15)

$$r^2 = -\mu_1/a = 8.8954 \ \mu \ . \tag{5.17}$$

It is seen that a real limit-cycle amplitude, r, exists only for $\mu \equiv u - u_{cr} > 0$. For $\mu < 0$, the origin (undeformed equilibrium) is stable, and a limit cycle does not exist.

We shall present the phase plots for our system in Figure 5.1(a) for $u = 2.73 < u_{cr}$, where $u_{cr} = 2.7396$, i.e., for $\mu = -0.0096 < 0$, where the origin is stable. If $u = 2.74 > u_{cr}$, then $\mu = 0.0004 > 0$ and the origin becomes unstable; we then obtain a limit cycle, as seen in the phase plot in Figure 5.1(b).

We have also compared the maximum amplitude of the system as a function of μ , as obtained by (i) the centre manifold approximation and (ii) the Runge-Kutta numerical integration. Agreement between the two is very good for $\mu < 0.02$, as can be seen in Figure 5.2; in terms of order of magnitude, it is quite acceptable up to $\mu \simeq 0.08$. This gives a taste for the power of the centre manifold method, on the one hand, and gives confidence to the veracity of the numerical results, on the other.

5.2.2 Pitchfork bifurcation

For the same system, but for $u_{cr}=1.6946$, the threshold flow velocity for the pitchfork bifurcation, the matrix Λ is found to be

$$\mathbf{\Lambda} = \begin{bmatrix} -1.8371 & -21.5414 & 0 & 0 \\ 21.5414 & -1.8371 & 0 & 0 \\ 0 & 0 & 0 & 0 \\ 0 & 0 & 0 & -2.4111 \end{bmatrix}. \tag{5.18}$$

Application of centre manifold theory in this case (see Section 5.1.2) reduces the full system into a one-dimensional sub-system,

$$\dot{x}_3 = \mu_2 \, x_3 - 11.5757 \, x_3^3 = -\left(4.919 \, \mu \, x_3 + 11.5757 \, x_3^3\right) \,, \tag{5.19}$$

where $\mu_2 = -4.919 \,\mu$, obtained in Section 5.1.2, has been utilized.

For $u=1.6 < u_{cr}=1.6946$ (i.e., for $\mu < 0$), the origin is stable, as can been seen in the phase plot in Figure 5.3(a); but for $\mu > 0$, e.g. u=1.7, the origin becomes unstable, as can be seen in Figure 5.3(b), where the trajectory ends at one of the new fixed points.

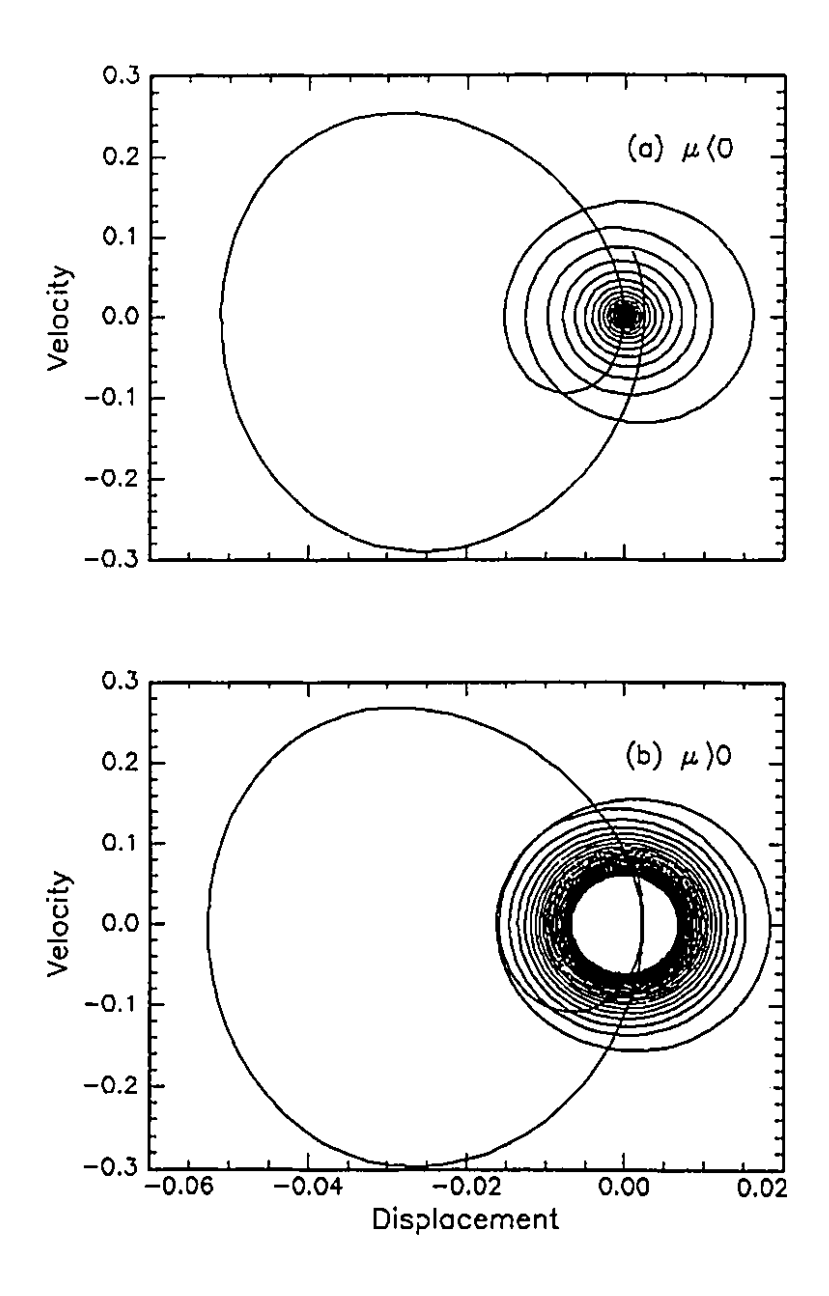


Figure 5.1. Analytical, centre-manifold representations of the system of Case 1: $h = 0.5, c = 0.38, f = 0.8, \kappa_c = 5 \times 10^3$, (a) just before and (b) just after the Hopf bifurcation.

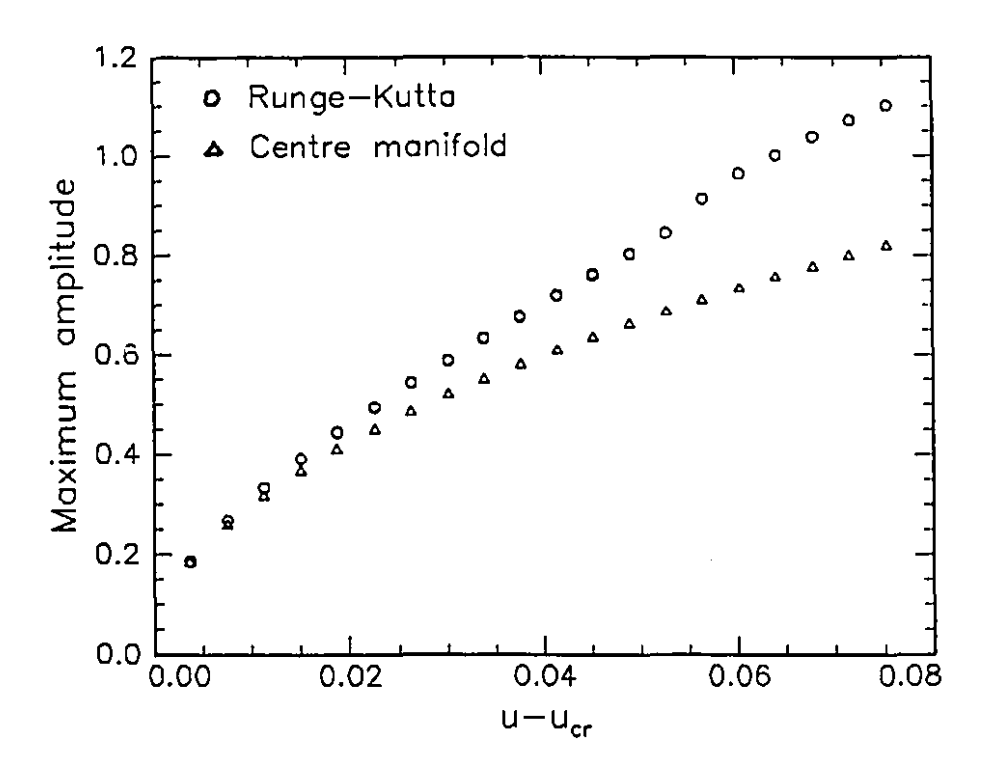


Figure 5.2. The post-Hopf limit-cycle amplitude versus $\mu = u - u_c$ for the system of Case 1: h = 0.5, c = 0.38, f = 0.8, $\kappa_c = 5 \times 10^3$, as obtained numerically (Runge-Kutta) and analytically by centre-manifold reduction.

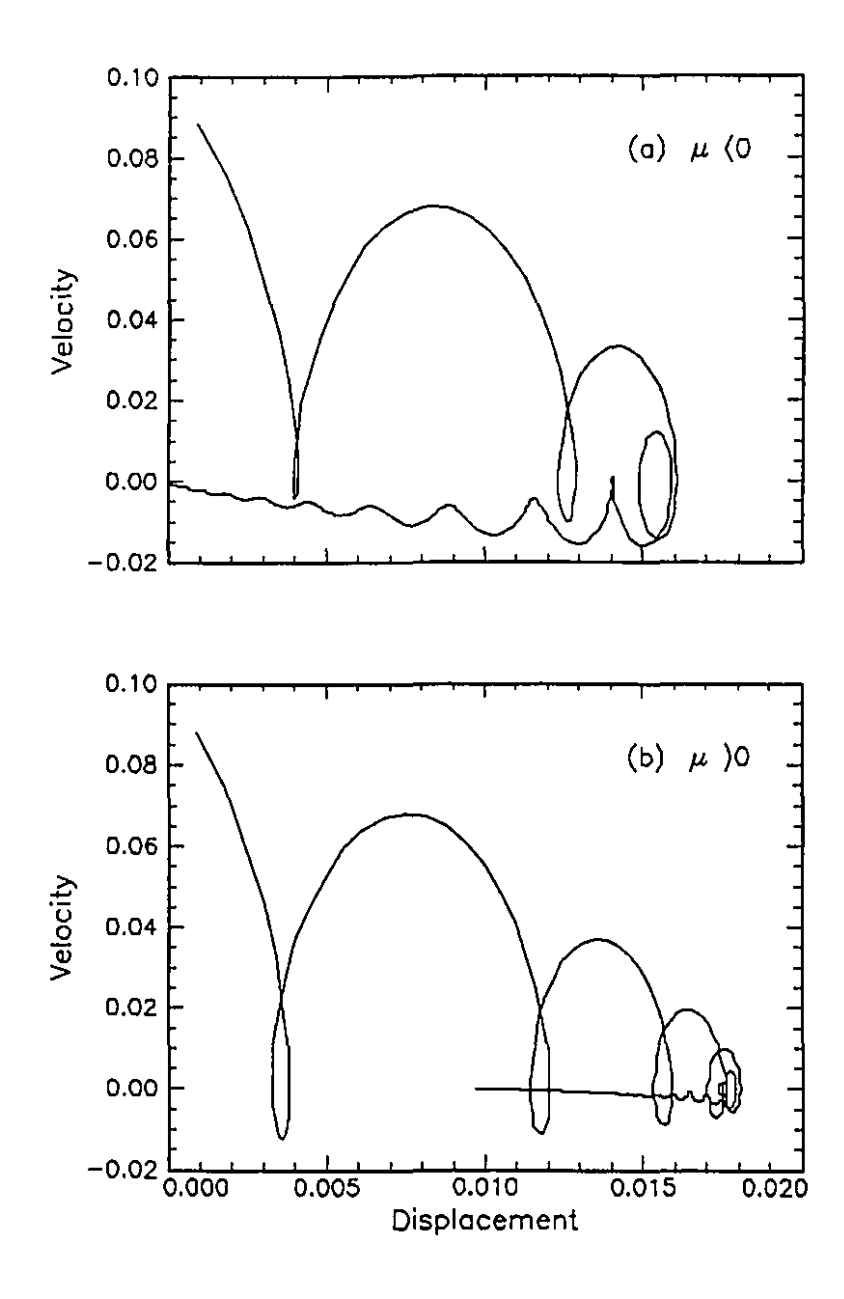


Figure 5.3. Analytical, centre-manifold representations of the system of Case 1: h = 0.5, c = 0.38, f = 0.8, $\kappa_c = 5 \times 10^3$, (a) just prior to and (b) just after divergence ($u_c = 1.695$ for pitchfork bifurcation), showing: (a) that the origin (0,0) is a stable fixed point, and (b) that the origin is no longer stable, but another fixed point (0.009,0) has arisen.

Chapter 6

NUMERICAL RESULTS FOR THE FIRST MODEL WITH N = 3 AND N = 4

In Chapter 4, the numerical results for the two-cylinder, two-degree-of-freedom (N=2) system were presented for Cases 1-4 (defined at the beginning of Chapter 4). Then, some analytical results, obtained via centre-manifold theory, were presented in Chapter 5 for Case 1.

It is of interest to know how representative these results are for N > 2. This is the reason for undertaking numerical calculations for N = 3 and 4. These will be presented in what follows for each of the same Cases 1-4, sequentially for N = 3 and N = 4 in each case; another system, Case 5, is also analyzed, in Section 6.5.

6.1 CASE 1: h = 0.5, f = 0.8 and $\kappa_c = 5 \times 10^3$

6.1.1 Case 1 for the three-cylinder system, N = 3

As the flow velocity u is increased in Figure 6.1, both the real and imaginary components of the first-mode eigenvalue approach zero; this corresponds to a divergence instability (pitchfork bifurcation), which occurs at u = 1.711. As u is increased further, the real part of the eigenvalues becomes negative again, so that the system is restabilized, at u = 2.887. Furthermore, at u = 3.167, in the second mode, purely imaginary eigenvalues arise, which corresponds to a flutter instability (Hopf bifurcation). For u = 3.8958, the real part of eigenvalues again becomes negative, so that the system is restabilized.

For u = 3.9688, both the real and imaginary components of the first-mode eigenvalue again approach zero; this corresponds to a second divergence instability (pitchfork bifurcation). The system remains unstable for u > 3.9688, and another flutter instability (Hopf bifurcation) occurs in the third mode for u = 4.058.

Figures 6.2 to 6.5 show bifurcation diagrams and phase-plane portraits for the first-cylinder displacement of the system, for flow velocities above the critical flow velocity for flutter.

The bifurcation diagram for flow velocities u between 3.1 and 3.7, is shown in Figure 6.2(a); there, u = 3.167 is the flow velocity for which flutter instability occurs. A stable, symmetric limit-cycle develops after the Hopf bifurcation, as shown in Figure 6.3(a) for u = 3.35. Different shapes for the phase plane portraits are shown for different flow velocities, as for example in Figure 6.3(b,c) for (b) u = 3.6 and (c) u = 3.7, respectively. These shapes remain always symmetrical with respect to the origin (central symmetry). As the ratio of the two dominant frequencies $f_1/f_2 = 1/3$ in all these cases, then these motions are periodic with period $T = T_1 = 3T_2$. For (a) u = 3.4, then the period T = 0.59, for (b) u = 3.6,

then T = 0.49, and for (c) u = 3.7, then T = 0.44.

As may be seen further in the bifurcation diagram of Figure 6.2(b), the system becomes chaotic at $u \simeq 4.09$. The route to chaos is clarified via Figures 6.4 and 6.5. The system is restabilized between u = 3.8958 and 3.9688 (not completely shown in the two bifurcation diagrams, Figures 6.2(a,b)). At u = 3.9688, a pitchfork bifurcation occurs, and for u > 3.9688 (Figure 6.2(b)), the origin is no longer a stable fixed point (S.F.P), but new stable fixed points on either side are generated.

The stability of these new fixed points was investigated by linearizing the system in their vicinity. As seen in Figure 6.4(a), as u is increased (to u=4.05) the eigenvalues become purely imaginary, at the extreme right of the figure, signifying the occurrence of another Hopf bifurcation and the development of limit-cycle motions for higher u, the onset of which is marked by the kink in the curves in Figure 6.2(b). This is further clarified by the phase-plane plots of Figures 6.4(b,c). For u=4.052, the fixed point is still stable and the trajectory of Figure 6.4(b) approaches that point with time. For u=4.053, however, which is beyond the Hopf bifurcation, a limit-cycle develops, as seen in Figure 6.4(c). This limit-cycle is symmetric about the fixed point which gave it birth, but asymmetric vis-a-vis the origin; only the upper (maximum) branch of the limit-cycle is shown in the bifurcation diagram of Figure 6.2(b) for each of the two limit-cycles, each arising from one of the two fixed points.

Furthermore, for u > 4.053, phase-plane portraits were constructed in Figure 6.5 in order to clarify the bifurcation diagram (Figure 6.2(b)). One can see in Figure 6.5(a) that a symmetric limit-cycle arises from a pitchfork bifurcation for u = 4.06; the motion becomes quasiperiodic-two in Figure 6.5(b) for u = 4.0885, quasiperiodic-three in Figure 6.5(c) for u = 4.09, and chaotic in Figure 6.5(d) for u = 4.0965.

Figure 6.6 again verifies these results for (a) u = 4.0885, (b) u = 4.0900, and (c) u = 4.0965: in the first column (panels (a₁), (b₁) and (c₁)) are the Poincaré

maps, and in the second column the corresponding power spectra (panels (a_2) , (b_2) and (c_2)). Before analysing the Poincaré maps depicted in Figure 6.6, it has to be mentioned that these maps were constructed with 10,000 time steps, and they were obtained by plotting $\dot{\phi}_2(\tau)$ versus $\phi_2(\tau)$ for $\phi_1 \simeq 0.1$. As in the computer program for Poincaré map calculations it was very difficult to obtain exactly $\phi_1 = 0.1$, ϕ_1 was taken in the interval (0.1, 0.100001).

The closed nature of the curves depicted in the Poincaré map of Figure $6.6(a_1, b_1)$ suggests the quasiperiodic motion of the system for the flow velocities (a_1) u = 4.0885, and (b_1) u = 4.0900. The Poincaré map shown in Figure $6.6(c_1)$ for u = 4.0965, on the other hand, suggests that the system is chaotic at that stage.

The nature of the dynamical states depicted in Figure 6.6 may best be assessed by the power spectra, which are presented in the second column of that figure. In Figure 6.6(a₂), for u = 4.0885, two fundamental frequencies are found: $f_1 = 0.934$ 4006 and $f_7 = 6.612$ 681, from which all other frequency peaks may be constructed, occurring at $nf_1 \pm mf_7$, where n and m are integers. Thus, these peaks occur at $f_n = nf_1$ for n = 2, 3, ..., 9, $f_{10} = 3f_1 + f_7$, $f_{11} = 4f_1 + f_7$, $f_{12} = 12f_1$, $f_{13} = 6f_1 + f_7$, $f_{14} = 14f_1$, $f_{15} = 2f_7$, $f_{16} = 15f_1$, $f_{17} = 9f_1 + f_7$, $f_{18} = 10f_1 + f_7$. Whether the ratio f_1/f_7 is rational or irrational depends on the accuracy of the determination of the frequencies f_1 and f_7 . If one presumes that the values given here are absolutely precise, then by the continued fraction technique and Mathematica, one finds a rational ratio $f_1/f_7 = 0.1413044 = 13/92$. As the motion of the system involves two fundamental frequencies, and the Poincaré map is represented by a closed curve, that means, finally that the motion is indeed quasiperiodic-two.

The power spectrum for u = 4.0900 in Figure 6.6(b₂) is found to involve three fundamental frequencies, $f_1 = 0.862$ 5236, $f_2 = \frac{5}{4} f_1$ and $f_5 = \frac{10}{3} f_1$. All other frequencies may be constructed by $nf_1 \pm mf_2 \pm pf_5$, with n, m, and p being integers. Thus, for example, $f_3 = 2f_1$, $f_4 = f_1 + f_2$, $f_6 = f_1 + f_5$, $f_7 = 2f_1 + f_5$, $f_8 = f_1 + f_2 + f_5$, $f_9 = 2f_1 + f_2 + f_5$, $f_{10} = 3f_1 + f_2 + f_5$, $f_{11} = 12f_1 - f_5$, and so

on. In this case, the ratios of the fundamental frequencies are definitely rational $\left(\frac{5}{4}\right)$ and $\left(\frac{10}{3}\right)$. As the motion of the system involves three fundamental frequencies, and the Poincaré map is again represented by closed curves, the motion of the system at this value of u also is quasiperiodic-three.

The system at u = 4.0965 is clearly chaotic, as evidenced already by the Poincaré map shown in Figure 6.6(c₁), as well as by the phase plot of Figure 6.5(d) and the power spectrum of Figure 6.6(c₂). In the latter, although the principal frequencies (twin peak) and their harmonics are still very prominent, the subharmonic content is fundamentally flat.

This route to chaos may be explained by means of the Ruelle-Takens-Newhouse theory (Ruelle and Takens 1971; Bergé et al. 1984), the overall process involving three successive Hopf bifurcations. The first leads from an initial static steady state (fixed point, dimension zero) to a periodic one (limit cycle, dimension one). The second transforms the periodic regime into a quasiperiodic-two regime (Figure 6.6(a)). The third gives a transition to quasiperiodic-three motions (Figure 6.6(b)), which finally gives rise to chaos (Figure 6.6(c)).

6.1.2 Case 1 for the four-cylinder system, N = 4

As the flow velocity u is increased in Figure 6.7, both the real and imaginary components of the first-mode eigenvalue approach zero; this corresponds to a divergence instability (pitchfork bifurcation), which occurs at u = 1.71. As u is increased further, the real part of the eigenvalues again becomes negative, so that the system is restabilized, at u = 3.01.

Furthermore, at u = 3.42, in the second mode, purely imaginary eigenvalues arise, which corresponds to flutter instability (Hopf bifurcation). For u = 4.465, the system is restabilized.

For u = 4.65, a second divergence instability (pitchfork bifurcation) in the first mode is obtained. The system remains unstable for u > 4.65, and another flutter instability (Hopf bifurcation) occurs in the third mode for u = 4.78.

In the fourth mode, the real part of the eigenvalues is always negative; so, from the linear stability point of view, only the other three modes are of interest.

For this case, we have obtained the bifurcation diagram and the corresponding phase-plane portraits for flow velocities u between 3.35 (which is the critical flow velocity for flutter), and 3.70. They were shown in Figures 6.8 and 6.9, respectively. The phase-plane portraits obtained for (a) u = 3.35, (b) u = 3.60 and (c) u = 3.70 are symmetric about the origin. These motions were already described in the previous chapter as periodic motions with two frequencies, which ratios were equal to 1/3. The periods of motion for these cases are the following: T = 0.71 for (a) u = 3.35; T = 0.58 for (b) u = 3.6; and T = 0.53 for u = 3.7, so that for a higher number of articulated cylinders N = 4, higher values for the periods of oscillations are obtained.

The system is restabilized for higher flow velocities, between $u \simeq 3.70$ and 4.55 (not shown in the bifurcation diagrams of Figures 6.8 and 6.10), and becomes unstable through a flutter instability (Hopf bifurcation) for $u \simeq 4.56$. For flow velocities higher than u = 4.56, as may be seen further in the bifurcation diagram of Figure 6.10, the system probably becomes chaotic for u between 4.595 and 4.61; the doubt exists because it is difficult to distinguish between quasiperiodic and chaotic motion in this case. To clarify this question, it will be necessary to construct the phase-plane portraits and their corresponding power spectra for the system.

The phase-plane portraits for (a) u = 4.59, (b) u = 4.60, (c) u = 4.6095, and (d) u = 4.6098 are shown in Figure 6.11. The closed two-segment curves of the Poincaré maps of Figure $6.12(a_1 \cdot a_1)$ establish the quasiperiodic nature of the motion of the system for (a_1) u = 4.6 and (b_1) u = 4.6095, while the closed four-segment curves of Figure $6.12(c_1)$ show that the motion is quasiperiodic for

 (c_1) u = 4.6098. In addition, power spectra for the same flow velocities are presented in the second column of Figure 6.12, which reinforce the same conclusions, as will further be discussed in the following paragraphs.

In Figure 6.12(a_2), for u=4.6, two fundamental frequencies are found: $f_1=1.074\ 220$ and $f_2=1.660\ 158$, from which all the other frequency peaks are calculated; they occur at $mf_1\pm nf_2$, where m and n are integers. Thus, $f_3=f_1+2f_2$, $f_4=2f_1+3f_2$, $f_5=4f_1+2f_2$, $f_6=6f_1+2f_2$, $f_7=5f_1+3f_2$, $f_8=7f_1+3f_2$, $f_9=6f_1+4f_2$ and $f_{10}=5f_1+5f_2$.

For u=4.6095, in Figure 6.12(b₂), the same two fundamental frequencies were found, f_1 and f_2 . Different values for the other frequencies f_n (where n>3) were found, as follows: $f_3=-f_1+2f_2$, $f_4=-f_1+3f_2$, $f_5=f_1+2f_2$, $f_6=3f_2$, $f_7=4f_2$, $f_8=2f_1+3f_2$, $f_9=4f_1+2f_2$ and $f_{10}=3f_1+3f_2$.

For (c_2) u = 4.6098, again the same two fundamental frequencies as in the other two cases were found, the other frequencies being linear combinations of f_1 and f_2 . Finally, it may be concluded that the Winding number $(W = f_1/f_2 = 0.6471)$ is the same for (a_2) u = 4.60, (b_2) u = 4.6095 and (c_2) u = 4.6098, and that the motion of the system for these flow velocities is quasiperiodic.

For u > 4.6098, the amplitudes of motion become too large, while the basic analytical model has been constructed for small amplitude motions; so, this may explain why no convergent solutions were obtained. No chaotic motion was obtained for this case; the motion remains quasiperiodic.

Last, a comparison between the behaviour of a three- and the four-articulated-cylinder systems will be done. For flow velocities u between 3.35 and 3.70, the bifurcation diagram and the corresponding phase plots of Figures 6.8 and 6.9 obtained here for N=4 were compared to those for the N=3 system discussed before (Figures 6.2(a) and 6.3). It may be seen that the two sets of diagrams are similar, and hence the dynamical behaviour of the system is qualitatively similar in this range of u.

The amplitudes in the two cases are compared next. It is noted that the maximum displacement for the first cylinder in the system, ϕ_{1max} , for the system with N=4, is 1.3 to 1.35 times higher than ϕ_{1max} for the N=3 system for flow velocities u between 3.35 and 3.7; (for this range of flow velocities u, the system is not chaotic)

For flow velocities u > 3.70, the route to chaos for the N = 3 system presented by the bifurcation diagram and the corresponding phase-plots of Figures 6.2(b) to 6.5 is compared with the dynamical behaviour of the N = 4 system presented by the bifurcation diagram, the phase-plane plots and the corresponding Poincaré maps and power spectra of Figures 6.10 to 6.12. For the N = 3 system, a symmetric limit cycle arises from a pitchfork bifurcation and it will be symmetrical about the fixed point which gave it birth, but asymmetric vis-a-vis the origin, and chaotic motion occurs. For the N = 4 system, the limit cycle arises from a Hopf bifurcation and is symmetric about the origin and no chaotic motion will occur.

6.2 CASE 2:
$$h = 0.2$$
, $f = 0.8$ and $\kappa_c = 5 \times 10^3$

This case corresponds to a system with a narrower annulus than Case 1.

6.2.1 Case 2 for the three-cylinder system, N = 3

As u is increased, it is seen in Figure 6.13(a) that the first mode undergoes a pitchfork bifurcation at u = 1.1733. As u is increased further, the system is restabilized in this mode at u = 1.9544.

For u = 2.287, purely imaginary eigenvalues arise in the second mode (Figure 6.13(b)), signalling a Hopf bifurcation (flutter). This dynamical state persists up to u = 2.6568, at which point the system regains stability and remains stable in that mode thereafter. Then, for u = 2.7, the system undergoes a second pitchfork bifurcation and remains unstable in that mode to at least u = 5. At a slightly

higher flow velocity (u = 2.995), the system also loses stability in its third-mode, by another Hopf bifurcation, as seen in Figure 6.13(c). Thus, for u > 2.995, up to at least u = 5, the system is subject concurrently to divergence in its first mode and flutter in its third.

Figure 6.14 gives the bifurcation diagram in the range 2.25 < u < 2.85 with impacting modelled by a cubic-spring; the evolution of the limit-cycle amplitude beyond the first Hopf bifurcation is clearly seen in the phase-plane plots in Figure 6.15 for 2.30 < u < 2.658. In Figure 6.15(a,b), the limit cycle is symmetric about the origin for (a) u = 2.3 and (b) u = 2.55; there is a unique value for the maximum amplitude for these two cases. In Figure 6.14, for 2.60 < u < 2.66, approximately, three values of amplitude are shown, corresponding to local maxima of $\phi_{1\max}$, as clarified by the phase-plane diagram of Figure 6.15(c,d) for (c) u = 2.625 and (d) u=2.658, respectively: by taking a line close to $\dot{\phi}=0$, three local maxima are counted for ϕ , as well as three local minima. These phase-plane portraits remain symmetric about the origin and the motion of the system is periodic for all the cases mentioned in Figure 6.15. For u = 2.55, the frequency of the system is f = 1.52; for u = 2.625 the frequency of the system increases and is f = 1.79; while for u=2.658 then f=2.04. In the power spectra all these frequencies will have odd subharmonics; it means that the motions of the system are periodic with two dominant frequencies, which ratio is $f_1/f_2 = 1/3$.

At u = 2.6568 the origin regains its stability and is a simple fixed point, up to $u \simeq 2.70$, the threshold of the second divergence (pitchfork bifurcation), in the first mode of our system, which has been observed already in Figure 6.14. The two branches of the pitchfork were determined via opposite-sign initial conditions. Thus, for u > 2.7, the origin is no longer a stable fixed point, but new stable fixed points (S.F.P.s) on either side are generated.

The stability of these new fixed points was investigated by linearizing the system in their vicinity. As seen in Figure 6.16(a), as u is increased (to u = 2.7225)

the eigenvalues become purely imaginary, at the extreme right of the figure, signifying the onset of another Hopf bifurcation and the development of limit-cycle motions (L.C.) for higher u, the onset of which is marked by the kink in the curves in Figure 6.14. This is further clarified by the phase-plane plots of Figure 6.16(b,c). For u=2.7225 the fixed point is still stable and the trajectory of Figure 6.16(b) approaches that point with time. For u=2.725, however, which is beyond the Hopf bifurcation, a limit cycle develops, as seen in Figure 6.16(c). This limit cycle is symmetric about the fixed point which gave it birth, but asymmetric $vis-\dot{a}-vis$ the origin of course; only the upper (maximum) branch of the limit cycle is shown in the bifurcation diagram of Figure 6.14 for each of the two limit cycles — arising from one or the other of the two fixed points.

For u > 2.74, a cascade of period-doubling bifurcations is seen in Figure 6.17, leading to chaos. Period-1, period-2 and period-4 motions are displayed in the corresponding phase portraits of Figure 6.17(a,b,c), for (a) u = 2.74, (b) u = 2.77, and (c) u = 2.778, respectively. The thresholds for period-2 to period-16 motion were pin-pointed as follows: u = 2.765, 2.7769, 2.782 and 2.7831, from which a Feigenbaum number based on the last three is Fei = 4.64, close to the "ideal". Figure 6.17(d), for u = 2.79, shows chaotic motion.

As shown in Figure 6.18, for higher flow velocities, the motion of the system becomes period-two for (a) u=2.80 of period T=1.42, (b) period-four for u=2.8011 (its period is T=2.82 twice previous period) and finally the motion becomes chaotic through these period-doubling bifurcations for u=2.8012 to (c) u=2.8018. The chaotic motions of the system for u=2.8018 depends of the sign of the initial condition: the phase-plane portrait for (c) u=2.8018 was obtained with $\dot{\phi}_1=0.1$, while the one for (d) u=2.8018 with $\dot{\phi}_1=-0.1$. By merging these two phase-plane portraits, one may obtain for a higher flow velocity, i.e., (e) u=2.82 a chaotic motion of the system which visits both positive and negative parts of the phase-plane, and hence is independent of the sign of the initial conditions.

The corresponding Poincaré map, shown in Figure 6.19 for u=2.835, displays an interesting "nebula" shape, characteristic of chaotic motion; it was obtained by plotting $\dot{\phi}_2(\tau)$ versus $\phi_2(\tau)$ when $\phi_1(\tau)=0$.

As discussed in conjunction with the eigenvalue analysis, interesting dynamical behaviour was expected to arise for u > 2.995, when the system should be subject concurrently to (i) flutter associated with the third mode (via Hopf bifurcation of the origin) and (ii) flutter associated with the first mode (via Hopf bifurcations of the new stable points emanating from the second pitchfork bifurcation shown in Figure 6.14). Unfortunately, no convergent solutions could be obtained for u > 2.84 approximately; this was confirmed not to be a fault of the solution algorithm. The most likely cause is that the amplitudes of motion become too large, while the basic analytical model is for small amplitude motions.

6.2.2 Case 2 for the four-cylinder system, N = 4

As the flow velocity u is increased in Figure 6.20, it is seen that the system is first subjected to a divergence instability (pitchfork bifurcation), at u = 1.17. As u is increased further, the system is restabilized, at u = 2.036. Furthermore, at u = 2.4, always in the first mode, the system becomes unstable by flutter (Hopf bifurcation), and for u = 3.03, the system is restabilized.

For u = 3.16, a divergence instability (pitchfork bifurcation) occurs, associated with the second mode. For u = 3.488, the real part of the eigenvalues again becomes negative, so that the system is restabilized in the second mode.

At u=3.52, purely imaginary eigenvalues arise, in the third mode, which correspond to another flutter instability. Furthermore, at u=3.56, in its second mode, another pair of purely imaginary eigenvalues arise, which correspond to yet another flutter instability. For u=3.86, however, the system is restabilized in its third mode, although it continues to be unstable in its second mode.

A second (third) flutter instability reappears in the third mode for u = 4.36, so that the system remains unstable in the second and third modes for u > 4.36.

In the fourth mode, the real part of the eigenvalues is always negative; so, from the linear stability point of view, only the other three modes are of interest.

We have obtained the bifurcation diagram for u = 2.2 - 2.7, which is shown in Figure 6.21, and corresponding phase-plane plots in Figure 6.22, for (a) u = 2.3, (b) u = 2.55, (c) u = 2.625 and (d) u = 2.658, which are always symmetric about the origin and periodic with odd subharmonics, as are the ones mentioned in the previous subsection 6.2.1, for N = 3. For N = 4, there are obtained the following frequencies for different flow velocities: for u = 2.55, the frequency of the system is f = 1.11; for u = 2.625, the frequency of the system increases to f = 1.20, while for u = 2.658, it is f = 1.3. It might be concluded from the last two subsections that the frequency of the system increases with u, as well as with the number of degrees of freedom.

For higher flow velocities, i.e., u > 2.7, the amplitudes of motion become too large, which is inconsistent with this analytical model which is valid for small amplitude motions. This may be the reason why for u > 2.7, no convergent solutions could be obtained. No chaotic motion could be found for this system.

Finally, the phase-plane plots in Figure 6.22 can be compared to the phase-plane plots for N=3 (already shown in Figure 6.15) for the same flow velocities u. We can see that we have obtained almost the same qualitative behaviour. From the quantitative point of view, for flow velocities 2.2 < u < 2.7, ϕ_{1max} for the N=3 system is between 1.1 and 1.3 times higher than ϕ_{1max} for the N=4 system; but this agreement does not extend to other values of u. For u>2.7 the N=3 system becomes chaotic for $u \simeq 2.8$ (Figure 6.14), while the N=4 system does not become chaotic.

6.3 CASE 3: h = 0.5, f = 0 and $\kappa_c = 5 \times 10^5$

Physically, the system in this case is similar to that of Case 1, but the free end is blunt in this case.

6.3.1 Case 3 for the three-cylinder system, N = 3

For this case, the system becomes unstable through a flutter instability (Hopf bifurcation) for a flow velocity $u \simeq 4.9$.

By comparing the bifurcation diagram presented in Figure 6.23, together with the corresponding phase-plane portraits for (a) u = 6.15, (b) u = 6.235, (c) u = 6.25 and (d) u = 6.4, shown in Figure 6.24, it is seen that the quasiperiodic route to chaos (Ruelle-Takens-Newhouse theory) is followed in this case.

Poincaré maps shown in Figure 6.25 for (a) u = 6.235, (b) u = 6.25 and (c) u = 6.265 are represented by closed curves, which verifies the quasiperiodic motion of the system, while the Poincaré map for (d) u = 6.2695 shows its chaotic behaviour at that flow velocity.

6.3.2 Case 3 for the four-cylinder system, N = 4

By comparing the bifurcation diagram (Figure 6.26) with the corresponding phaseplane portraits obtained in Figure 6.27, the route to chaos is seen to arise through period-odd motions (period-three, -six, etc.).

Poincaré maps are shown in Figure 6.28 for (a) u = 6.235 and (b) u = 6.365, respectively, and they verify (a) the period-three motion for our system for u = 6.235 and (b) its period-six motion for u = 6.365. Furthermore, Poincaré maps shown in Figure 6.28(c,d) show the period-twelve motion for (c) u = 6.37, and chaotic motion for (d) u = 6.4.

From a quantitative point of view, the maximum displacement for the first cylinder in the system, ϕ_{1max} , for the system with N=4 was found to be 1.1 to 1.3 times higher than ϕ_{1max} for the three-degree-of-freedom system for flow velocities u between 5 and 6.4; but the dynamics of the two systems are quite different, the routes to chaos being completely different.

6.4 CASE 4: h = 0.2, f = 0.4 and $\kappa_c = 5 \times 10^5$

This system is similar to Case 2, but with an intermediately blunt free end — blunter than for Case 2.

6.4.1 Case 4 for the three-cylinder system, N = 3

For this system, we shall study its behaviour for flow velocities u higher than the critical flow velocity for pitchfork bifurcation $u_{pf} \simeq 2.7$.

The route to chaos for the bifurcation diagram of Figure 6.29 is clarified via the phase-plane portraits of Figure 6.30. For u = 2.7, a pitchfork bifurcation occurs. The two branches of the pitchfork bifurcation were determined via opposite-sign initial conditions. Thus, for 2.7 < u < 3.4, the origin is no longer a stable fixed point, but new stable fixed points (S.F.P.s) on either side are generated. By analysing the stability of these new fixed points by linearizing the system in their vicinity (in the same way as in Figures 6.4 and 6.16), limit-cycle motions are seen to develop for u > 3.4, the onset of which is marked by the kink in the curves in Figure 6.29.

The phase-plane portraits presented in Figure 6.30 for only one initial condition $\dot{\phi_1} = 0.1$ and for different flow velocities (a) u = 3.5, (b) u = 3.525, (c) u = 3.54, (d) u = 3.57 and (e) u = 3.58 show the period-doubling of the motions leading to chaos.

As the motion of the system becomes period-two for u = 3.5155 (with period T = 2.04 compared to the previous period for u = 3.5 which was T = 1.02), period-

four for u = 3.5375 and period-eight for u = 3.542, the Feigenbaum number may be calculated and is found to be equal to 4.89, which is very close to the ideal Feigenbaum number.

The chaotic motion of the system for u = 3.57 and u = 3.58 may also be verified by constructing their corresponding Poincaré maps in Figures 6.32(a,b). For longer time steps, for $\tau > 500$, at u = 3.58 the motion of the system is transformed from chaotic into a limit cycle, so that for this flow velocity u = 3.58 we have a "transient" chaos.

In Figure 6.31, the motion of the system becomes again a symmetric limit cycle (period-one) for (a) u = 3.59, quasiperiodic for (b) u = 3.595 and (c) u = 3.6, which may be verified by constructing the Poincaré maps in Figure 6.32(d,e), which have the form of closed curves. The Poincaré map for u = 3.61 presented in Figure 6.32(f) is characteristic of chaotic motion.

In order to verify the quasiperiodic nature of the motion of the system for (b) u = 3.595 and (c) u = 3.6, the power spectra were calculated from which two fundamental frequencies were found: $f_1 = 0.431$ 483 and $f_2 = 2.445$ 070, all the other frequencies being linear combinations of f_1 and f_2 , as $f_n = mf_1 \pm nf_2$ with n > 3. For u = 3.595, $f_3 = 3f_1$, $f_4 = 10f_1$, $f_5 = 5f_1 + f_2$, $f_6 = -3f_1 + 3f_2$, $f_7 = 14f_1 + 2f_2$, $f_8 = 24f_1 + f_2$, $f_9 = 17f_1 + 3f_2$ and $f_{10} = 28f_1 + 3f_2$. For u = 3.6, $f_3 = -4f_1 + f_2$, $f_4 = -3f_1 + f_2$, $f_5 = -4f_1 + 2f_2$, $f_6 = -7f_1 + 3f_2$, $f_7 = 6f_1 + f_2$, $f_8 = -3f_1 + 3f_2$, $f_9 = 4f_1 + 2f_2$ and $f_{10} = -f_1 + 3f_2$.

6.4.2 Case 4 for the four-cylinder system, N = 4

The period-doubling route to chaos for the bifurcation diagram of Figure 6.33 is clarified via the phase-plane portraits of Figure 6.34. For u = 3.65, a Hopf bifurcation occurs, which corresponds to a symmetric limit cycle. For higher flow velocities, the motion of the system looks as if it is developing around two fixed

points: $(\phi_1 = -0.045; \dot{\phi_1} = 0)$ and $(\phi_1 = 0.03; \dot{\phi_1} = 0)$; as seen in the phase-plane plots and in the Poincaré maps presented in Figures 6.34 and 6.35, respectively, the system executes (a) period-one motion for u = 3.961, for which the period T = 1.02; (b) period-two motion for u = 3.963, its period being T = 2.04; (c) period-three motion for u = 3.97, in which the period is three times higher than in the previous motion; (d) slightly chaotic motion for u = 3.9953.

The slightly chaotic character of the motion for u = 3.9953 has been verified through the time traces, power spectra and the Poincaré maps in Figure 6.36(a,b,c). As seen in Sections 6.4.1 and 6.4.2, the system in this case displays a completely different behaviour for N = 3 and for N = 4.

6.5 CASE 5:
$$h = 0.5$$
, $f = 0.4$, $\kappa_c = 5 \times 10^5$ and for $N = 3$

This system is similar to Case 1, but with an intermediately blunt free end-which is the same as for Case 4, but in this case the annulus is wider.

In this case, as the flow velocity u is increased, both the real and imaginary components of the second-mode eigenvalue approach zero, leading to a pitchfork bifurcation (divergence) at u=4.15. The system remains unstable for u>4.15. Furthermore, a Hopf bifurcation occurs at u=4.7, in the third mode. The first mode remains stable throughout this range of u.

Figure 6.37 shows the bifurcation diagram with the cubic-spring representation $(\kappa_c = 10^5)$ for the range of u beyond the pitchfork bifurcation. Figure 6.37(b) covers the range of u where chaos apparently arises in Figure 6.37(a), i.e., 4.91 < u < 4.925. The two stable branches after the pitchfork bifurcation were determined via opposite-sign initial conditions (Figure 6.37(a)). Thus, for 4.15 < u < 4.90941, the origin is no longer a stable fixed point, but new stable fixed points (S.F.P.s) on

either side are generated. The stability of these new fixed points was investigated by linearizing the system in their vicinity. As u is increased (from $u_{\rm pf}=4.15$ to u=4.90942) the eigenvalues become purely imaginary, signifying the onset of another Hopf bifurcation and the development of limit-cycle motions (L.C.) for higher u. This was further clarified by phase-plane plots (not shown). For u=4.90941, the fixed point is still stable and the trajectories approach that point with time, while the first chaotic motion through intermittency develops for $u\simeq 4.90942$. As the interval in u between fixed point and chaotic behaviour of the system is too small (it is equal to 0.00001), then the exact value of the critical flow velocity $u_{\rm cr}$ at which a stable limit cycle occurs could not be pin-pointed; furthermore, because of the small interval in u, $u_{\rm cr}$ is assumed to be equal to $u_{\rm cr}=4.90942$.

The chaotic motion of the system through intermittency is further verified by the phase-plane plots and time traces shown in Figures 6.38 and 6.39 for the same flow velocity u=4.91 but for different ranges of time τ , as follows: In Figure 6.38(a,c), for $0<\tau<4$, after the initial transient has died out, for $0<\tau<2$, an unstable limit cycle develops; the instability is weak and, although trajectories are attracted to the vicinity of the limit cycle, the limit cycle amplitude increases gradually but continuously with time τ , for $2<\tau<4$. At a higher time interval, $152<\tau<162$ (Figure 6.38(b,d)), one of the bursts of "turbulence" is captured, which are characteristic of this type of chaos; the associated phase-plane diagram (Figure 6.38(b)) reinforces the view that, in that time period, the oscillation is chaotic.

Similar behaviour is seen in Figure 6.39(a,c), showing a quiescent, nearly steady oscillation for 700 $< \tau <$ 705, and in Figure 6.39(b,d), showing chaotic oscillations at higher τ with several unsteady bursts.

In Figures 6.40 and 6.41 bifurcation diagrams are presented for this system, showing the maximum displacement of the first cylinder of the articulated system,

 ϕ_{1max} or I_k (in the intermittency notation), as a function of the nondimensional time τ ; for $0 < \tau < 5,000$ in Figures 6.40(a,b), and for a larger range of τ , $5,000 < \tau < 10,000$ in Figure 6.41(a,b), as follows:

- in Figure 6.40(a) for $0 < \tau < 2,500$;
- in Figure 6.40(b) for $2,500 < \tau < 5,000$;
- in Figure 6.41(a) for $5,000 < \tau < 7,500$;
- in Figure 6.41 (b) for $7,500 < \tau < 10,000$.

In these figures one may see the turbulent fluctuations represented through vertically clustered points in the diagrams, which are interrupted by laminar fluctuations, or laminar phases.

It has already been discussed, in Figure 6.39, that the laminar phases are in fact associated with "growing" limit cycles, and these limit cycles are presented in the four bifurcation diagrams (Figures 6.40 and 6.41) through one single point.

Another signature of the intermittency is the statistical distribution of the lengths $P(\tau)$ of the laminar phases versus τ and it is is presented in Figure 6.42. The distribution in this case has a maximum for short times ($\tau=20$) and decreases exponentially at large times, which is characteristic for type III intermittency. The most significant feature for this figure is the long tail for τ large; in Figure 6.42 the long τ interval is $190 < \tau < 300$ in which only one laminar phase exists.

Furthermore, one may observe a very large number of laminar phases in Figures 6.40 and 6.41, and the number of laminar phases $N(\tau > \tau_0)$ lasting longer than τ_0 are counted versus τ_0 , and an exponential function is obtained in Figure 6.43; it is a function of τ_0 and μ . It is difficult to find out the exact value of u_{cr} at which a Hopf bifurcation occurs; we know already from the previous page that u_{cr} is between 4.90941 and 4.90942; as this interval is very small, u_{cr} will be taken as $u_{cr} = 4.90942$. It is concluded that, even if a formula is considered for $N(\tau > \tau_0)$, in this case it is

not the classical one, as u_{cr} is not the real flutter velocity. The critical flow velocity at which a divergence instability occurs might also be considered as $u_{cr} = 4.15$. Once more, this u_{cr} is again not the classical one used in intermittency calculation (Bergé et al. 1984), in which u_{cr} has always been considered as u at which a Hopf bifurcation occurs.

All calculations for Figures 6.42 and 6.43 are done for a total nondimensional time $\tau=10,000$ (as shown in Figures 6.40 and 6.41). As in the bifurcation diagrams of Figures 6.40 and 6.41, it is very difficult to see the beginning and the end of a laminar phase. One may see the behaviour of the system, and especially its laminar phase, in a smaller range of τ , as for example, for $960 < \tau < 1080$, in which two laminar phases are shown in Figure 6.44(a). In Figure 6.44(a) for $960 < \tau < 970$ turbulent fluctuations appear (many points) which are followed by period-two motions for $970 < \tau < 974$ (two points), then by a growing limit cycle motion (one point) for $974 < \tau < 1058$, a very small intermittent region followed for $\tau > 1060$ by the second laminar phase (presented again through two and one points).

Then the same bifurcation diagram, but for a smaller range of τ , is presented in Figure 6.44(b) in order to see clearly only the first laminar phase behaviour for $966 < \tau < 978$, so we already know that a period-two motion precedes a chaotic motion, in case of intermittency type III. In our example, chaotic motion is followed by period-two motion, and again by period-one motion (or laminar phases).

Furthermore, I_k , I_{k+1} , I_{k+2} are defined in Figure 6.45 as corresponding to the kth, (k+1)th and (k+2)th maximum displacement of the first cylinder in time τ . These quantities are used in graphing the first and the second return maps presented further in Figures 6.46 and 6.47.

Figure 6.46 shows the first return map I_{k+1} versus I_k , in which I_{k+1} is the new maximum displacement of the first cylinder and I_k is its previous maximum displacement. In this figure, a curve tangent to an inverse diagonal is obtained, its

slope being equal to -1. The second return map I_{k+2} versus I_k is shown in Figure 6.47 and it is seen that this curve is a graph of a function

$$I_{k+2} = (1+2\mu)I_k + \alpha I_k^2 + bI_k^3, \tag{6.1}$$

with a and b constants and a << b. As μ is very small, and is equal to 0.00058, then a and b are further calculated; they are found to be $a \simeq -12$, $b \simeq 451$.

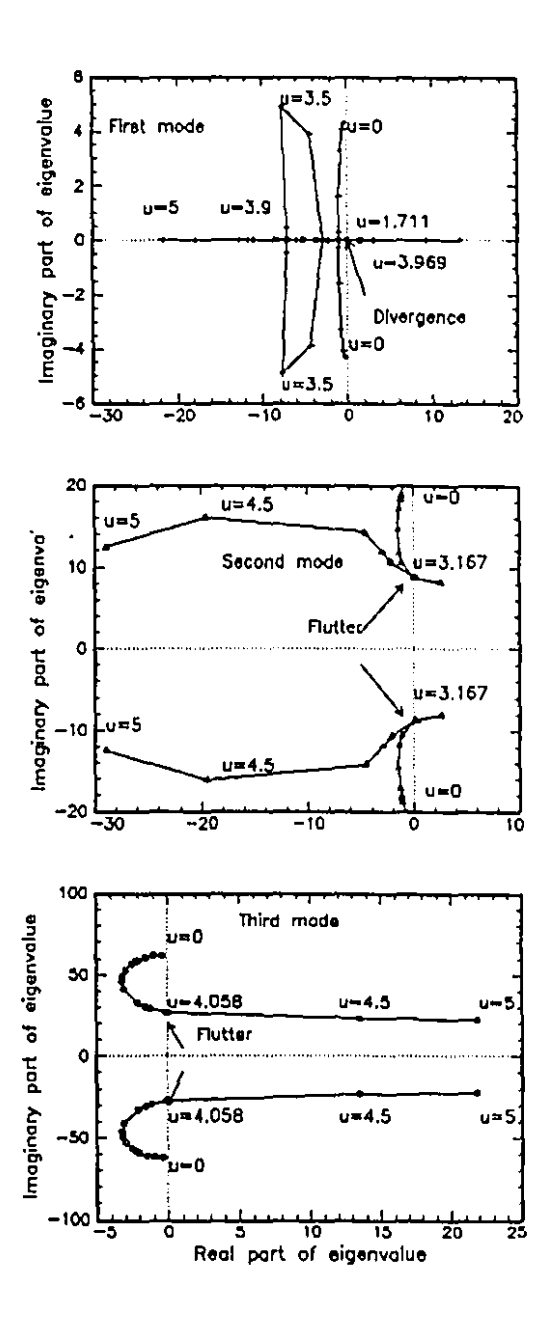


Figure 6.1. Argand diagrams for (a) the first mode, (b) the second mode and (c) the third mode of the system of Case 1: h = 0.5, c = 0.38, f = 0.8 and $\kappa_c = 5 \times 10^3$. The imaginary part of the eigenvalue, $\text{Im}(\lambda)$, is plotted versus the real part, $\text{Re}(\lambda)$, with the nondimensional flow velocity, u, as parameter.

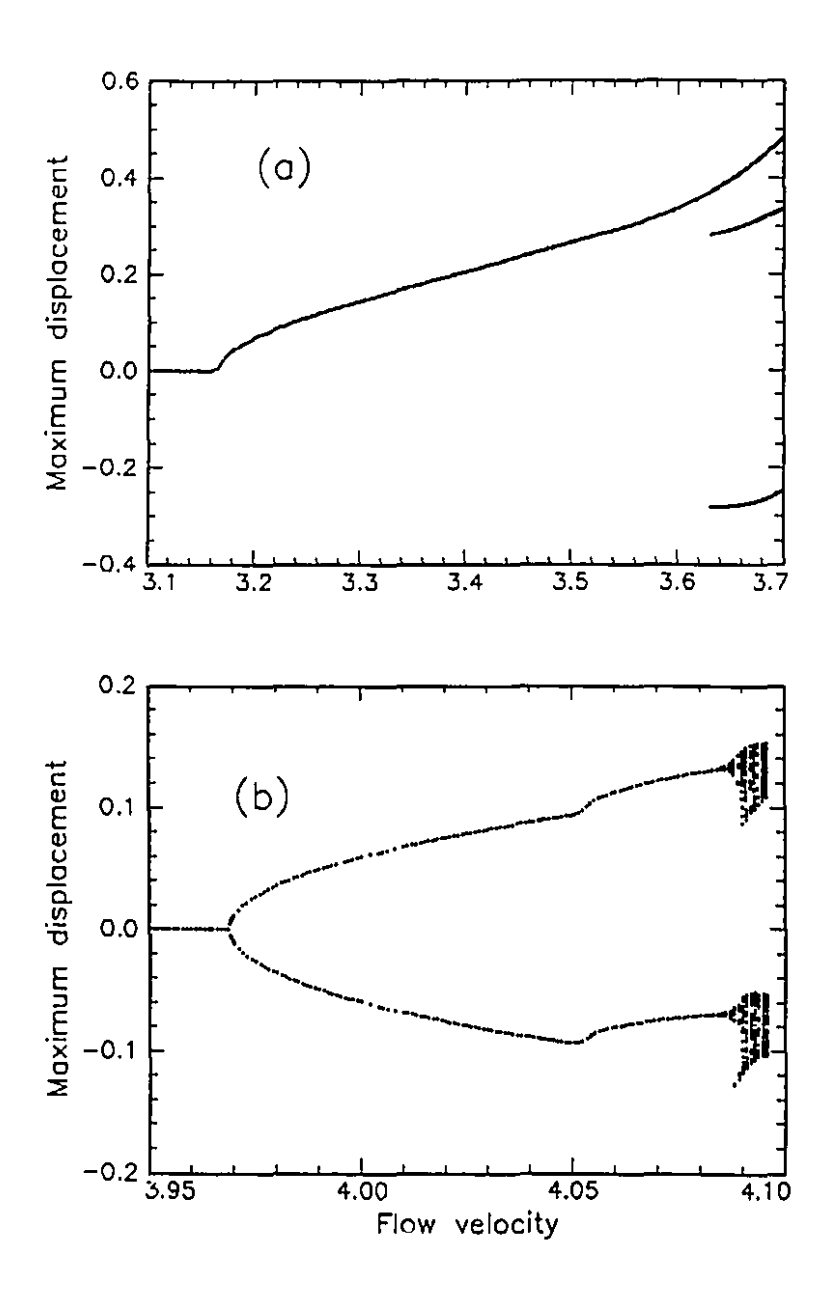


Figure 6.2. Bifurcation diagram for the system of Case 1: h=0.5, c=0.38, f=0.8, with the cubic-spring model ($\kappa_c=5\times 10^3$) for impacting with the channel; the maximum displacement $\phi_1(\tau)$ versus the dimensionless flow velocity, u, for (a) 3.35 < u < 3.70 and (b) 3.95 < u < 4.10.

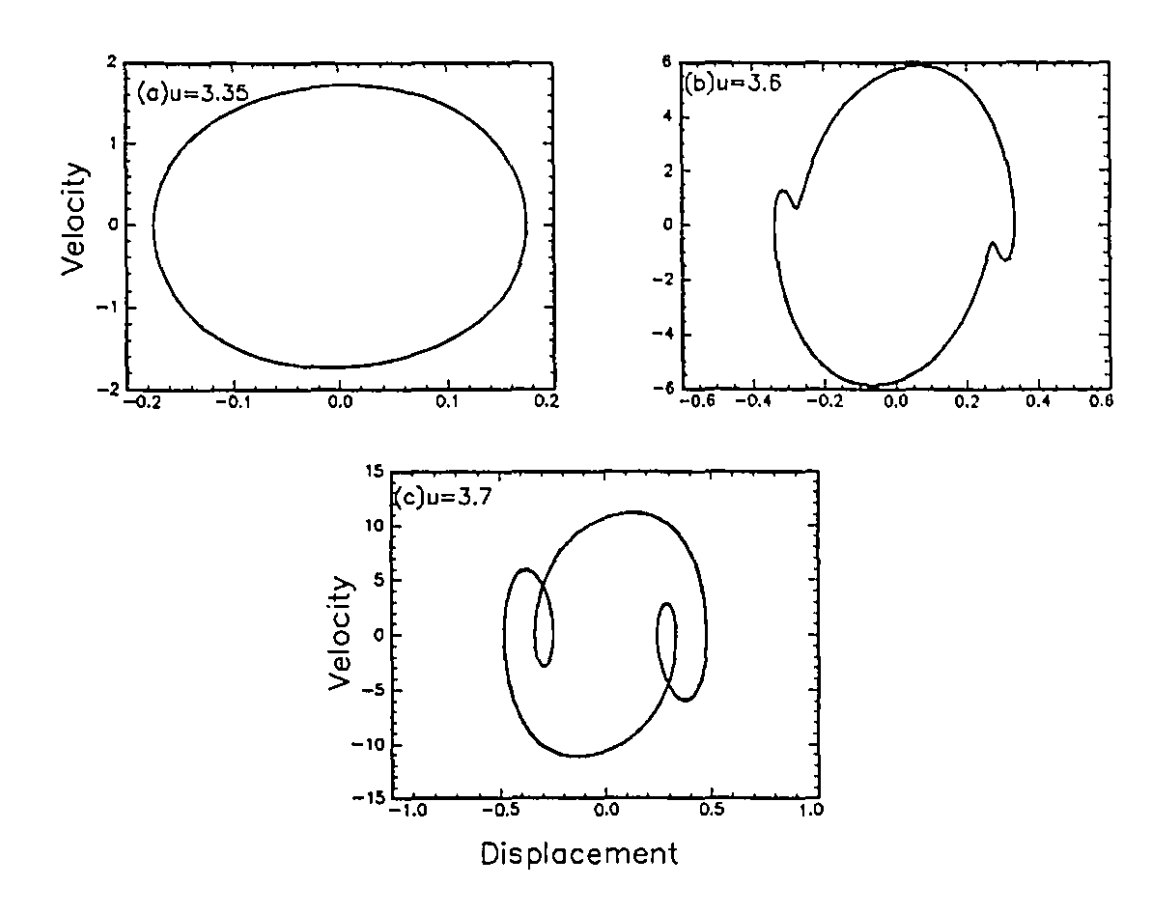


Figure 6.3. Phase-plane plots of $\dot{\phi}_1(\tau)$ versus $\phi_1(\tau)$ at (a) u=3.35, (b) u=3.60 and (c) u=3.70 for the system of Case 1: h=0.5, c=0.38, f=0.8 and $\kappa_c=5\times 10^3$.

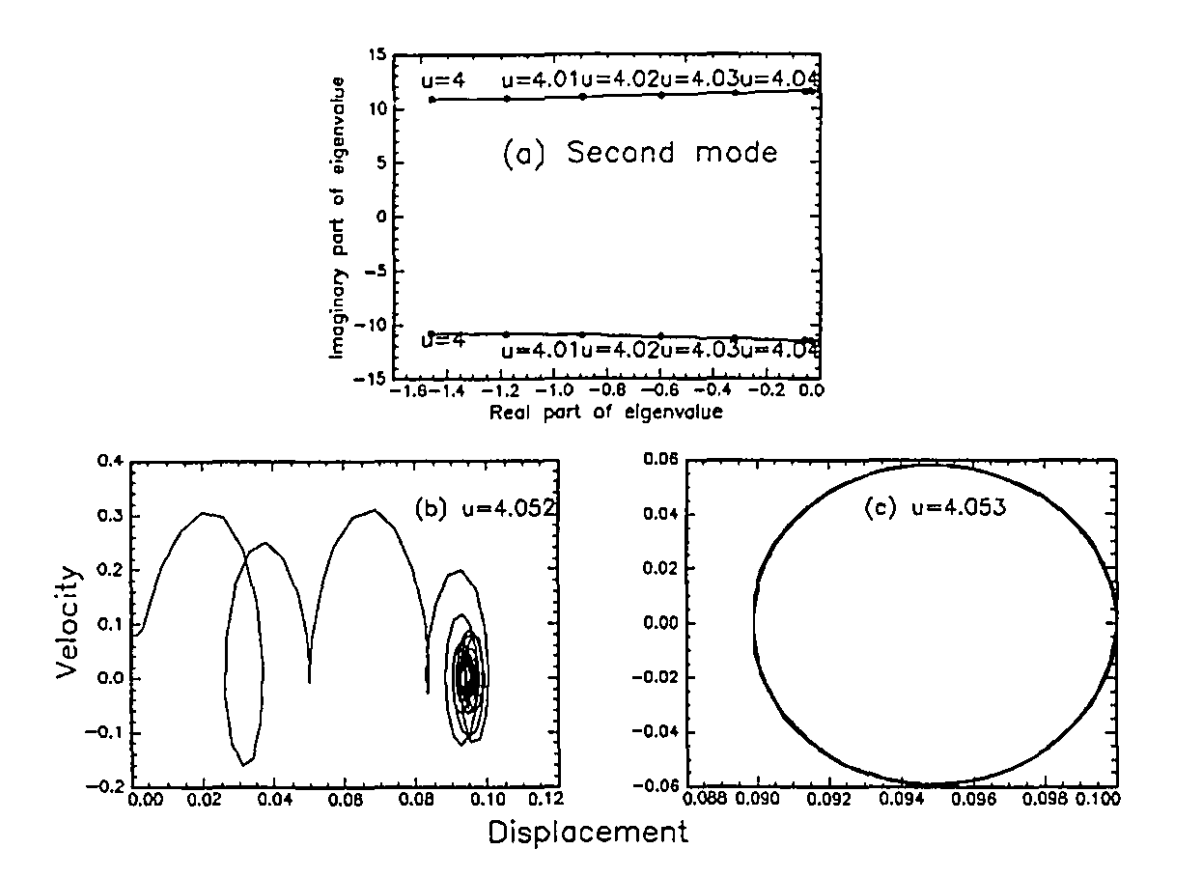


Figure 6.4. (a) Argand diagram for the second mode of the linearized system around the stable fixed points (S.F.P.) of Figure 6.2 (Case 1: h = 0.5, c = 0.38, f = 0.8, $\kappa_c = 5 \times 10^3$). (b,c) Phase-plane plots of $\dot{\phi}_1(\tau)$ versus $\phi_1(\tau)$ for the system of Figure 6.2 for (b) u = 4.052 and (c) u = 4.053; the trajectory in (b) ends at a stable fixed point, while (c) leads to a limit cycle.

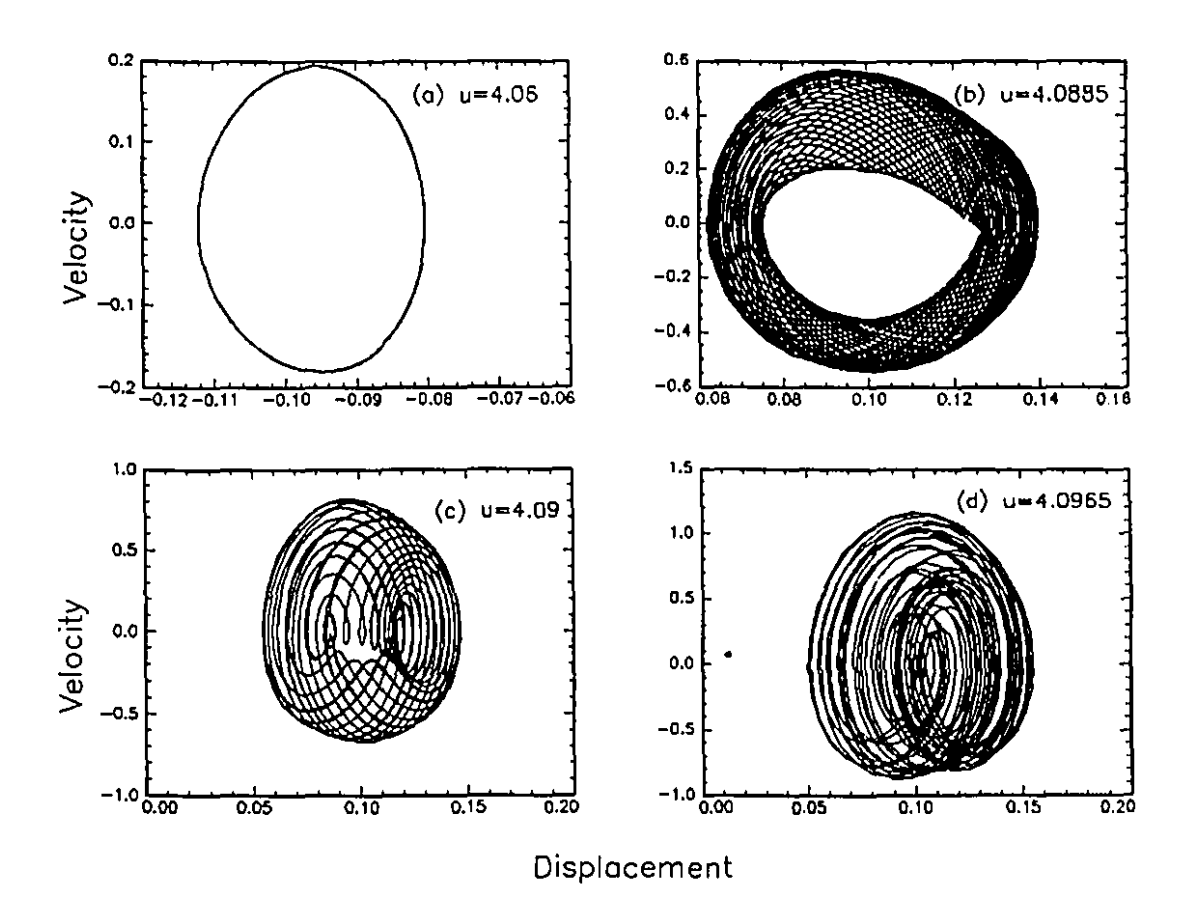


Figure 6.5. Phase-plane plots of $\dot{\phi}_1(\tau)$ versus $\phi_1(\tau)$ at (a) u=4.06, (b) u=4.0885, (c) u=4.0900 and (d) u=4.0965 for the system of Case 1: h=0.5, c=0.38, f=0.8 and $\kappa_c=5\times 10^3$.

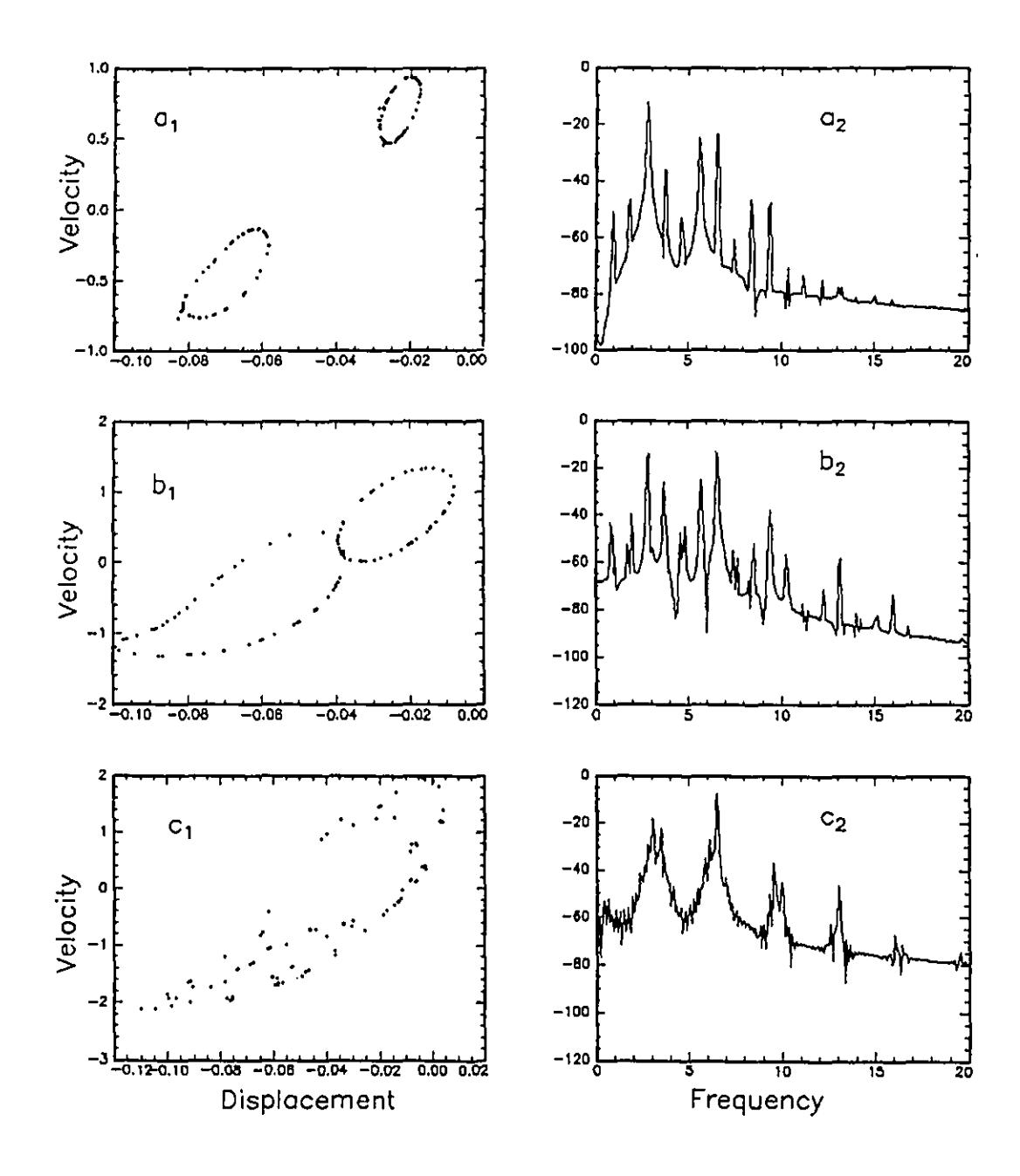


Figure 6.6. Poincaré maps (first column) and power spectra (second column) for the system of Case 1: h = 0.5, c = 0.38, f = 0.8 and $\kappa_c = 5 \times 10^3$, for (a) u = 4.0885, (b) u = 4.0900 and (c) u = 4.0965.

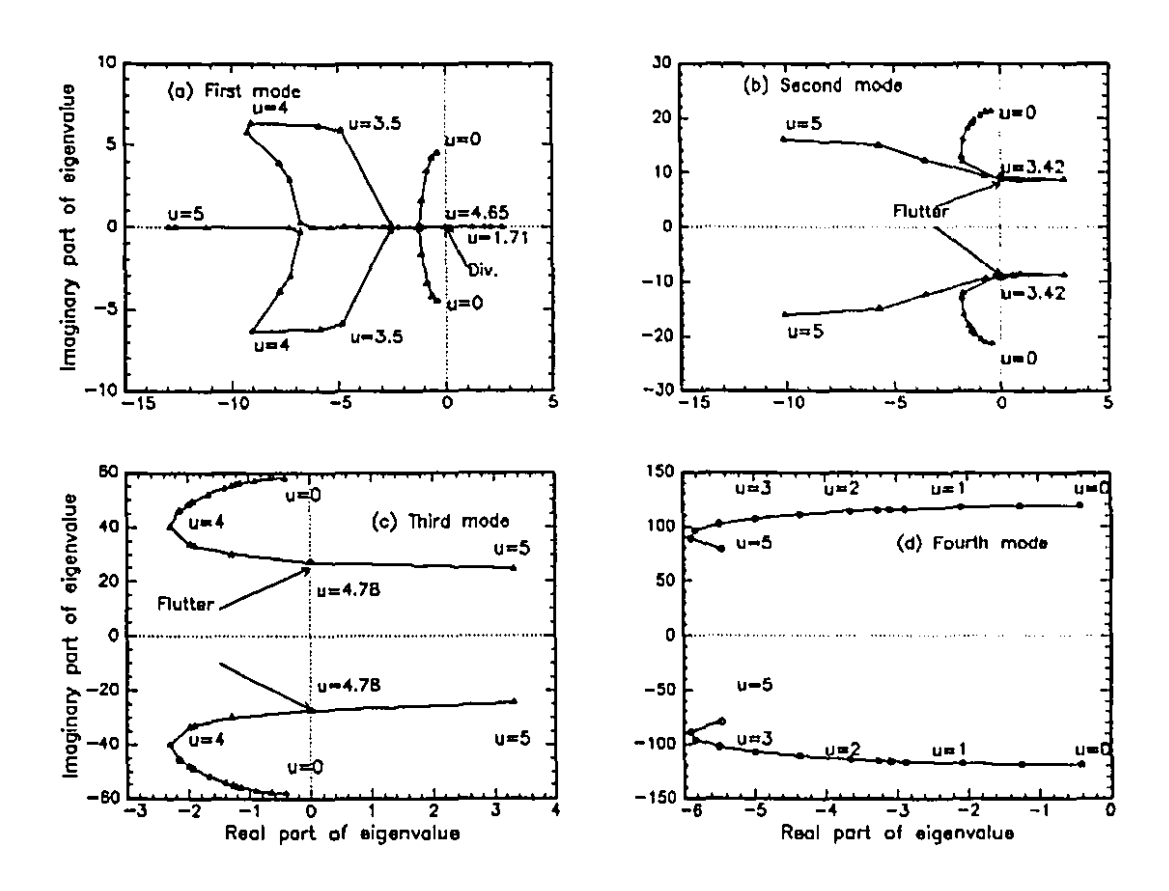


Figure 6.7. Argand diagrams for (a) the first mode, (b) the second mode, (c) the third mode and (d) the fourth mode of the system of Case 1: h = 0.5, c = 0.38, f = 0.8 and $\kappa_c = 5 \times 10^3$. The imaginary part of the eigenvalue, $\text{Im}(\lambda)$, is plotted versus the real part, $\text{Re}(\lambda)$, with the nondimensional flow velocity, u, as parameter.

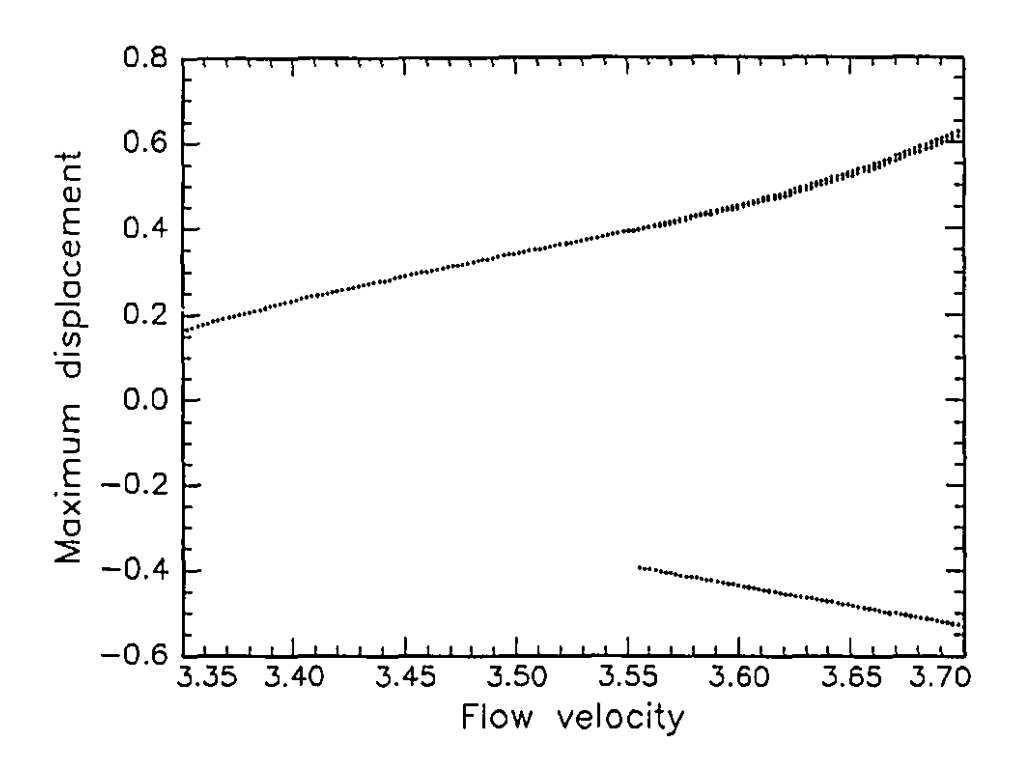


Figure 6.8. Bifurcation diagram for the system of Case 1: h = 0.5, c = 0.38, f = 0.8, with the cubic-spring model ($\kappa_c = 5 \times 10^3$) for impacting with the channel; the maximum displacement $\phi_1(\tau)$ versus the dimensionless flow velocity, u.

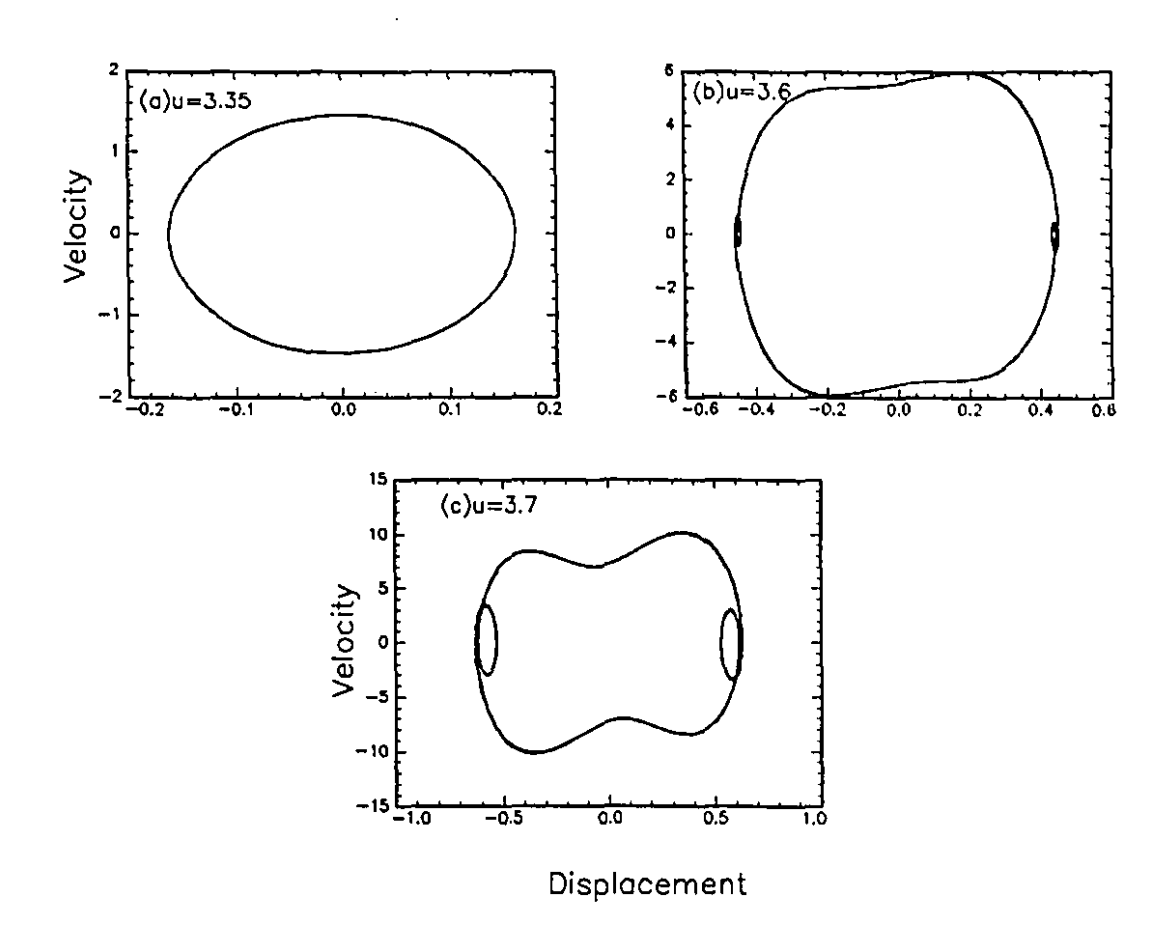


Figure 6.9. Phase-plane plots of $\dot{\phi}_1(\tau)$ versus $\phi_1(\tau)$ at (a) u=3.35, (b) u=3.60 and (c) u=3.70 for the system of Case 1: h=0.5, c=0.38, f=0.8, and $\kappa_c=5\times 10^3$.

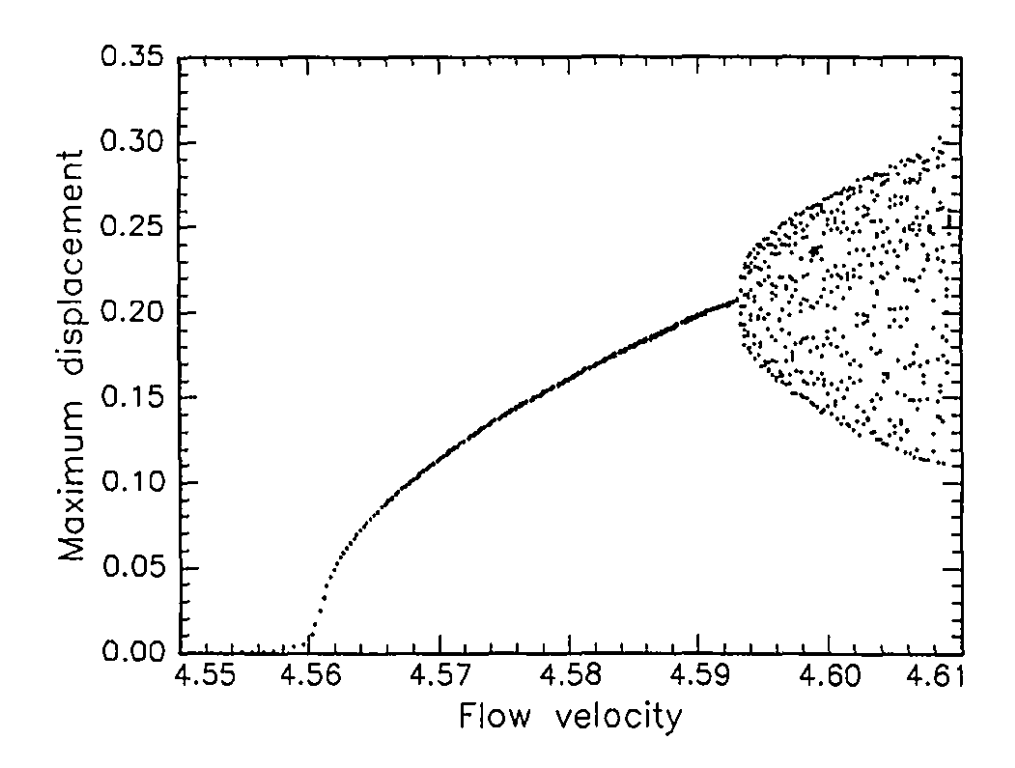


Figure 6.10. Bifurcation diagram for the system of Case 1: h=0.5, c=0.38, f=0.8, N=4 with the cubic-spring model ($\kappa_c=5\times 10^3$) for impacting with the channel; the maximum displacement $\phi_1(\tau)$ versus the dimensionless flow velocity, u.

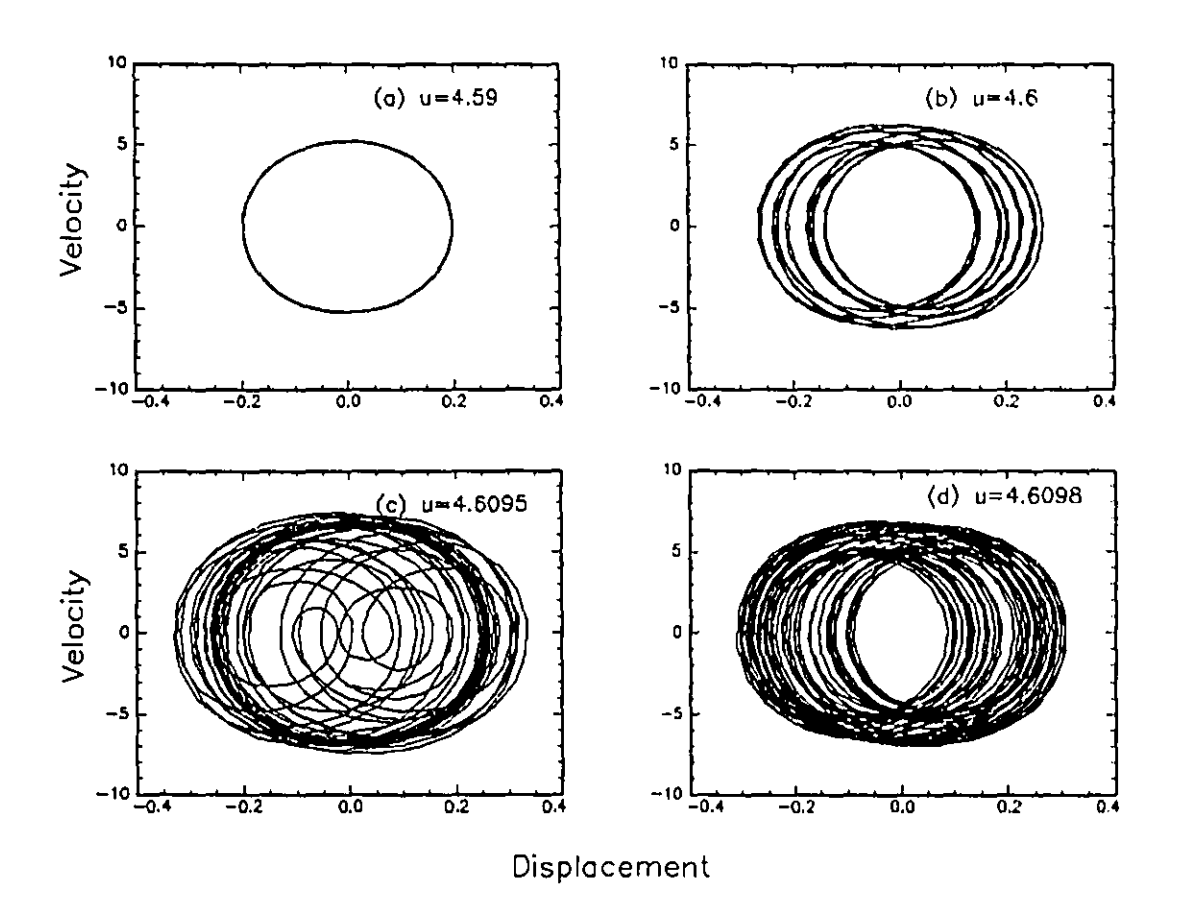


Figure 6.11. Phase-plane plots of $\dot{\phi}_1(\tau)$ versus $\phi_1(\tau)$ for the system of Case 1: h=0.5, c=0.38, f=0.8, N=4, with the cubic-spring model ($\kappa_c=5\times 10^3$) for impacting with the channel.

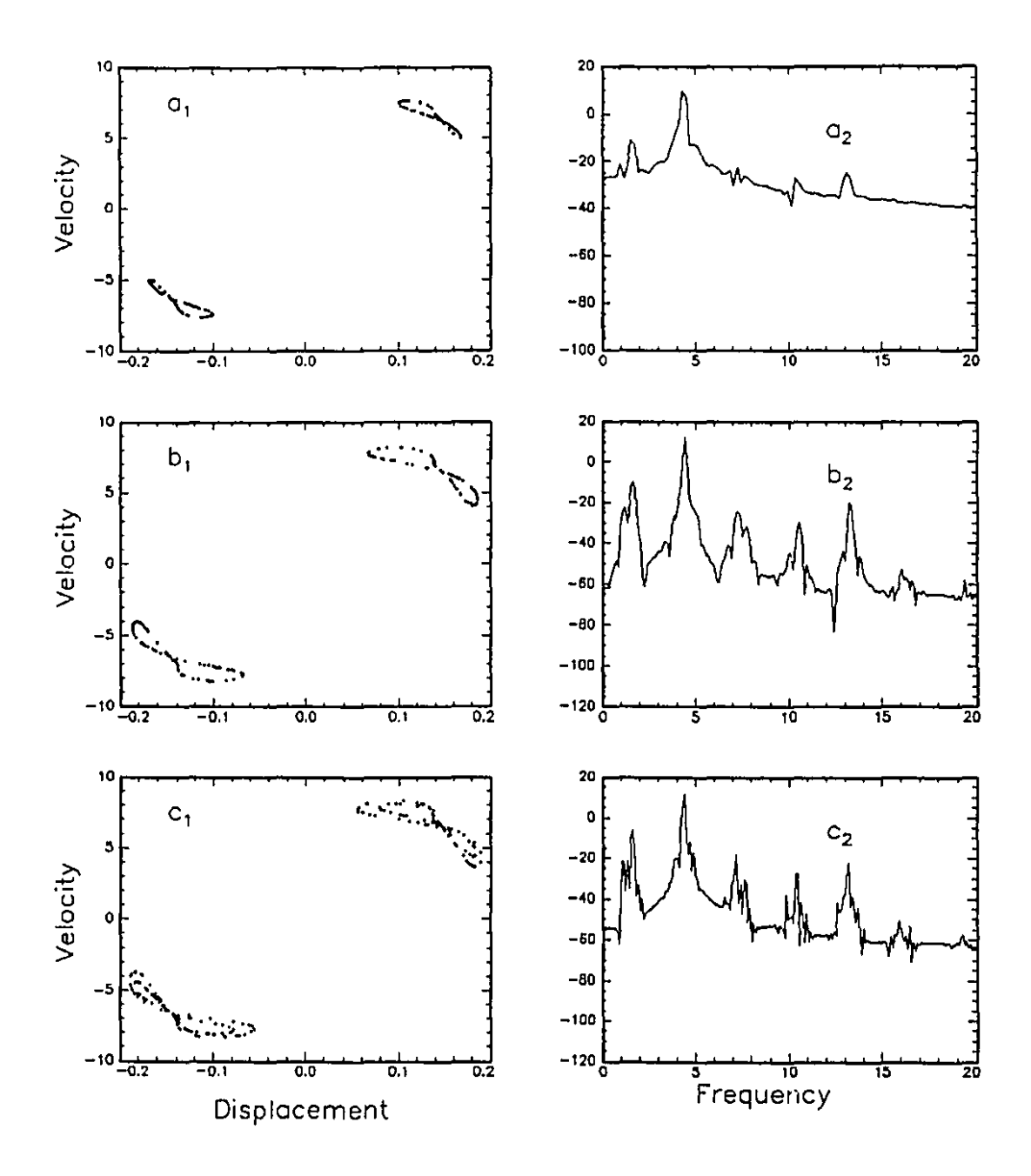


Figure 6.12. Poincaré maps (first column) and power spectra (second column) for the system of Case 1: h=0.5, c=0.38, f=0.8, N=4 and $\kappa_c=5\times 10^3$, for (a) u=4.60, (b) u=4.6095 and (c) u=4.6098.

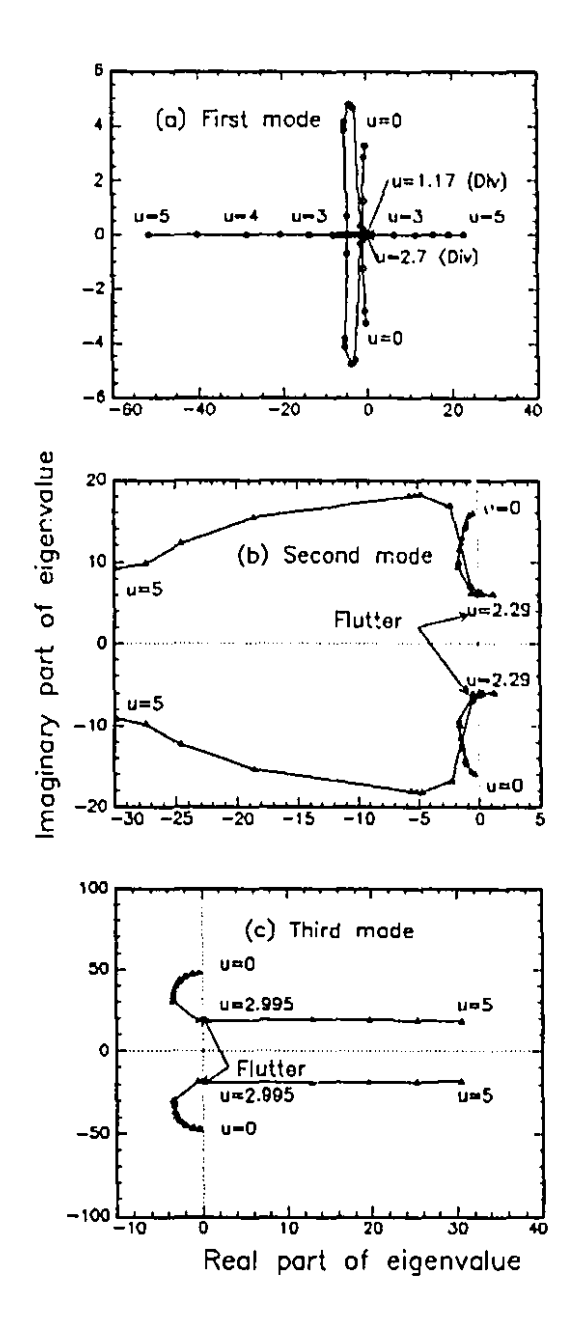


Figure 6.13. Argand diagrams for (a) the first mode, (b) the second mode and (c) the third mode of the system of Case 2: h = 0.2, c = 0.79, f = 0.8 and $\kappa_c = 5 \times 10^3$. The imaginary part of the eigenvalue, $\text{Im}(\lambda)$, is plotted versus the real part, $\text{Re}(\lambda)$, with the nondimensional flow velocity, u, as parameter.

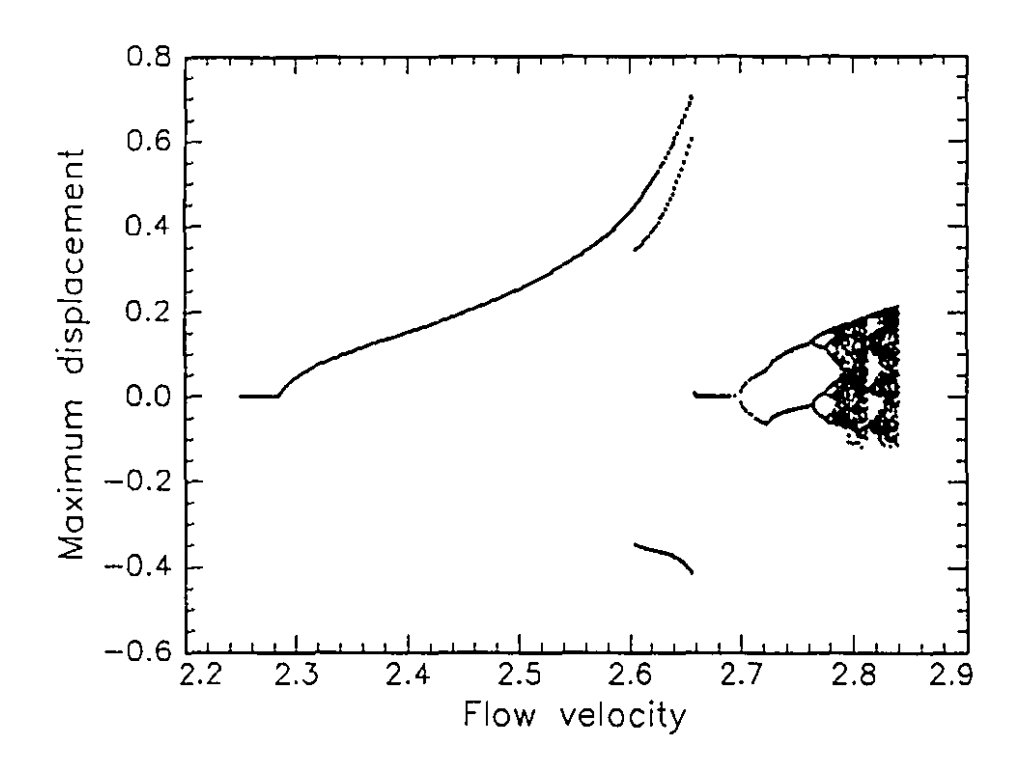


Figure 6.14. Bifurcation diagram for the system of Case 2: h=0.2, c=0.79, f=0.8, with the cubic-spring model ($\kappa_c=5\times 10^3$) for impacting with the channel; the maximum displacement $\phi_1(\tau)$ versus the dimensionless flow velocity, u.

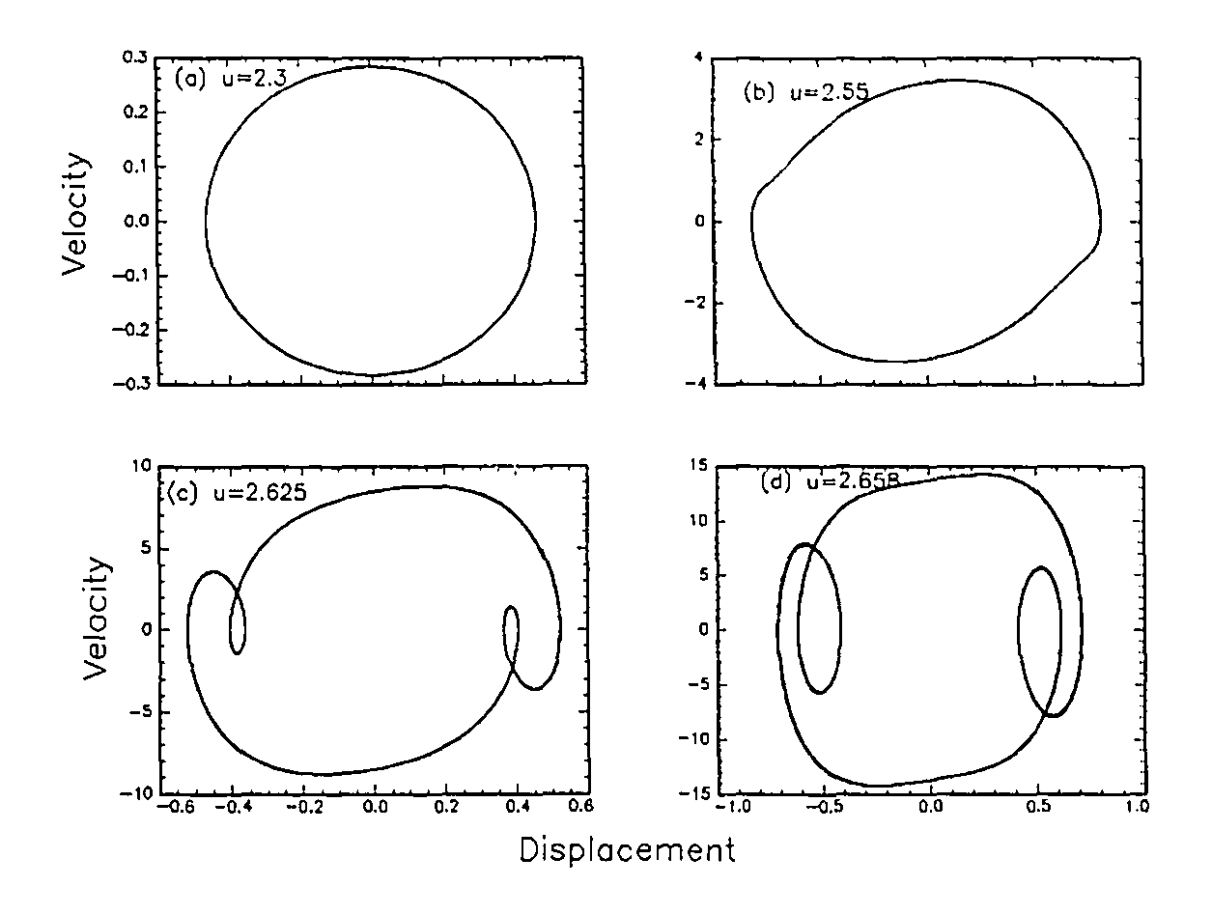


Figure 6.15. Phase-plane plots of $\dot{\phi}_1(\tau)$ versus $\phi_1(\tau)$ at (a) u=2.3, (b) u=2.55, (c) u=2.625 and (d) u=2.658 for the system of Case 2: h=0.2, c=0.79, f=0.8 and $\kappa_c=5\times10^3$.

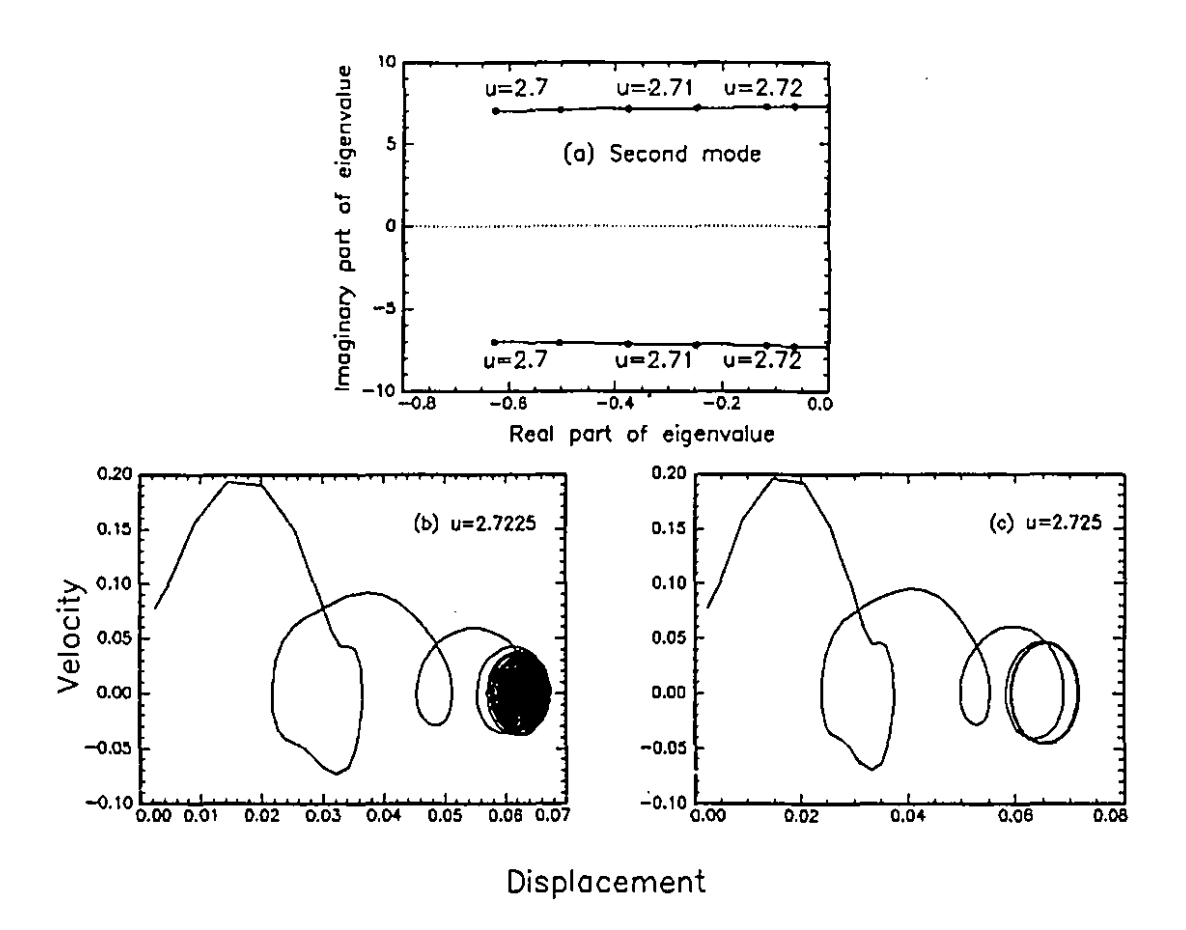


Figure 6.16. (a) Argand diagram for the second mode of the linearized system around the stable fixed points (S.F.P.) of Figure 6.13 (Case 2: h = 0.2, c = 0.79, f = 0.8, $\kappa_c = 5 \times 10^3$). (b,c) Phase-plane plots of $\dot{\phi}_1(\tau)$ versus $\phi_1(\tau)$ for the system of Figure 6.9 for (b) u = 2.7225 and (c) u = 2.725; the trajectory in (b) ends at a stable fixed point, while (c) leads to a limit cycle.

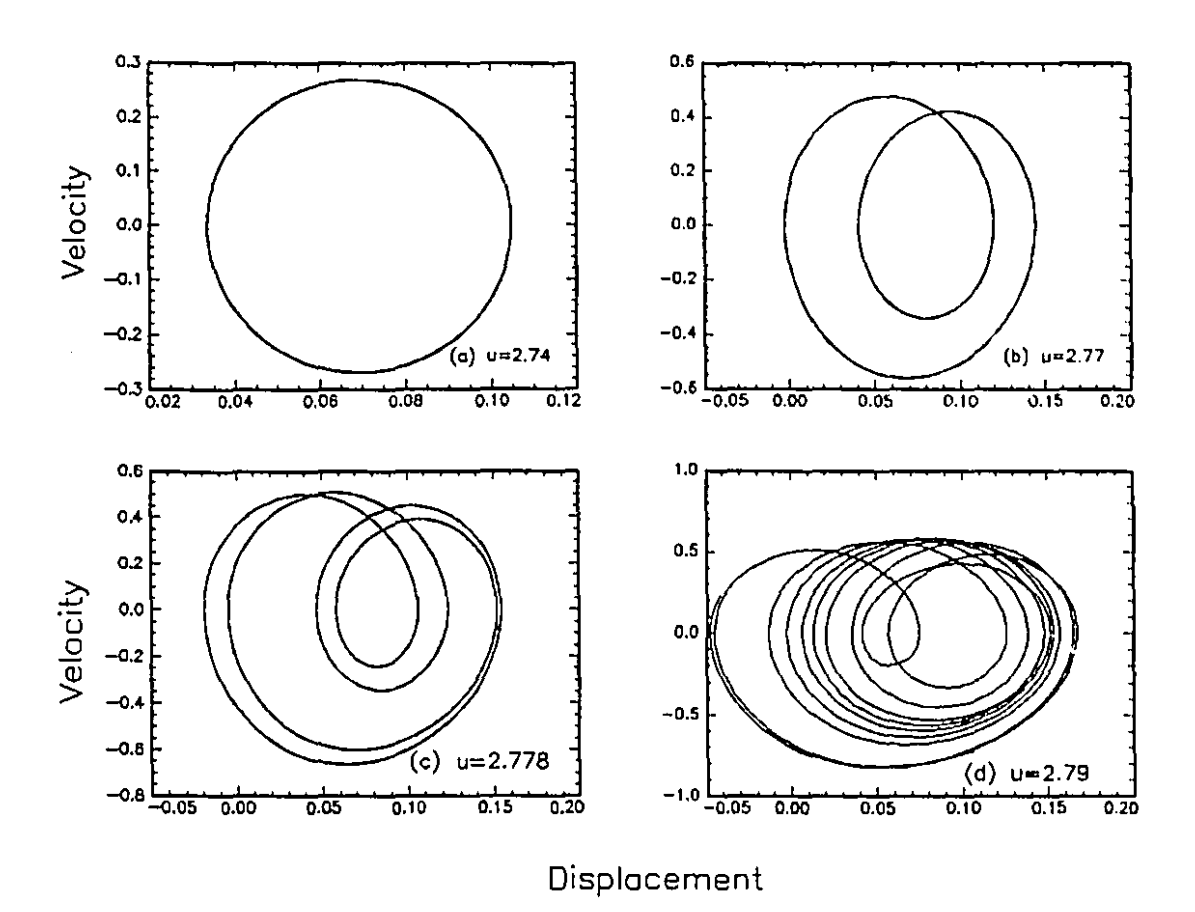


Figure 6.17. Phase-plane plots of $\dot{\phi}_1(\tau)$ versus $\phi_1(\tau)$ at (a) u=2.74, (b) u=2.77, (c) u=2.778 and (d) u=2.835 for the system of Case 2: h=0.2, c=0.79, f=0.8 and $\kappa_c=5\times 10^3$.

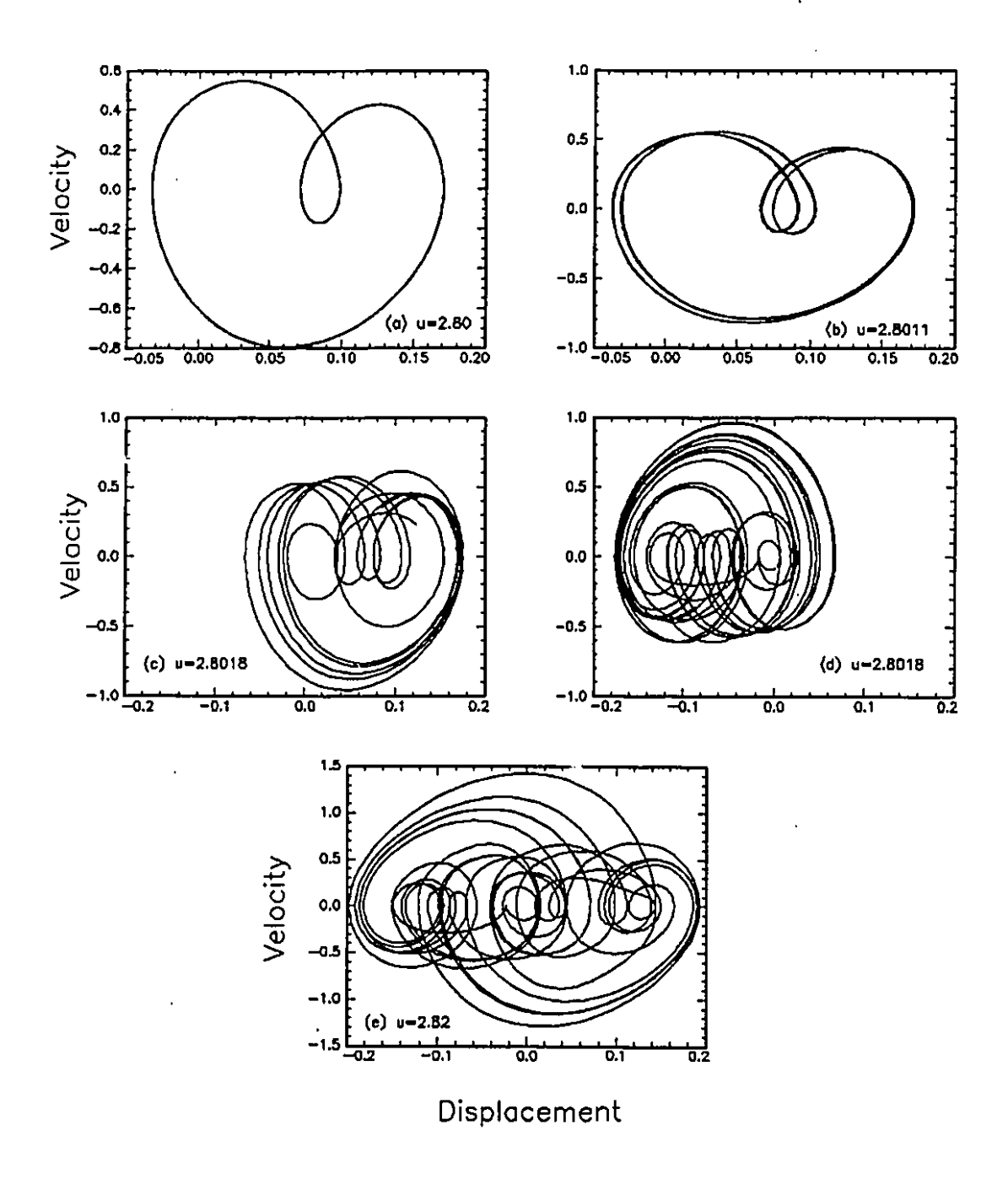


Figure 6.18. Phase-plane plots of $\dot{\phi}_1(\tau)$ versus $\phi_1(\tau)$ at (a) u=2.80, (b) u=2.8011, (c,d) u=2.8018 (c) for positive initial condition, (d) for negative initial condition, and (e) u=2.82 for the system of Case 2: h=0.2, c=0.79, f=0.8 and $\kappa_c=5\times10^3$.

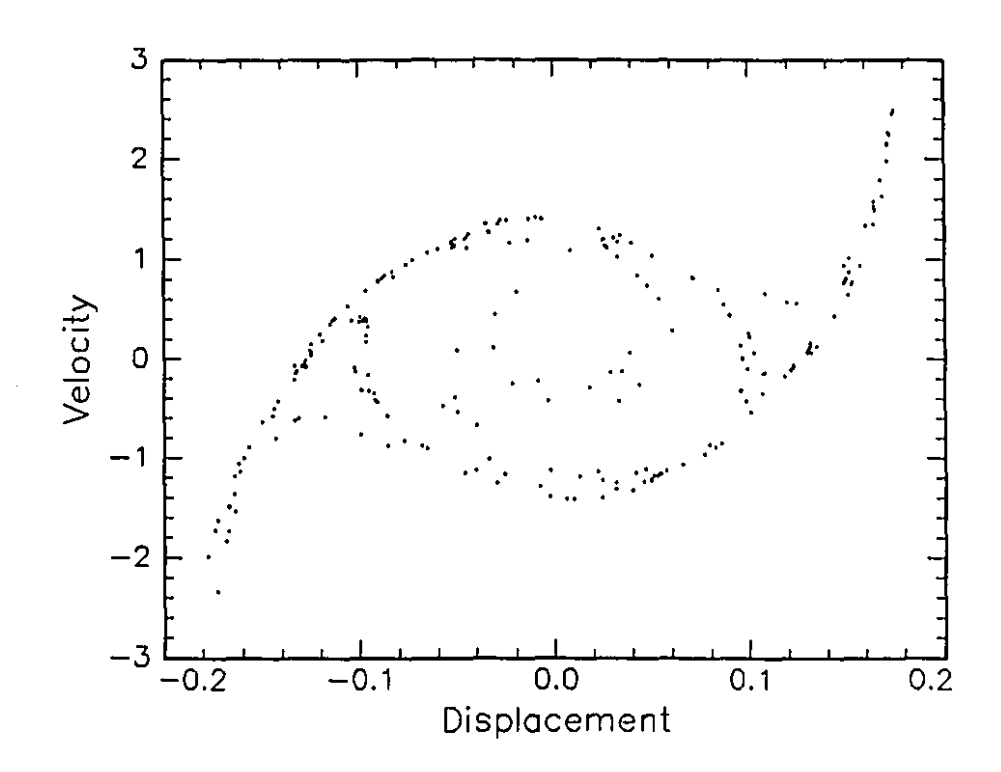


Figure 6.19. Poincaré map of $\dot{\phi}_2(\tau)$ versus $\phi_2(\tau)$ when $\phi_1(\tau) = 0$ for Case 2: h = 0.2, c = 0.79, f = 0.8, $\kappa_c = 5 \times 10^3$, for u = 2.835.

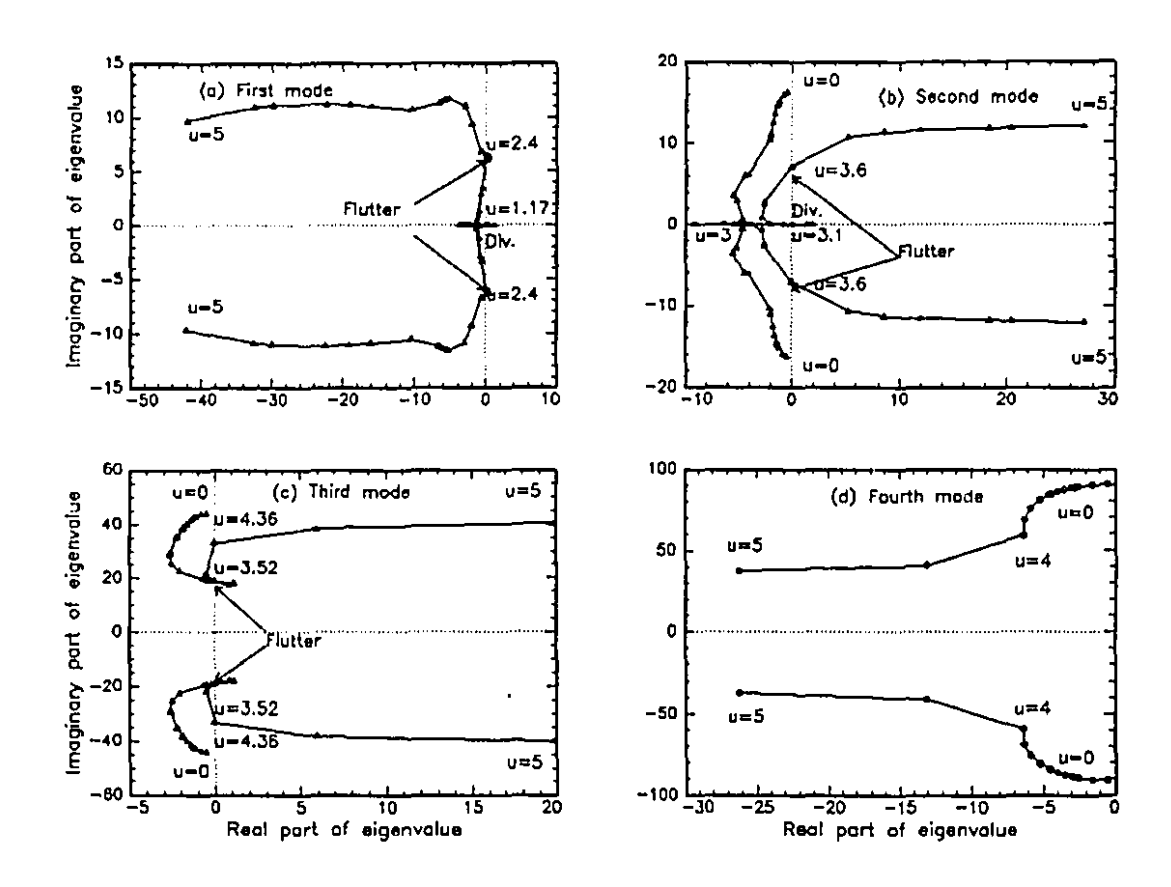


Figure 6.20. Argand diagrams for (a) the first mode, (b) the second mode, (c) the third mode and (d) the fourth mode of the system of Case 2: h = 0.2, c = 0.79, f = 0.8 and $\kappa_c = 5 \times 10^3$. The imaginary part of the eigenvalue, $\text{Im}(\lambda)$, is plotted versus the real part, $\text{Re}(\lambda)$, with the nondimensional flow velocity, u, as parameter.

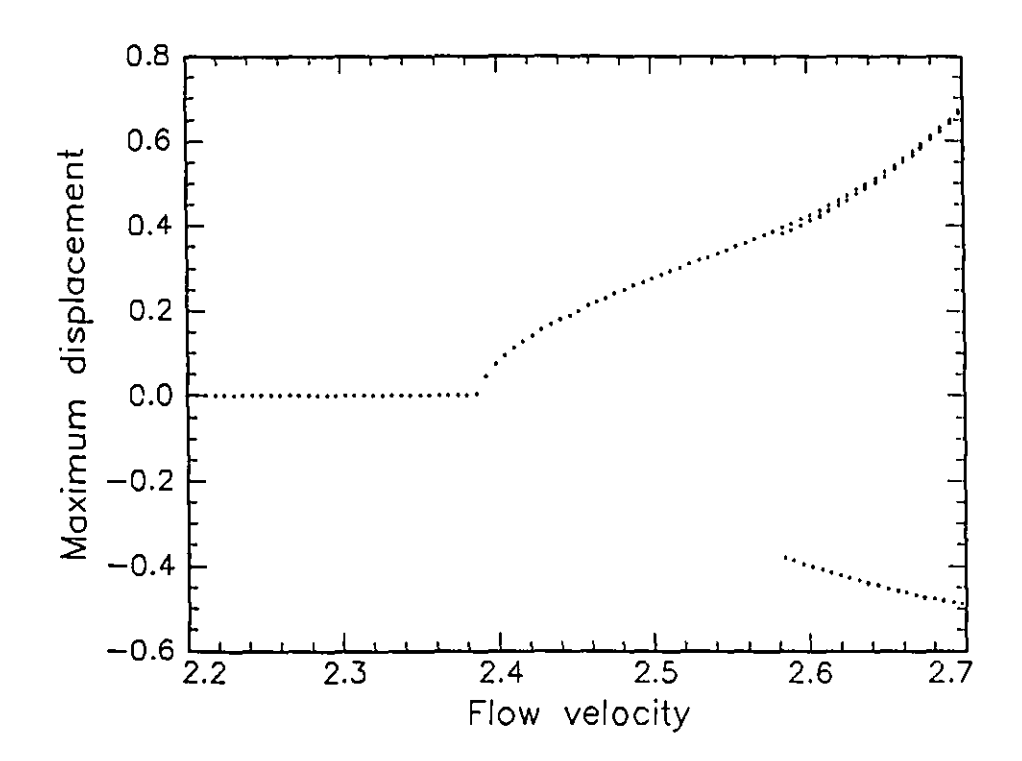


Figure 6.21. Bifurcation diagram for the system of Case 2: h=0.2, c=0.79, f=0.8, with the cubic-spring model ($\kappa_c=5\times 10^3$) for impacting with the channel; the maximum displacement $\phi_1(\tau)$ versus the dimensionless flow velocity, u.

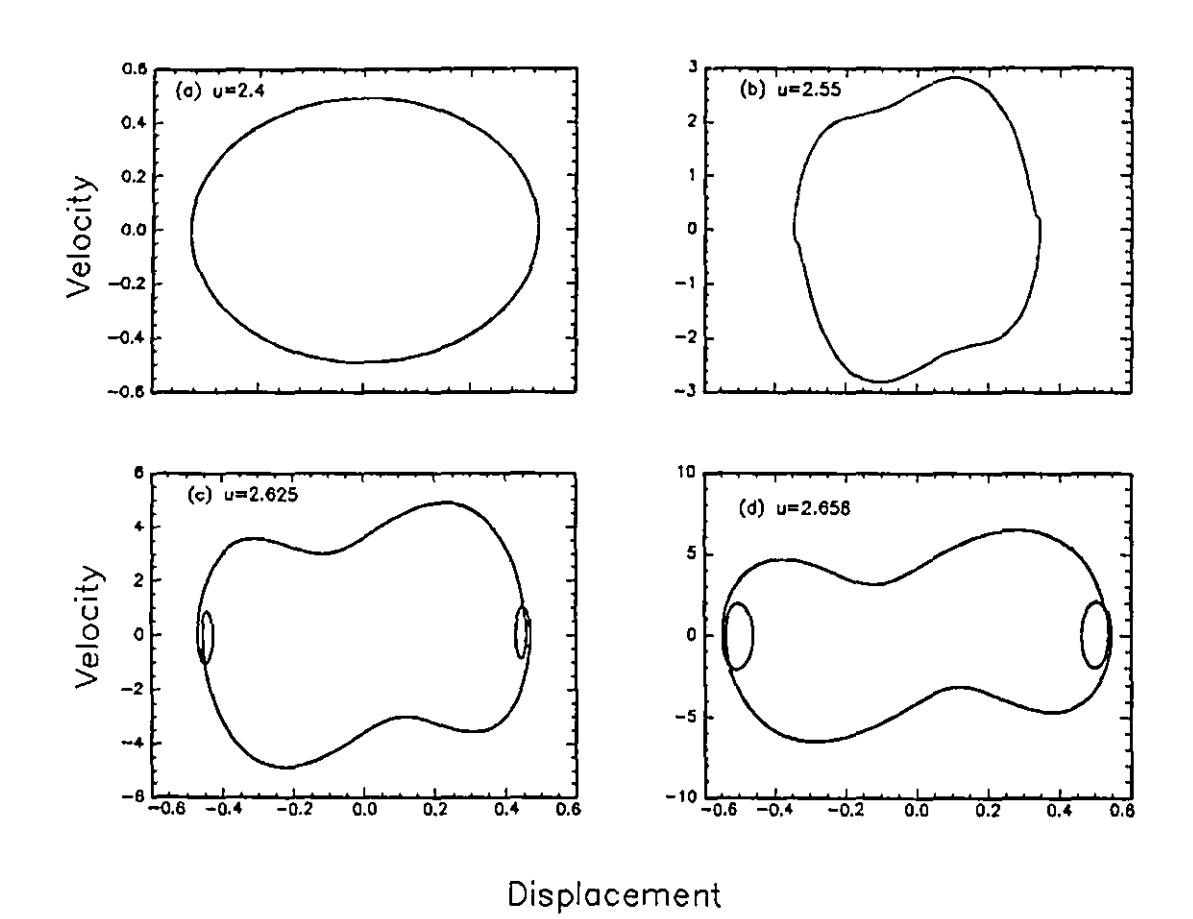


Figure 6.22. Phase-plane plots of $\dot{\phi}_1(\tau)$ versus $\phi_1(\tau)$ at (a) u=2.4, (b) u=2.55, (c) u=2.625 and (d) u=2.658 for the system of Case 2: h=0.2, c=0.79, f=0.8 and $\kappa_c=5\times10^3$.

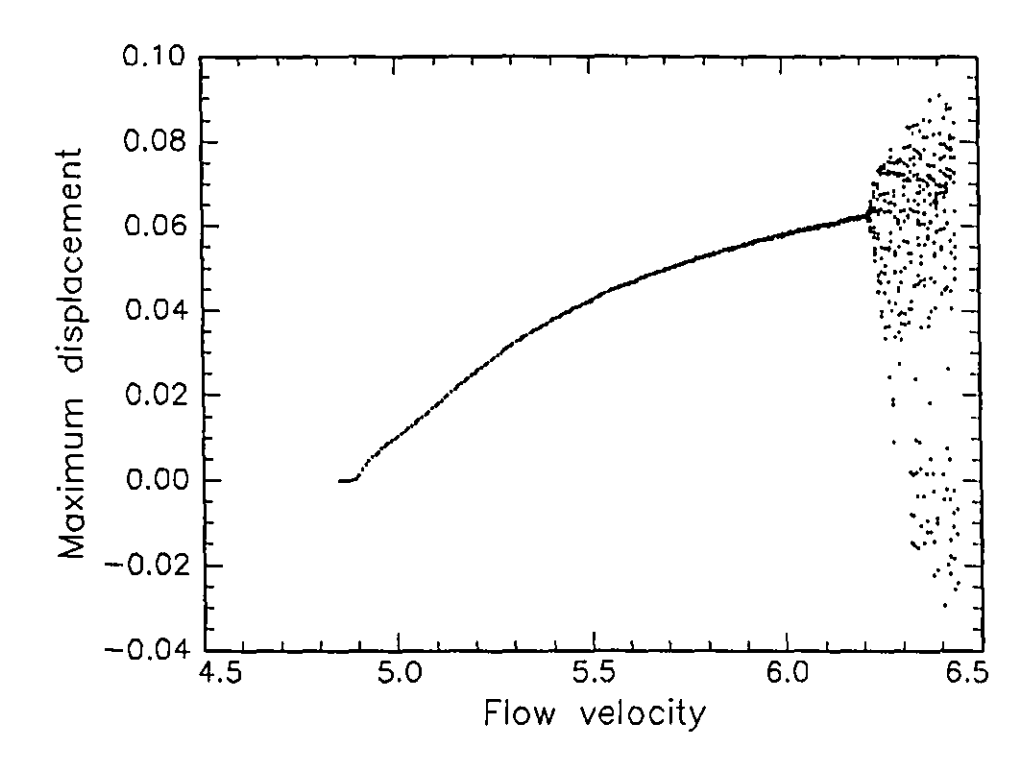


Figure 6.23. Bifurcation diagram for the system of Case 3: h = 0.5, c = 0.38, f = 0, with the cubic-spring model ($\kappa_c = 5 \times 10^5$) for impacting with the channel; the maximum displacement $\phi_1(\tau)$ versus the dimensionless flow velocity, u.

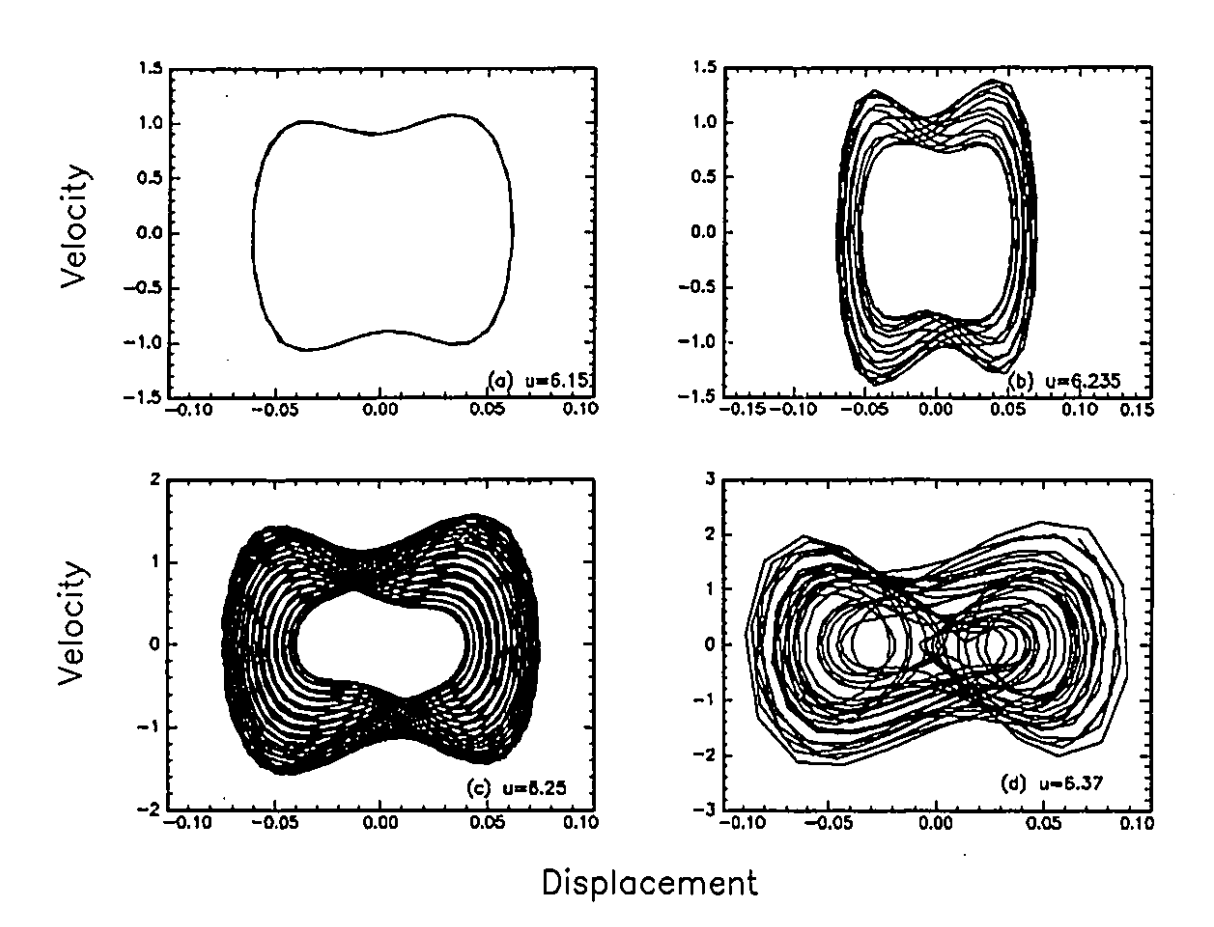


Figure 6.24. Phase-plane plots of $\dot{\phi}_1(\tau)$ versus $\phi_1(\tau)$ at (a) u = 6.15, (b) u = 6.235, (c) u = 6.25 and (d) u = 6.37 for the system of Case 3: h = 0.5, c = 0.38, f = 0 and $\kappa_c = 5 \times 10^5$.

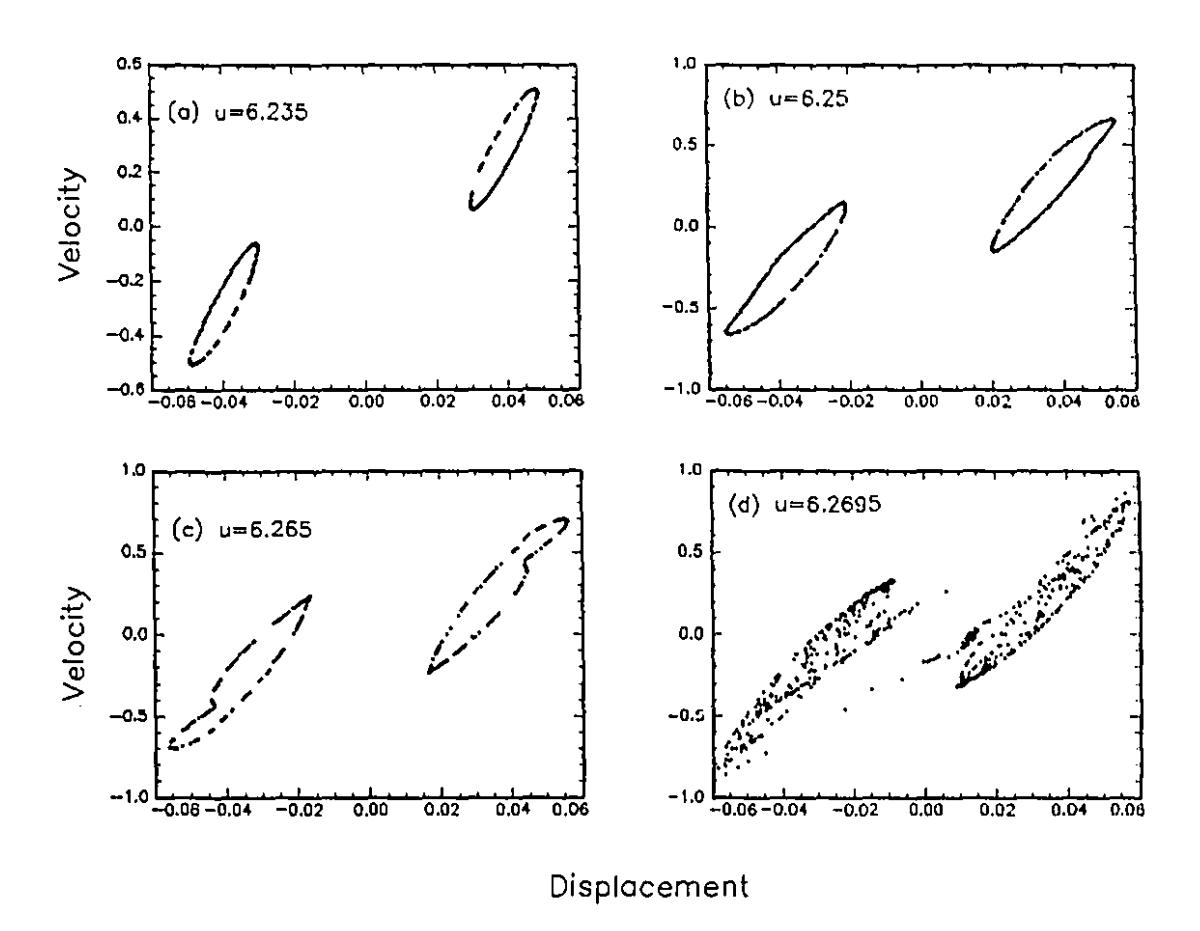


Figure 6.25. Poincaré maps of $\dot{\phi}_2(\tau)$ versus $\phi_2(\tau)$ when $\phi_1(\tau)=0$ for the system of Case 3: $h=0.5, c=0.38, f=0, \kappa_c=5\times 10^5$.

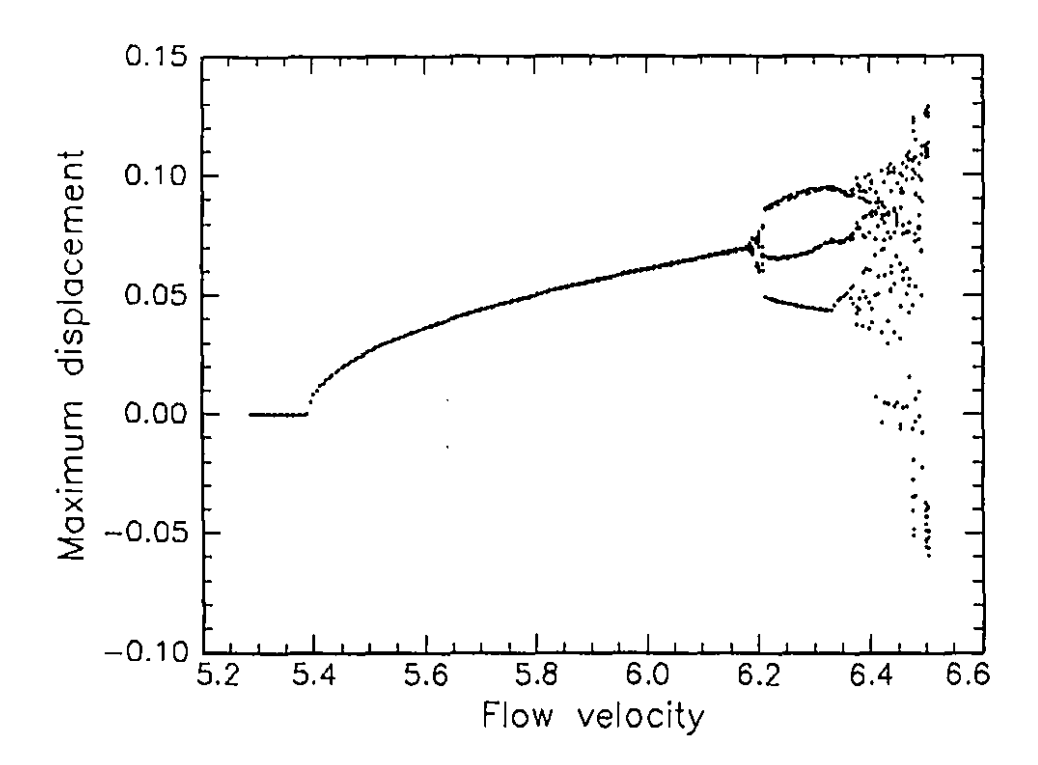


Figure 6.26. Bifurcation diagram for the system of Case 3: h = 0.5, c = 0.38, f = 0, with the cubic-spring model ($\kappa_c = 5 \times 10^5$) for impacting with the channel; the maximum displacement $\phi_1(\tau)$ versus the dimensionless flow velocity, u.

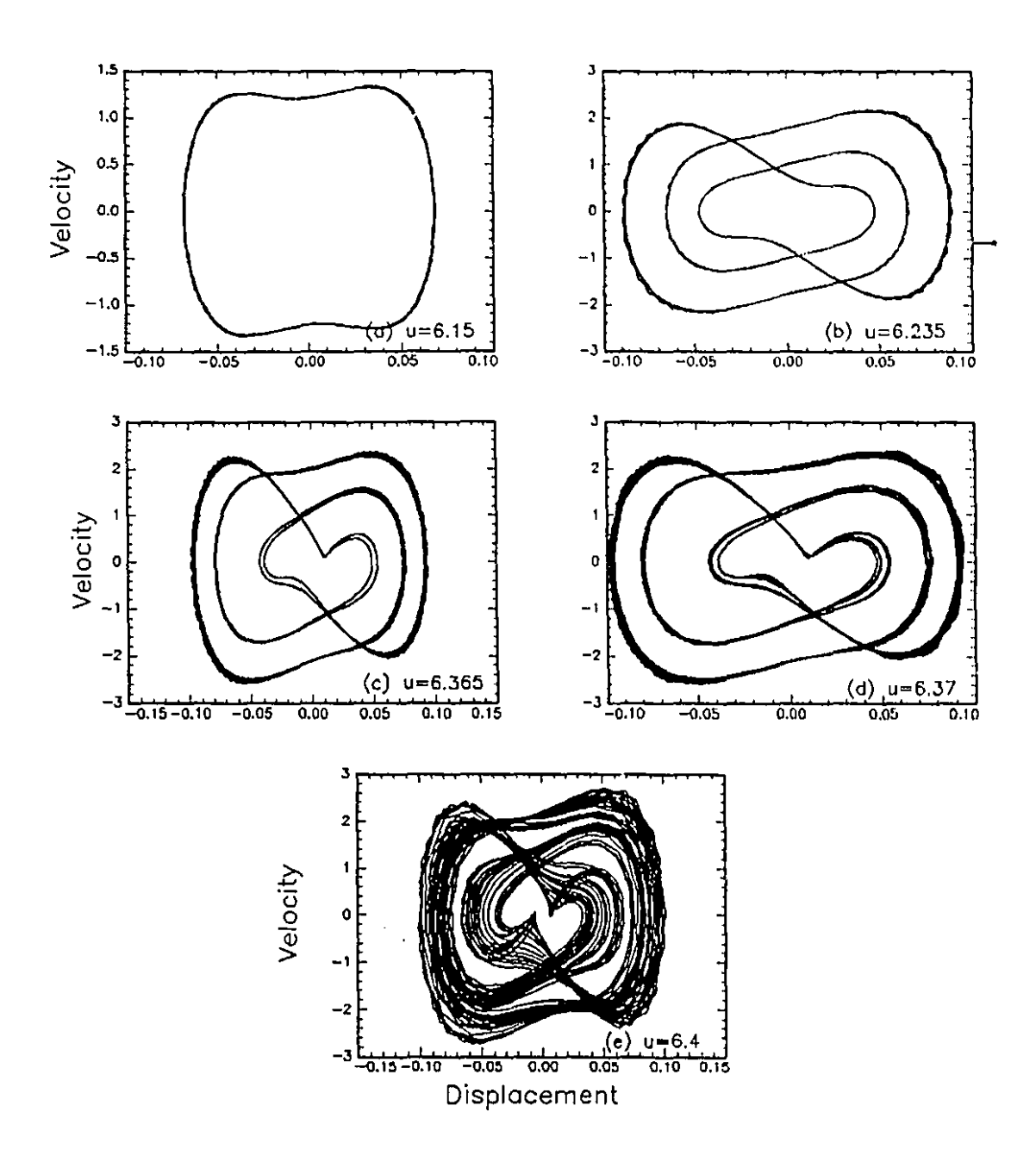


Figure 6.27. Phase-plane plots of $\dot{\phi}_1(\tau)$ versus $\phi_1(\tau)$ at (a) u = 6.15, (b) u = 6.235, (c) u = 6.365, (d) u = 6.37 and (e) u = 6.4 for the system of Case 3: h = 0.5, c = 0.38, f = 0 and $\kappa_c = 5 \times 10^5$.

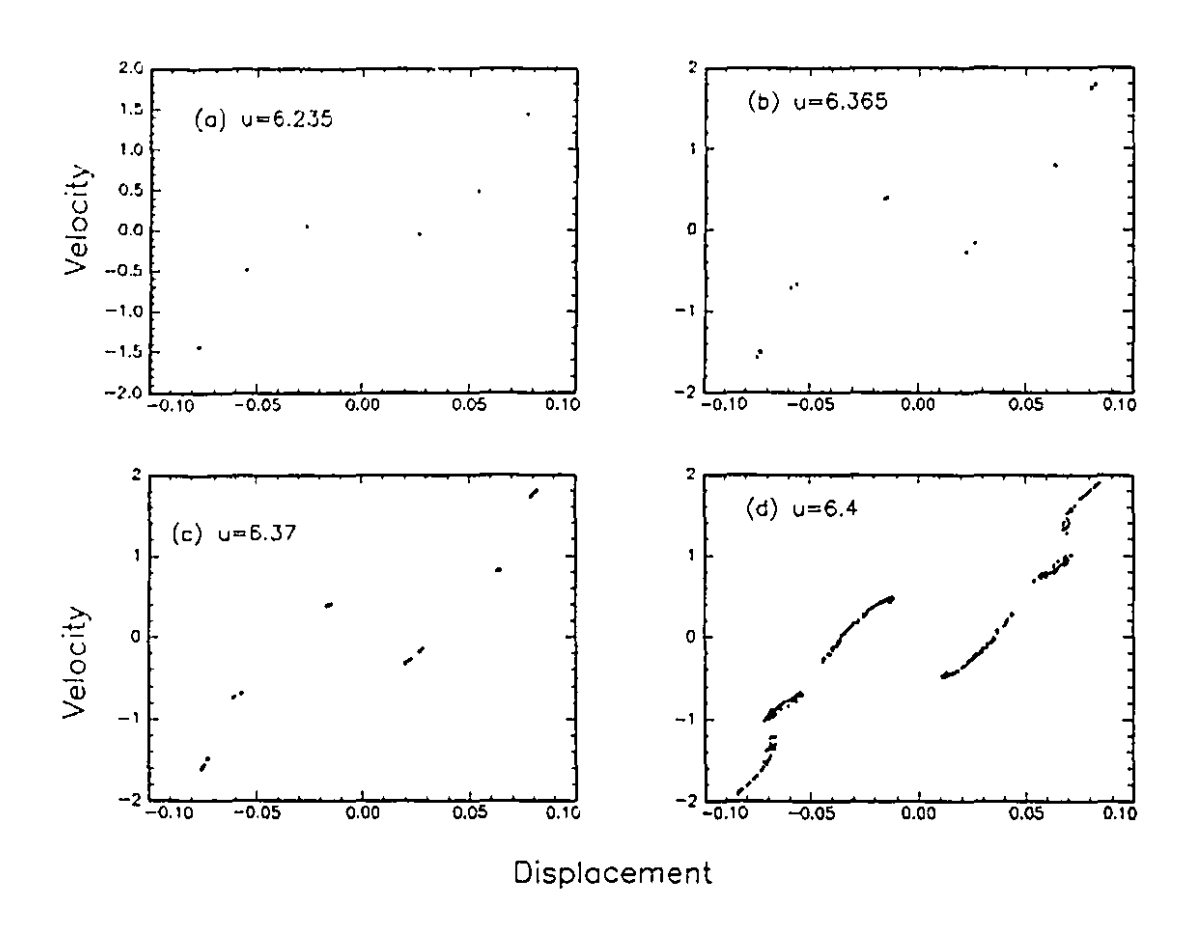


Figure 6.28. Poincaré maps of $\dot{\phi}_2(\tau)$ versus $\phi_2(\tau)$ when $\phi_1(\tau)=0$ for the system of Case 3: h=0.5, c=0.38, f=0 and $\kappa_c=5\times 10^3$, for N=4 system, for (a) u=6.235, (b) u=6.365, (c) u=6.37 and (d) u=6.4.

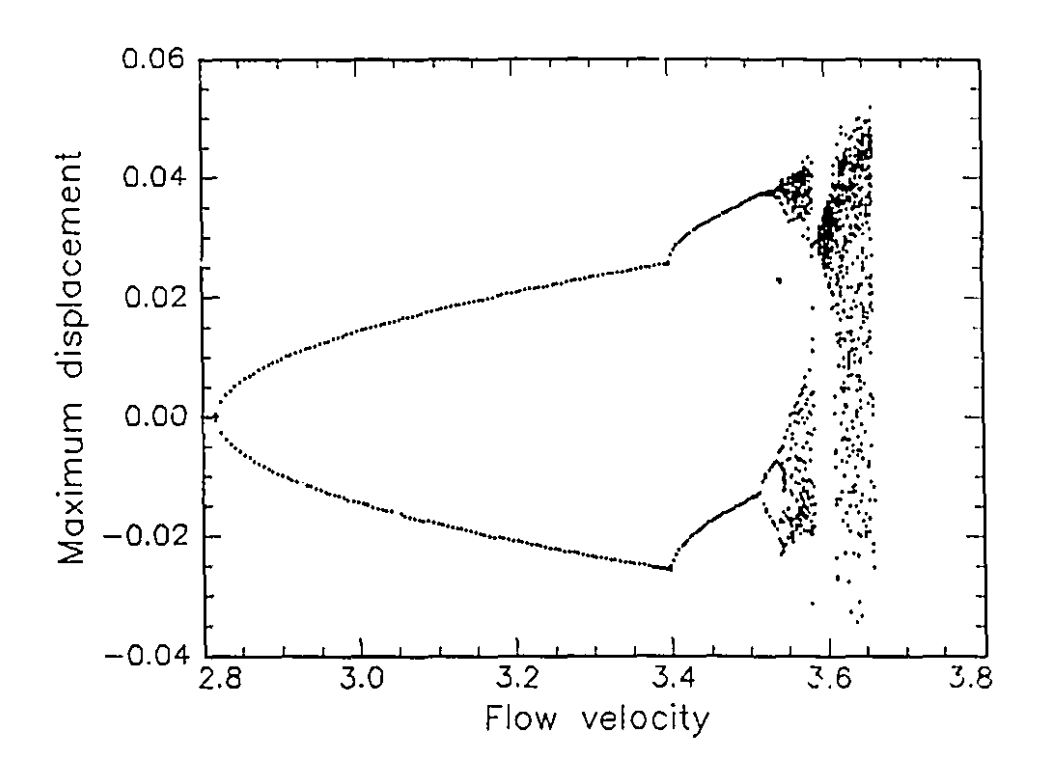


Figure 6.29. Bifurcation diagram for the system of Case 4: h=0.2, c=0.79, f=0.4, N=3, with the cubic-spring model ($\kappa_c=5\times10^5$) for impacting with the channel; the maximum displacement $\phi_1(\tau)$ versus the dimensionless flow velocity, u.

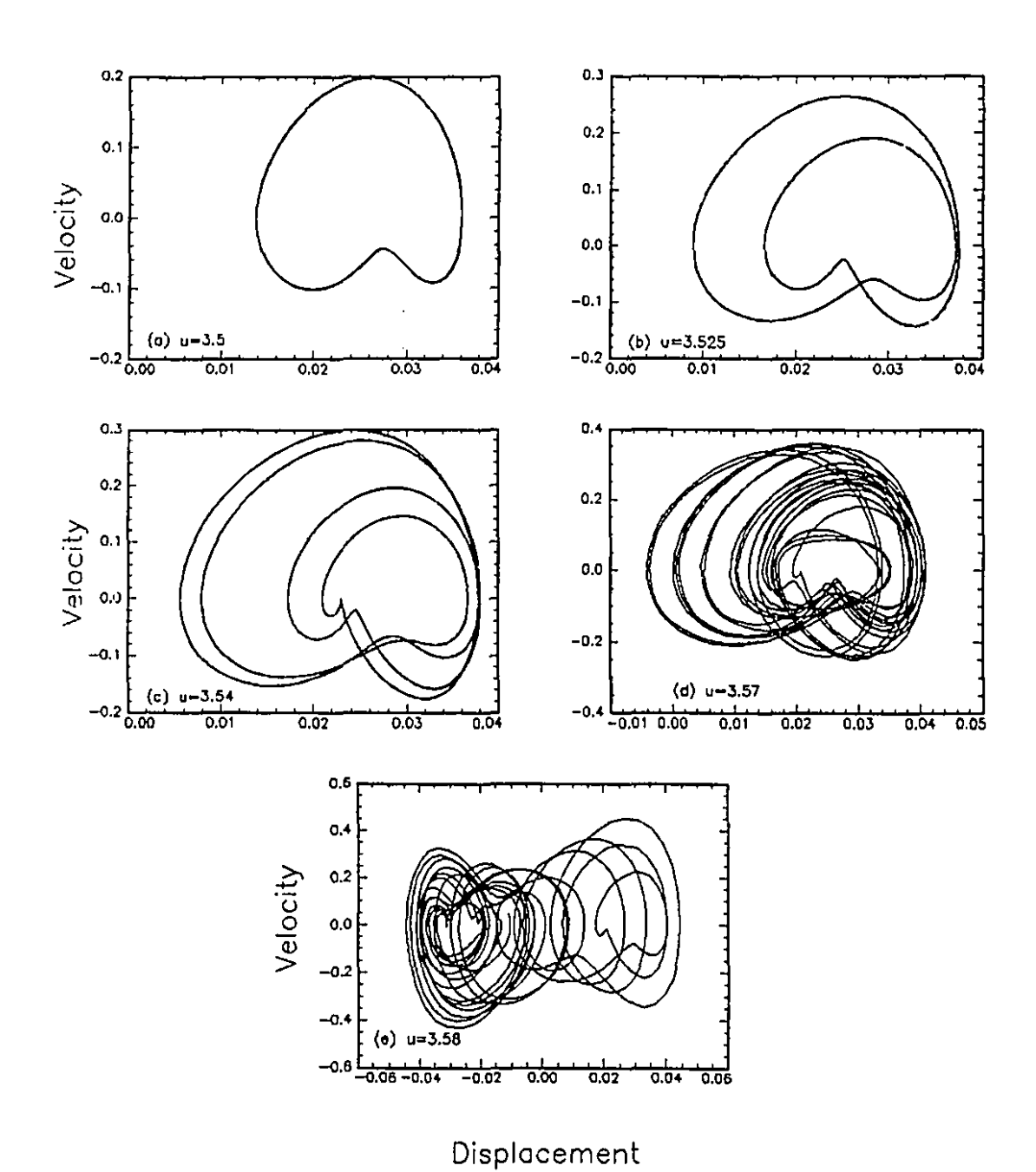


Figure 6.30. Phase-plane plots of $\dot{\phi}_1(\tau)$ versus $\phi_1(\tau)$ at (a) u = 3.5, (b) u = 3.525, (c) u = 3.54, (d) u = 3.57 and (e) u = 3.58 for the system of Case 4: h = 0.2, c = 0.79, f = 0.4 and $\kappa_c = 5 \times 10^5$.

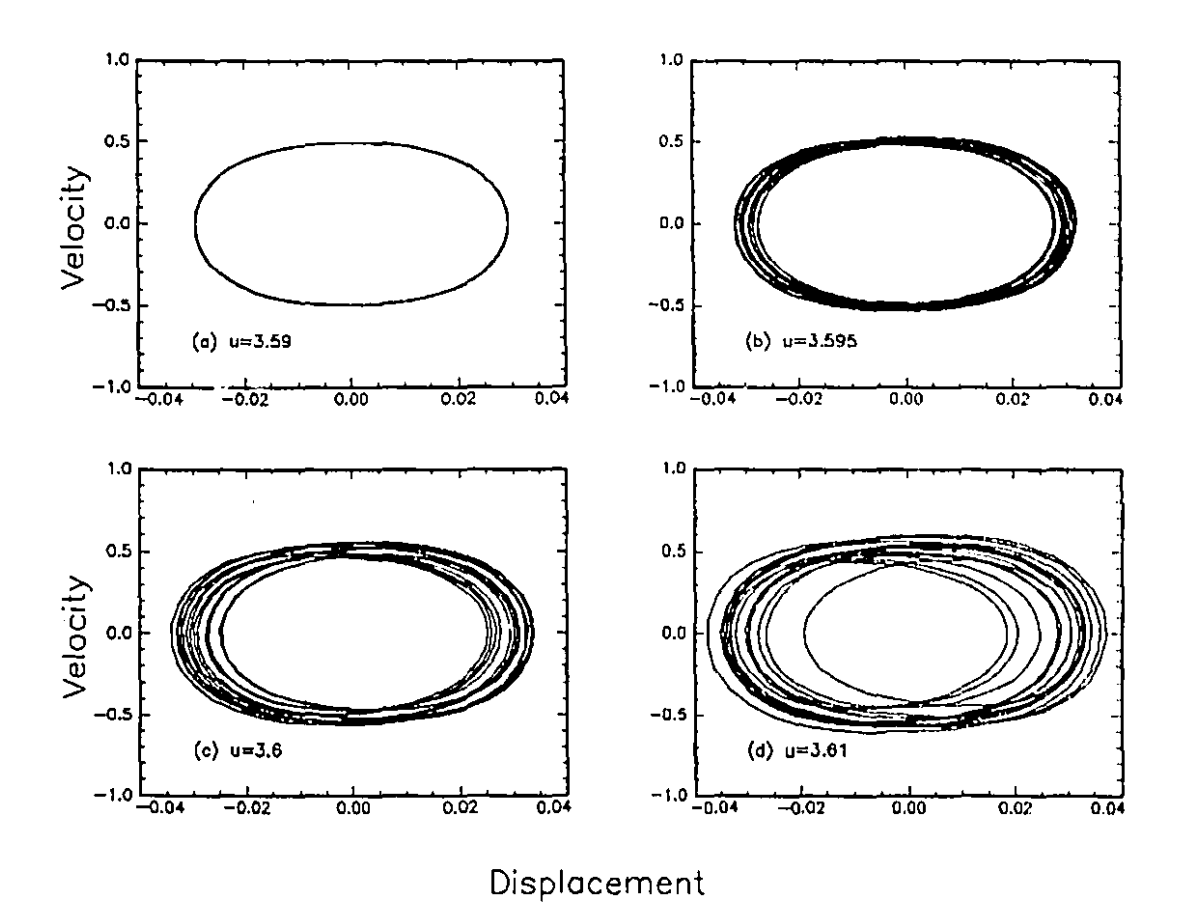


Figure 6.31. Phase-plane plots of $\dot{\phi}_1(\tau)$ versus $\phi_1(\tau)$ at (a) u=3.59, (b) u=3.595, (c) u=3.6, (d) u=3.61 for the system of Case 4: h=0.2, c=0.79, f=0.4, $\kappa_c=5\times 10^5$ and N=3.

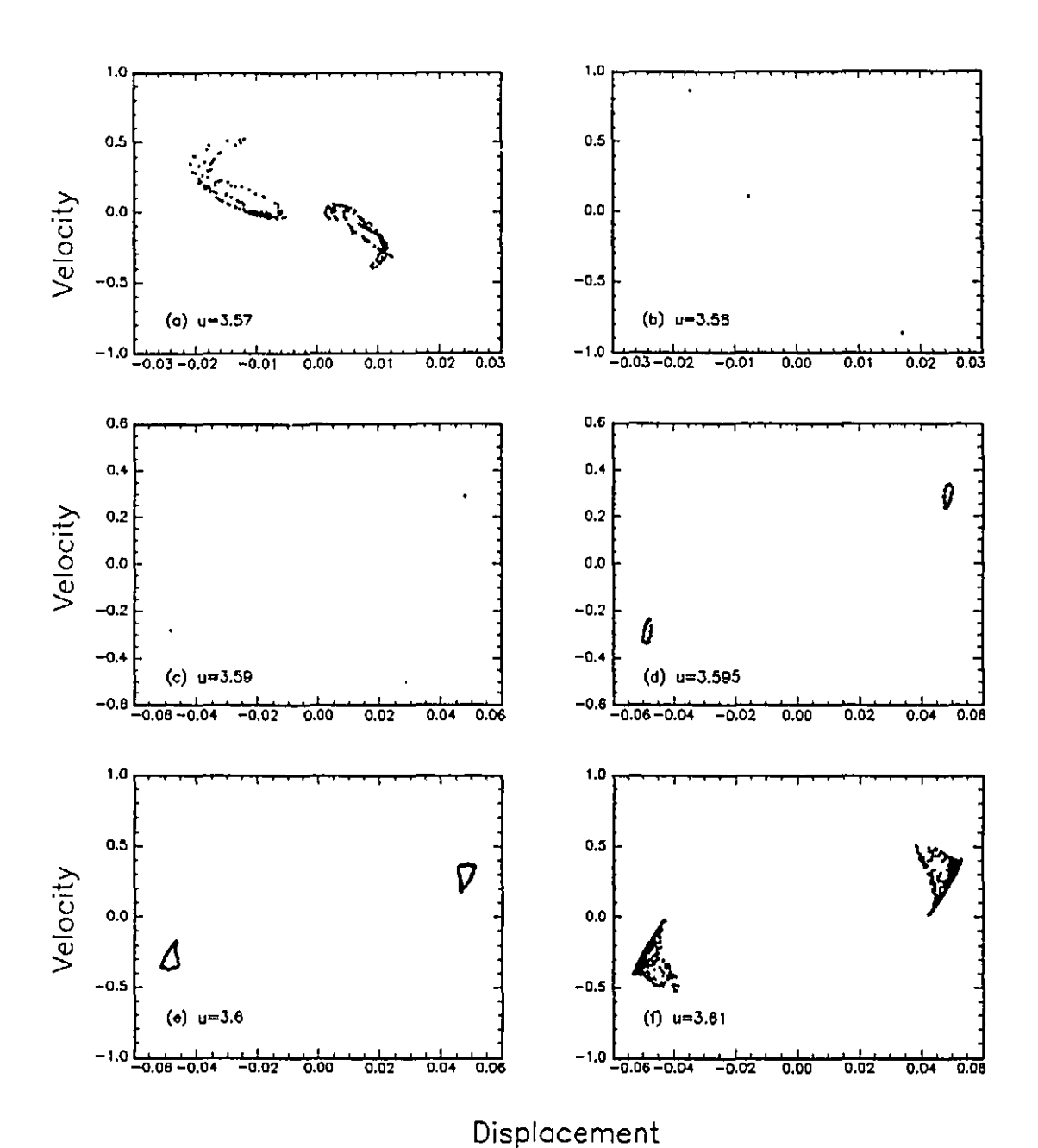


Figure 6.32. Poincaré maps of $\dot{\phi}_2(\tau)$ versus $\phi_2(\tau)$ when $\dot{\phi}_1(\tau) = 0$ for the system of Case 4: h = 0.2, c = 0.79, f = 0.4, $\kappa_c = 5 \times 10^5$ and N = 3, at (a) u = 3.57 and (b) u = 3.58, and when $\phi_1(\tau) = 0$ for (c) u = 3.59, (d) u = 3.595, (e) u = 3.6 and (f)

u = 3.61.

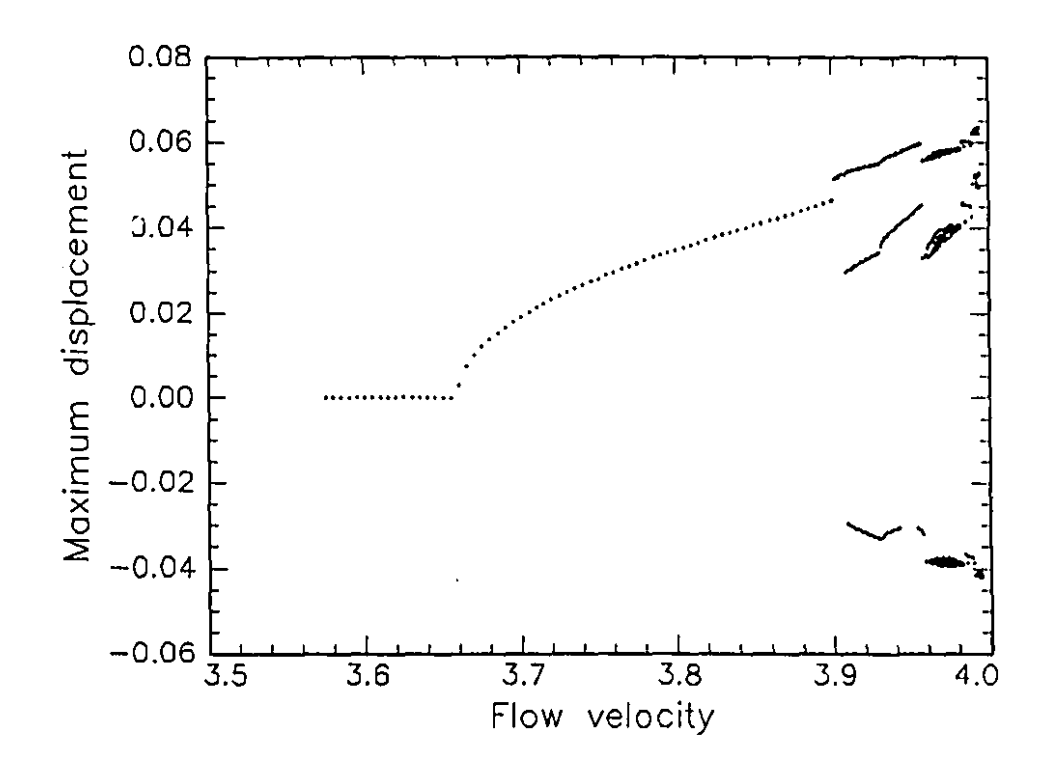


Figure 6.33. Bifurcation diagram for the system of Case 4: h = 0.2, c = 0.79, f = 0.4, with the cubic-spring model ($\kappa_c = 5 \times 10^5$) for impacting with the channel; the maximum displacement $\phi_1(\tau)$ versus the dimensionless flow velocity, u.

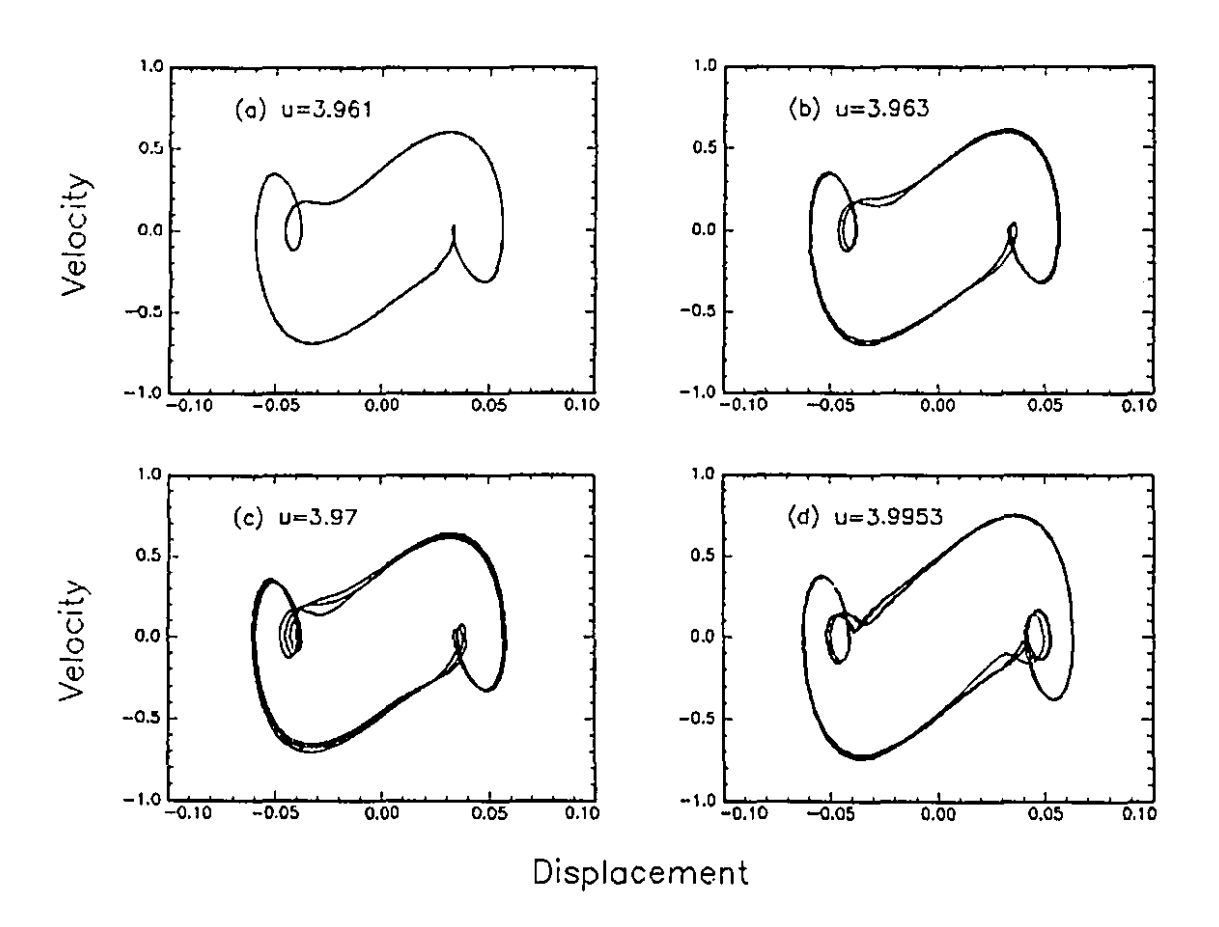
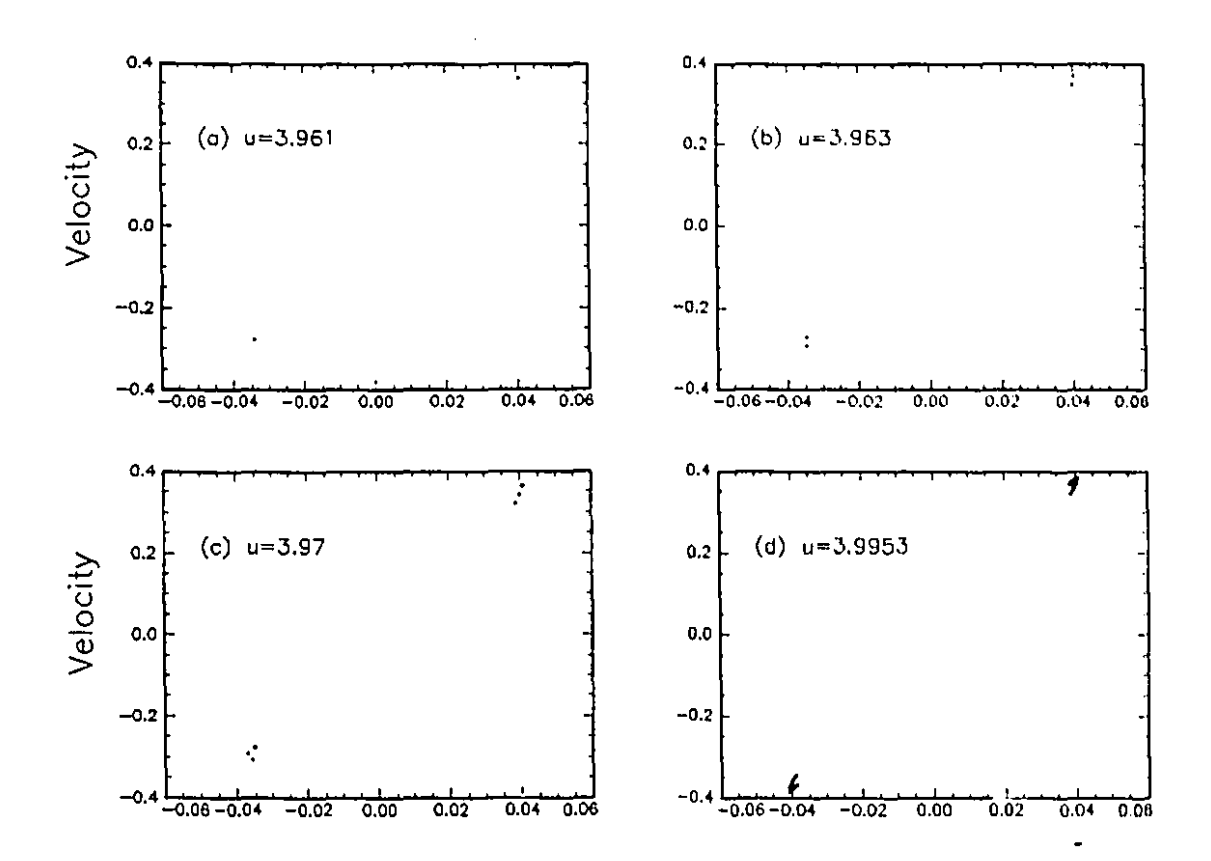


Figure 6.34. Phase-plane plots of $\dot{\phi}_1(\tau)$ versus $\phi_1(\tau)$ at (a) u=3.961, (b) u=3.963, (c) u=3.97 and (d) u=3.9953 for the system of Case 4: h=0.2, c=0.79, f=0.4 and $\kappa_c=5\times 10^5$.



Displacement

Figure 6.35. Poincaré maps of $\dot{\phi}_2(\tau)$ versus $\phi_2(\tau)$ when $\phi_1(\tau) = 0$ for the system of Case 4: h = 0.2, c = 0.79, f = 0.4 and $\kappa_c = 5 \times 10^5$; at (a) u = 3.961, (b) u = 3.963, (c) u = 3.97 and (d) u = 3.9953.

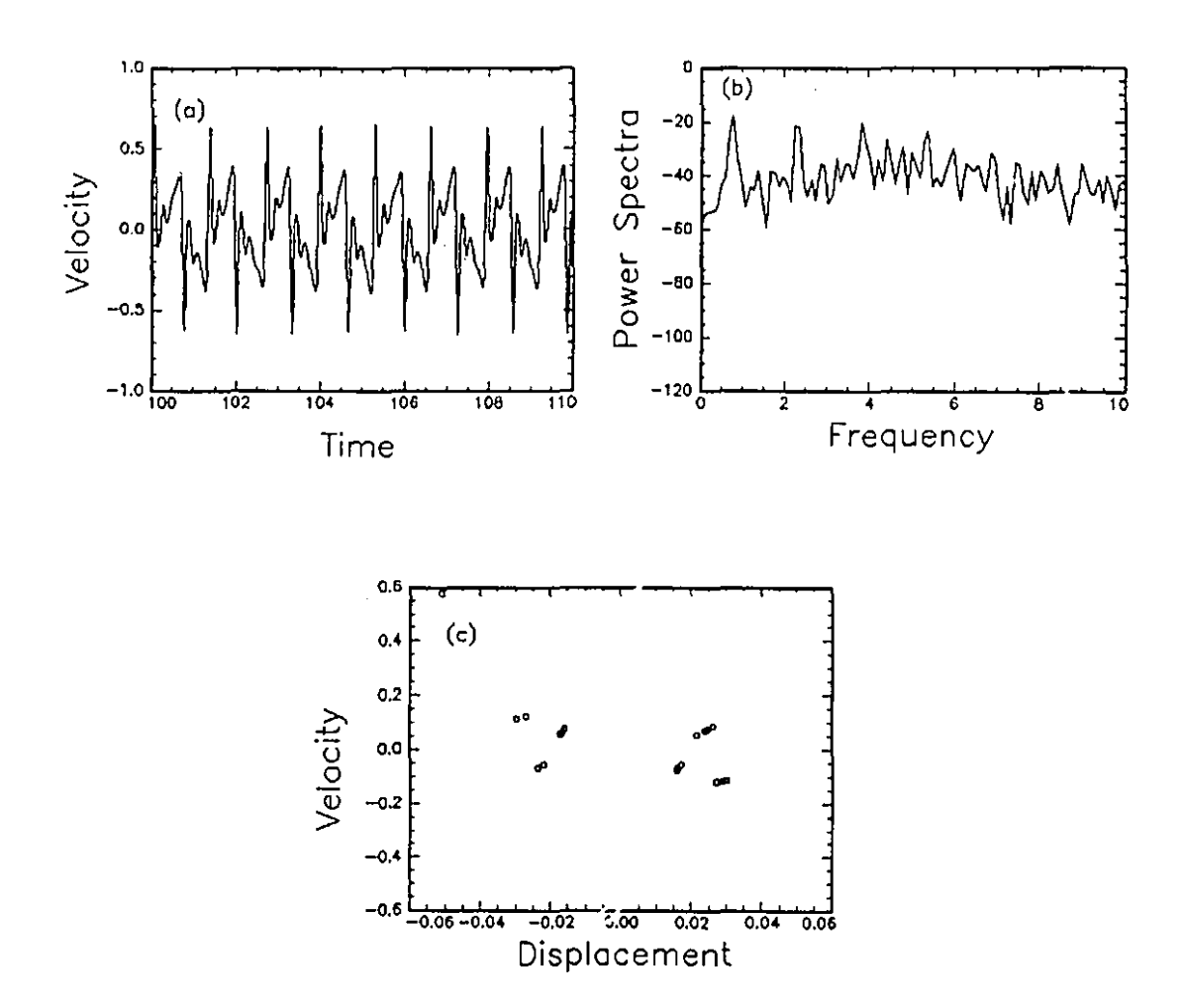


Figure 6.36. (a) Time traces, (b) Power Spectra and (c) Poincaré maps for the system of Case 4: h=0.2, c=0.79, f=0.4 and $\kappa_c=5\times10^5$; for u=3.9953.

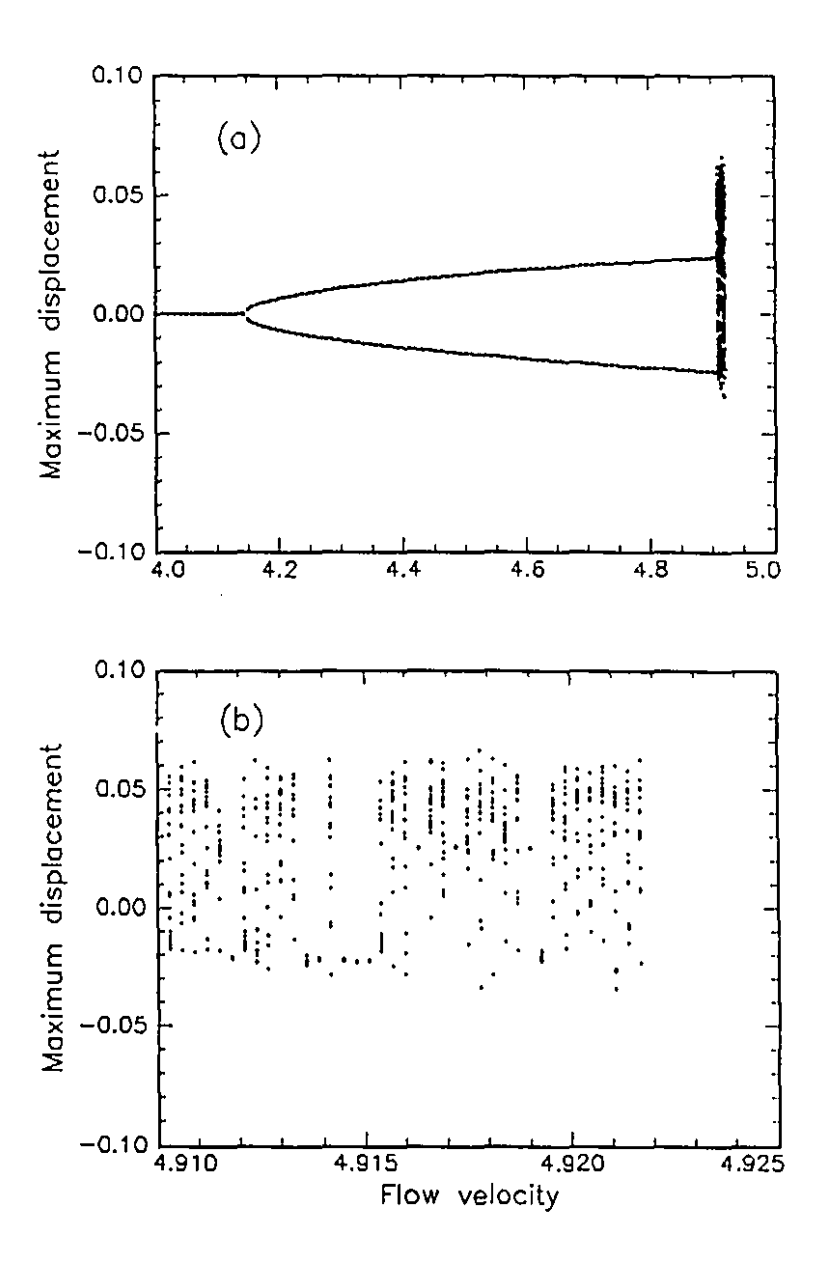


Figure 6.37. Bifurcation diagram for the system of Case 5: h = 0.5, c = 0.38, f = 0.4, with the cubic-spring model ($\kappa_c = 5 \times 10^5$) for impacting with the channel; the maximum displacement $\phi_1(\tau)$ versus the dimensionless flow velocity, u, for (a) 4 < u < 5 and (b) 4.9i < u < 4.925.

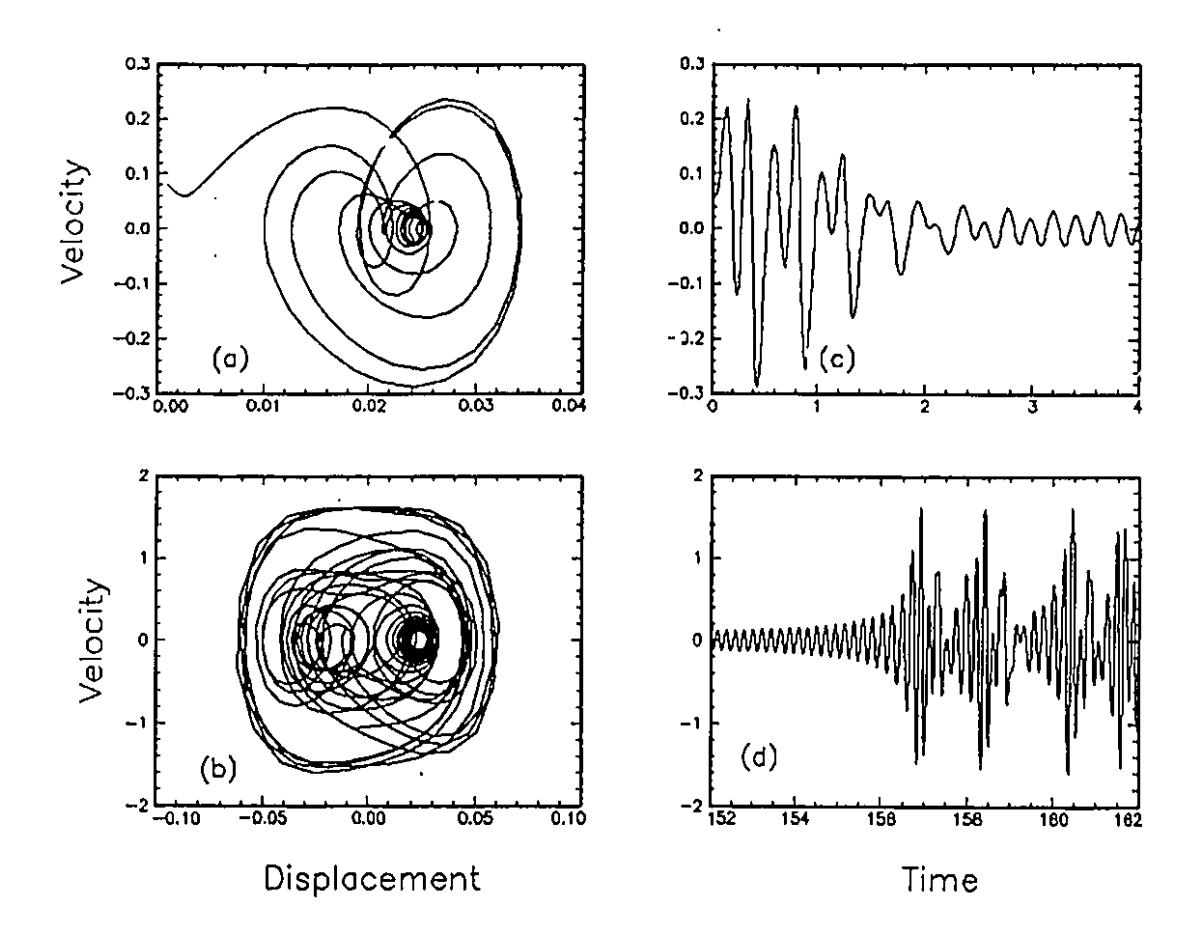


Figure 6.38. Phase-plane plots of $\dot{\phi}_1(\tau)$ versus $\phi_1(\tau)$ for the system of Case 5: $h=0.5,\ c=0.38,\ f=0.4,\ \kappa_c=5\times 10^5,\ {\rm at}\ u=4.91$ for (a) $0<\tau<4$ and (b) $152<\tau<162$. Time traces of $\dot{\phi}_1(\tau)$ versus τ for (c) $0<\tau<4$ and (d) $152<\tau<162$.

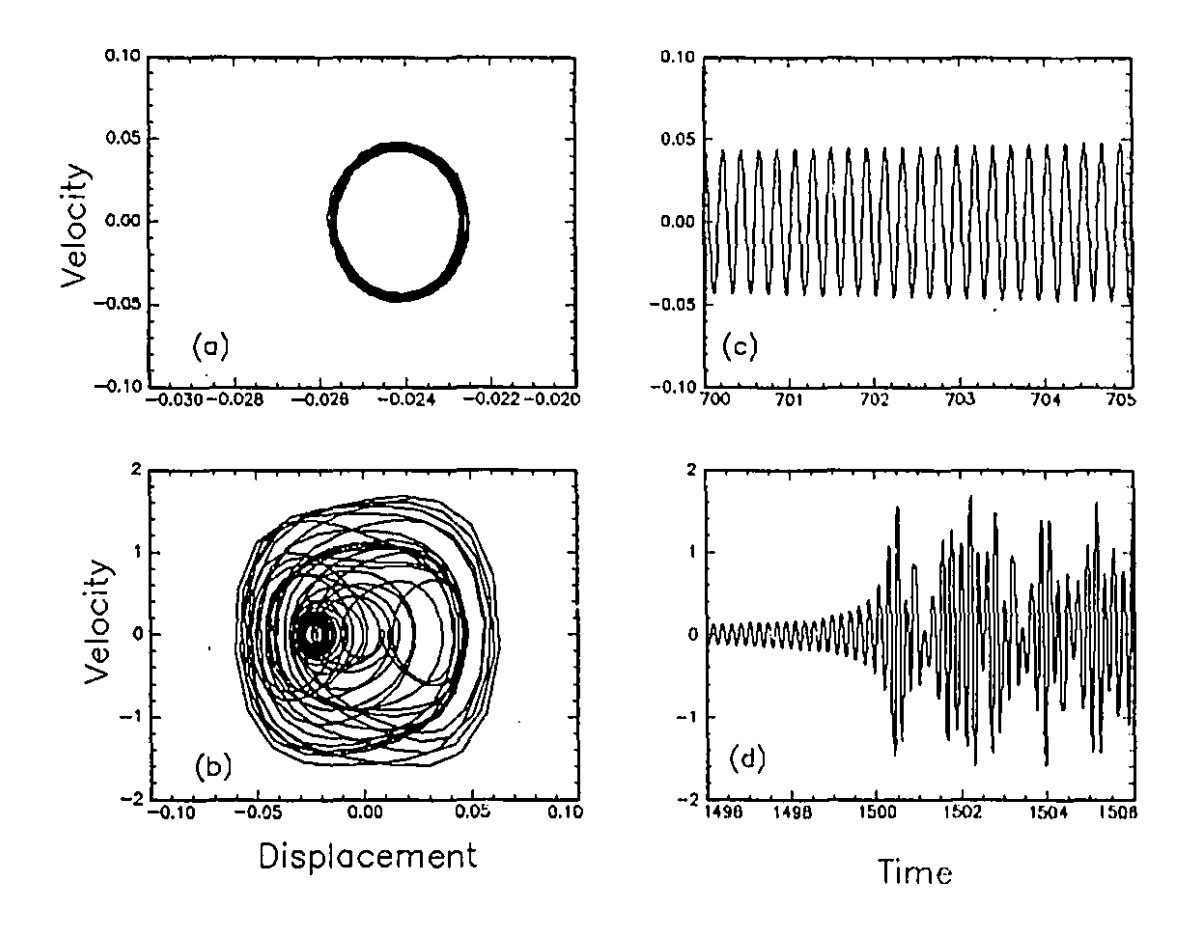


Figure 6.39. Phase-plane plots of $\dot{\phi}_1(\tau)$ versus $\phi_1(\tau)$ for the system of Case 5: $h=0.5, c=0.38, f=0.4, \kappa_c=5\times 10^5, \text{ at } u=4.91 \text{ for (a) } 700<\tau<705 \text{ and (b) } 1496<\tau<1506.$ Time traces of $\dot{\phi}_1(\tau)$ versus τ for (c) $700<\tau<705$ and (d) $1496<\tau<1506$.

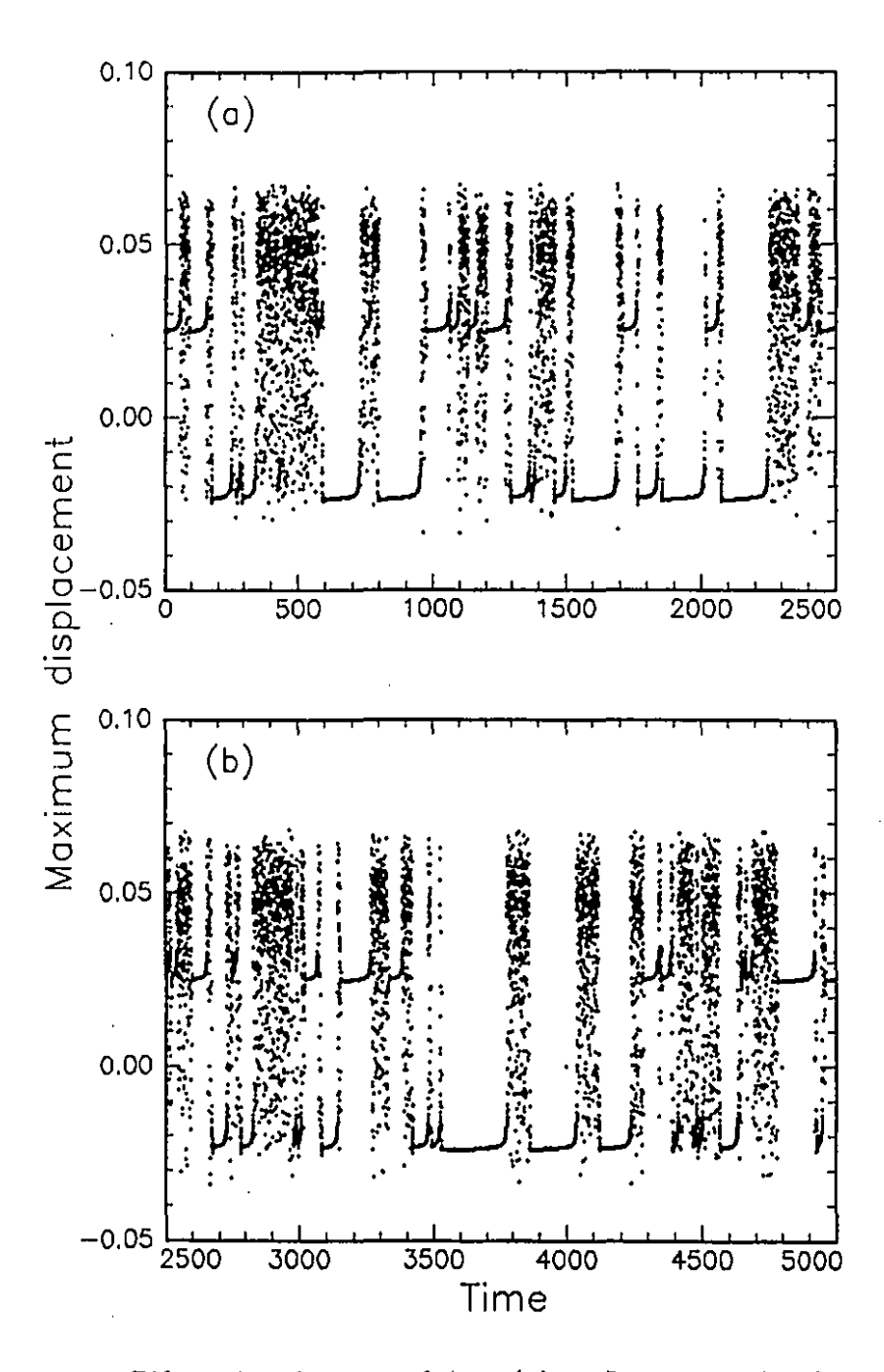


Figure 6.40. Bifurcation diagram of $\phi_{1max}(\tau)$ or I_k versus τ for the system of Case 5: h = 0.5, c = 0.38, f = 0.4 and $\kappa_c = 5 \times 10^5$, at u = 4.91 for (a) $0 < \tau < 2500$ and (b) $2500 < \tau < 5000$.

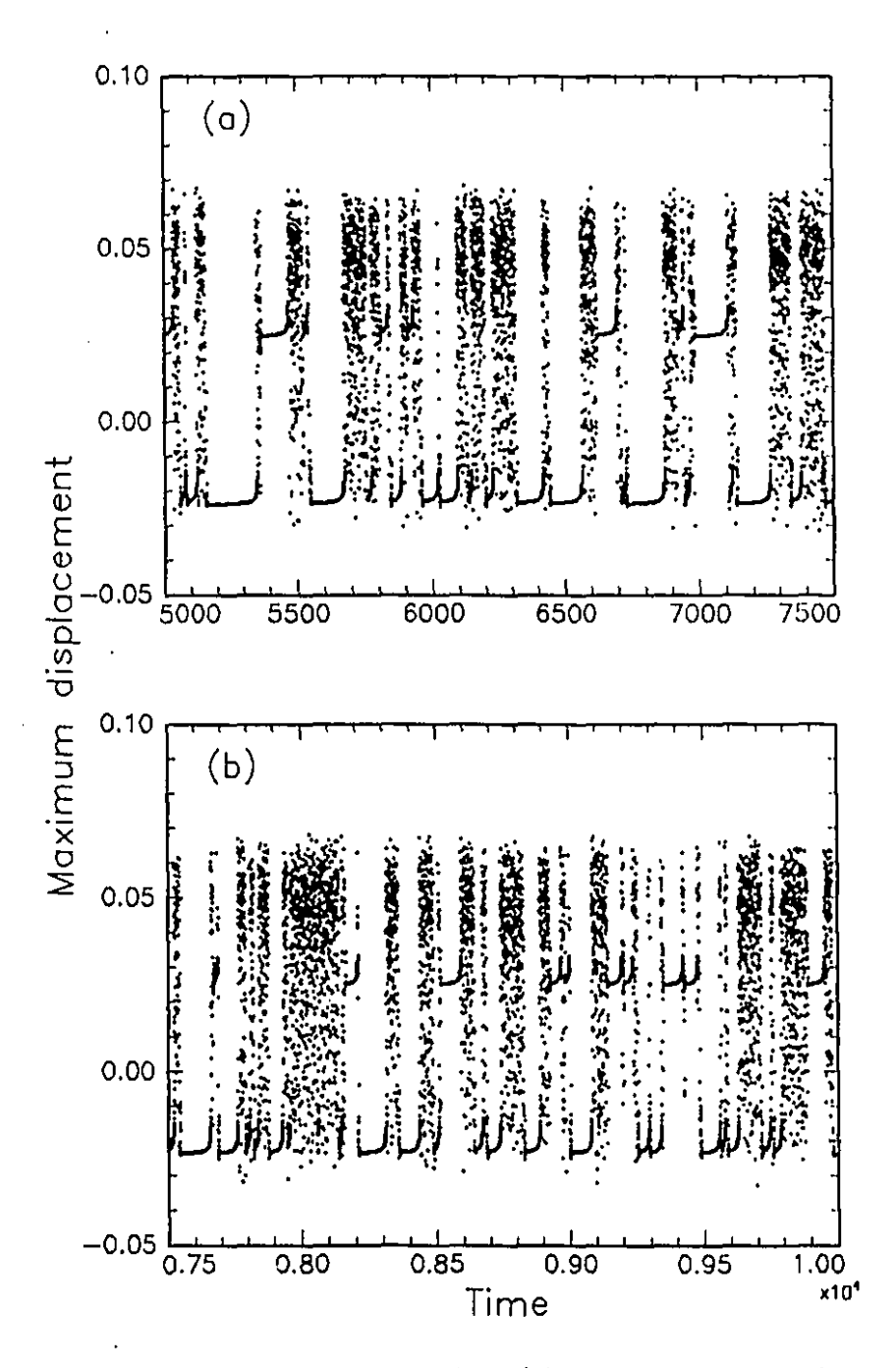


Figure 6.41. Bifurcation diagram of $\phi_{1max}(\tau)$ or I_k versus τ for the system of Case 5: h = 0.5, c = 0.38, f = 0.4 and $\kappa_c = 5 \times 10^5$, at u = 4.91 for (a) $5000 < \tau < 7500$ and (b) $7500 < \tau < 10000$.

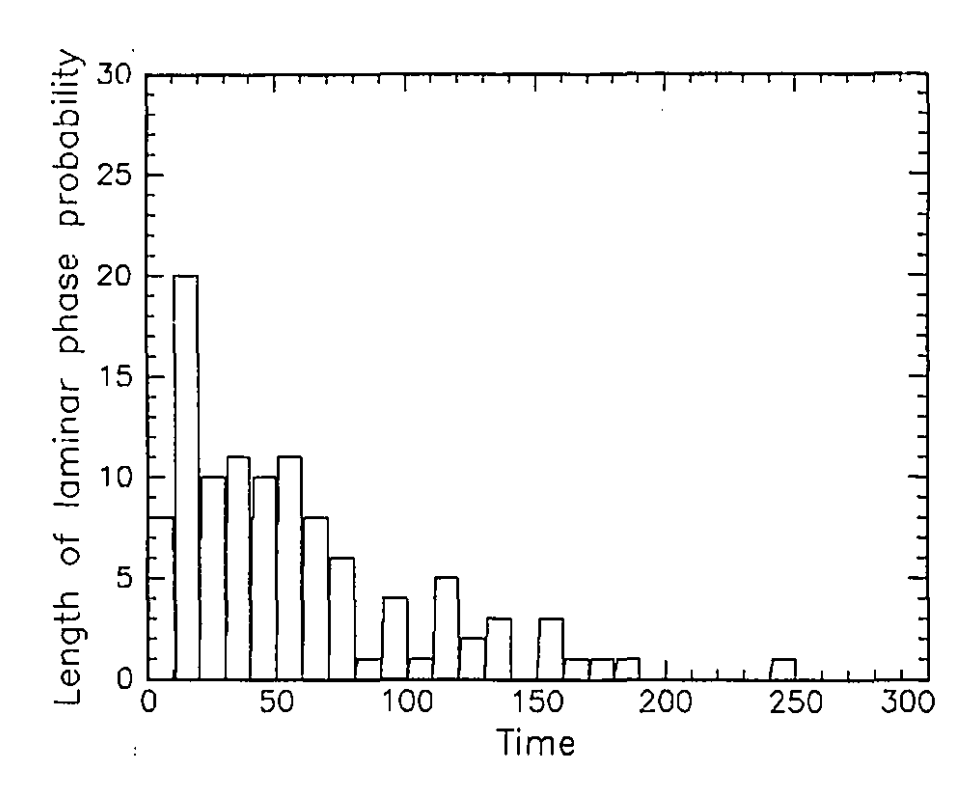


Figure 6.42. Distribution of the lengths of laminar phases $P(\tau)$ versus τ for the system of Case 5: h=0.5, c=0.38, f=0.4, with the cubic-spring model $(\kappa_c=5\times10^5)$ for impacting with the channel, at u=4.91.

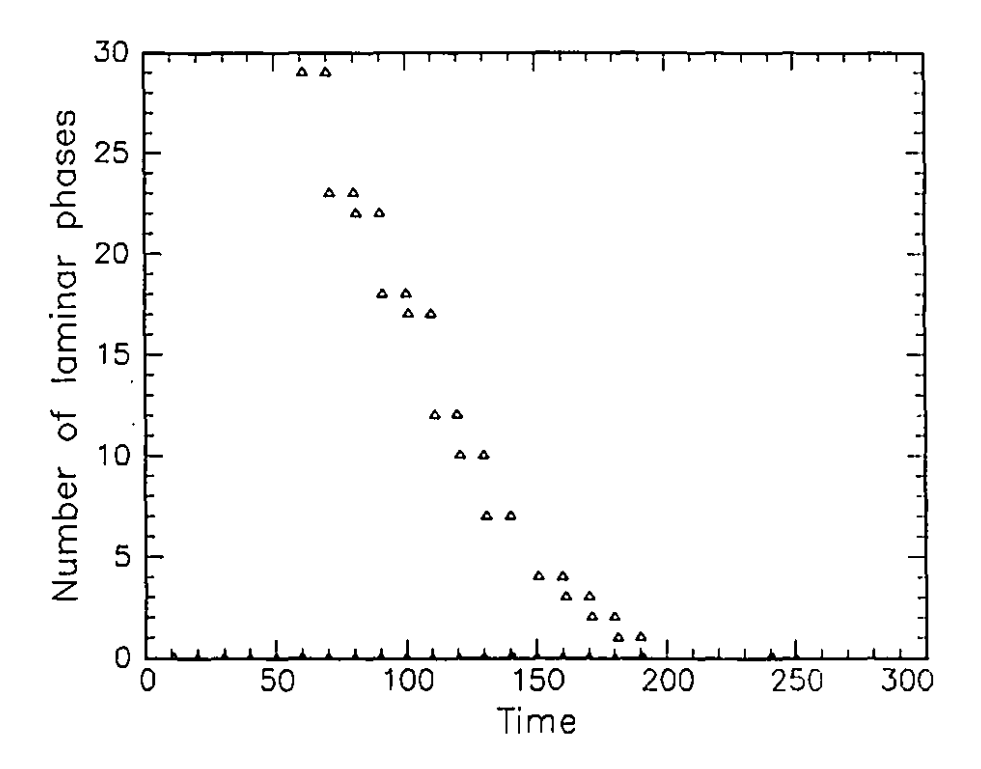


Figure 6.43. Number of laminar phases lasting longer than τ_0 , $N(\tau > \tau_0)$, versus τ_0 for the system of Case 5: h = 0.5, c = 0.38, f = 0.4, with the cubic-spring model $(\kappa_c = 5 \times 10^5)$ for impacting with the channel, at u = 4.91.

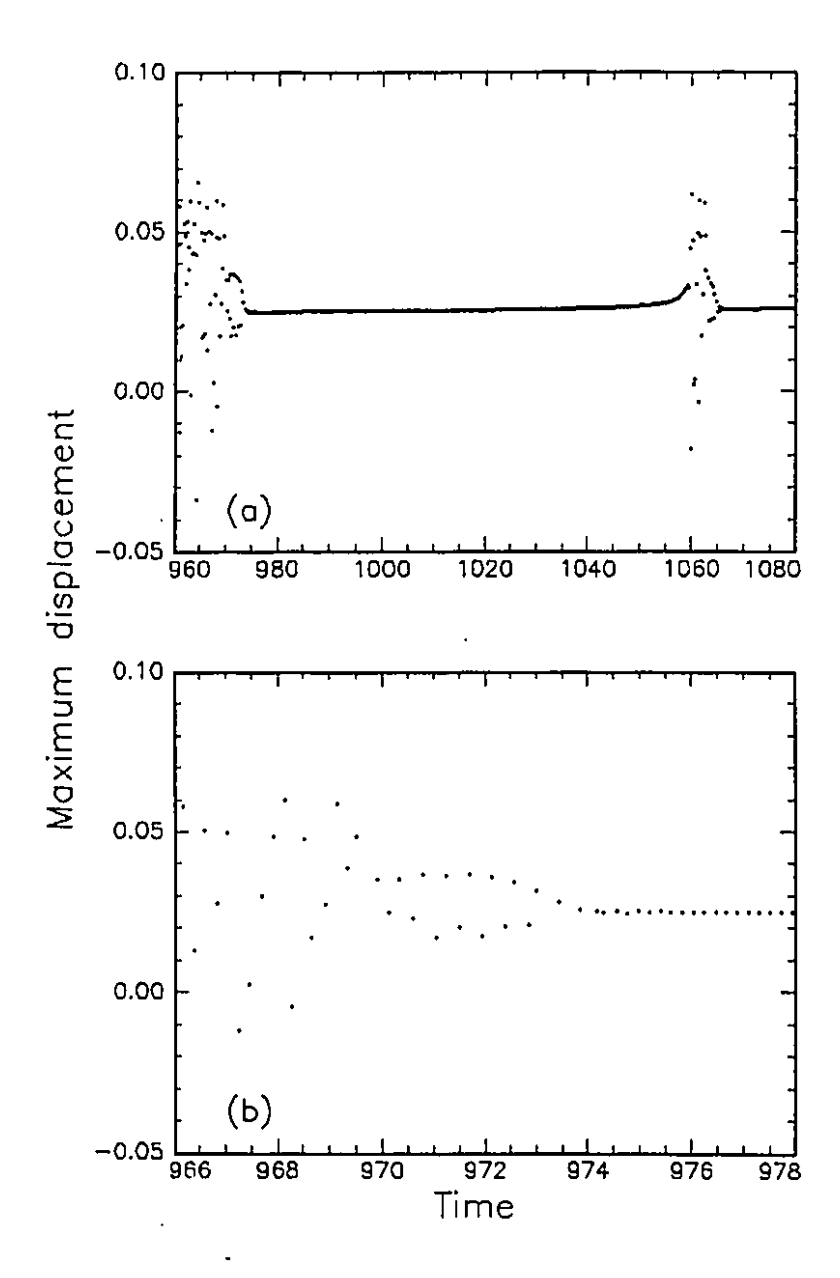


Figure 6.44. Bifurcation diagram of $\phi_{1max}(\tau)$ or I_k versus τ for the system of Case 5: h = 0.5, c = 0.38, f = 0.4 and $\kappa_c = 5 \times 10^5$ for (a) $960 < \tau < 1080$ and (b) $966 < \tau < 978$, at u = 4.91.

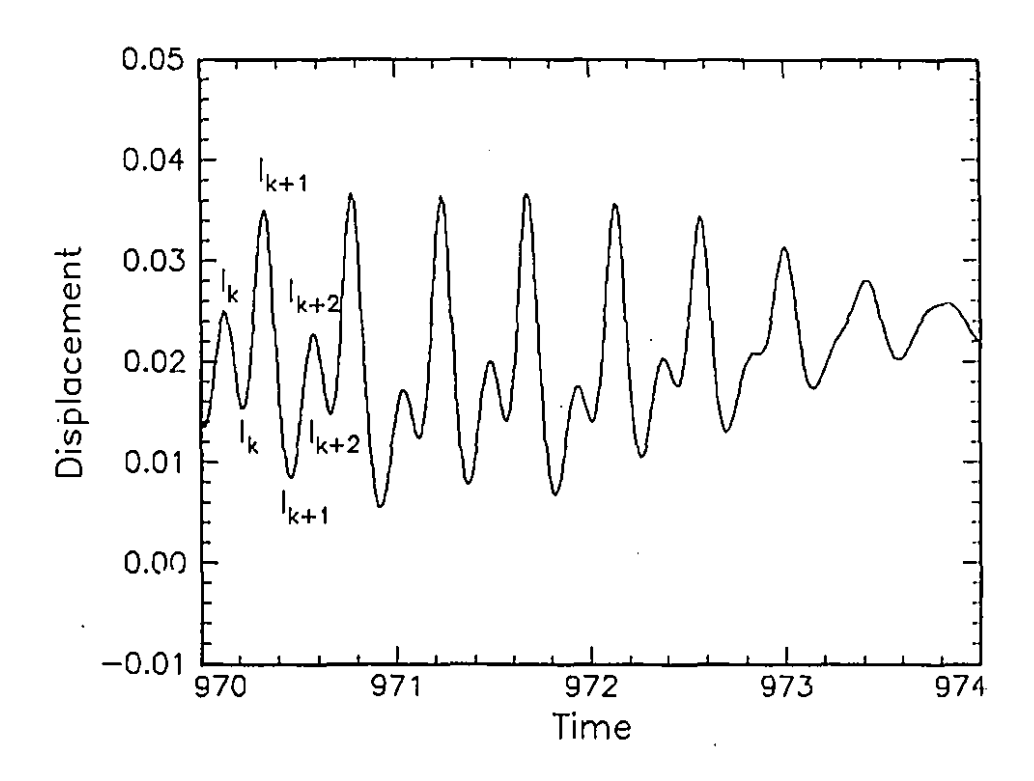


Figure 6.45. Time traces of $\phi_1(\tau)$ versus τ for 970 $<\tau<$ 974 for the system of Case 5: h=0.5, c=0.38, f=0.4, with the cubic-spring model ($\kappa_c=5\times 10^5$) for impacting with the channel, at u=4.91. I_k definition.

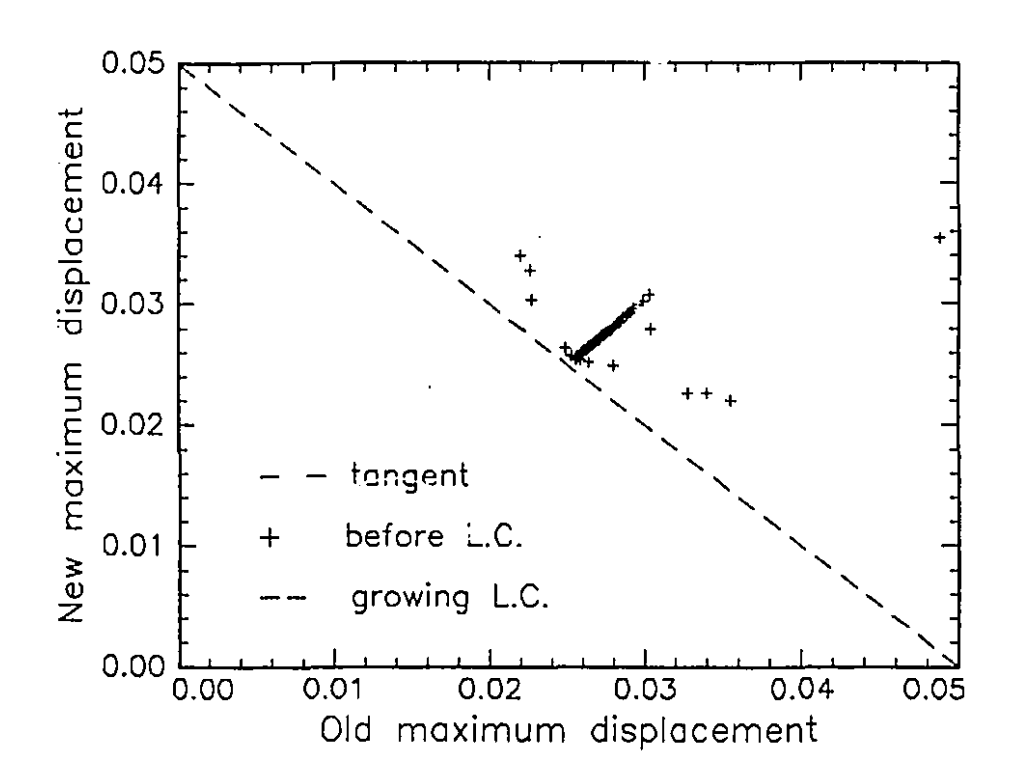


Figure 6.46. Graph of the first return map I_{k+1} versus I_k for the system of Case 5: h = 0.5, c = 0.38, f = 0.4, with the cubic-spring model ($\kappa_c = 5 \times 10^5$) for impacting with the channel, at u = 4.91.

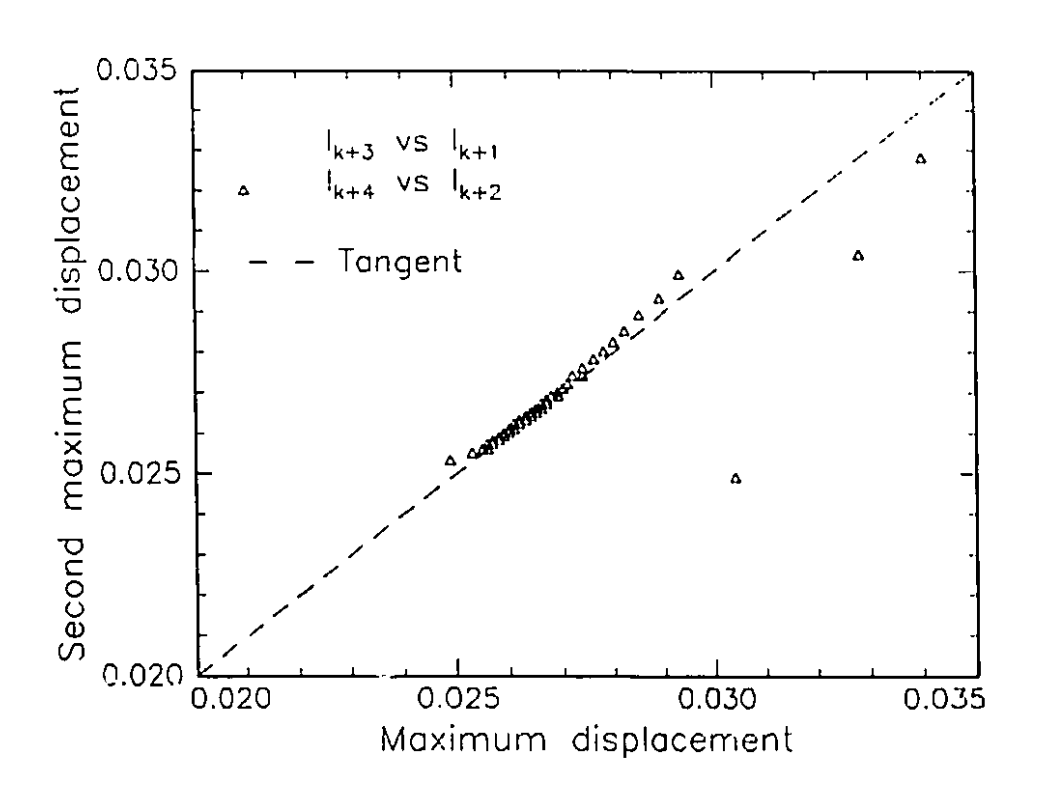


Figure 6.47. Graph of the second return map I_{k+2} versus I_k for the system of Case 5: h = 0.5, c = 0.38, f = 0.4, with the cubic-spring model ($\kappa_c = 5 \times 10^5$) for impacting with the channel, at u = 4.91.

Chapter 7

GLOBAL COMPARISON OF THE RESULTS OBTAINED WITH THE FIRST MODEL WITH N=2 AND N=3

In this chapter, bifurcation diagrams, phase plane portraits and tables are constructed for the first model with the cubic spring representation, for N=2 and N=3, and compared. Also, some results are presented in the form of bifurcation diagrams and phase plane portraits for the first model with the trilinear spring representation for N=2, in order to compare these two types of impact modelling.

The dynamical behaviour is analyzed by varying the flow velocity u, for $u > u_{cr}$, where u_{cr} is the flow velocity for which a Hopf or a pitchfork bifurcation occurs; two other parameters, h and f, are also varied, where h corresponds to the dimensionless hydraulic diameter, and f to the form-coefficient of the downstream end of the articulated system. Specifically, for h = 0.2 and h = 0.5 and for five endform coefficients, f = 0, f = 0.2, f = 0.4, f = 0.6 and f = 0.8, the behaviour

of the first model with the cubic spring is analyzed for N=2 and N=3 (Sections 7.1—7.4).

After discussing in some detail the behaviour of the model for different parameters, the final results will be summarized in Tables 7.1 to 7.3 on pp. 99-101, where Table 7.1 explains the symbols used in Tables 7.2 and 7.3.

Then, in Section 7.5, the first model with the trilinear spring is analyzed for h = 0.5 and N = 2, and f = 0, f = 0.4 and f = 0.8; the results obtained are compared to those for the first model with a cubic spring.

7.1 N=2, FIRST MODEL WITH CUBIC SPRING; h=0.2

7.1.1 N = 2, h = 0.2 and f = 0

From linear analysis, a flutter instability occurs for $u_{fl} \simeq 3$. The bifurcation diagram corresponding to this case is shown in Figure 7.1(a) for $u > u_{fl}$. At u = 3, a symmetric stable limit cycle about the origin develops after the Hopf bifurcation. For higher flow velocities, 4.6 < u < 5.881, the perfect shape of this limit cycle is modified into another type of periodic motion, which remains always symmetric about the origin but also develops around two symmetrical points, as shown in the phase plane portraits constructed in Figure 7.2(a) for u = 5.6. For 5.882 < u < 5.885, weakly chaotic motion develops around one pair of two symmetrical points, while period-two motion develops around another point (Figure 7.2(b) for u = 5.885); for 5.886 < u < 6.05, chaotic motion develops again around one pair of two symmetrical points, while period-one motion develops around another point (Figure 7.2(c) for u = 5.887). For 6.052 < u < 6.0538, a period-two motion develops around one pair of two points, while around the other pair of points the motion will remain period-one, as shown in Figure 7.2(d) for u = 6.0535.

Furthermore, for higher u, the motion of the system develops around one or the other point, depending on initial condition chosen. The motion of the system is chaotic for 6.05385 < u < 6.064, and is followed by period-bubbling motions as follows: period-eight for 6.0645 < u < 6.0649, period-four for 6.065 < u < 6.067, period-two for 6.0671 < u < 6.0771, and period-one for 6.0772 < u < 6.189, and finally the motion reduces to fixed points, for u > 6.19. The phase-plane portraits corresponding to the chaotic, period-two, period-one motion and fixed point of this system for u > 6.05385, are the same from a qualitative point of view as those presented in Figure 4.17(b,c,d,e).

The behaviour of the model may be summarized in the following words: period-1,2; chaos; period-bubbling or period-8,4,2; period-1; fixed points (Tables 7.2 and 7.3).

7.1.2 N = 2, h = 0.2 and f = 0.2

From linear analysis, a flutter instability is found to occur for $u_{fl} \simeq 2.5$.

The bifurcation diagram corresponding to this case has been shown in Figure 7.1(b) for $u > u_{fl}$. For u = 2.5, a symmetric stable limit cycle about the origin develops after the Hopf bifurcation, and remains symmetric for u < 4. Phase-plane portraits were shown in Figure 7.3 for u > 4. For 4.05 < u < 4.75, a periodic motion around one pair of two symmetrical points develops as in Figure 7.3(a) for u = 4.7; for 4.8 < u < 5.2, periodic motions develop around two or three pairs of symmetrical points as in Figure 7.3(b) for u = 5 and in Figure 7.3(c) for u = 5.2. By analyzing the time traces corresponding to these periodic motions, the dominant periods of motion are found to be: T = 1.41 for (a) u = 4.7; T = 1.7 for (b) u = 5, and T = 2.4 for (c) u = 5.2. As these periods are not related between them, that means no period-two, -three, -four,... -n motions exist for successive periodic motions for different u.

Finally, the motion of this system never becomes chaotic; it remains periodic.

The behaviour of the model is summarized in Tables 7.2 and 7.3 as: periodic; no chaos.

7.1.3 N = 2, h = 0.2 and f = 0.4

From a linear analysis, the flutter instability was found to occur in this case at $u_{fl} \simeq 2.38$.

The bifurcation diagram corresponding to this case is shown in Figure 7.1(c) for $u > u_{fl}$. This case has already been discussed in detail in Chapter 4, Section 4.4. For u = 2.38 a symmetric stable limit cycle develops after the Hopf bifurcation. For higher u, i.e. for u = 2.75, a symmetry-breaking pitchfork bifurcation occurs, through which the limit cycle loses its symmetry and becomes asymmetric. At u > 2.75, a cascade of period-doubling bifurcations occurs: at u = 2.952 (period-two), u = 2.9703 (period-four), and so on; this cascade eventually leads to chaotic motions at u > 2.975. In this range of u, periodic windows appear, such as period-three and period-five motions for u = 2.98 and u = 3, respectively.

The dynamical behaviour of this system is summarized in Tables 7.2 and 7.3 as: period-2,4,8, i.e. period-doubling followed by chaos.

7.1.4 N = 2, h = 0.2 and f = 0.6

The flutter instability in this case occurs at $u_{fl} \simeq 2.14$. The corresponding bifurcation diagram is shown in Figure 7.1(d) for $u > u_{fl}$. For u = 2.14, a symmetric stable limit cycle about the origin develops after the Hopf bifurcation for 2.14 < u < 2.31. For $u \simeq 2.31$ a symmetry-breaking pitchfork bifurcation occurs, and the limit cycle becomes asymmetric for 2.31 < u < 2.349. Then, period-doubling bifurcations occur for u = 2.35 - 2.359 (period-two motion), u = 2.36 - 2.3615 (period-four motion), u = 2.3616 - 2.362 (period-eight motion),

which lead to chaotic motions for 2.3621 < u < 2.48 for this system. The behaviour of this system may be summarized in Tables 7.2 and 7.3 as: Period-2,4,8 or period-doubling followed by chaos.

7.1.5 N = 2, h = 0.2 and f = 0.8

From a linear analysis it is found that a divergence instability occurs at $u_{div} \simeq 1.16$, the system is restabilized at $u \simeq 1.71$, and a flutter instability occurs at $u_{fl} \simeq 1.95$.

The bifurcation diagram corresponding to this case is shown in Figure 7.1(e) for $u > u_{fl}$. This case has already been discussed in detail in Chapter 4, Section 4.2 A stable symmetric limit cycle develops after the Hopf bifurcation (u = 1.95), and becomes asymmetric through a symmetry-breaking pitchfork bifurcation at $u \simeq 2.023$. Then, period-two motions occur for $2.04 \le u \le 2.049$, followed by period-one motion for $2.05 \le u \le 2.0525$. The motion finally becomes quasiperiodic and leads to chaos for u > 2.0526.

This dynamical behaviour is also summarized in Tables 7.2 and 7.3 as: period-1,2,1; quasiperiodic; chaos.

7.2 N=2, FIRST MODEL WITH CUBIC SPRING; h=0.5

7.2.1 N = 2, h = 0.5 and f = 0

From a linear analysis, a flutter instability occurs at $u_{fl} = 4.47$, and it stabilizes for u = 4.965.

The bifurcation diagram corresponding to this case is shown in Figure 7.4(a) for $u > u_{fl}$. The bifurcation diagram and the phase-plane portraits corresponding to this case have already been explained in Chapter 4, Section 4.3 and in Figures 4.15 to 4.17.

For u = 4.47 a stable symmetric limit cycle develops after the Hopf bifurcation. For higher u, i.e. for 7 < u < 8.2365 approximately, a periodic motion develops around a pair of symmetrical points. For 8.2366 < u < 8.498, another periodic motion develops around two pairs of symmetrical points, while for 8.499 < u < 8.982 this periodic motion develops around three pairs of symmetrical points. In Figure 4.16 the phase-plane portraits were constructed for (a) u = 5, (b) u = 7.25, (c) u = 8.4 and (d) u = 8.6.

For 8.983 < u < 9.0275 a chaotic motion followed by a period-four motion develops for 9.028 < u < 9.06 around four pairs of symmetrical points. Again, a chaotic motion develops for 9.062 < u < 9.076 around one pair of symmetrical points.

For higher flow velocities, the motion of the system will develop around only one of the two symmetrical points, depending on the initial conditions chosen, as follows: chaotic for 9.077 < u < 9.089, period-four for 9.09 < u < 9.093, period-two for 9.0931 < u < 9.109, period-one for 9.11 < u < 9.285 motion. Finally, for u > 9.286, the motion is reduced to fixed points. The phase-plane portraits showing the chaotic motion of the system followed by period-bubbling bifurcations were already explained in Chapter 4, Section 4.3, Figure 4.17 for (a) u = 9.075, (b) u = 9.085, (c) u = 9.1, (d) u = 9.25 and (e) u = 9.30.

The dynamics of this system may be summarized in Tables 7.2 and 7.3 as follows: period-1,2; chaos; period-8,4,2 or period-bubbling; period-1; fixed points.

7.2.2 N = 2, h = 0.5 and f = 0.2

The bifurcation diagram corresponding to this case is shown in Figure 7.4(b) for $u > u_{fl} = 3.82$. For $u \simeq 3.82$ a symmetric stable limit cycle develops after the Hopf bifurcation. For higher u, i.e. for $u \simeq 5$, a symmetry-breaking pitchfork bifurcation occurs, the limit cycle remains asymmetric for 5 < u < 5.3426, then

chaos develops through period-doubling; so that for 5.3427 < u < 5.3869 the motion of the system is period-two, for 5.387 < u < 5.39649 its motion is period-four, for 5.3965 < u < 5.3972 it is period-eight, and for higher u (for 5.4 < u < 7) the motion of the system becomes chaotic, except for a small range of flow velocities, 5.8 < u < 5.86, where periodic motion develops around two symmetrical points. The behaviour of this model is summarized in Tables 7.2 and 7.3 as: Period-2,4,8 (period-doubling), followed by chaos.

7.2.3 N = 2, h = 0.5 and f = 0.4

The bifurcation diagram corresponding to this case is shown in Figure 7.4(c) for $u > u_{fl} = 3.3$. For u > 3.3, i.e. $u \simeq 3.75$, a symmetry-breaking pitchfork bifurcation destroys the symmetry of the original limit cycle, and the limit cycle remains asymmetric for 3.75 < u < 3.9019. A period-two motion occurs for 3.902 < u < 3.9296, a period-four motion for 3.9297 < u < 3.9359, a period-eight motion for 3.936 < u < 3.937, followed by chaotic motions for higher u, 3.9375 < u < 4.15. A periodic window (period-five motion) may be observed in this range of u, i.e., for u = 4. For u = 4.2 to u = 4.242 a period-one motion develops around one pair of two symmetrical points. For higher u, i.e., 4.243 < u < 4.247, period-two motion occurs, which is followed by a period-four metion for u = 4.248 and, once again, by chaotic motion for u > 4.249.

The behaviour of this system is summarized in Tables 7.2 and 7.3 as: period-2,4,8 (period-doubling) followed by chaos, and again period-2,4,8 (period-doubling) followed by chaos.

7.2.4 N = 2, h = 0.5 and f = 0.6

The bifurcation diagram corresponding to this case is shown in Figure 7.4(d) for $u > u_{fl}$. For $u \ge u_{fl} \simeq 2.97$, a symmetric stable limit cycle develops after the Hopf

bifurcation. For higher u, i.e. $u \simeq 3.13$, a symmetry breaking pitchfork bifurcation occurs, and the limit cycle is asymmetric for 3.13 < u < 3.2032. Chaos arises through period-doubling as follows: period-two for 3.2033 < u < 3.2170, period-four for 3.2171 < u < 3.2201, period-eight for 3.2202 < u < 3.2208, chaotic for 3.221 < u < 3.31. The behaviour of this system is summarized in Tables 7.2 and 7.3 as: period-2,4,8 (period-doubling), followed by chaos.

7.2.5 N = 2, h = 0.5 and f = 0.8

This case has already been discussed in Chapter 4, Section 4.1. From a linear analysis it is found that a divergence instability occurs at $u_{div} = 1.69$; the system is then stabilized at u = 2.53, and a flutter instability occurs at $u_{fl} = 2.74$.

The bifurcation diagram corresponding to this case is shown in Figure 7.4(e) for $u > u_{fl}$. For $u \simeq 2.74$, there is a stable symmetric limit cycle after the Hopf bifurcation. The symmetry of the limit cycle is lost by a symmetry-breaking pitchfork bifurcation, which occurs at u = 2.795. A cascade of period-doubling bifurcations occurs: u = 2.8195 (period-two), u = 2.8235 (period-four), u = 2.8243 (period-eight). Finally, chaotic motions develop for this system for 2.8244 < u < 2.849.

The behaviour of this model may be summarized in Tables 7.2 and 7.3 as follows: period-2,4,8 (period-doubling), followed by chaos.

7.3 N=3, FIRST MODEL WITH CUBIC SPRING; h=0.2

7.3.1 N = 3, h = 0.2 and f = 0

The bifurcation diagram corresponding to this case is shown in Figure 7.5(a) for u > 3.2. For $u \ge u_{fl} \simeq 3.33$, a symmetric limit cycle around the origin develops

after the Hopf bifurcation. Furthermore, the limit cycle changes its shape and develops around one pair of two symmetrical points for 4.21 < u < 4.3679, as shown in Figure 7.6(a) for u = 4.3 (period T = 1.61), while for higher u, 4.368 < u < 4.374 (period T = 1), another periodic motion develops around two pairs of symmetrical points, and the phase plane portraits corresponding to u = 4.37 are presented in Figure 7.6(b).

The behaviour of this system is summarized in Tables 7.2 and 7.3 (pp. 99-101) as periodic motion with two dominant frequencies (odd subharmonics), their ratio being 1/3.

7.3.2 N = 3, h = 0.2 and f = 0.2

From a linear analysis, it is found that a divergence instability occurs at $u_{div} = 2.95$, followed by a flutter instability for $u_{fl} = 3.77$.

The bifurcation diagram corresponding to this case is shown in Figure 7.5(b) for u > 3.8. A pitchfork bifurcation occurs for u = 2.95, so that for 2.95 < u < 3.86 the origin is no longer a stable fixed point, but new stable fixed points on either side are generated. For u = 3.87, by linearizing the system in its vicinity, a flutter instability occurs, which gives birth to a limit cycle or to a period-one motion around the new fixed point; period-one motions persist for 3.87 < u < 3.926. For higher flow velocities, as for 3.927 < u < 3.931, another period-one motion develops (Figure 7.7(a) for u = 3.93, period T = 0.5), followed for 3.932 < u < 3.935 by a period-two motion, as shown in Figure 7.7(b) for u = 3.934, and for which T = 1, so that this period is twice that of the previous one, and by a period-one motion for 3.936 < u < 3.9405 (not shown); the system finally develops quasiperiodic motions for 3.941 < u < 3.945 (Figure 7.7(c) for u = 3.944), which lead to chaotic motions for u > 3.95, as shown in Figure 7.7(d) for u = 3.95.

The dynamics of this system may be summarized in Tables 7.2 and 7.3 as follows: period-1,2,1, followed by quasiperiodic and chaotic motions.

7.3.3 N = 3, h = 0.2 and f = 0.4

This case has already been discussed in Chapter 6, Section 6.4.1. From a linear analysis, a divergence instability occurs at $u_{div} = 2.82$, followed by a flutter instability for $u_{II} = 3.51$.

The bifurcation diagram corresponding to this case is shown in Figure 7.5(c) for $u > u_{div}$. The pitchfork bifurcation occurs at $u \simeq 2.8$. Thus, for 2.8 < u < 3.4, the origin is no longer a stable fixed point, but new stable fixed points on either side are generated. Then, for u = 3.4 to u = 3.5162, through a Hopf bifurcation, limit cycle motions develop around the new fixed points (found by linearizing the system in its vicinity), and for higher u, i.e., for 3.5163 < u < 3.5372, period-two motions occur, followed by period-four motions for 3.5373 < u < 3.5414 and by period-eight motions for 3.5415 < u < 3.5422. These period-two motions lead to chaotic motions for 3.5423 < u < 3.578. Then, a period-one motion symmetric about the origin occurs for 3.579 < u < 3.591, followed by quasiperiodic motions for 3.592 < u < 3.608 and then, again, chaotic motions for 3.609 < u < 3.66. The behaviour of this model may be summarized in Tables 7.2 and 7.3 as follows: fixed points; period-1; period-2,4,8, followed by chaotic motions.

7.3.4 N = 3, h = 0.2 and f = 0.6

The bifurcation diagram corresponding to this case has been shown in Figure 7.5(d) for $u > u_{div} = 2.75$. For $u \simeq 2.75$ a pitchfork bifurcation occurs, and new stable fixed points on either side are generated. By linearizing the system in its vicinity for u = 3.02, it is found that there exists a flutter instability, which gives rise to a symmetric limit cycle around one or the other fixed point. A cascade of

period-doubling bifurcations occurs for higher u, i.e. a period-two motion for 3.14 < u < 3.1632, followed by a period-four motion for 3.1633 < u < 3.1686, period-eight motion for 3.1687 < u < 3.1697, and by a period-sixteen motion for 3.1698 < u < 3.17. This cascade of period-doubling bifurcations finally leads to chaos for higher u, i.e., 3.18 < u < 3.29.

The behaviour of this system is summarized in Tables 7.2 and 7.3 as follows: fixed points; period-1; period-2,4,8 (period-doubling motions), followed by chaotic motions.

7.3.5 N = 3, h = 0.2 and f = 0.8

This case has already been analyzed in Chapter 6, Section 6.2.1. Linear analysis shows that a flutter instability occurs at $u_{fl} = 2.29$, followed by a divergence instability for $u_{div} = 2.7$.

The bifurcation diagram corresponding to this case is shown in Figure 7.5(e) for $u > u_{div}$. For $u \simeq 2.7$, a pitchfork bifurcation occurs, and for u > 2.7, the origin is no longer a stable fixed point, but new stable fixed points on either side are generated. By linearizing the system in the vicinity of the new stable fixed points, we find a flutter instability via a Hopf bifurcation for u = 2.725. The limit cycle at u = 2.725 is symmetric about the fixed point which gave it birth. For u > 2.74, a cascade of period-doubling bifurcations occurs: period-two, period-four and period-eight motion for u = 2.7641, 2.7760 and 2.782, respectively. These period-two motions finally lead to chaotic motions for higher u.

The behaviour of this system is summarized in Tables 7.2 and 7.3 as follows: fixed points; period-1; period-2,4,8 or period-doubling motions followed by chaotic ones.

7.4 N=3, FIRST MODEL WITH CUBIC SPRING; h=0.5

7.4.1 N = 3, h = 0.5 and f = 0

This case has already been analyzed in Chapter 6, Section 6.3.1. From a linear analysis, a flutter instability is found to occur at $u_{fl} \approx 4.9$.

The bifurcation diagram corresponding to this case is shown in Figure 7.8(a) for $u > u_{fl}$. For u = 4.9, a stable symmetric limit cycle around the origin develops after the Hopf bifurcation. The motion of the system becomes quasiperiodic for u = 6.231 to u = 6.2681 and chaotic for u > 6.2682.

The behaviour of this model is summarized in Tables 7.2 and 7.3 as follows: Period-one; quasiperiodic and chaotic motions.

7.4.2 N = 3, h = 0.5 and f = 0.2

From a linear analysis, a divergence instability occurs at u = 4.335, followed by a flutter instability at u = 5.193.

The bifurcation diagram corresponding to this case is shown in Figure 7.8(b). For $u \simeq 4.34$, a pitchfork bifurcation occurs, and then new stable fixed points on either side develop for u = 5.69. By linearizing the system around these fixed points, purely imaginary eigenvalues then arise for $u \simeq 5.695$, which correspond to the occurrence of a flutter instability in the linear analysis, or to a Hopf bifurcation in the nonlinear analysis. Chaotic motion occurs for 5.7 < u < 5.73 through type III intermittency, this route to chaos being the same as the one already discussed in Chapter 6, Section 6.5, for other parameters (those for Section 7.4.3).

The behaviour of this system is summarized in Tables 7.2 and 7.3 as: fixed points, followed by chaotic motions.

7.4.3 N = 3, h = 0.5 and f = 0.4

This route to chaos has already been discussed in Chapter 6, Section 6.5. Linear analysis predicts a divergence instability at u = 4.15, and then flutter at u = 4.71.

The bifurcation diagram for this case is shown in Figure 7.8(c). For $u \simeq 4.15$ a pitchfork bifurcation occurs, and new stable fixed points on either side develop as u is increased to u = 4.909. Chaotic motion occurs for u = 4.91 to u = 4.925 through type III intermittency.

The behaviour of this system is summarized in Tables 7.2 and 7.3 as: fixed points, followed by chaotic motions.

7.4.4 N = 3, h = 0.5 and f = 0.6

Linear analysis shows that a divergence instability occurs at u = 4.04, and is followed by a flutter instability at u = 4.31. The bifurcation diagram is shown in Figure 7.8(d). For u = 4.04, a pitchfork bifurcation occurs, and new stable fixed points on either side develop as u is increased to u = 4.4. No chaotic motion occurs, and eventually the amplitudes of motion become too large for the model to remain valid (no convergence in the solutions).

The behaviour in this case is summarized in Tables 7.2 and 7.3 as: fixed points; no chaotic motion.

7.4.5 N = 3, h = 0.5 and f = 0.8

This case has already been discussed in Chapter 6, Section 6.1.1. The bifurcation diagram for this case is shown in Figure 7.8(e). From a linear analysis, a divergence instability occurs at u = 1.71, followed by a flutter instability at u = 3.166, the system is restabilized at u = 3.896, and another divergence instability occurs at u = 3.97, followed again by a second flutter instability at u = 4.06.

For $u \simeq 3.9688$ a pitchfork bifurcation occurs, and for u > 3.9688, the origin is no longer a stable fixed point, but new stable fixed points on either side are generated. By linearizing the system in the vicinity of these new stable fixed points for increasing u, a flutter instability appears for $u \simeq 4.052$, through a Hopf bifurcation, giving rise to a symmetric limit cycle around the fixed point concerned. For 4.052 < u < 4.0882 the motion of the system remains always period—one. Chaos eventually arises, and the route to chaos in this case is through quasiperiodicity; the motion of the system is quasiperiodic for 4.0883 < u < 4.094 and finally chaotic for 4.095 < u < 4.0965.

The behaviour of this system is summarized in Tables 7.2 and 7.3 as: fixed points; quasiperiodic; followed by chaotic motions.

7.5 N=2, FIRST MODEL WITH TRILINEAR SPRING; h=0.5

7.5.1 N = 2, h = 0.5 and f = 0

The bifurcation diagram and the corresponding phase-plane portraits for this model are presented in Figure 7.9(a) and in Figure 7.10. A periodic motion of period T=2.5 develops for 4.47 < u < 4.69, which is shown in Figure 7.10(a) for u=4.5; then, for 4.7 < u < 4.86 another periodic motion develops around two symmetrical points, as shown in the phase plane portraits constructed in Figure 7.10(b) for u=4.8, for which the period T=3.15; and finally, a periodic motion develops around two or three pairs of symmetrical points, as shown in the phase-plane portraits in Figure 7.10(c,d) for (c) u=4.9 (of period T=3.95) and (d) u=4.96 (of period T=6.06), respectively. All the motions mentioned above are periodic with odd subharmonics. For u>4.97 the motion of the system is reduced to fixed points.

By comparing this model with the one with cubic spring representation, it may be concluded that the motions of both models develop around symmetrical points (with respect to the origin), and reduce finally to fixed points.

7.5.2 N = 2, h = 0.5 and f = 0.4

The bifurcation diagram for this model is presented in Figure 7.9(b), and the route to chaos is presented through period-doubling bifurcations. For 3.33 < u < 3.34, a limit cycle appears after the Hopf bifurcation, which occurs at u = 3.33. For $u \simeq 3.34$ the limit cycle becomes asymmetric through a symmetry-breaking pitchfork bifurcation. For higher u, a cascade of period-doubling motions occurs: period-two for 3.36 < u < 3.369, period-four for 3.37 < u < 3.3711, and period-eight motions for 3.3712 < u < 3.3714, which lead to chaotic motions for u > 3.3715.

For this model, as for the one with cubic spring representation (Section 7.2.3), period-doubling bifurcations are followed by chaotic motions.

7.5.3 N = 2, h = 0.5 and f = 0.8

Chaotic motions occur in this model through period-doubling bifurcations, as seen in Figure 7.9(c). For $u \ge u_{fl} \simeq 2.74$, a symmetric stable limit cycle develops after the Hopf bifurcation. For higher u, i.e. $u \simeq 2.744$ a symmetry-breaking pitchfork bifurcation occurs, and the limit cycle is asymmetric for 2.744 < u < 2.747.

For higher u, a cascade of period-doubling motions occurs: for 2.748 < u < 2.7501 period-two, for 2.7502 < u < 2.7503 period-four, and for 2.7504 < u < 2.7507 period-eight motions, followed for u > 2.751 by chaotic motions.

Again for this model, as for the one with cubic spring representation, the route to chaos is through period-doubling bifurcations.

7.6 COMMENTS

The behaviour for the N=2 and N=3 systems according to the first model, with a cubic or a trilinear spring representation, has been studied in this chapter.

Considering first the case of N=2, as seen in the bifurcation diagrams shown in Figures 7.1 and 7.4, when the end-form coefficient f increases, u_{fl} decreases, which eventually results in chaotic motions occurring at lower u as f increases. It is also seen that, as h increases, the critical flow velocity at which flutter occurs, u_{fl} , increases; this results in chaotic motions occurring at higher flow velocities as the diameter of the external cylinder increases. By varying f, the behaviour of the first model with N=2 but for two different h was found to be qualitatively the same for f=0, f=0.4 and f=0.6, while for f=0.2 and f=0.8 it was found different.

As it has already been concluded in Section 7.5, the behaviour for the N=2 first model with trilinear spring representation (Figure 7.9) is qualitatively the same as for the model with cubic spring representation (Figure 7.4). Three values for f were considered: for f=0, the motion of the both models develops around symmetrical points, while for f=0.4 and f=0.8, chaotic motions arise through period-doubling bifurcations.

The bifurcation diagrams in Figures 7.5 and 7.8 obtained for the N=3 first model, for two different values of h, display considerably different behaviour (as compared to the N=2 model) for the same end-form coefficients f. Nevertheless, the observed behaviour in most cases has been observed for the N=2 system, but with different system parameters. One main difference (see Table 7.2) is that, for N=3, a divergence (and hence the existence of fixed points) precedes flutter (emanating from instability of these fixed points). Unfortunately, the critical flow velocity u_{cr} for flutter could not be pin-pointed, because the interval in u between fixed point and chaotic behaviour is too small.

For higher u, however, in the case of h=0.2 and for $f\geq 0.4$, the dynamics for N=2 and 3 is not too different. Another difference overall, in this case for h=0.5, is the preponderance of period-doubling leading to chaos for N=2, while this is associated with intermittence for N=3.

Table 7.1: Explanation of symbols

C	E14:		
Symbols	Explanation		
FP	Fixed points		
P	Periodic motions		
P-1	Period-one motion		
P-2	Period-two motion		
P-1,2	Period-one and -two motion		
P-2,4,8	Period-doubling motions		
P-8,4,2	Period-bubbling motions		
PB	Period-bubbling motions		
PD	Period-doubling motions		
QP	Quasiperiodic motions		
СН	Chaotic motions		
NOCH	No chaotic motion		

Table 7.2: Routes to chaos for N=2 and N=3 systems

	h = 0.2		h = 0.5	
f	N = 2	N = 3	N = 2	N = 3
0	Period-1,2	Periodic	Period-1,2	Period-1
	Chaos	No chaos	Chaos	Quasiperiodic
	Period-8,4,2		Period-8,4,2	Chaos
	Fixed points		Fixed points	
0.2	Periodic	Period-1,2,1	Period-2,4,8	Fixed points
	No chaos	Quasiperiodic	Chaos	Chaos
		Chaos		
0.4	Period-2,4,8	Fixed points	Period-2,4,8	Fixed points
	Chaos	Period-1	Chaos	Chaos
		Period-2,4,8	Period-2,4,8	
		Chaos	Chaos	
0.6	Period-2,4,8	Fixed points	Period-2,4,8	Fixed points
	Chaos	Period-1	Chaos	No chaos
		Period-2,4,8		
		Chaos		
0.8	Period-1,2,1	Fixed points	Period-2,4,8	Fixed points
	Quasiperiodic	Period-1	Chaos	Quasiperiodic
	Chaos	Period-2,4,8		Chaos
		Chaos		

Table 7.3: Comparison between N=2 and N=3 systems

	h = 0.2		h = 0.5	
f	N = 2	N = 3	N = 2	N = 3
0	P-1,2;CH	P	P-1,2;CH	P-1;QP
	PB;P-1;FP	NOCH	PB;P-1;FP	СН
0.2	P	P-1,2,1	PD	FP
	NOCH	QP;CH	СН	СН
0.4	PD	FP;P-1	PD;CH	FP
	СН	PD;CH	PD;CH	СН
0.6	PD	FP;P-1	PD	FP
	СН	PD;CH	СН	NOCH
0.8	P-1,2,1	FP;P-1	PD	FP;QP
	QP;CH	PD;CH	СН	СН

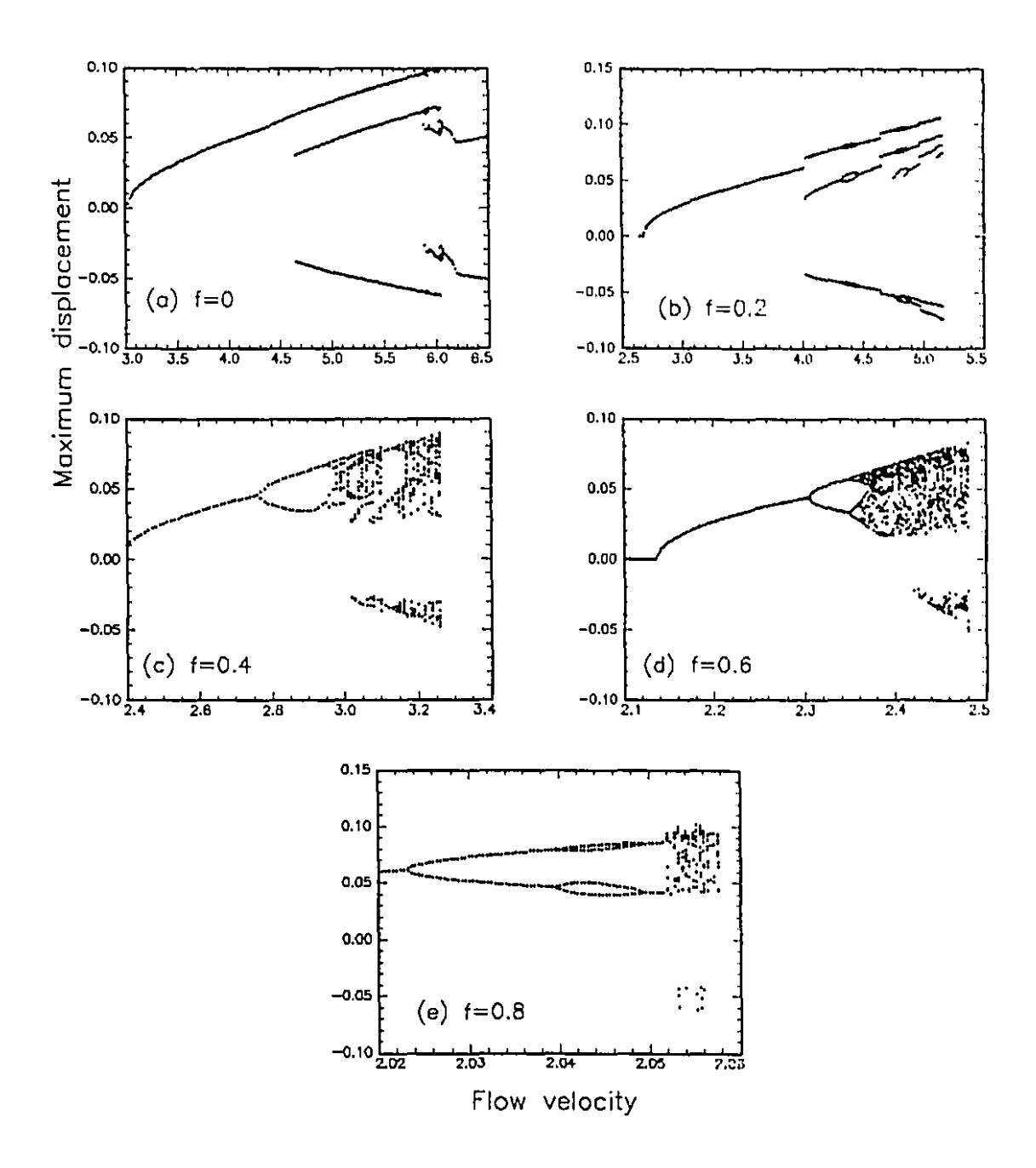


Figure 7.1. Bifurcation diagrams for the first model with cubic spring, for N=2 and h=0.2: (a) f=0, (b) f=0.2, (c) f=0.4, (d) f=0.6 and (e) f=0.8.

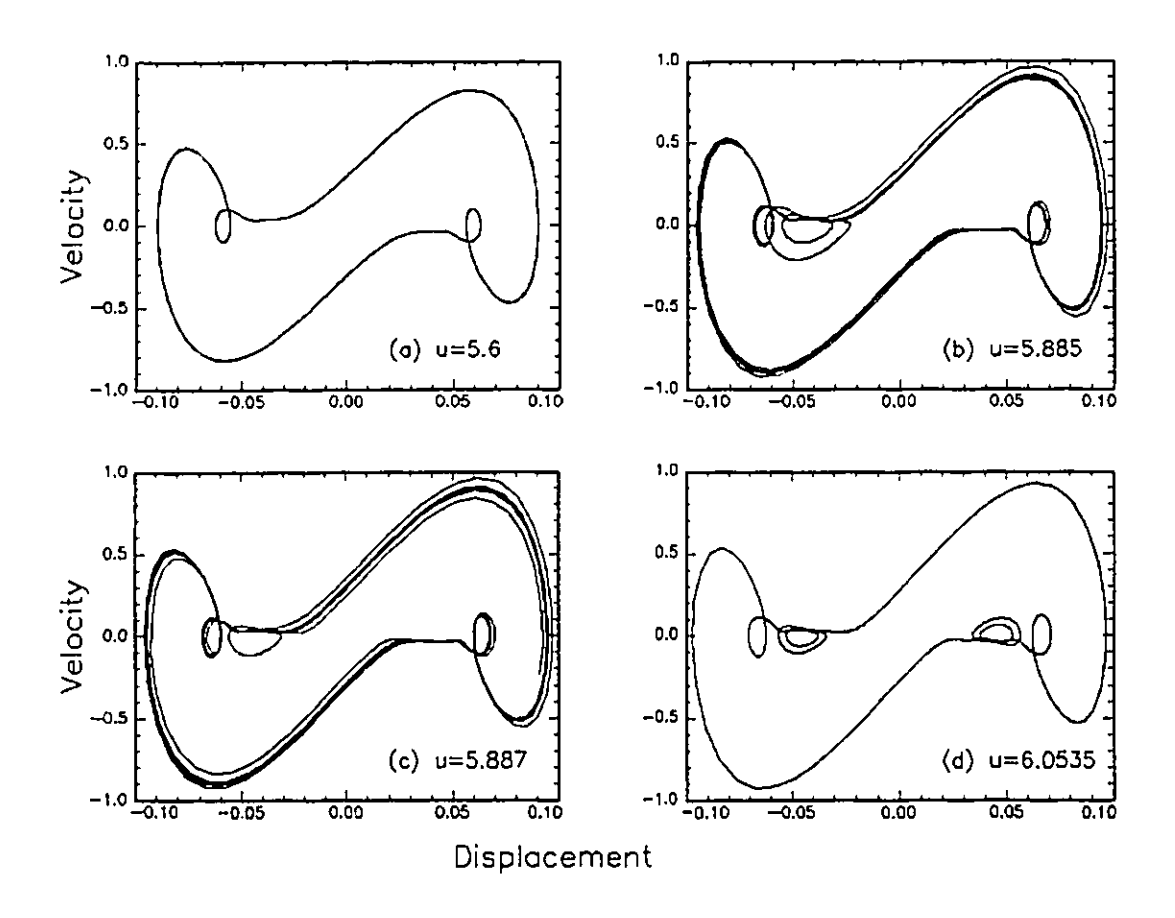


Figure 7.2. Phase-plane portraits of $\dot{\phi}_1(\tau)$ versus $\phi_1(\tau)$ at (a) u=5.6, (b) u=5.885, (c) u=5.887, (d) u=6.0535 for the first model with cubic spring: N=2, h=0.2 and f=0.

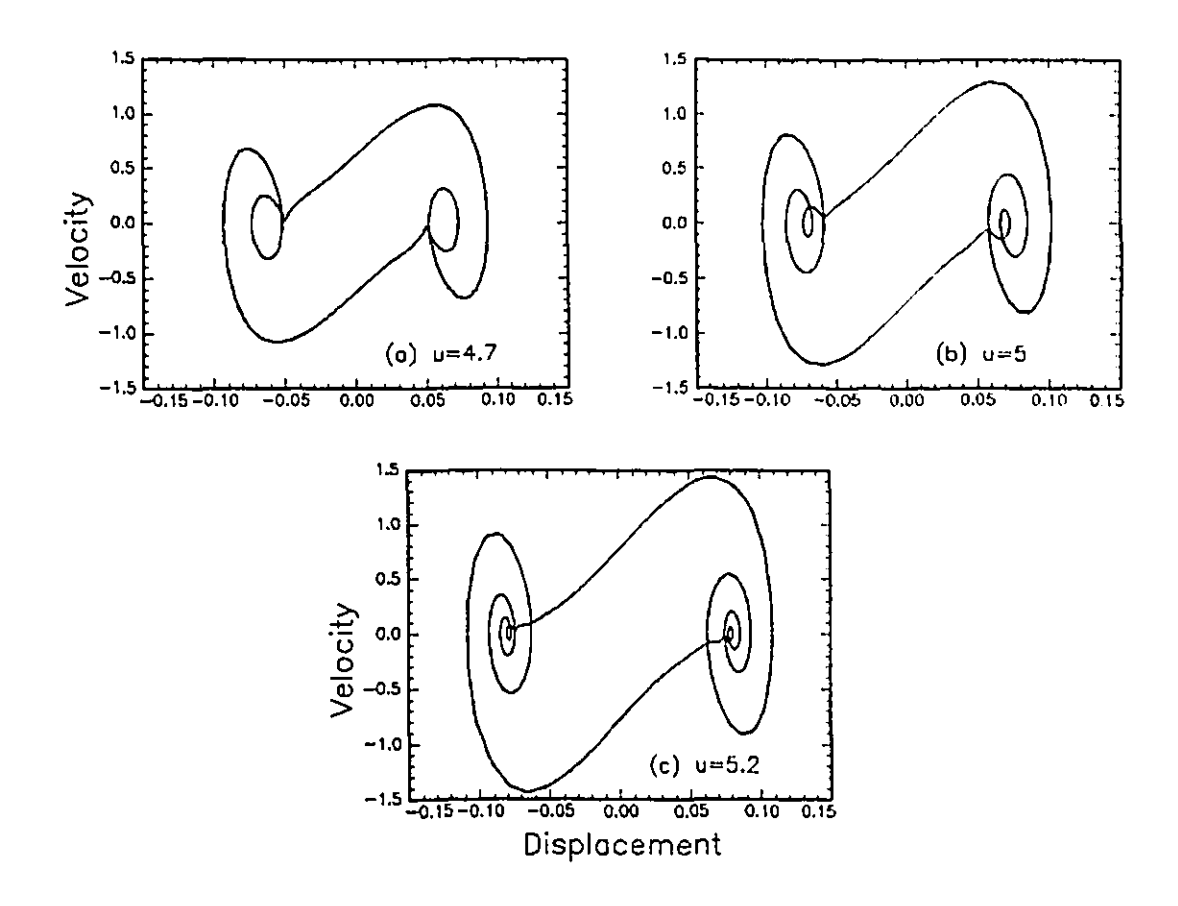


Figure 7.3. Phase-plane portraits of $\dot{\phi}_1(\tau)$ versus $\phi_1(\tau)$ at (a) u=4.7, (b) u=5, (c) u=5.2 for the first model with cubic spring: N=2, h=0.2 and f=0.2.

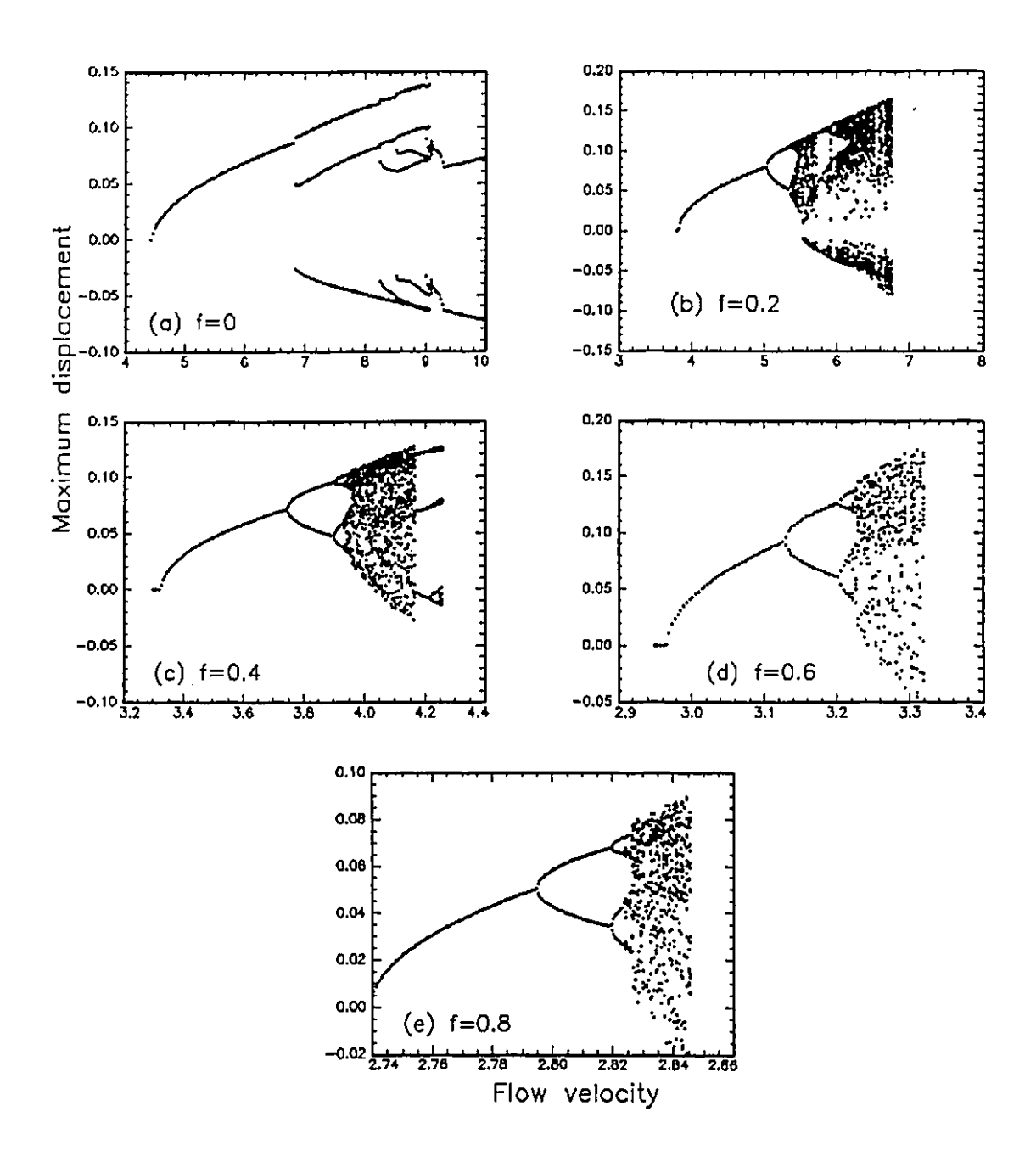


Figure 7.4. Bifurcation diagrams for the first model with cubic spring, for N=2 and h=0.5: (a) f=0, (b) f=0.2, (c) f=0.4, (d) f=0.6 and (e) f=0.8.

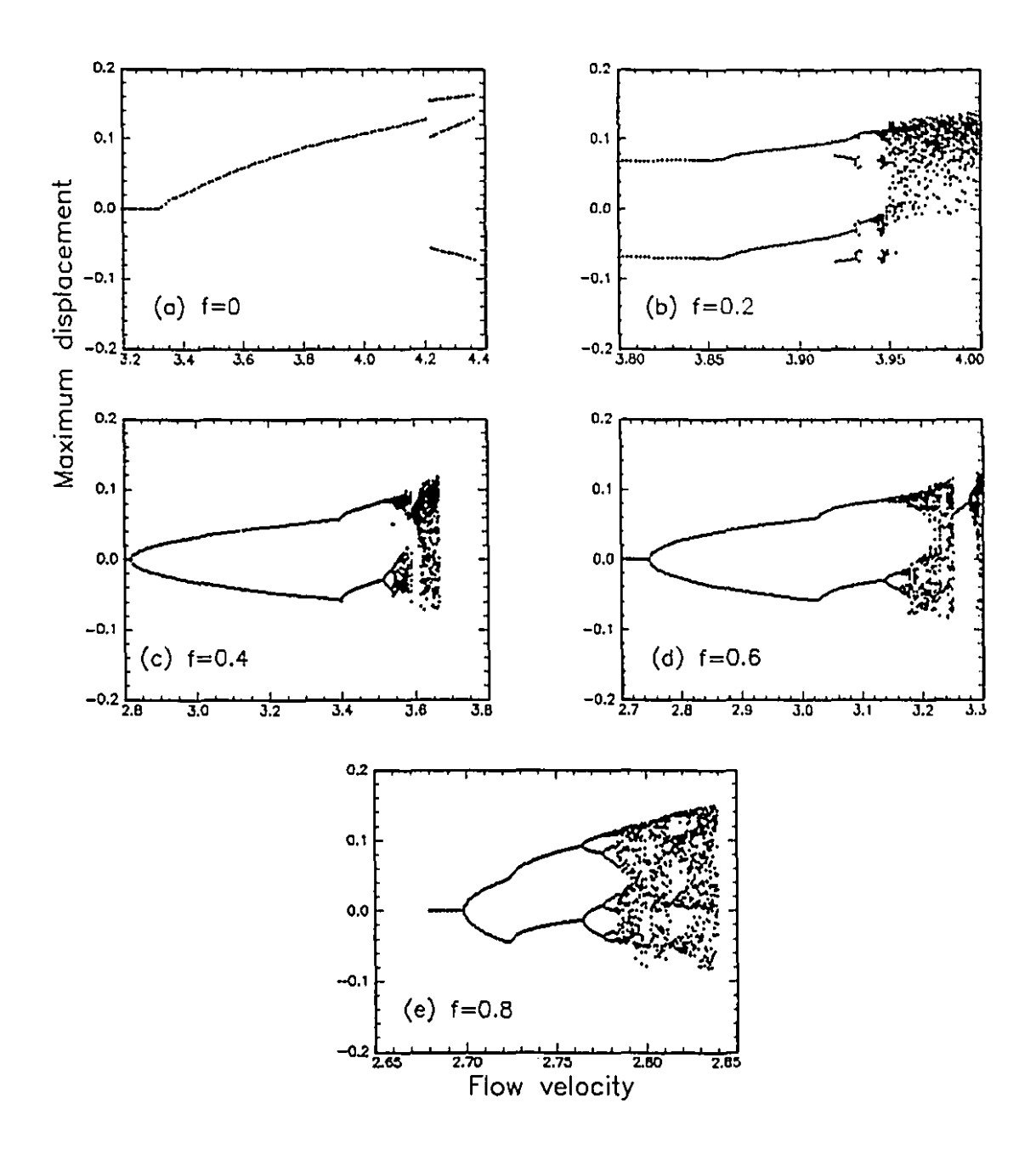


Figure 7.5. Bifurcation diagrams for the first model with cubic spring model, for N=3 and h=0.2: (a) f=0, (b) f=0.2, (c) f=0.4, (d) f=0.6 and (e) f=0.8.

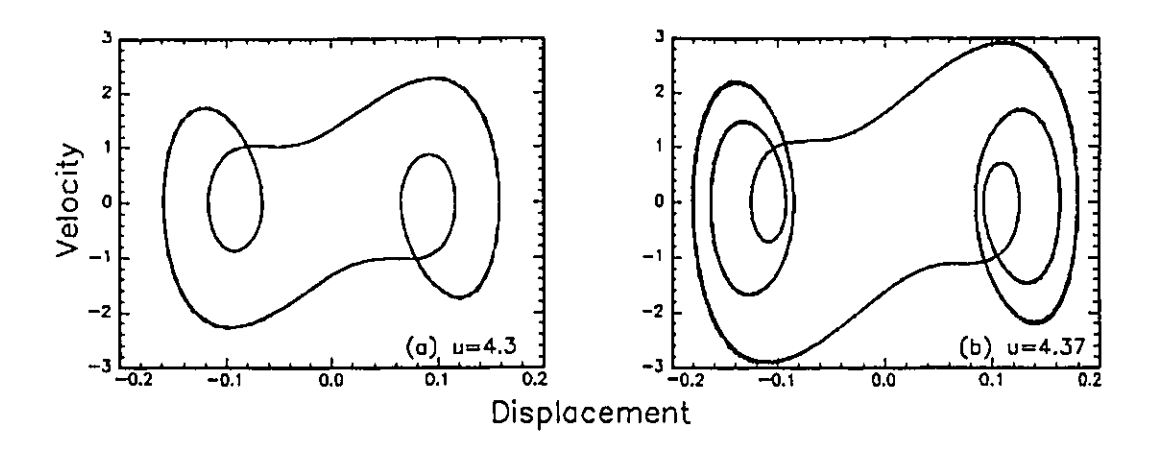


Figure 7.6. Phase-plane portraits of $\dot{\phi}_1(\tau)$ versus $\phi_1(\tau)$ at (a) u=4.3 and (b) u=4.37 for the first model with cubic spring: N=3, h=0.2 and f=0.

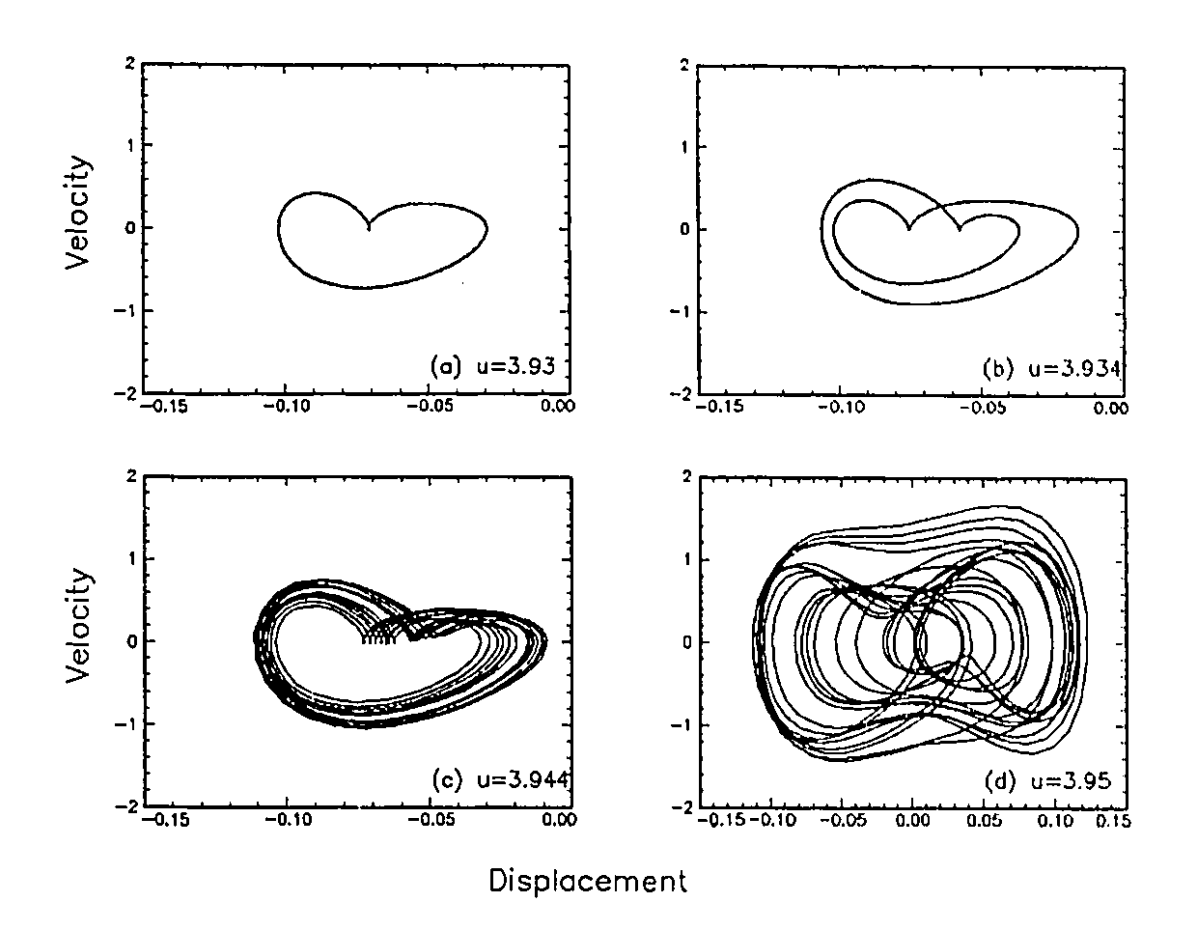


Figure 7.7. Phase-plane portraits of $\dot{\phi}_1(\tau)$ versus $\phi_1(\tau)$ at (a) u=3.93, (b) u=3.934, (c) u=3.944 and (d) u=3.95 for the first model with cubic spring: N=3, h=0.2 and f=0.2.

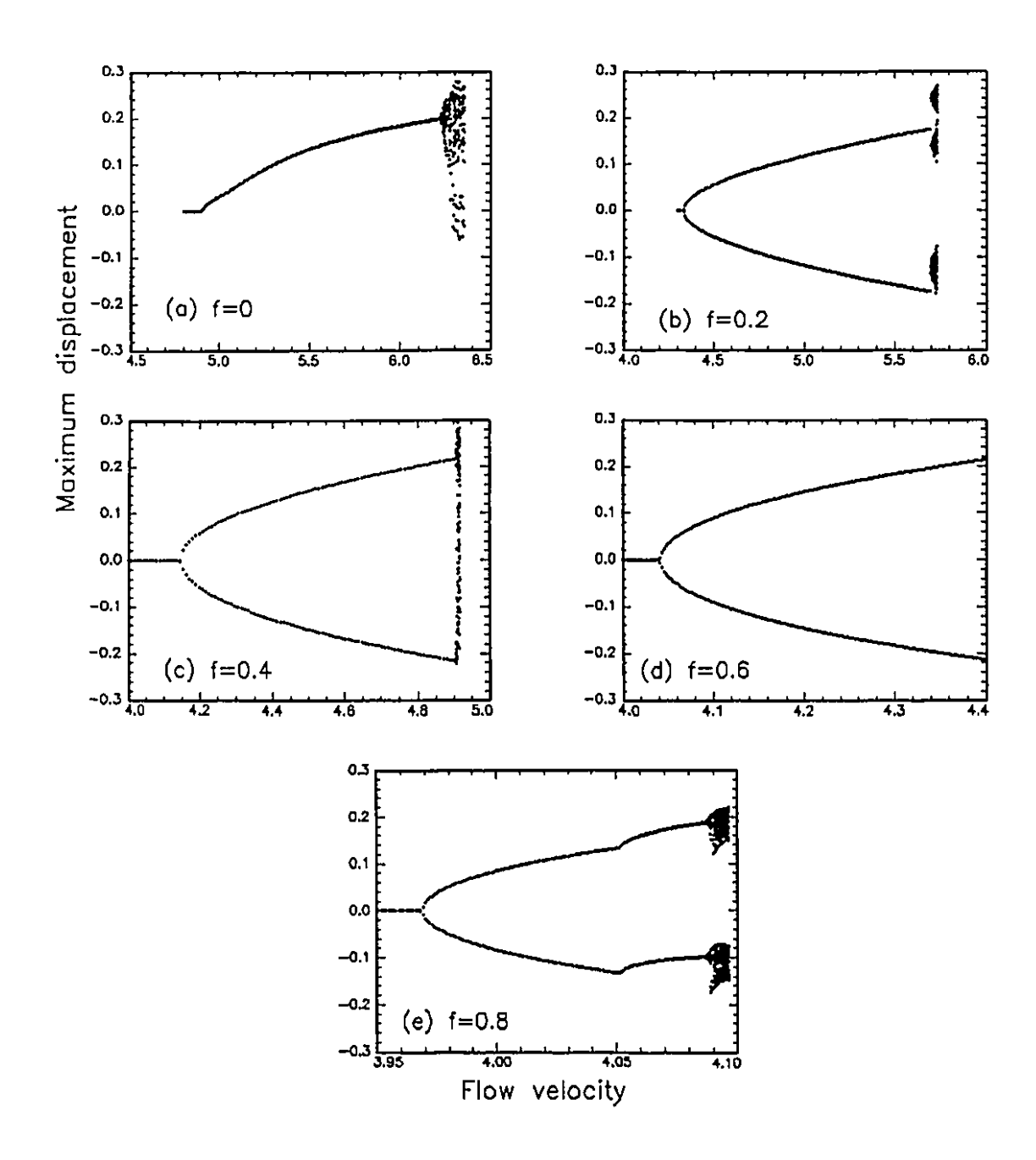


Figure 7.8. Bifurcation diagrams for the first model with cubic spring, for N=3 and h=0.5: (a) f=0, (b) f=0.2, (c) f=0.4, (d) f=0.6 and (e) f=0.8.

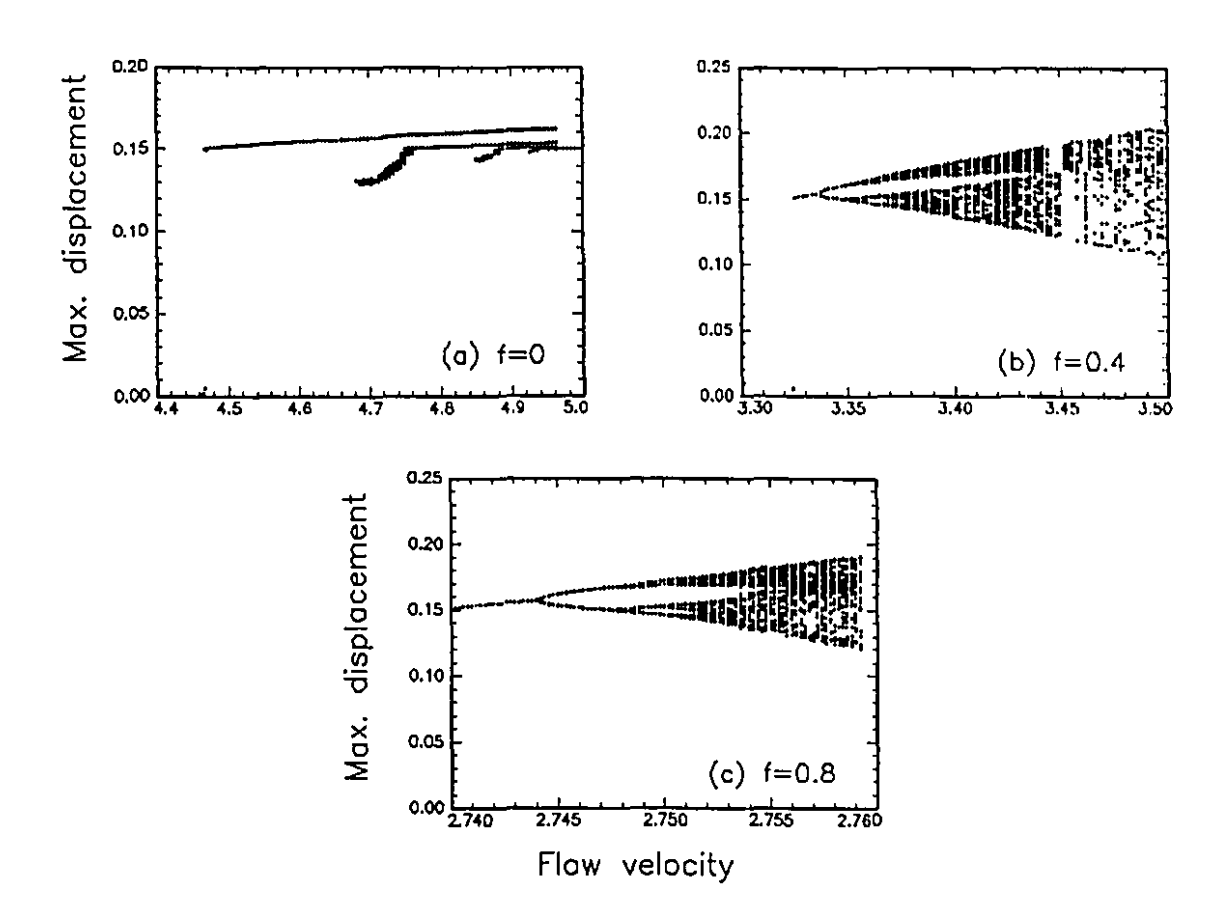


Figure 7.9. Bifurcation diagrams for the first model with trilinear spring, for N=2 and h=0.5: (a) f=0, (b) f=0.4 and (c) f=0.8.

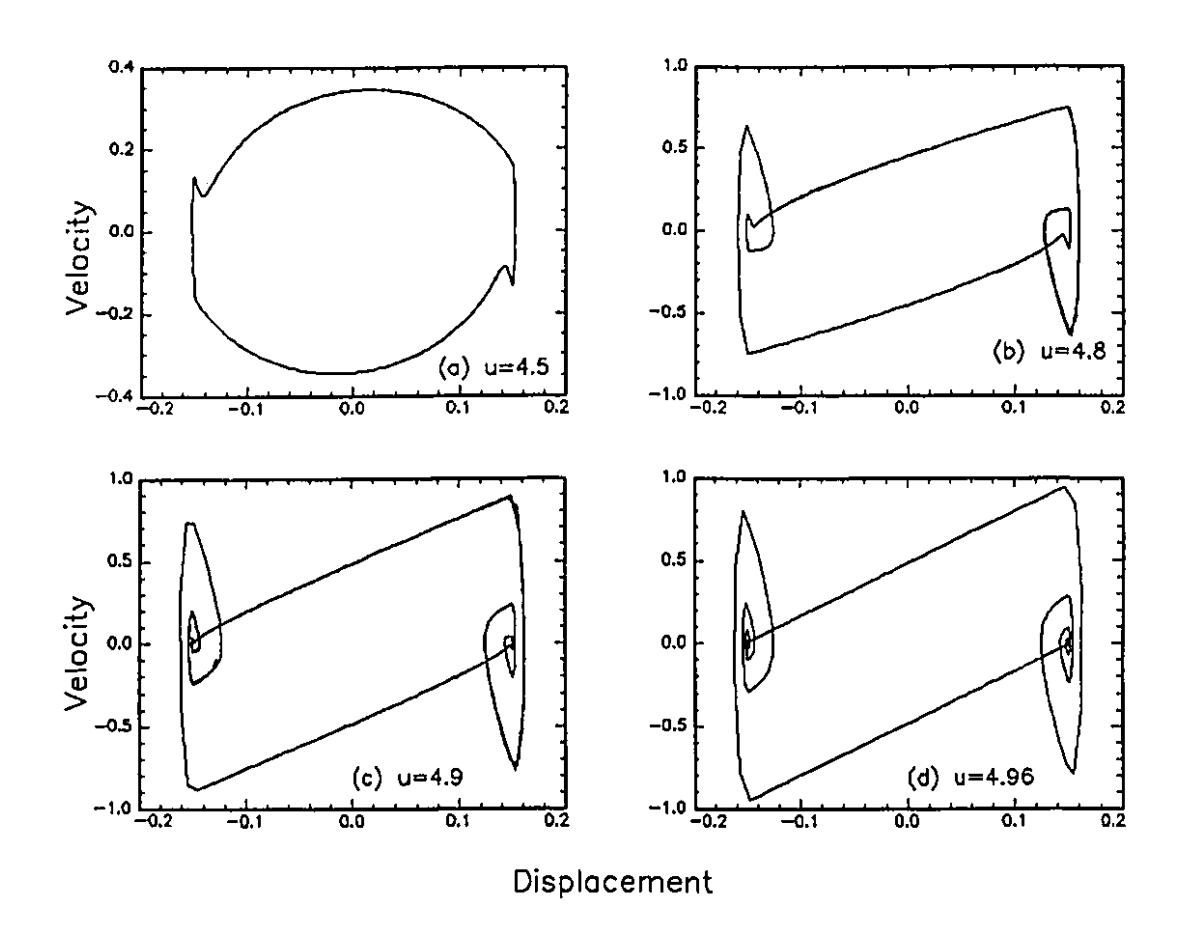


Figure 7.10. Phase-plane portraits of $\dot{\phi}_1(\tau)$ versus $\phi_1(\tau)$ at (a) u=4.5, (b) u=4.8, (c) u=4.9 and (d) u=4.96 for the first model with trilinear spring: N=2, h=0.5 and f=0.

Chapter 8

THE SECOND THEORETICAL MODEL

8.1 ASSUMPTIONS MADE

As it has already been mentioned in Chapter 1, Section 1.3, a second model of the system of cylinders subject to a confined axial flow has been developed; it is described in this chapter. The model is essentially the same as that described in Section 2.1, with some differences in the assumptions; however, some of the system nonlinearities have been taken into account.

While the dynamics of the system when no impact occurs with the confining pipe were described by a linearized set of equations in the first model (Section 2.1, assumption (d)), in the second model, the nonlinearities in the equations of motion are taken into account approximately, mainly via Taylor expansions of the trigonometric functions of the state variables; nonlinear terms are retained up to $O(\epsilon^3)$. Assumptions (a), (b) and (c) of Section 2.1 remain essentially the same. In both models, impacting with the external pipe is modelled by a trilinear or a cubic spring, presumed to exist between the pipe and the element of the articulated system contacting it; most of the calculations will be done with a cubic-spring at

the end of the first articulation, for analytical convenience.

We now proceed to the calculation of the same terms as those considered in Chapter 2 that enter in Lagrange's equations.

8.2 ENERGIES OF THE SYSTEM

8.2.1 Kinetic and potential energies of the structure, T_s and V_s

In this section, the kinetic and potential energies of the structure, of the articulated system itself, are determined in terms of generalized coordinates, which are the angles of deformation, ϕ_j (Figure 2.1(b)).

The system of coordinates (x, y) and the corresponding system of unit vectors (i, j) have already been defined in Figure 2.1.

The local coordinate ξ is defined along the length of each cylinder segment, $0 \le \xi \le l_j$ (Figure 2.1). In order to calculate the velocity vector at point ξ of the jth cylinder, $\mathbf{v}_j(\xi)$, the displacement vectors in the \mathbf{x} and \mathbf{y} directions are calculated, as shown in Figure 2.1. The displacement vectors $\mathbf{x}_j(\xi)$ and $\mathbf{y}_j(\xi)$ at point ξ of the jth cylinder are

$$\mathbf{x}_{j}(\xi) = -\left(\sum_{q=1}^{j-1} l_{q} \cos \phi_{q} + \xi \cos \phi_{j}\right) \mathbf{i}, \qquad (8.1)$$

$$\mathbf{y}_{j}(\xi) = \left(\sum_{q=1}^{j-1} l_{q} \sin \phi_{q} + \xi \sin \phi_{j}\right) \mathbf{j}.$$
 (8.2)

Thus, $\mathbf{v}_{j}(\xi)$ is given by

$$\mathbf{v}_{j}(\xi) = \frac{d}{dt} \left[-(\sum_{q=1}^{j-1} l_{q} \cos \phi_{q} + \xi \cos \phi_{j}) \mathbf{i} + (\sum_{q=1}^{j-1} l_{q} \sin \phi_{q} + \xi \sin \phi_{j}) \mathbf{j} \right], \quad (8.3)$$

which, after differentiation, may be written as

$$\mathbf{v}_{j}(\xi) = (\sum_{q=1}^{j-1} l_{q} \sin \phi_{q} \,\dot{\phi}_{q} + \xi \,\sin \phi_{j} \dot{\phi}_{j})\mathbf{i} + (\sum_{q=1}^{j-1} l_{q} \cos \phi_{q} \dot{\phi}_{q} + \xi \cos \phi_{j} \dot{\phi}_{j})\mathbf{j} \,. \tag{8.4}$$

Hence, the kinetic energy of the jth cylinder is

$$T_{sj} = \frac{1}{2} \int_0^{l_j} m_j \left[\left(\sum_{q=1}^{j-1} l_q \sin \phi_q \dot{\phi}_q + \xi \sin \phi_j \dot{\phi}_j \right)^2 + \left(\sum_{q=1}^{j-1} l_q \cos \phi_q \dot{\phi}_q + \xi \cos \phi_j \dot{\phi}_j \right)^2 \right] d\xi,$$
(8.5)

where m_j is the mass per unit length of the jth cylinder. The total kinetic energy of the structure, T_s , neglecting the small ogival part of the last cylinder, is

$$T_s = \frac{1}{2} \sum_{j=1}^{N} \int_0^{l_j} m_j \left[\left(\sum_{q=1}^{j-1} l_q \sin \phi_q \dot{\phi}_q + \xi \sin \phi_j \dot{\phi}_j \right)^2 + \left(\sum_{q=1}^{j-1} l_q \cos \phi_q \dot{\phi}_q + \xi \cos \phi_j \dot{\phi}_j \right)^2 \right] d\xi.$$
(8.6)

The potential energy is composed of a gravity component and a component due to strain of the intercylinder connecting springs. It may be written in the following form:

$$V_s = \sum_{j=1}^{N} \int_0^{l_j} m_j g \left(\sum_{q=1}^{j-1} l_q (1 - \cos \phi_q) + \xi (1 - \cos \phi_j) \right) d\xi + \frac{1}{2} \sum_{j=1}^{N} k_j (\phi_j - \phi_{j-1})^2.$$
 (8.7)

8.2.2 Kinetic energy of the fluid, T_f

In order to calculate the normal flow velocity at a point ξ of the jth cylinder, we shall consider again Figures 2.1 and 2.2 with their corresponding systems of unit vectors (i,j) and (i_1,j_1) , where i_1 has the same direction as the structure and the j_1 th direction is normal to it.

The flow velocity of the jth cylinder is due to motion of the structure and to the flow in the confining pipe, and its components in the i_1 and j_1 directions will be calculated next.

The relative fluid-body velocity component in a direction normal to the element (i.e., in the j_1 direction) at a point ξ of the jth cylinder, is defined as $v_{f,1}(\xi)$ and is given by

$$v_{fj1}(\xi) = -\frac{dx_j(\xi)}{dt}\sin\phi_j + \frac{dy_j(\xi)}{dt}\cos\phi_j + U\sin\phi_j, \qquad (8.8)$$

where the displacements of the jth cylinder in the system, $x_j(\xi)$ and $y_j(\xi)$, are

$$x_j(\xi) = -\left(\sum_{q=1}^{j-1} l_q \cos \phi_q + \xi \cos \phi_j\right) , \qquad (8.9)$$

$$y_j(\xi) = \left(\sum_{q=1}^{j-1} l_q \sin \phi_q + \xi \sin \phi_j\right). \tag{8.10}$$

The derivatives $dx_j(\xi)/dt$ and $dy_j(\xi)/dt$ have already been calculated to obtain equation (8.4); by replacing these results into equation (8.8), one obtains

$$v_{fj1}(\xi) = \sum_{q=1}^{j-1} l_q \cos(\phi_q - \phi_j) \dot{\phi}_q + \xi \dot{\phi}_j + U \sin \phi_j.$$
 (8.11)

The fluid velocity component in the same direction as the element, that is in the i₁th direction, is

$$v_{fi1}(\xi) = U\cos\phi_j. \tag{8.12}$$

Hence, the total velocity of the fluid at point ξ of the jth cylinder, $\mathbf{v}_{fj}(\xi)$, is composed of two components in the \mathbf{i}_1 and \mathbf{j}_1 directions and may be written as

$$\mathbf{v}_{fj}(\xi) = U \cos \phi_j \mathbf{i}_1 + \left[\sum_{q=1}^{j-1} l_q \cos(\phi_q - \phi_j) \dot{\phi}_q + \xi \dot{\phi}_j + U \sin \phi_j \right] \mathbf{j}_1.$$
 (8.13)

Therefore, the kinetic energy of the fluid at point ξ of the jth cylinder, T_{fj} , is

$$T_{fj} = \frac{1}{2} \int_0^{l_j} (U \cos \phi_j)^2 M_{i1} d\xi + \frac{1}{2} \int_0^{l_j} \left[\sum_{q=1}^{j-1} l_q \cos(\phi_q - \phi_j) \dot{\phi}_q + \xi \dot{\phi}_j + U \sin \phi_j \right]^2 M_{j1} d\xi$$
(8.14)

where M_{i1} and M_{j1} are the corresponding virtual or added masses of the fluid in the i_1 and j_1 directions. As M_{i1} is much smaller than M_{j1} , usually of $O(\epsilon^2)$, then even if v_f in direction i_1 is greater than v_f in direction j_1 , i.e., $v_{fi1} > v_{fj1}$, since they are usually of the same order, $\frac{1}{2}M_{i1}v_{fi1}^2$ still remains much smaller than $\frac{1}{2}M_{j1}v_{fj1}^2$, possibly of order $O(\epsilon^2)$ or smaller. Clearly, for very slender cylinders it can be of much smaller order. Hence, although the first term in (8.14) could have been retained, for convenience here it will be neglected. M_{j1} is equal to $\chi \rho A$ for confined flow, where ρ is the fluid density, A the cylinder cross-sectional area, and χ is given by

$$\chi = \left[(1+h)^2 + 1 \right] / \left[(1+h)^2 - 1 \right] , \tag{8.15}$$

in which $h = D_h/D$; D is the cylinder diameter, and $D_h = D_{ch} - D$ is the hydraulic diameter, D_{ch} being the internal diameter of the external pipe (Figure 2.1).

Therefore, the total fluid kinetic energy becomes

$$T_f = \frac{1}{2} \chi \rho A \int_0^{l_j} \left[\sum_{q=1}^{j-1} l_q \cos(\phi_q - \phi_j) \dot{\phi}_q + \xi \dot{\phi}_j + U \sin \phi_j \right]^2 d\xi . \tag{8.16}$$

8.3 THE FLUID-DYNAMIC FORCES

Similarly to Chapter 2, the fluid forces will be determined in several parts: inviscid unsteady forces, hydrostatic forces and viscous forces. The formulation of these forces will be presented in the following subsections.

8.3.1 Nonconservative inviscid force, F_{nc}

If both ends of the articulated system were supported, expression (8.16) would represent the whole of the inviscid component of the fluid-dynamic forces. However, as discussed in Section 2.3, the cantilevered system is generally nonconservative, and hence there will generally be work done at the free end of the system by a nonconservative inviscid force, F_{nc} (cf. Benjamin, 1961; Païdoussis, 1966b). This force is associated with the noncylindrical, ogival end of the last cylinder, which may be approximated by a paraboloid of the form $y^2 = 4aw$. In our system, a is the focal distance of the downstream end and w is its total length. For an ideally streamlined end, $f \to 1$, and for a blunt end, $f \to 0$, so that different values for a, w and f can be obtained as function of the free end shape. These values with the corresponding free-end shapes are presented in Appendix F.

 F_{nc} , acting at the end of the jth last cylinder, will be

$$F_{nc} = \rho(1-f)\chi \int_0^w \left[\frac{\partial}{\partial t} + U \frac{\partial}{\partial x} \right] \left[\sum_{q=1}^{j-1} l_q \cos(\phi_q - \phi_j) \dot{\phi}_q + l_j \dot{\phi}_j + U \sin \phi_j \right] 4\pi a(w-\xi) d\xi$$
(8.17)

As $x = \xi \cos \phi_j$, then, in equation (8.17) we replace $(\partial/\partial x)$ by $(\partial/\partial \xi)(1/\cos \phi_j)$. By Taylor series, $(\cos \phi_j)^{-1} \simeq \left(1 - \frac{1}{2}\phi_2^2\right)^{-1} \simeq 1 + \frac{\phi_2^2}{2}$. Thus, the final expression for F_{nc} has been obtained by integrating with respect to ξ and by Taylor series expansion, namely

$$F_{nc} = \chi(1-f)M\frac{w}{2}l\ddot{\phi}_{1}\left(1-\frac{(\phi_{2}-\phi_{1})^{2}}{2}\right) - \chi MU(1-f)l\dot{\phi}_{1}\left(1+\phi_{1}\phi_{2}-\frac{\phi_{1}^{2}}{2}\right)$$

$$\chi(1-f)M\frac{w}{2}l\ddot{\phi}_{1}\left(\phi_{1}\dot{\phi}_{1}\dot{\phi}_{2}-\phi_{2}\dot{\phi}_{1}\dot{\phi}_{2}-\phi_{1}\dot{\phi}_{1}^{2}+\phi_{2}\dot{\phi}_{1}^{2}\right) +$$

$$\chi(1-f)M\frac{w}{2}l\ddot{\phi}_{1}\frac{l}{2}\ddot{\phi}_{2} + \chi(1-f)M\frac{w}{2}l\ddot{\phi}_{1}U\dot{\phi}_{2}\left(1-\frac{\phi_{2}^{2}}{2}\right) -$$

$$+\chi MU(1-f)\frac{l}{2}\left(\dot{\phi}_{2}+\dot{\phi}_{2}\frac{\phi_{2}^{2}}{2}\right) + \chi MU^{2}(1-f)\left(\phi_{2}+\frac{\phi_{2}^{3}}{3}\right). \tag{8.18}$$

8.3.2 The hydrostatic pressure forces, F_{px} and F_{py}

.

The hydrostatic pressure forces, F_{px} and F_{py} , were already determined in chapter 2.3.2 for the first model. For the second model, we may use the same formulae as in Chapter 2.3.2, so that $(F_{px})_j$ and $(F_{py})_j$ will be the same as those given by equation (2.15), Chapter 2.3.2:

$$(F_{px})_j = 0, \quad (F_{py})_j = A \frac{dp}{dx} \tan \phi_j.$$
 (8.19)

A(dp/dx) was determined in Chapter 2.3.2, equation (2.19) so that

$$A\frac{dp}{dx} = -\frac{1}{2}\rho DU^2 C_f \frac{D}{D_h} + \rho g A. \tag{8.20}$$

Therefore, one obtains

$$(F_{py})_j = \left(-\frac{1}{2}\rho DU^2 C_f \frac{D}{D_h} + \rho g A\right) \tan \phi_j. \tag{8.21}$$

8.3.3 Viscous hydrodynamic forces F_N and F_L

The viscous mean-flow-related forces acting on long inclined cylinders as formulated by Taylor (1952) have been discussed in Chapter 2. They are given by equation (2.21) of Section 2.3.3:

$$F_N = \frac{1}{2}\rho DU^2 \left(C_{Dp} \sin^2 \phi + C_f \sin \phi \right), \quad F_L = \frac{1}{2}\rho DU^2 C_f \cos \phi , \qquad (8.22)$$

as discussed also in Appendix B, where it is also shown that these formulae agree with the empirical results gathered by Hoerner (1958).

However, for the purposes of this model, things are modified, e.g., by the fact that the instantaneous normal velocity is not $U \sin \phi_j$ but $\mathbf{v}_{fj1}(\xi)$, where $\mathbf{v}_{fj1}(\xi)$ is the relative fluid-body velocity in the direction \mathbf{j}_1 , normal to the element, which it has already been calculated and is given by equation (8.11). Then, the foregoing expressions become

$$(F_{N})_{j} = \frac{1}{2} \rho D C_{dp} \left[U \sin \phi_{j} + \sum_{q=1}^{j-1} l_{q} \cos(\phi_{q} - \phi_{j}) \dot{\phi}_{q} + \xi \dot{\phi}_{j} \right]^{2}$$

$$\frac{1}{2} \rho D U C_{f} \left[U \sin \phi_{j} + \sum_{q=1}^{j-1} l_{q} \cos(\phi_{q} - \phi_{j}) \dot{\phi}_{q} + \xi \dot{\phi}_{j} \right]$$
(8.23)

and

$$(F_L)_j = \frac{1}{2} \rho DU C_f \left[U \cos \phi_j - \sum_{q=1}^{j-1} l_q \sin(\phi_q - \phi_j) \dot{\phi}_q \right]$$
 (8.24)

for the jth cylinder of the articulated system. Comments on the signs of the various terms appearing in F_N and F_L are discussed in Appendix G.

8.4 THE EQUATIONS OF MOTION

8.4.1 The total kinetic and potential energies of the system

The total kinetic energy of the system, T, is given by

$$T = T_s + T_f \,, \tag{8.25}$$

where T_s and T_f are given by equations (8.6) and (8.16), respectively. The potential energy is associated only with the articulated system, so with equation (8.7).

8.4.2 The generalized forces

The generalized forces Q_j , j=1,2,...N, may be determined by considering the virtual work δW_j associated with virtual displacements $\delta \phi_j$ in the generalized coordinates ϕ_j . Then the generalized force Q_j is defined via $\delta W_j = Q_j \delta \phi_j$. We proceed to determine the generalized force Q_1 , associated with the generalized coordinate ϕ_1 and cylinder 1, which is denoted by $\delta W_{1,1}$ and is given by

$$\delta W_{1,1} = -\int_0^{l_1} (F_N)_1 \, \xi \, \delta \phi_1 \, d\xi + \int_0^{l_1} (F_{py})_1 \, \xi \, \delta \phi_1 \cos \phi_1 \, d\xi \,. \tag{8.26}$$

Similarly, the virtual work associated with the forces acting on the second cylinder, $\delta W_{1,2}$ due to a virtual displacement associated with $\delta \phi_1$, is given by

$$\delta W_{1,2} = -\int_0^{l_2} (F_N)_2 \, l_1 \delta \phi_1 \cos(\phi_2 - \phi_1) d\xi + \int_0^{l_2} (F_{py})_2 \, l_1 \delta \phi_1 \cos\phi_1 d\xi$$

$$+ \int_0^{l_2} (F_L)_2 \, l_1 \, \delta \phi_1 \sin(\phi_2 - \phi_1) d\xi$$

$$-(\partial p/\partial x)_2 \, A_2 \, l_2 \, l_1 \, \delta \phi_1 \, \sin(\phi_2 - \phi_1); \tag{8.27}$$

and so on. The virtual work associated with the last cylinder will have the additional terms

$$\frac{1}{2} \rho D^2 U^2 C_b l_1 \delta \phi_1 \sin(\phi_N - \phi_1) + F_{nc} l_1 \delta \phi_1 \cos(\phi_N - \phi_1), \tag{8.28}$$

where C_b is the base drag coefficient (Appendix II), and F_{nc} has been discussed in Section 8.3.1.

Hence, the generalized forces associated with the generalized coordinate ϕ_j are

$$Q_{j} = -\int_{0}^{l_{j}} (F_{N})_{j} \xi \, d\xi + \int_{0}^{l_{j}} (F_{py})_{j} \xi \, \cos \phi_{j} d\xi - \sum_{i=j+1}^{N} \int_{0}^{l_{i}} (F_{N})_{i} \, l_{j} \, \cos(\phi_{i} - \phi_{j}) d\xi$$

$$+ \int_{0}^{l_{i}} (F_{py})_{i} \, l_{j} \, \cos \phi_{j} d\xi + \int_{0}^{l_{i}} (F_{L})_{i} \, l_{j} \, \sin(\phi_{i} - \phi_{j}) d\xi - F_{nc} \, l_{j} \, \cos(\phi_{N} - \phi_{j})$$

$$- (\partial p / \partial x)_{i} \, A_{i} \, l_{i} \, l_{j} \, \sin(\phi_{i} - \phi_{j}) + \frac{\rho D^{2} \, U^{2} \, C_{b}}{2} \, l_{j} \sin(\phi_{N} - \phi_{j}) , \qquad (8.29)$$

where $(F_N)_j$, $(F_L)_j$, $(F_{py})_j$, and F_{nc} are given by the equations (8.23), (8.24), (8.21) and (8.18), respectively.

8.4.3 Perivation of the equations of motion

Equations (8.16), (8.6), (8.7) and (8.29) are substituted into Lagrange's equations which take the form

$$\frac{d}{dt}\left(\frac{\partial T}{\partial \dot{\phi}_i}\right) - \frac{\partial T}{\partial \phi_j} + \frac{\partial V}{\partial \phi_j} = Q_j, \qquad j = 1, 2, ..., N,$$
(8.30)

for a system of N articulated cylinders, where the dots denote differentiation with respect to time t.

The equations of motion obtained may be rendered non-dimensional with the aid of the same dimensionless parameters as those used for the first model (see Chapter 2.6, equation (2.34)); however, the additional nondimensional parameter λ for the free end of the last cylinder will be required. All these nondimensional parameters are given here below:

$$\beta = \rho A/(\rho A + m), \quad \gamma = (m - \rho A)gL^{2}N/k, \quad u = (\rho ALN/k)^{1/2}U,$$

$$\epsilon = L/D, \quad l_{N} = el, \quad \lambda = w/l, \quad c = (4/\pi)C_{d}[\rho ALN/k]^{1/2},$$

$$c_{f} = 4C_{f}/\pi, \quad c_{b} = 4C_{b}/\pi \quad h = D_{b}/D, \quad \tau = [(\rho A + m)L^{3}N/k]^{-1/2}t. \quad (8.31)$$

Details of the derivation of the equations of motion, the nondimensional parameters and the nonlinear moments, are the same as those in Chapter 2.6. The equations of motion for a system of two articulated cylinders (N = 2) in their final form are the following:

$$\begin{split} & \left[1+(\chi-1)\beta\right]\left[\frac{1}{3}+\epsilon\right]\ddot{\phi}_{1}+\chi\beta\left(-e\,\phi_{1}^{2}+\phi_{1}\phi_{2}-e\,\phi_{2}^{2}\right)\ddot{\phi}_{1}+\frac{1}{2}\left[1+(\chi-1)\beta\right]e^{2}\ddot{\phi}_{2} \\ & +\frac{1}{2}\left[1+(\chi-1)\beta\right]\left[-\frac{1}{2}e^{2}\phi_{1}^{2}-\frac{1}{2}\epsilon^{2}\phi_{2}^{2}+e^{2}\phi_{1}\phi_{2}\right]\ddot{\phi}_{2}+\frac{1}{2}\,\epsilon^{2}\left[1+(\chi-1)\beta\right](\phi_{1}-\phi_{2})\,\dot{\phi_{2}}^{2} \\ & -\chi\,\beta\left(\dot{\phi}_{2}\phi_{2}-\dot{\phi}_{2}\phi_{1}-\frac{1}{2}\dot{\phi}_{1}\phi_{2}+\frac{1}{2}\dot{\phi}_{1}\phi_{1}\right)\,\dot{\phi}_{1}+N\gamma\left(1-\frac{1}{6}\phi_{1}^{2}\right)\,\phi_{1}-\chi u^{2}N^{2}\left(1-\frac{2}{3}\phi_{1}^{2}\right)\phi_{1} \\ & +N^{4}\left(2\phi_{1}-\phi_{2}\right)+\chi\,u\,N\,\sqrt{\beta}\left[e-\phi_{2}^{2}+\phi_{1}\,\phi_{2}-\frac{1}{4}\phi_{1}^{2}\right]\dot{\phi}_{2}-\frac{\beta}{1-2\beta}\,N\,\gamma\,\left(\frac{1}{4}\phi_{2}^{3}-\frac{1}{4}\phi_{1}\phi_{2}^{2}\right) \\ & +u^{2}\,N\,\epsilon\,c_{f}\,h^{-1}\left(\frac{1}{2}\phi_{1}-\frac{1}{12}\phi_{1}^{3}+\frac{1}{8}\phi_{2}^{3}-\frac{1}{8}\phi_{1}\phi_{2}^{2}\right)+u^{2}\,N^{2}\,c_{b}\left(\frac{1}{2}\phi_{1}-\frac{1}{2}\phi_{2}+\frac{1}{12}\phi_{2}^{3}-\frac{1}{4}\phi_{1}\phi_{2}^{2}\right) \\ & +u^{2}\,N^{2}\,c_{b}\left(\frac{1}{4}\phi_{1}^{2}\phi_{2}-\frac{1}{12}\phi_{1}^{3}\right)+\frac{1}{2}\,\lambda(1-f)\chi\,u\,N\sqrt{\beta}\,\left(1-\phi_{1}^{2}-\frac{1}{2}\phi_{2}^{2}+\phi_{1}\,\phi_{2}\right)\dot{\phi}_{1} \\ & +(1-f)\,\chi\,\beta\left(\frac{1}{6}\lambda^{2}-1\right)\ddot{\phi_{1}}\left(1-\frac{1}{2}\phi_{1}^{2}-\frac{1}{2}\phi_{2}^{2}+\phi_{1}\phi_{2}\right)-(1-f)\chi\,u\,N\sqrt{\beta}\left(3-\phi_{1}^{2}\right) \end{split}$$

$$\begin{split} &+(1-f)\chi\;u\;N\sqrt{\beta}\left(\frac{3}{2}\phi_{1}\phi_{2}^{2}-3\phi_{1}\phi_{2}\right)\dot{\phi_{1}}-(1-f)\;\chi\;u^{2}\;N^{2}\left(1-\frac{1}{6}\phi_{1}^{2}-\frac{1}{2}\phi_{2}^{2}+\phi_{1}\phi_{2}\right)\phi_{1}\\ &+\frac{1}{4}\;u^{2}\;N\;\epsilon\;c\;|\;\phi_{1}\;|\;\phi_{1}+\frac{3}{8}\;\epsilon\;c\;\frac{\beta}{N}\;|\;\dot{\phi_{1}}\;|\;\dot{\phi_{1}}+\frac{1}{6}\;u\;c\;\epsilon\;\sqrt{\beta}\left(|\;\dot{\phi_{1}}\;|\;\phi_{1}+\dot{\phi_{1}}\;|\;\phi_{1}\;|\right)\\ &+\frac{1}{6}\;\frac{1}{N}\;\epsilon\;\beta\;c\;e^{3}\;\dot{\phi_{2}}\;|\;\dot{\phi_{2}}\;|\;+u^{2}\;N\;\epsilon\;c\;\frac{e}{2}\;\phi_{2}\;|\;\phi_{2}\;|\;+\epsilon\;c\;\beta\;e^{2}\;\frac{1}{N}\;\frac{1}{4}\left[\dot{\phi_{1}}\;|\;\dot{\phi_{2}}\;|\;+\;|\;\dot{\phi_{1}}\;|\;\dot{\phi_{2}}\right]\\ &+\frac{1}{4}\;e^{2}\;u\;\epsilon\;c\;\sqrt{\beta}\left[|\;\dot{\phi_{2}}\;|\;\phi_{2}+\dot{\phi_{2}}\;|\;\phi_{2}\;|\right]+\frac{1}{2}\;e\;u\;\epsilon\;c\;\sqrt{\beta}\;\left[|\;\dot{\phi_{1}}\;|\;\phi_{2}+\dot{\phi_{1}}\;|\;\phi_{2}\;|\right]\\ &+u^{2}\;N\;\epsilon\;c_{f}\left[\frac{1}{2}\;\phi_{1}-\frac{1}{12}\;\phi_{1}^{3}\right]+\mathcal{M}_{c}(\mathcal{M}_{t})=0, \end{split}$$

$$\frac{1}{3}e^{3}[1+(\chi-1)\beta] \ddot{\phi}_{2} + \frac{1}{2}e^{2}[1+(\chi-1)\beta] \left\{ 1 - \frac{1}{2}(\phi_{1}-\phi_{2})^{2} \right] \ddot{\phi}_{1} \\
+ \frac{1}{2}e^{2}[1+(\chi-1)\beta] \dot{\phi}_{1}^{2}(\phi_{2}-\phi_{1}) - \chi \beta e(\phi_{1}-\phi_{2}) \dot{\phi}_{1}^{2} - \chi u^{2} N^{2} c \left(1 - \frac{2}{3}\phi_{2}^{2}\right) \phi_{2} \\
+ N^{4}(\phi_{2}-\phi_{1}) - \chi u N \sqrt{\beta} e \dot{\phi}_{1} \left(1 - 2\phi_{2}^{2} - \frac{1}{2}\phi_{1}^{2} + 2\phi_{1}\phi_{2}\right) + N \gamma \frac{1}{2}e^{2} \left(\phi_{2} - \frac{1}{6}\phi_{2}^{3}\right) \\
+ \epsilon c \beta e^{2} \frac{1}{N} \frac{1}{4} \dot{\phi}_{1} |\dot{\phi}_{1}| + \epsilon c \beta e^{4} \frac{1}{N} \frac{1}{8} \dot{\phi}_{2} |\dot{\phi}_{2}| + \epsilon c \beta e^{3} \frac{1}{N} \frac{1}{6} \left(|\dot{\phi}_{1}| \dot{\phi}_{2} + \dot{\phi}_{1}| \dot{\phi}_{2}|\right) \\
+ u^{2} \epsilon c N e^{2} \frac{1}{4} \phi_{2} |\dot{\phi}_{2}| + u \epsilon c \sqrt{\beta} e^{3} \frac{1}{6} \left[|\dot{\phi}_{2}| \phi_{2} + \dot{\phi}_{2}| \phi_{2}|\right] \\
+ u \epsilon c \sqrt{\beta} e^{2} \frac{1}{4} \left[|\dot{\phi}_{1}| \phi_{2} + \dot{\phi}_{1}| \phi_{2}|\right] + \frac{1}{4}u^{2} N \epsilon c_{f} e^{2} (1 + h^{-1}) \left(\phi_{2} - \frac{1}{6}\phi_{2}^{3}\right) \\
+ \frac{1}{4}\chi \beta (1 - f)(\lambda - 1)\ddot{\phi}_{1} \left[1 - \frac{1}{2}(\phi_{2} - \phi_{1})^{2}\right] + \frac{1}{4}\chi \beta (\lambda - 1)(1 - f)(\dot{\phi}_{1}^{2}\phi_{2} - \phi_{1}\dot{\phi}_{1}^{2}) \\
+ \frac{1}{4}\chi \beta (\lambda - 1)(1 - f)(-\dot{\phi}_{1}\dot{\phi}_{2}\phi_{2} + \phi_{1}\dot{\phi}_{1}\dot{\phi}_{2}) + (1 - f)\chi \beta \left(\frac{1}{12}\lambda^{2} - \frac{1}{8}\right)\ddot{\phi}_{2} \\
+ \frac{1}{4}(1 - f)\chi u N \sqrt{\beta} \dot{\phi}_{1}\phi_{1}^{2} - \frac{1}{2}(1 - f)\chi u N \sqrt{\beta}\dot{\phi}_{2} \left(1 + \frac{1}{2}\phi_{2}^{2}\right) - \frac{1}{2}(1 - f)\chi u^{2} N^{2} \phi_{2} \\
- \frac{1}{6}(1 - f)\chi u^{2} N^{2} \phi_{2}^{3} = 0. \tag{8.32}$$

Chapter 9

NUMERICAL RESULTS FOR THE SECOND MODEL WITH

N=2

In this chapter, the same four cases as in Chapter 4 are presented, with the only difference that in Chapter 9 these results are obtained with the second model, while in Chapter 4 the results were obtained with the first model.

9.1 CASE 1:
$$h = 0.5$$
, $f = 0.8$ and $\kappa_c = 5 \times 10^3$

From a linear, eigenvalue analysis, a divergence instability occurs for u = 1.67 and the system is unstable for 1.67 < u < 2.6925; then it stabilizes for u = 2.693 and is stable for 2.693 < u < 2.795; and finally, a flutter instability occurs for u = 2.8 and the system remains unstable for u > 2.8.

Figure 9.1 shows the bifurcation diagram with the cubic spring representation for this case, i.e., the maximum displacement of the first cylinder $\phi_1(\tau)$ versus u, and the dynamic behaviour of the system may be described as follows.

For u = 1.67, a pitchfork bifurcation occurs, so that the motion of the first cylinder will reduce to a fixed point; for higher u, as for 1.67 < u < 2.6925, new fixed points occur as the flow velocity increases: for 1.67 < u < 2.1, the fixed points increase with u; for 2.1 < u < 2.4, the fixed points decrease with u; and for 2.4 < u < 2.6925, they increase again with u. Then the system is stable for flow velocities u between 2.693 and 2.795. And finally, for u = 2.80, there exists a stable, symmetric limit cycle that develops after a Hopf bifurcation. The symmetry of the limit cycle is lost by a symmetry-breaking pitchfork bifurcation at u = 2.832, the first bifurcation shown in Figure 9.1 — where the two branches are obtained with different-sign initial conditions; the limit cycle remains asymmetric for 2.832 < u < 2.8677. For higher u, i.e. u > 2.867705, the limit cycle collapses to fixed points; in the bifurcation diagram two fixed points exist because of the two opposite sign-initial conditions. This transition of the motion of the system from a limit cycle to a fixed point happens suddenly, and it is impossible to determine what happens between these two motions, and is characteristic to all four cases considered in this Chapter, that means to the second model.

In accordance with the bifurcation diagram, two phase-plane portraits were constructed in Figure 9.2(a,b). For u = 2.83, there exists a stable symmetric limit cycle, which has been represented in Figure 9.2(a); an unstable asymmetric limit cycle has been represented in Figure 9.2(b) for u = 2.855.

By comparing the bifurcation diagram for this system (Figure 9.1) with those for the first model (Figure 4.3), it may be seen that the route to chaos for the first model is through period-doubling bifurcations (2.74 < u < 2.85), while the second model never becomes chaotic; its motion is either period-one, with symmetric limit cycles for 2.79 < u < 2.83 and asymmetric limit cycles for 2.83 < u < 2.86, or (for u > 2.86) it is associated with fixed points, while for the first model the amplitudes become too large for higher u (for u > 2.85), and convergence of solutions will not be possible.

9.2 CASE 2: h = 0.2, f = 0.8 and $\kappa_c = 5 \times 10^3$

This case corresponds to a narrower annulus than Case 1.

From the linear or eigenvalues analysis, a divergence instability occurs for u = 1.16 and the system is unstable for 1.16 < u < 1.75; then it stabilizes for u = 1.75 and is stable for 1.75 < u < 1.945; and finally, a flutter instability occurs for u = 1.95 and the system remains unstable for u > 1.95.

Figure 9.3 shows the bifurcation diagram for this case, i.e., the maximum displacement of the first cylinder $\phi_1(\tau)$ versus u, and the dynamic behaviour of the system may be described as follows:

For u=1.16 a pitchfork bifurcation occurs, so that the motion of the first cylinder will reduce to a fixed point; for higher u, as for 1.16 < u < 1.75, new fixed points occur as the flow velocity increases: for 1.16 < u < 1.45 the fixed points increase with u, for 1.5 < u < 1.72 the fixed points decrease with u, and for 1.72 < u < 1.745 they increase again with u. Then the system is stable for flow velocities u between 1.75 and 1.945. And finally for u > 1.95, the route to chaos for the bifurcation diagram of Figure 9.3 is clarified via the phase-plane portraits of Figure 9.4.

For u=1.95, there exists a stable, symmetric limit cycle that develops after the Hopf bifurcation (not shown). The symmetry of the limit-cycle is lost by a symmetry-breaking pitchfork bifurcation at u=2.0275, the first bifurcation shown in Figure 9.3. An asymmetric limit cycle is obtained for 2.0275 < u < 2.08, as for example the one shown for u=2.05 in Figure 9.4(a). At higher u (u>2.08), a cascade of period-doubling bifurcations occurs, and Figure 9.4(b,c) shows period-2 and period-4 motions, for (b) u=2.09, and (c) u=2.095, respectively. Figure 9.4(d) shows chaotic motion for u=2.096, corresponding to the first dense cloud of points in the bifurcation diagram. For higher u, as i.e., u>2.097, the limit cycle reduces suddenly to one of two fixed points.

By comparing the bifurcation diagrams for this system, with the first model (Figure 4.9) and with the second model (Figure 9.3), it may be seen that the route to chaos for the first model is via quasiperiodicity (for 2.02 < u < 2.06), while the route to chaos for the second model is via period-doubling (2.02 < u < 2.10); then, both models will become chaotic, but their routes to chaos will be very different. For higher u, the motion for the second model reduces finally to a fixed point (u > 2.10), while for the first model the amplitudes become too large, and the convergence of solutions will not be possible.

9.3 CASE 3: h = 0.5, f = 0 and $\kappa_c = 5 \times 10^5$

From the linear analysis, a flutter instability occurs for u = 4.47. Physically, the system in this case is similar to that of Case 1, but the free end is blunt in this case. Figures 9.5 show the bifurcation diagrams for motions of the first cylinder in the system, for flow velocities above the critical flow velocity for which a Hopf bifurcation occurs ($u \simeq 4.47$). The route to chaos is clarified via the phase-plane portraits of Figures 9.6. Figure 9.5(a) represents the bifurcation diagram for 5 < u < 8.5, while Figure 9.5(b) represents the detailed bifurcation diagram for a smaller range of flow velocities, 8 < u < 8.20. On the phase-plane portraits, the behaviour of the system is seen much better, e.g., in Figure 9.6(a): at u = 5 an asymmetric limit cycle develops after the Hopf bifurcation. For 6.90 < u < 8.05 approximately, a periodic asymmetrical motion develops, which is shown in Figure 9.6(b) for u = 7.5, and it looks as if it was developping around two symmetrical points; for $\dot{\phi_1}=0,\,\phi_1\simeq0.02$ or $\phi_1 \simeq -0.02$, depending on the initial conditions. For u = 8.10 and u = 8.15, a periodic motion develops around two pairs of symmetrical points mentioned above; the odd subharmonics of the dominant frequency may be calculated from the power spectrum. The phase-plane plot for u = 8.15, Figure 9.6(c), shows the chaotic motion of the system. Furthermore, chaotic motion around one of the symmetrical

points ($\phi_1 \simeq -0.02$ and $\dot{\phi}_1 = 0$) is observed in Figure 9.6(d) for u = 8.18. The chaotic motion of the system may be verified by constructing the time traces and their corresponding power spectra in Figure 9.7(a,b), for u = 8.175. For the same flow velocity, u = 8.175, a Poincaré map was constructed, as shown in Figure 9.7(c), and the chaotic character of the motion of the system may be verified.

For higher flow velocities, a period-bubbling event takes place, for which a period-four motion may be observed for u = 8.1825 (not shown). A period-two motion has been presented in Figure 9.6(e), for u = 8.19, which is followed by an inversion, back to period-1, as seen in Figure 9.6(f) for u = 8.20, and the motion will reduce further to a fixed point, as seen also in the bifurcation diagram of Figure 9.5.

Thus, this case displays a very rich dynamical behaviour. Chaos arises around two stable fixed points, through period-odd bifurcations, then a period-bubbling phenomenon takes place, from period-four, to period-two and back to period-one motion, and finally the motion will reduce to fixed points.

By comparing the bifurcation diagrams for this system, with the first model (Figure 4.15) and with the second model (Figure 9.5), it may be concluded that the route to chaos is the same, but differences in the quantitative sense do exist, as expected. For higher u, the motion of the system, for both models, will reduce to a fixed point.

9.4 CASE 4: h = 0.2, f = 0.4 and $\kappa_c = 5 \times 10^5$

From the linear analysis, a flutter instability occurs for u = 2.38. This system is similar to Case 2, but with an intermediately blunt free end—blunter than for Case 2. Figures 9.8 and 9.9 show the bifurcation diagram and the phase-plane plots for the first cylinder in this system, for flow velocities u higher than the critical flow velocity for which a Hopf bifurcation occurs (u = 2.38). As before, the route

to chaos for the bifurcation diagram of Figure 9.8 is clarified via the phase-plane portraits of Figure 9.9.

There exists a symmetric stable limit cycle after the Hopf bifurcation at u = 2.38 (not shown). The symmetry of the limit cycle is lost by a symmetry-breaking pitchfork bifurcation at $u \simeq 2.8$, the first bifurcation shown in Figure 9.8. An asymmetric limit cycle motion is represented in Figure 9.9(a) for u = 2.85.

At flow velocities u > 2.85, a cascade of period-doubling bifurcations occurs. Figure 9.9(b,c) shows period-two and period-four motions for (b) u = 2.95 and (c) u = 2.96. Figure 9.9(d) shows chaotic motion for u = 3, which is followed by period-odd motions which will lead again to chaos. The motion of the system will reduce finally to fixed points for u > 3.35.

In this case, chaos arises firstly through period-doubling (period -2, -4, -8), and then the motion reduces finally to fixed points as in all cases studied till now with the second model.

Finally, by comparing the bifurcation diagrams for models one and two (Figures 4.22 and 9.8), the routes to chaos for the two models are found to be the same for 2.4 < u < 3.4. For higher u, the motion of the system for the second model reduces to fixed point, while for the first model the amplitudes become large, and the convergence of solutions will not be possible.

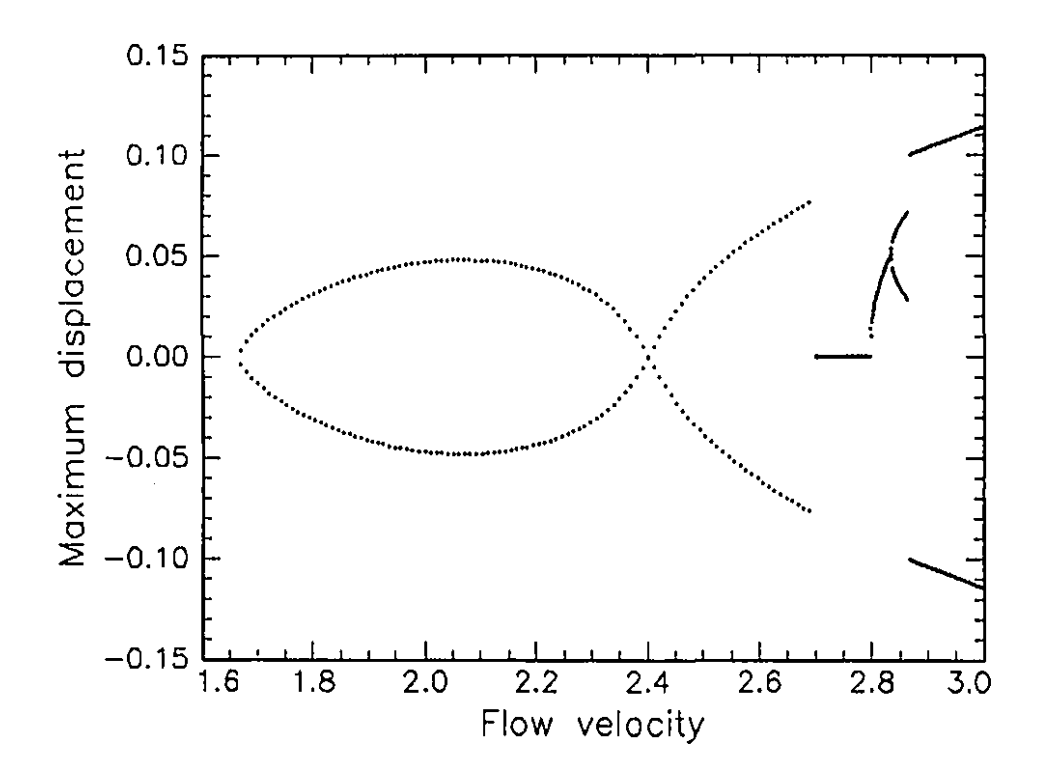


Figure 9.1. Bifurcation diagram for the system of Case 1 obtained by the second model: h=0.5, c=0.38, f=0.8, with the cubic spring model ($\kappa_c=5\times 10^3$) for impacting with the channel; the maximum displacement $\phi_1(\tau)$ versus the dimensionless flow velocity, u.

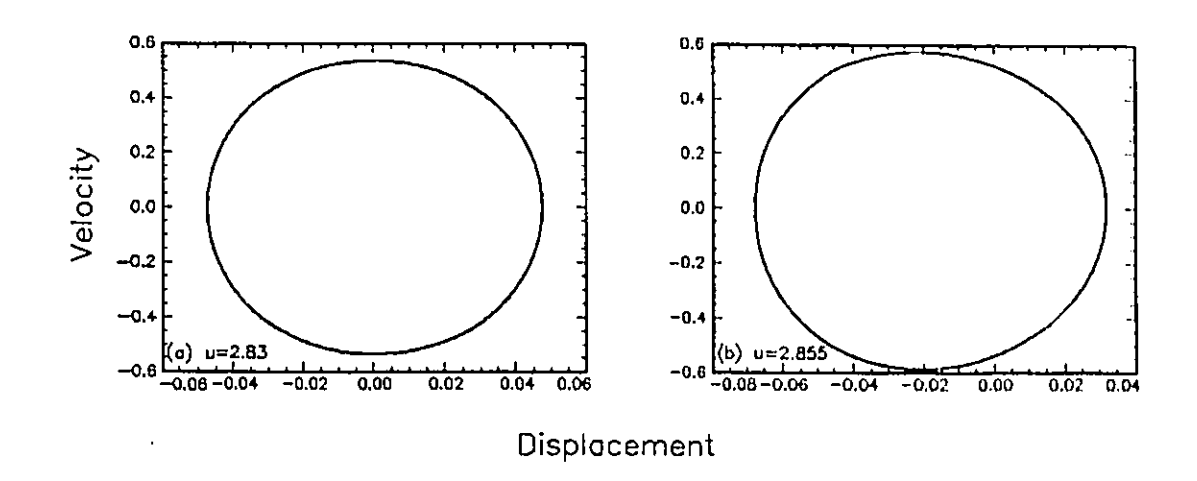


Figure 9.2. Phase-plane plots of $\dot{\phi}_1(\tau)$ versus $\phi_1(\tau)$ at (a) u=2.83 and (b) u=2.855 for the system of Case 1 (Figure 9.1): h=0.5, c=0.38, f=0.8, with the cubic spring model ($\kappa_c=5\times 10^3$).

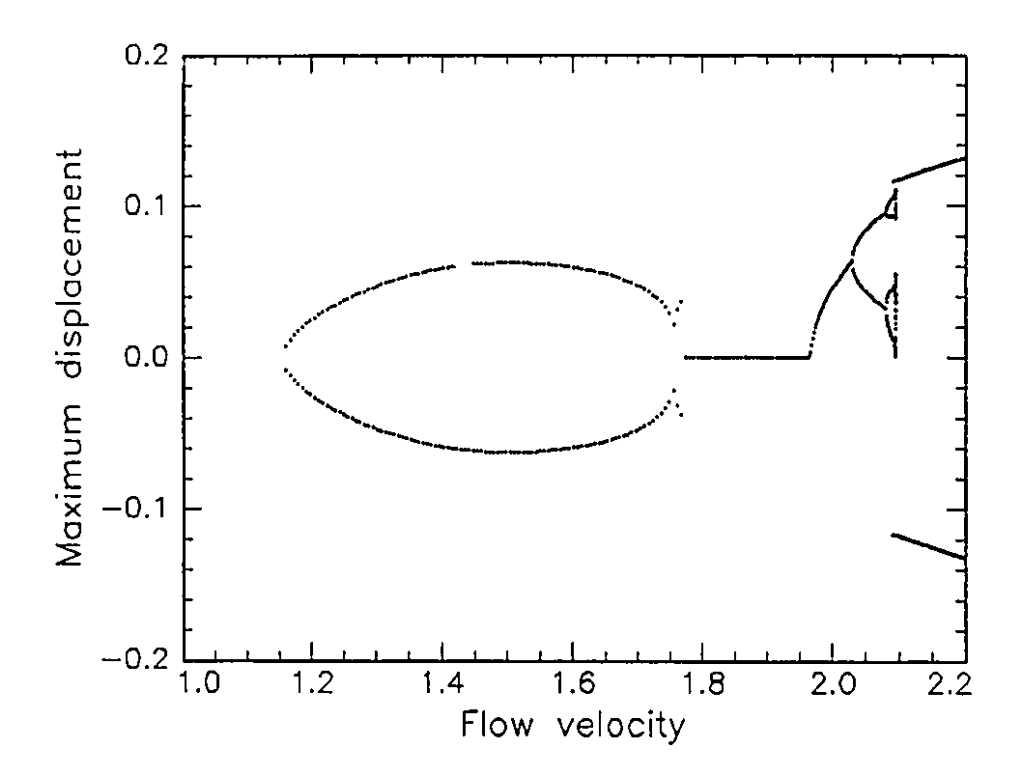


Figure 9.3. Bifurcation diagram for the system of Case 2 obtained by the second model: h = 0.2, c = 0.79, f = 0.8, with the cubic spring model ($\kappa_c = 5 \times 10^3$) for impacting with the channel; the maximum displacement $\phi_1(\tau)$ versus the dimensionless flow velocity, u.

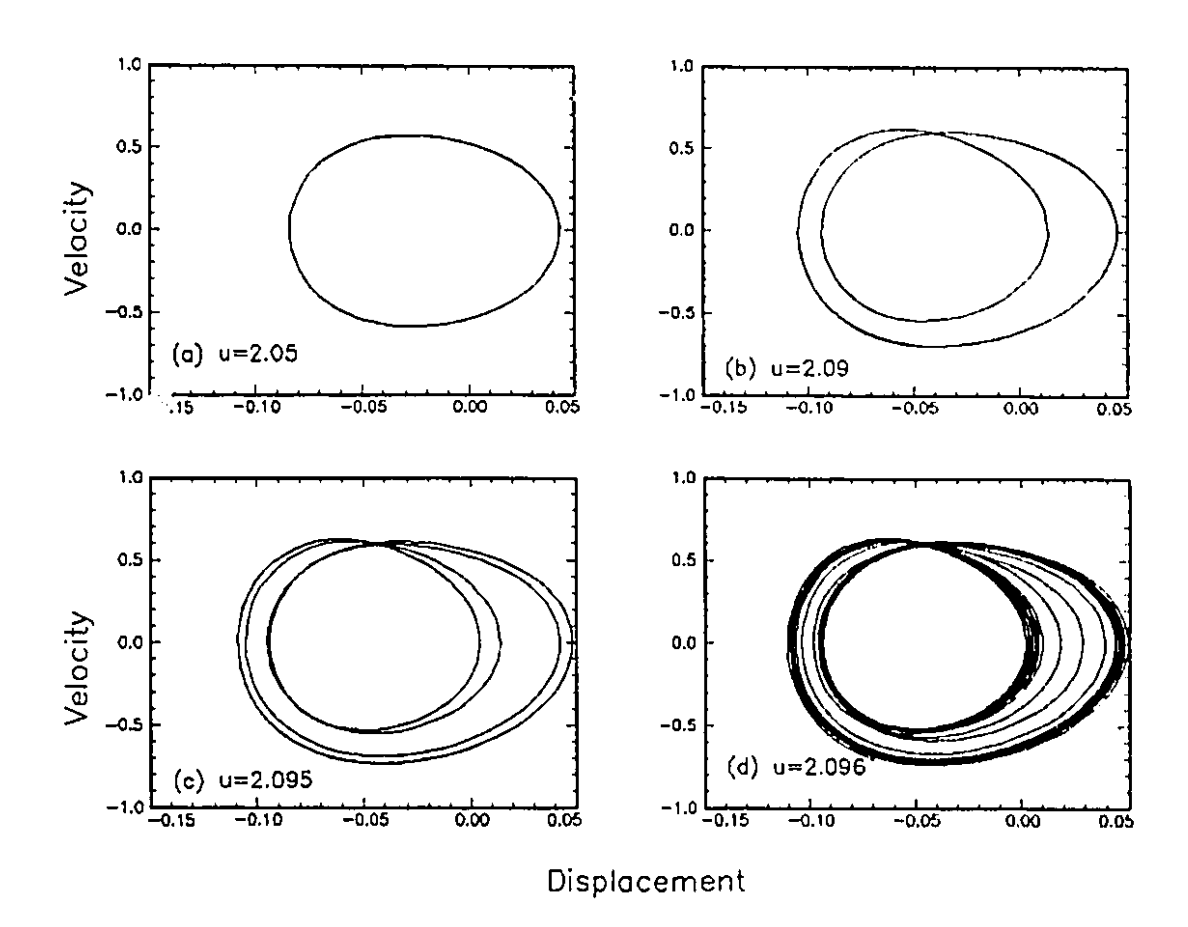


Figure 9.4. Phase-plane plots of $\dot{\phi}_1(\tau)$ versus $\phi_1(\tau)$ at (a) u=2.05, (b) u=2.09, (c) u=2.095 and (d) u=2.096 for the system of Case 2 (Figure 9.3): h=0.2, c=0.79, f=0.8, with the cubic spring model ($\kappa_c=5\times10^3$).

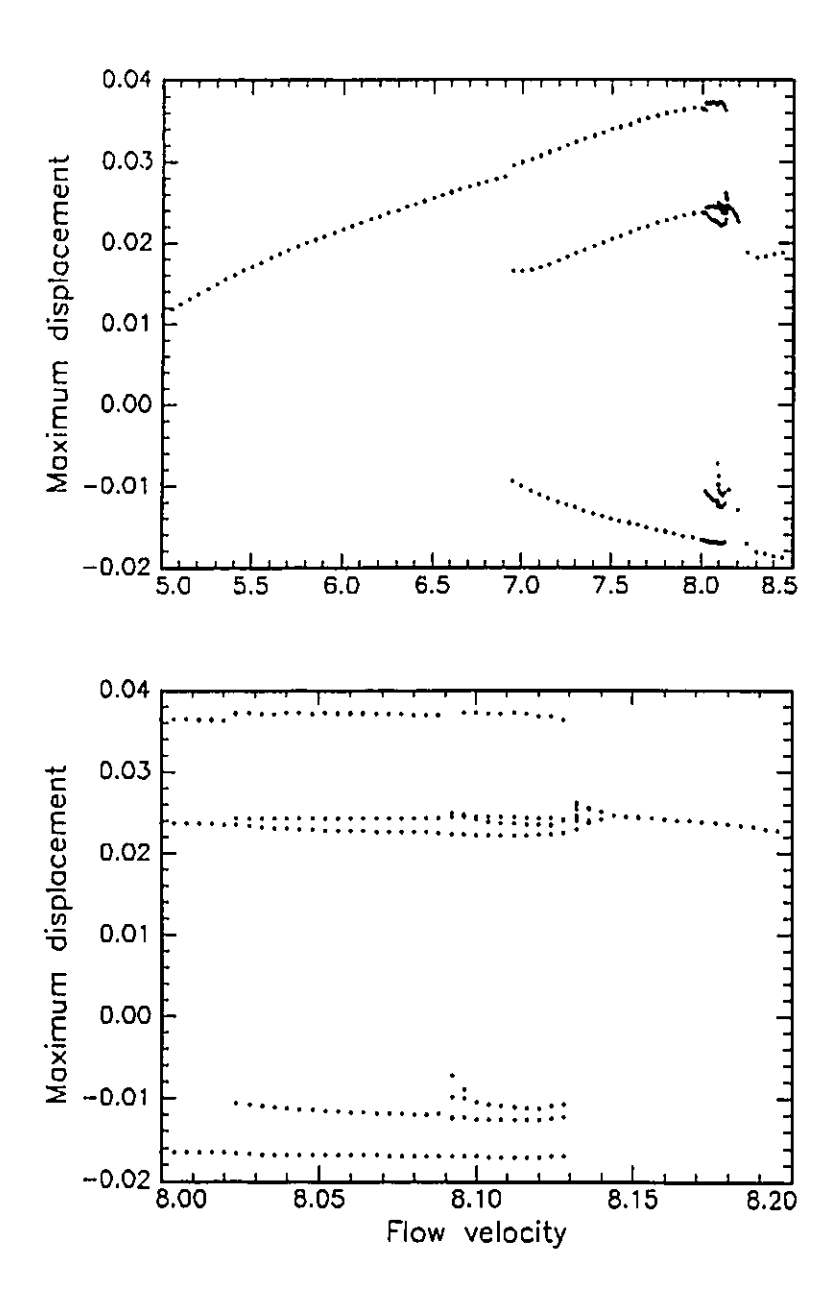


Figure 9.5. Bifurcation diagram for the system of Case 3 obtained by the second model: h=0.5, c=0.38, f=0, with the cubic spring model ($\kappa_c=5\times 10^5$) for impacting with the channel; the maximum displacement $\phi_1(\tau)$ versus the dimensionless flow velocity, u.

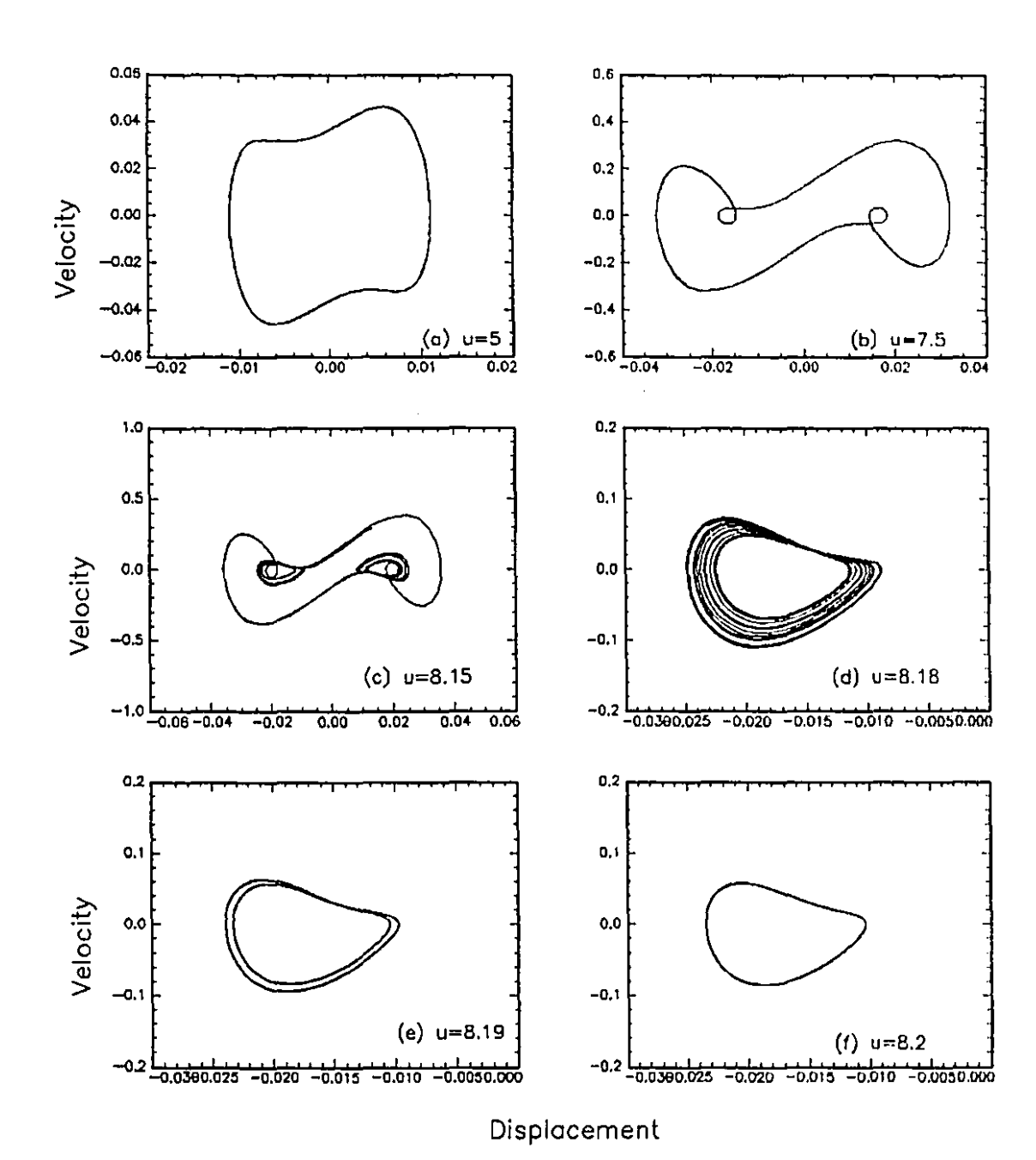


Figure 9.6. Phase-plane plots of $\dot{\phi}_1(\tau)$ versus $\phi_1(\tau)$ at (a) u = 5, (b) u = 7.5, (c) u = 8.15, (d) u = 8.18, (e) u = 8.19 and (f) u = 8.2 for the system of Case 3: h = 0.5, c = 0.38, f = 0, with the cubic spring model ($\kappa_c = 5 \times 10^5$).

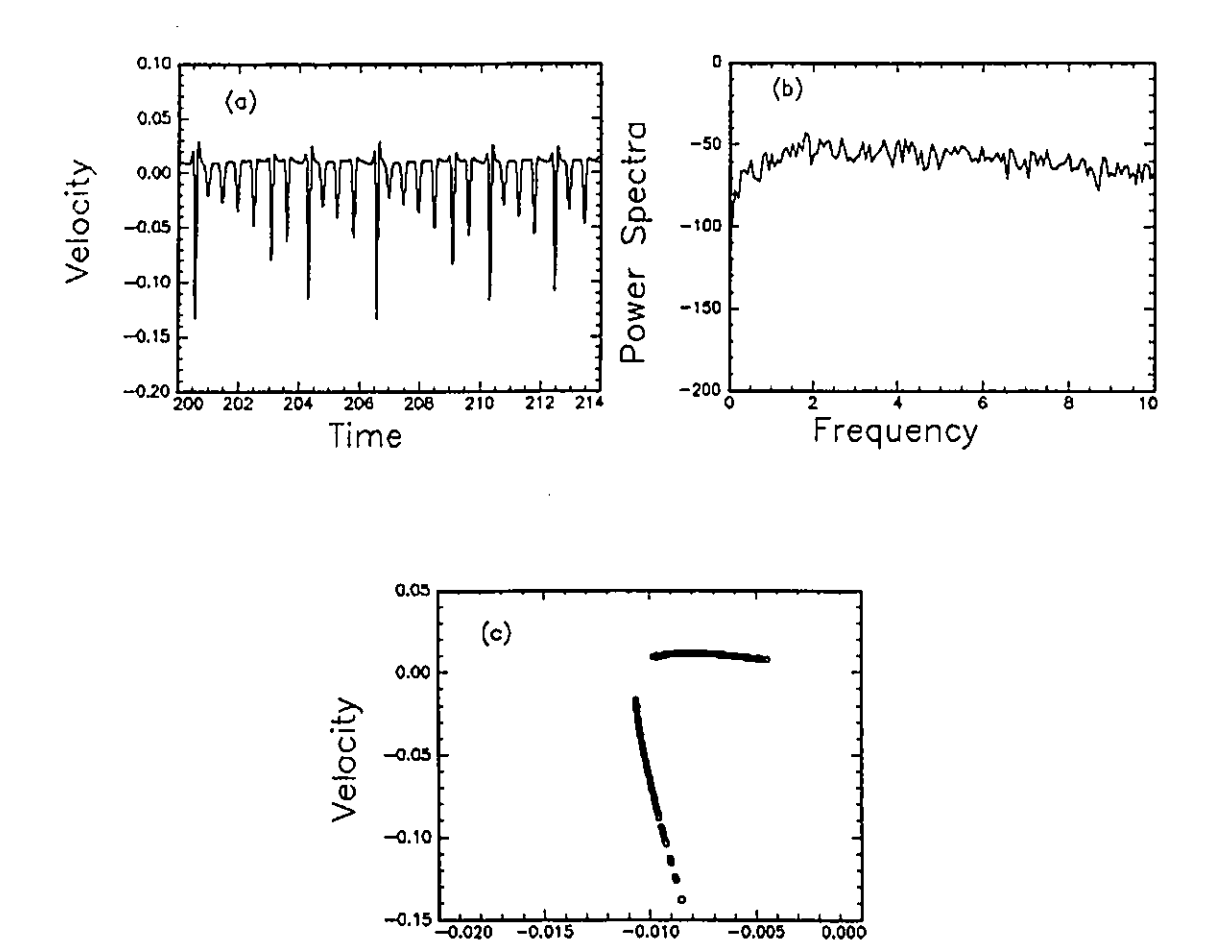


Figure 9.7. Time traces (a), Power Spectra (b) and Poincaré maps (c) for the system of Case 3: h = 0.5, c = 0.38, f = 0.4 and $\kappa_c = 5 \times 10^5$ for u = 8.175.

Displacement

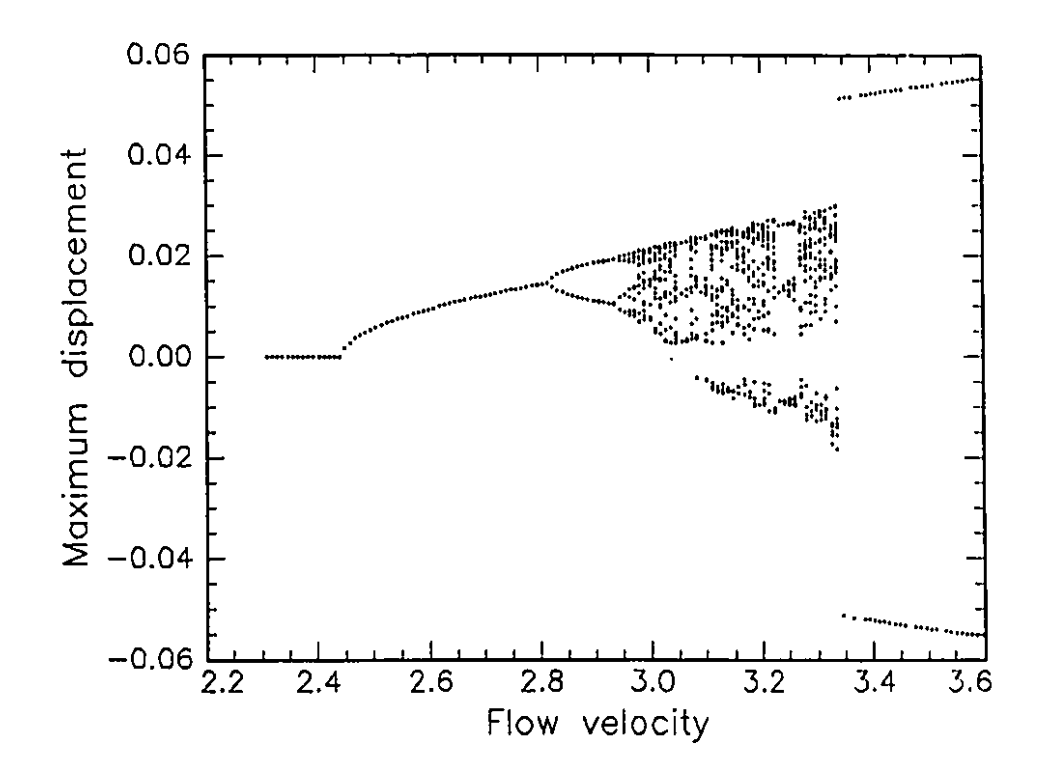


Figure 9.8. Bifurcation diagram for the system of Case 4 obtained by the second model: h = 0.2, c = 0.79, f = 0.4, with the cubic spring model ($\kappa_c = 5 \times 10^5$) for impacting with the channel; the maximum displacement $\phi_1(\tau)$ versus the dimensionless flow velocity, u.

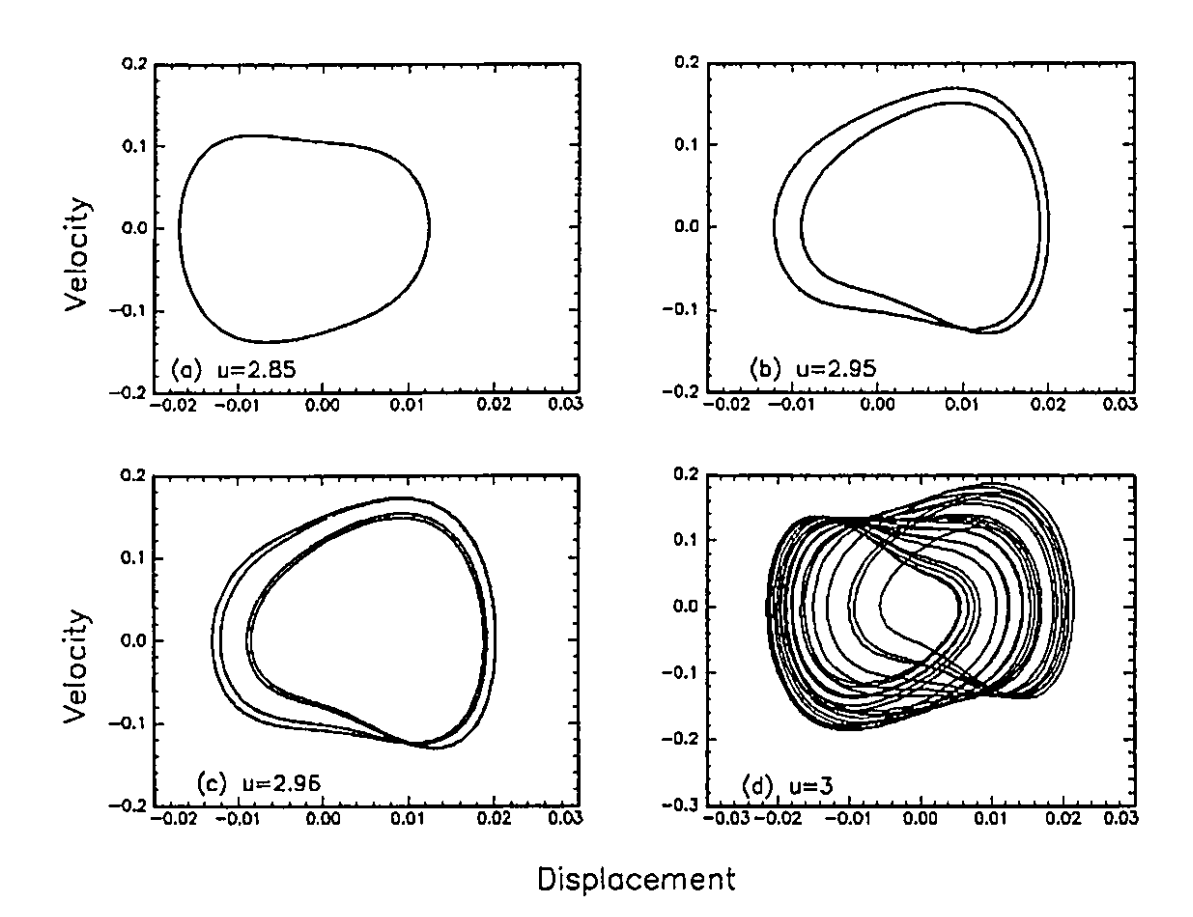


Figure 9.9. Phase-plane plots of $\dot{\phi}_1(\tau)$ versus $\phi_1(\tau)$ at (a) u=2.85, (b) u=2.95, (c) u=2.96 and (d) u=3 for the system of Case 4: h=0.2, c=0.79, f=0.4, with the cubic spring model ($\kappa_c=5\times 10^5$).

Chapter 10

COMPARISON BETWEEN MODELS 1 AND 2

In order to compare the nonlinear behaviour for the first and the second model, other than flow velocity u, two parameters f and h are varied. By taking into consideration that h corresponds to the hydraulic diameter, while f to the endform coefficient, as before (Chapter 7) two values for h and five values for f were chosen: h=0.2 and h=0.5, while f=0, f=0.2, f=0.4, f=0.6 and f=0.8. We shall compare the results for a two degree of freedom (N=2) system as obtained by the first model (in Chapter 7) and by the second model (herein). Also, in Section 10.4 the dynamics of the second model with impacting modelled by a restitution coefficient is investigated.

The dynamical behaviour of the second model will be summarized in Tables 10.1 and 10.2 (pp. 131 and 132).

10.1 N=2, SECOND MODEL WITH CUBIC SPRING; h = 0.2

10.1.1 N = 2, h = 0.2 and f = 0

The bifurcation diagram corresponding to this case is shown in Figure 10.1(a) for $u > u_{fl}$. At $u \simeq 3.1$, a symmetric stable limit cycle about the origin develops after the Hopf bifurcation. For 4.98 < u < 5.2916, a periodic motion develops around two symmetrical points and it has the same qualitative shape as the phase-plane portraits shown in Figure 7.2(a). For 5.34031 < u < 5.3405, another periodic motion develops around two pairs of symmetrical points. For 5.3406 < u < 5.342, a chaotic motion occurs around one point, while a period-four motion occurs around the other point, and a period-one motion develops around the other pair of symmetrical points. For u = 5.343, a period-four motion develops around one point, a period-two motion develops around the other pair of points. For 5.344 < u < 5.355, a period-one motion develops around one pair of symmetrical points, while a period-one motion develops around the other pair of symmetrical points, while a period-two motion develops around the other pair of symmetrical points, while a period-two motion develops around the other pair of symmetrical points.

For u=5.356, chaotic motions arise around one pair of symmetrical points, while around the other pair of points only a period-one motion exists. For 5.357 < u < 5.3605, chaotic motions occur around only one point. The shapes of the corresponding phase-plane portraits are similar from a qualitative point of view to those presented in Chapter 7, Figures 7.2 and 7.3. For higher flow velocities u, a period-bubbling phenomenon takes place around one of the four points (depending of the initial condition chosen), as for example, for u=5.3606 a period-sixteen, for u=5.3607 a period-eight, for 5.3608 < u < 5.3615 a period-four motion occurs, followed by a period-two motion for 5.3616 < u < 5.3659 and by a period-one

motion for 5.366 < u < 5.4240. Finally, for u > 5.4241 the motion collapses to fixed points.

The behaviour of this model may be summarized in the following words: period-2,4,8 or period-doubling motions leading to chaos; period-bubbling or period-8,4,2; period-one motions followed by fixed points (Tables 10.1 and 10.2).

10.1.2 N = 2, h = 0.2 and f = 0.2

The bifurcation diagram corresponding to this case is shown in Figure 10.1(b) for $u > u_{fl}$. For $u_{fl} = 2.8$, a symmetric stable limit cycle about the origin develops after the Hopf bifurcation, and remains symmetric for u < 4.316.

For 4.317 < u < 5.221, a periodic motion around one pair of two symmetrical points develops; for 5.222 < u < 5.797, periodic motions develop around two or three pairs of symmetrical points, and for u > 5.798, the motion of the system will reduce to fixed points. The phase-plane portraits corresponding to the motions of this system for u > 4.317 are similar from a qualitative point of view to the ones presented in Figure 7.3, Chapter 7. Finally, the motion of this system is always periodic or, for higher flow velocities, reduces to fixed points. This system never becomes chaotic.

The behaviour of this model is summarized in Tables 10.1 and 10.2 as: periodic followed by fixed points; no chaotic motions.

10.1.3 N = 2, h = 0.2 and f = 0.4

The bifurcation diagram corresponding to this case is shown in Figure 10.1(c) for $u > u_{fl}$. This case has already been discussed in detail in Chapter 9, Section 9.4. For u = 2.38, a symmetric stable limit cycle develops after the Hopf bifurcation. For higher u, i.e. for u = 2.75, a symmetry-breaking pitchfork bifurcation occurs, through which the limit cycle loses its symmetry and becomes asymmetric. At

u > 2.99, a cascade of period-doubling bifurcations occurs: period-two for 3 < u < 3.026, period-four for 3.027 < u < 3.032 and period-eight for 3.033 < u < 3.034, respectively. This cascade eventually leads to chaotic motions at u > 3.035. Finally, the motion of the system will reduce to fixed points for u > 3.44.

The dynamical behaviour of this system is summarized in Tables 10.1 and 10.2 as: period-2,4,8 or period-doubling followed by chaos; fixed points.

10.1.4 N = 2, h = 0.2 and f = 0.6

The corresponding bifurcation diagram is shown in Figure 10.1(d) for $u > u_{fl}$.

For u=2.18, a symmetric stable limit cycle about the origin develops after the Hopf bifurcation and persists for 2.18 < u < 2.345. For $u \simeq 2.345$, a symmetry-breaking pitchfork bifurcation occurs, and the limit cycle becomes asymmetric for 2.346 < u < 2.40. Then, period-doubling bifurcations occur: for u=2.4051-2.416 (period-two motion), and for u=2.4161-2.4162 (period-four motion), which lead to chaotic motions for u>2.4163. Again, a period-one motion develops around a pair of two symmetrical points for 2.498 < u < 2.5289, followed by a period-two motion around the same points for 2.529 < u < 2.5297, period-four motion for 2.5298 < u < 2.5299, then the motion of the system will become chaotic for 2.53 < u < 2.536, and its motion reduces further to fixed points for u > 2.537.

The behaviour of this system may be summarized in Tables 10.1 and 10.2 as: Period-2,4,8 or period-doubling bifurcations followed by chaotic motions; another set of period-doubling bifurcations or period-2,4,8 motions followed again by chaotic motions; fixed points.

10.1.5 N = 2, h = 0.2 and f = 0.8

The bifurcation diagram corresponding to this case is shown in Figure 10.1(e) for $u > u_{fl}$. This case has already been discussed in detail in Chapter 9, Section 9.2.

A stable, symmetric limit cycle develops after the Hopf bifurcation (u=1.95), and becomes asymmetric through a symmetry-breaking pitchfork bifurcation at u=2.0275. Then, period-doubling bifurcations occur for u>2.08, as for example period-two motion for u=2.0801, period-four motion for u=2.0926, period-eight motion for u=2.0953, followed by chaotic motions for u>2.0955. The motion of the system reduces to fixed points for u>2.0968.

This dynamical behaviour is also summarized in Tables 10.1 and 10.2 as period-doubling bifurcations or period-2,4,8 motions leading to chaotic motions; fixed points.

10.2 N=2, SECOND MODEL WITH CUBIC SPRING; h = 0.5

10.2.1 N = 2, h = 0.5 and f = 0

The bifurcation diagram corresponding to this case has been shown in Figure 10.2(a) for $u > u_{fl}$.

This case has already been discussed in Chapter 9, Section 9.3. For $u_{fl} \simeq 4.47$, there exists a symmetric limit cycle which develops after the Hopf bifurcation. For 6.771 < u < 6.915 approximately, a period-one motion around two symmetrical points develops, followed by a period-two motion around the same points for 6.916 < u < 7.071, a period-four motion around one point and a period-two motion around its symmetrical point for u = 7.072, by a period-eight around one point, while around its symmetrical point a period-two motion always develops for 7.073 < u < 7.074, and a period-eight motion develops around the same pair of points for u = 7.075.

For u = 7.076, a global period-sixteen motion develops around the same points, and for 7.077 < u < 7.391 a chaotic motion around these points finally

occurs. For higher u, as for 7.392 < u < 7.4 a period-one motion develops around one of the two points, depending on the initial condition chosen. Finally, fixed points develop for u > 7.45. Again, for these parameters, the shapes of the phase-plane portraits are qualitatively the same as the ones in Figures 9.6, Chapter 9, obtained by the first model.

10.2.2 N = 2, h = 0.5 and f = 0.2

The bifurcation diagram corresponding to this case is shown in Figure 10.2(b) for $u > u_{fl} = 4$. For $u_{fl} \simeq 4$, a symmetric stable limit cycle develops after the Hopf bifurcation. For higher u, i.e. for $u \simeq 5.62$, a symmetry-breaking pitchfork bifurcation occurs, the limit cycle remains asymmetric for 5.62 < u < 6.237, then chaos develops through the period-doubling route as follows: period-2 for 6.238 < u < 6.3, period-4 for 6.31 < u < 6.328; for 6.329 < u < 6.33 the motion of the system is slightly chaotic, and for 6.331 < u < 6.5863 its motion becomes strongly chaotic. A periodic window (period-four motion) occurs for 6.5856 < u < 6.586. For 6.5864 < u < 6.989, a period-one motion develops around two symmetrical points, and is followed by period-two motions for 6.99 < u < 7.034, and by period-four motions for 7.035 < u < 7.045; the final motion of the system becomes chaotic for 7.046 < u < 7.3. A periodic window occurs for 7.31 < u < 7.47 (which is, in fact, an asymmetric limit cycle), and chaos arises again for 7.471 < u < 8. The motion of the system is reduced to fixed points for u > 8.

The behaviour of this model is summarized in the following words: period-2,4,8 or period-doubling bifurcations; chaos; period-2,4,8 or period-doubling bifurcations; chaos and fixed points.

10.2.3 N = 2, h = 0.5 and f = 0.4

The bifurcation diagram corresponding to this case is shown in Figure 10.2(c) for $u > u_{fl} = 3.5$. For u > 3.5, i.e. $u \simeq 4.0715$, a symmetry-breaking pitchfork bifurcation destroys the symmetry of the original limit cycle, and the limit cycle is asymmetric for 4 < u < 4.353. For higher u, i.e. 4.354 < u < 4.4, period-two motion occurs, which is followed by a period-four motion for u > 4.401, period-eight motion for 4.412 < u < 4.413, and leads to strongly chaotic motion for flow velocities u higher than 4.414, and smaller than u = 5. Finally, for u > 5.1, the global motion of the system is reduced to fixed points.

The behaviour of this model is summarized in Tables 10.1 and 10.2 as: period-2,4,8 (period-doubling) followed by chaos; fixed points.

10.2.4 N = 2, h = 0.5 and f = 0.6

The bifurcation diagram corresponding to this case is shown in Figure 10.2(d) for $u > u_{fl}$. For $u \ge 3$, a symmetric stable limit cycle develops after the Hopf bifurcation. For higher u, i.e. $u \simeq 3.4$, a symmetry-breaking pitchfork bifurcation occurs, the limit cycle is asymmetric for 3.4 < u < 3.782. For u = 3.783, the motion of the system is quasiperiodic, the Poincaré map being presented in the form of closed curves. For 3.784 < u < 3.7999, the motion of the system is chaotic. For a very small range of u, 3.756 < u < 3.761, the motion of the system is period-five. Finally, for u > 3.8, the motion reduces to fixed points.

The behaviour of this system is summarized in Tables 10.1 and 10.2 as follows: periodic; quasiperiodic; chaotic; fixed points.

10.2.5 N = 2, h = 0.5 and f = 0.8

This case has already been discussed in Chapter 9, Section 9.1. The bifurcation diagram is shown in Figure 10.2(e) for $u > u_{fl}$. For $u \simeq 2.80$, there is a stable

symmetric limit cycle after the Hopf bifurcation. The symmetry of the limit cycle is lost by a symmetry-breaking pitchfork bifurcation, which occurs at u = 2.832. The limit cycle remains asymmetric for 2.832 < u < 2.8677. For higher u, i.e. for u > 2.8678, the motion of the system reduces to fixed points.

The behaviour of this model may be summarized in Tables 10.1 and 10.2 as: periodic motion and fixed points; no chaos.

10.3 COMPARISON BETWEEN MODELS 1 AND 2 FOR TWO DIFFERENT h

(a) Case h = 0.2 and f = 0

In this case, the routes to chaos for the two models are the same: chaos is obtained following period-doubling motions; then by period-bubbling the motion of the system reduces finally to a fixed point.

(b) Case
$$h = 0.2$$
 and $f = 0.2$

In this case, we obtained the same bifurcation diagrams: the motion of the system is never chaotic. The motion remains periodic, but for large enough u it collapses to fixed points.

(c) Case
$$h = 0.2$$
 and $f = 0.4$

The routes to chaos are the same for the two models, through period-doubling bifurcations. For the second model, its motion finally is reduced to fixed points.

(d) Case
$$h = 0.2$$
 and $f = 0.6$

In this case, the routes to chaos are almost the same, through period-doubling bifurcations. For the second model, the motion of the system reduces finally to fixed points.

(e) Case h = 0.2 and f = 0.8

As has already been described in Chapter 9, Section 9.2, the route to chaos for the first model is via quasiperiodicity, while the route to chaos for the second model is via period-doubling bifurcations. Thus, although both models become chaotic, their routes to chaos are different.

(f) Case
$$h = 0.5$$
 and $f = 0$

As already described in Section 9.3, the route to chaos for the two models is the same, although differences exist from a quantitative point of view.

(g) Case
$$h = 0.5$$
 and $f = 0.2$

The route to chaos is the same, the motion of the system becoming chaotic through two series of period-doubling bifurcations; the first series comes from a symmetric limit cycle around the origin which becomes asymmetric through a symmetry-breaking pitchfork bifurcation, while the second series comes from a periodic motion around two symmetrical points. The behaviour for the second model reduces finally to fixed points for higher u.

(h) Case
$$h = 0.5$$
 and $f = 0.4$

The route to cheos is the same for this case: through period-doubling bifurcations. The motion of the system of the second model reduces to fixed points.

(i) Case
$$h = 0.5$$
 and $f = 0.6$

In this case, the routes to chaos for the two models are very different. For the first model, the route to chaos is through period-doubling bifurcations, while that of the second model is through quasiperiodicity, and of course for higher u, the motion of the second model reduces to fixed points.

(j) Case
$$h = 0.5$$
 and $f = 0.8$

As has already been explained in Chapter 9, Section 9.1, the route to chaos for the first model is through period-doubling bifurcations, while the second model never becomes chaotic; it only displays period-one motions.

10.4 MODEL 2 WITH RESTITUTION

COEFFICIENT AND h = 0.5

As a final modification to the models for the system under study, the impacting of the system with the external cylinder is modelled by the restitution coefficient theory, in conjunction with model 2. In this theory, when the system (in our case, the first cylinder of the articulated system) impacts any of the two sides of the external cylinder (left or right), its velocity after impact changes its sign and its value is smaller than the one before impact. Another important detail in the computer programming is the reduction of the time step near the wall; δt may become very small. If we introduce the three following notations:

Velocity before impact: Vbi

Velocity after impact: V_{ai}

Coefficient of restitution: cr

then, we shall have: $V_{ai} = -V_{bi} c_r$

10.4.1 f = 0

In the bifurcation diagram, Figure 10.3(a), a period-one motion develops for $u > u_{fl} \simeq 4.7$. This period-one motion remains symmetric around the origin for flow velocities 4.7 < u < 5.1. For higher flow velocities, as for u > 5.1, the motion of the system reduces to fixed points.

In this model, the system develops a period-one motion followed by fixed points and no chaotic motion has occurred, while in the model with a cubic spring model for impacting, the system becomes chaotic through period-doubling bifurcations.

$10.4.2 \quad f = 0.4$

The bifurcation diagram for this case is presented in Figure 10.3(b). A Hopf bifurcation appears in this system for $u \simeq 3.5$. This gives rise to a period-one motion for u > 3.5, which is symmetric around the origin, and remains so, for 3.5 < u < 3.7955.

For $u \simeq 3.8$, the system develops a period-two motion and impacts only on one side of the external cylinder; the side is determined as function of the sign of the initial condition. In this case, for u = 3.8, the initial condition is the positive velocity of the first cylinder and the system will impact the left side of the external cylinder, while for an opposite sign-initial condition, as for a negative velocity of the first cylinder, we obtain the impact of the system on the right side of the external cylinder. This period-two motion develops, in fact, only for a very small range of flow velocities, for 3.7965 < u < 3.8. The phase-plane portrait corresponding to the period-two motion of the system for u = 3.8 is shown in Figure 10.4(a).

For higher u, as for 3.801 < u < 3.832, periodic motion develops for our system which is impacting on both sides of the external cylinder. This periodic motion is followed for 3.833 < u < 3.835 by another period-8 motion for this system which again impacts both sides of the external cylinder. The phase-plane portraits corresponding to the periodic motion are presented in Figure 10.4(b) for u = 3.83, while the one for period-8 motion in Figure 10.4(c) for u = 3.835. For u = 3.836 and u = 3.837 a chaotic motion occurs which is well presented in the phase-plane portrait in Figure 10.4(d) for u = 3.836.

For higher flow velocities, for u > 3.838 a period-bubbling phenomenon takes place: for u = 3.838 and u = 3.839 the system develops a period-four motion which impacts only one side of the external cylinder, a period-two motion develops for 3.84 < u < 3.844 and is followed by a period-one motion for 3.845 < u < 3.855.

The phase-plane corresponding to these flow velocities are presented in Figure 10.5(a,b,c) for (a) u=3.838, (b) u=3.84 and (c) u=3.85.

This period-one motion modifies its shape for 3.856 < u < 3.86 and starts to develop around one fixed point, as presented in Figure 10.5(d) for u = 3.86, while chaotic motion further develops for 3.861 < u < 3.865 (Figure 10.5(e) for u = 3.865). Furthermore, this motion develops with impacting on both sides of the external cylinder, while period-one motion around two symmetrical points exists for u = 3.875; fixed points develop for 3.876 < u < 3.9.

In this case, the system develops chaotic motion through period-two and period-eight motions, while for higher flow velocities the system develops a period-bubbling phenomenon, and its motion will finally reduce to fixed points.

It might be said that there are similarities between the model with the impact modelled by the restitution coefficient and the one modelled by a cubic spring; in both cases chaos arises through period-two motions.

$10.4.3 \quad f = 0.8$

The bifurcation diagram for this case is presented in Figure 10.3(c). For 2.79 < u < 2.85, a limit cycle develops after the Hopf bifurcation which occurs for $u = u_{fl} \simeq 2.79$. By comparing Figures 10.6 and 10.7 for (a) u = 2.85, (b) u = 2.855 and (c) u = 2.86 the motion of the system is found to be period—one for (a) and chaotic for (b) and (c). The motion of the system will finally reduce to fixed points for u > 2.86.

The model with cubic spring as impact modelling never becomes chaotic, its motion being presented by period-one motion and by fixed points, while the model with restitution coefficient as model of impact becomes chaotic for a very small range of flow velocities ($\delta u = 0.01$), except for this range, the motion of the system is always period-one or reduces to fixed points.

Table 10.1: Routes to chaos for Model 1 and Model 2 $\,$

	h = 0.2		h = 0.5	
f	MODEL 1	MODEL 2	MODEL 1	MODEL 2
0	Period-2,4,8 motions above 2 symmetrical fixed points; Chaos			
	Period-bubbling motions; Period-one; Fixed points			
0.2	Periodic	Periodic	Period-2,4,8	Period-2,4,8
	No chaos	Fixed points	Chaos	Chaos
		No chaos		Fixed points
0.4	Period-2,4,8 motions above 2 symmetrical fixed points; Chaos			
		Fixed points		Fixed points
0.6	Period-2,4,8	Period-2,4,8	Period-2,4,8	Periodic
	Chaos	Chaos	Chaos	Quasiperiodic
		Fixed points		Chaos
				Fixed points
0.8	Period-1,2,1	Period-2,4,8	Period-2,4,8	Periodic
	Quasiperiodic	Chaos	Chaos	Fixed points
	No chaos	Fixed points		No chaos

Table 10.2: Comparison between Model 1 and Model 2

	h = 0.2		h = 0.5	
f	MODEL 1	MODEL 2	MODEL 1	MODEL 2
0	P-2,4,8;CH	P-2,4,8;CH	P-2,4,8;CH	P-2,4,8
	PB;P-1;FP	PB;P-1;FP	PB;P-1;FP	CH;PB;FP
0.2	P	Р	P-2,4,8;CH	P-2,4,8;CH
	NOCH	FP;NOCH	P-2,4,8;CH	P-2,4,8;CH;FP
0.4	P-2,4,8;CH	P-2,4,8;CH	P-2,4,8;CH	P-2,4,8;CH
	P-2,4,8;CH	FP	P-2,4,8;CH	FP
0.6	P-2,4,8;	P-2,4,8;CH	P-2,4,8;	P;QP;
	СН	P-2,4,8;CH;FP	СН	CH;FP
0.8	P-1,2,1;QP	P-2,4,8;CH;	P-2,4,8;	Р;
	NOCH	FP	СН	FP

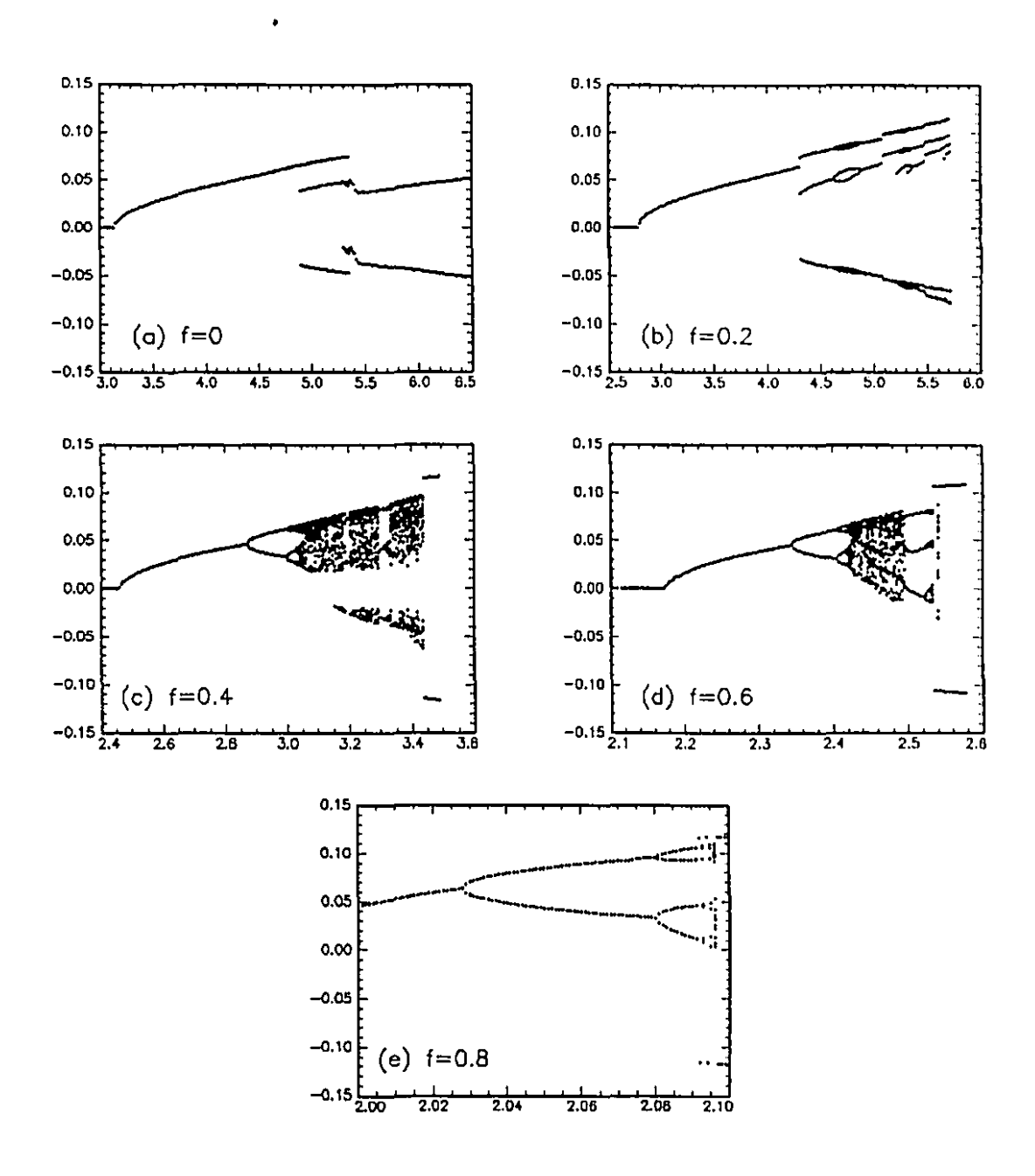


Figure 10.1. Bifurcation diagrams for the second model with cubic spring, for N=2 and h=0.2: (a) f=0, (b) f=0.2, (c) f=0.4, (d) f=0.6 and (e) f=0.8.

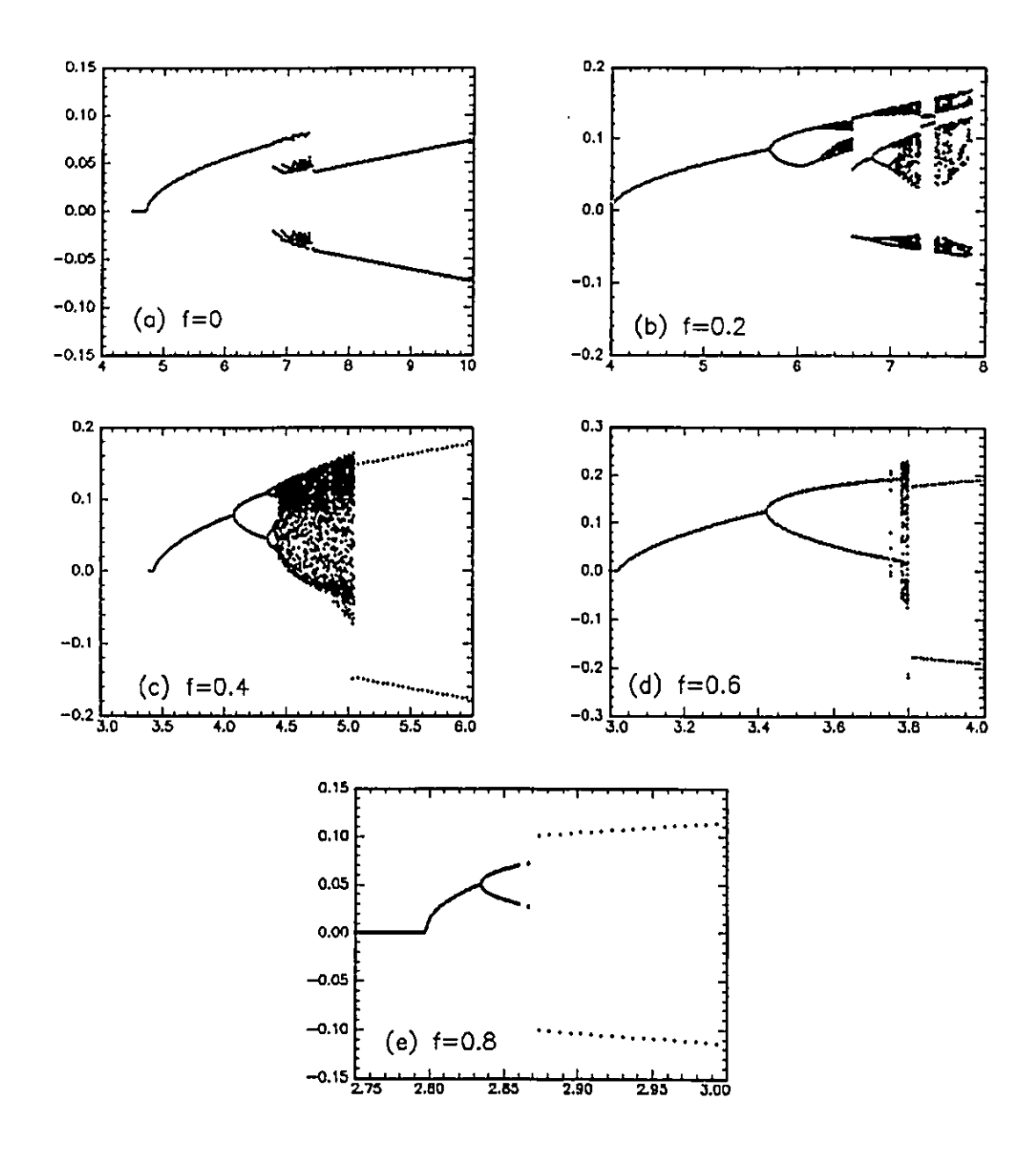


Figure 10.2. Bifurcation diagrams for the second model with cubic spring, for N=2 and h=0.5: (a) f=0, (b) f=0.2, (c) f=0.4, (d) f=0.6 and (e) f=0.8.

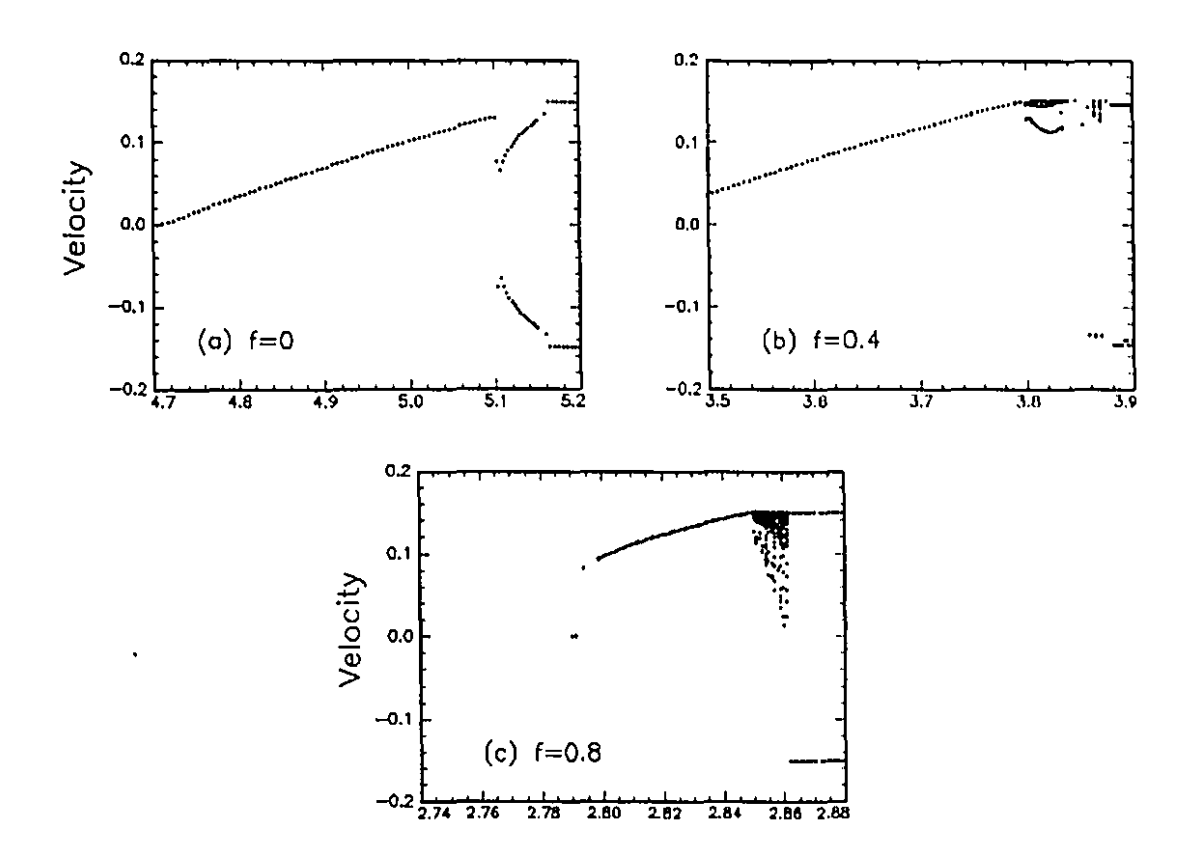


Figure 10.3. Bifurcation diagram for the second model with restitution coefficient, for N=2 and h=0.5: (a) f=0, (b) f=0.4 and (c) f=0.8.

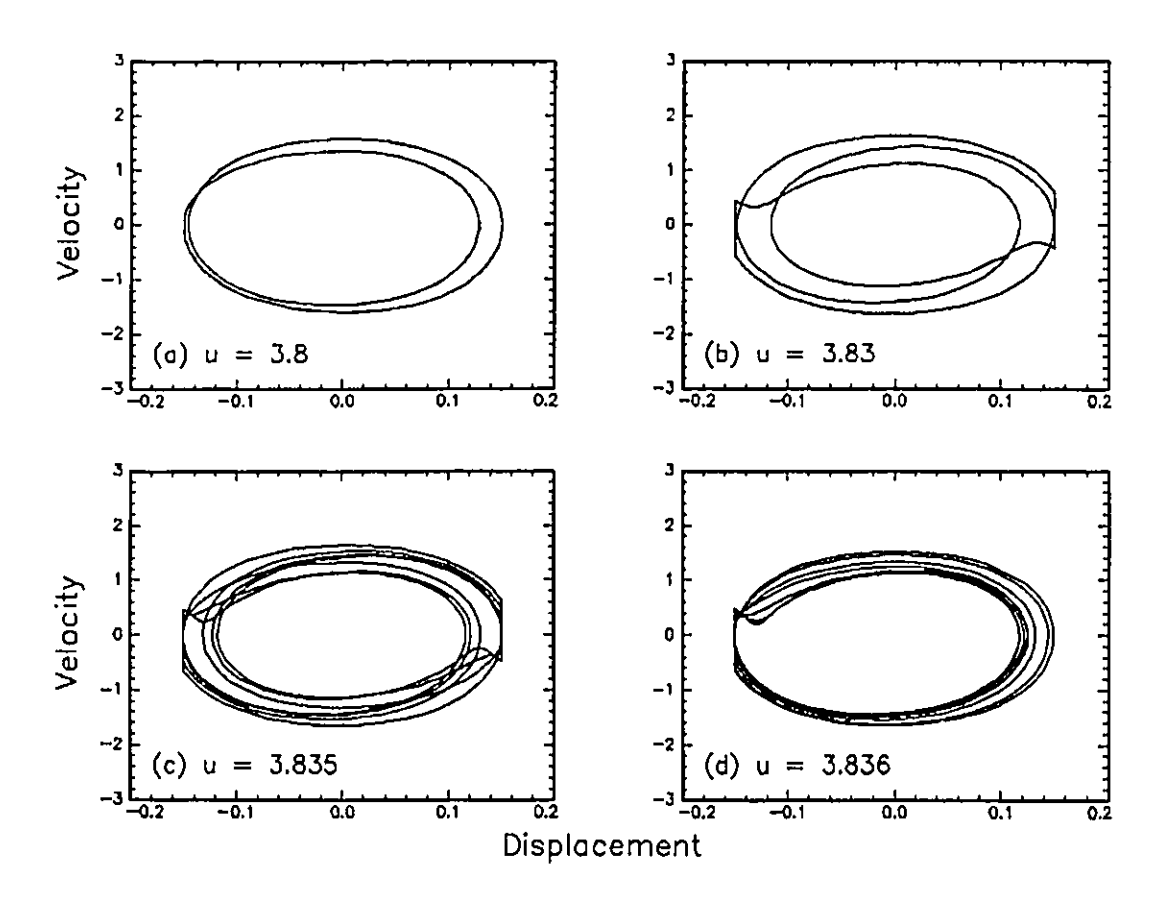


Figure 10.4. Phase-plane portraits of $\dot{\phi}_1(\tau)$ versus $\phi_1(\tau)$ at (a) u=3.8, (b) u=3.83, (c) u=3.835 and (d) u=3.836 for the second model with restitution coefficient: N=2, h=0.5 and f=0.4.

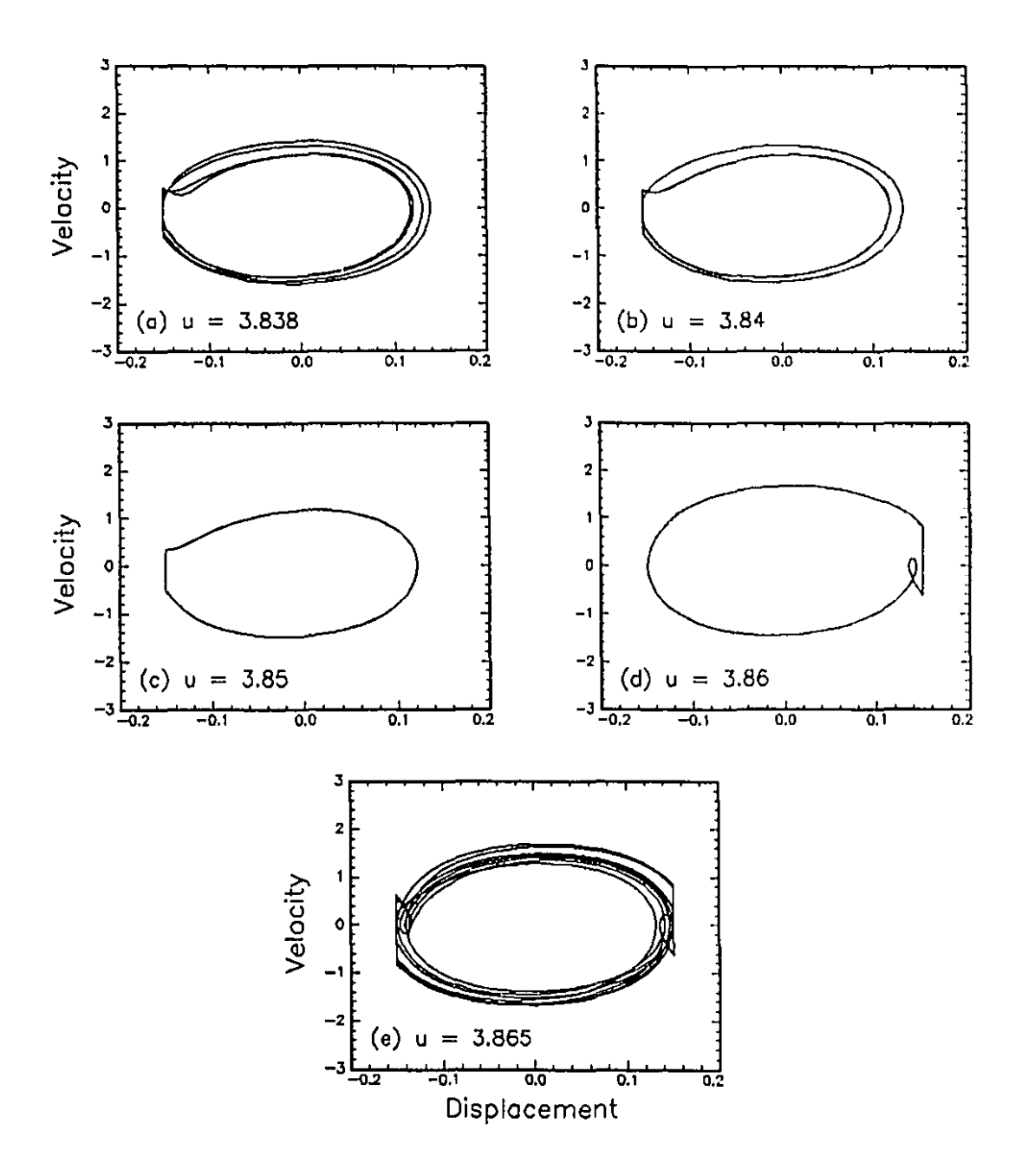


Figure 10.5. Phase-plane portraits of $\dot{\phi}_1(\tau)$ versus $\phi_1(\tau)$ at (a) u=3.838, (b) u=3.84, (c) u=3.85, (d) u=3.86 and (e) u=3.865 for the second model with restitution coefficient: N=2, h=0.5 and f=0.4.

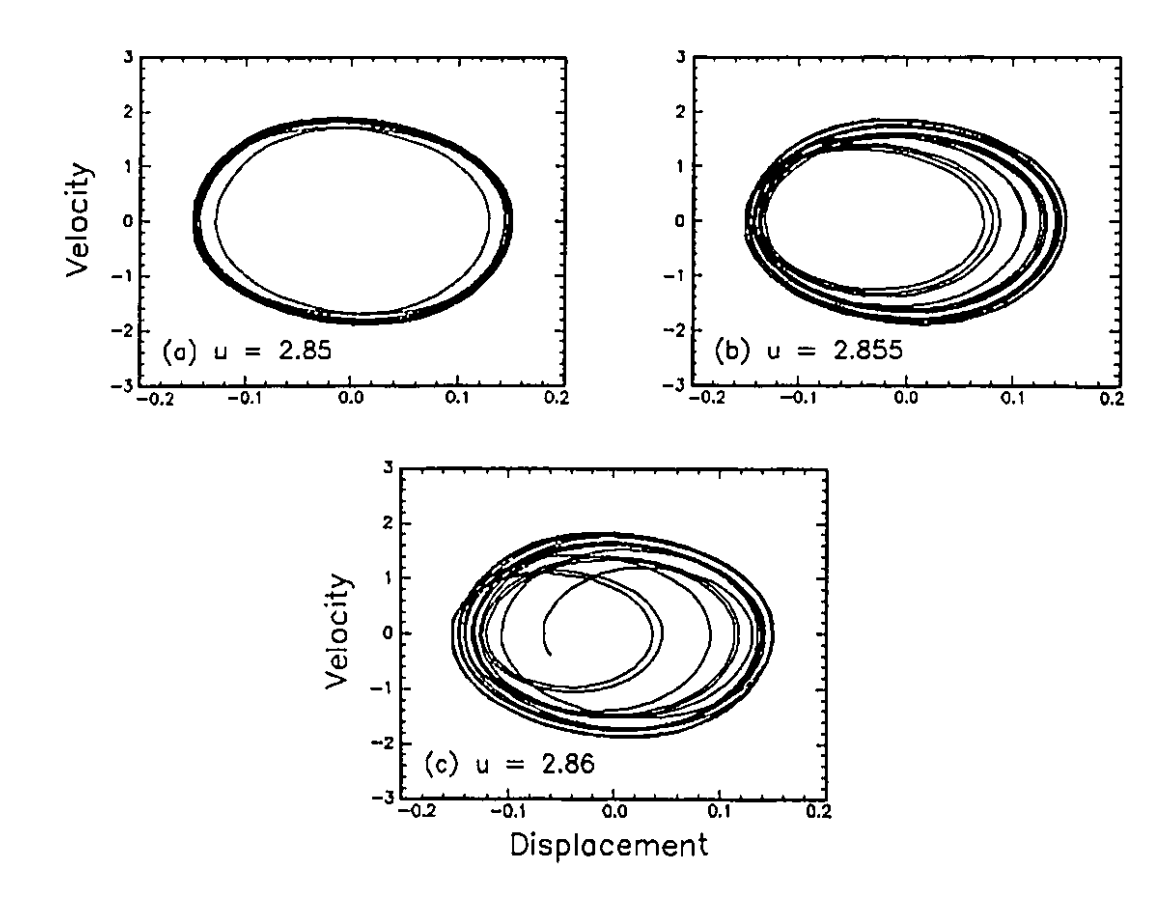


Figure 10.6. Phase-plane portraits of $\dot{\phi}_1(\tau)$ versus $\phi_1(\tau)$ at (a) u=2.85, (b) u=2.855 and (c) u=2.86 for the second model with restitution coefficient: N=2, h=0.5 and f=0.8.

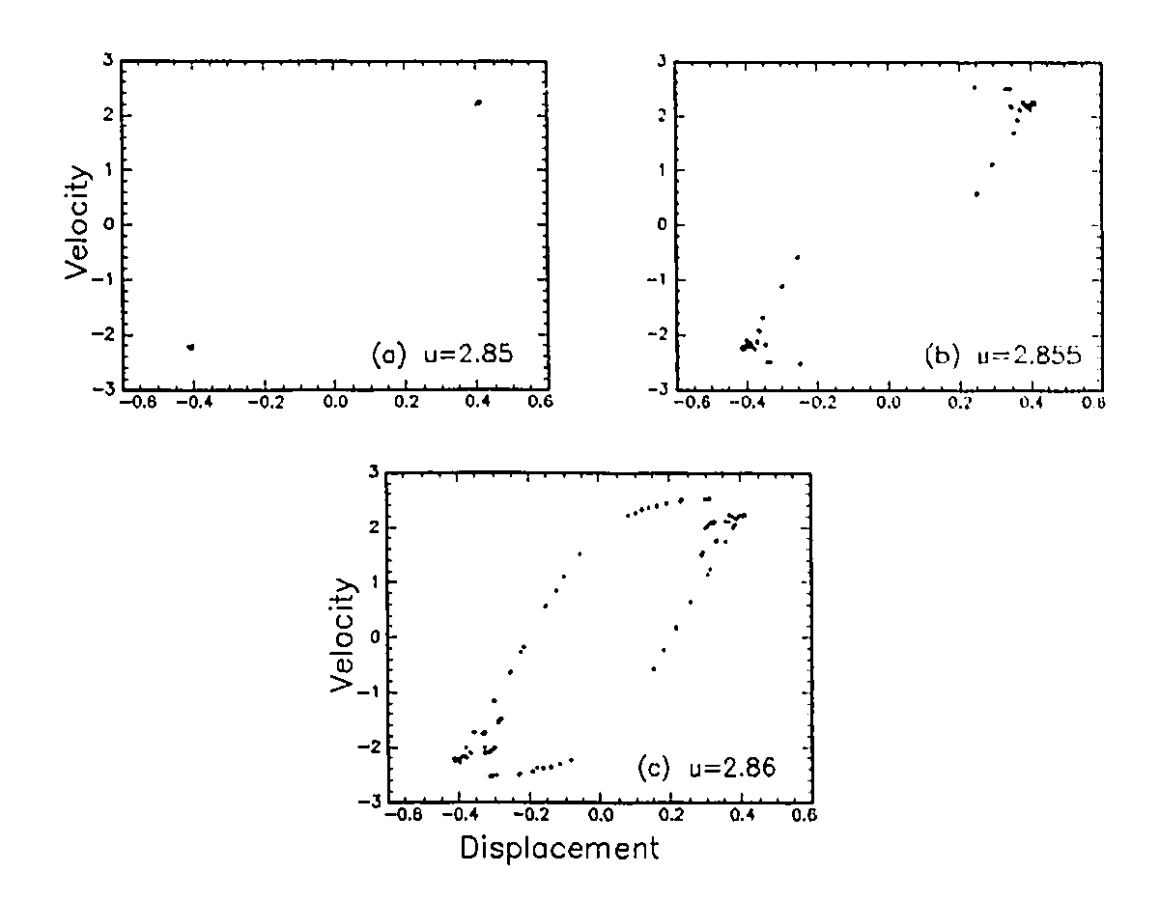


Figure 10.7. Poincaré maps of $\dot{\phi}_2(\tau)$ versus $\phi_2(\tau)$ when $\dot{\phi}_1(\tau) = 0$ for the second model with restitution coefficient: N = 2, h = 0.5 and f = 0.8, at (a) u = 2.85, (b) u = 2.855 and (c) u = 2.86.

Chapter 11

CONCLUSIONS

11.1 SUMMARY OF THIS THESIS WORK

In this thesis, the nonlinear dynamics of a system of rigid articulated cylinders subjected to external confined flow, has been studied for the first time. For this study, two original analytical models are used.

The equations of motion for both theoretical models were obtained by application of Lagrange's equations, in which the restoring, inertial and gravitational forces acting on the structure were taken into account in the kinetic and potential energies of the system. The hydrodynamic forces were incorporated partly in the kinetic energy and partly as generalized forces.

These two models, and hence the equations of motion, differ as follows: in the first model, the dynamics of the system when no impact occurs with the confining pipe is described by a set of linearized equations; in the second model, the motion-related nonlinearities are taken into account approximately and they are introduced mainly via Taylor expansions of the trigonometric functions of state variables; these nonlinear terms are retained up to order three. The first model was conceived for two, three or four articulated cylinders, while the second model only for two articulated cylinders.

In both models, impacting with the external channel is modelled by either a trilinear or a cubic spring, presumed to exist between the external cylinder and the articulated system contacting it. The impacting between the articulated system and the external channel has also been modelled in terms of a restitution coefficient.

An eigenvalue analysis was applied to the linearized model in order to find the values of the critical parameter (in our system, the critical flow velocity u_{cr}), at which divergence or flutter instability occurs; u_{cr} was found to be the same for both aforementioned models.

The nonlinear dynamics was found to be very varied, and many different routes to chaos for these models were discovered by varying only three parameters, not including the external flow velocity u, which is the main control parameter. The three nondimensional parameters correspond to: (a) the number of articulated cylinders, N, (b) the nondimensional annular gap, h, and (c) the paraboloid form of the end of the last cylinder, f. These routes to chaos were confirmed by various nonlinear dynamics tools, such as phase plane portraits, bifurcation diagrams, time trace and power spectrum plots, and by calculating the corresponding Lyapunov exponents.

An analytical study was further done by using centre manifold theory, in which the dimension of the system at the degenerate fixed point (for which one type of instability occurs) was reduced, in order to obtain a simplified subsystem. Using the method of averaging, supercritical Hopf bifurcations were obtained, and the approximation of the simplified subsystem on the centre manifold was compared with the actual flow computed numerically. Good agreement was found between these analytical and numerical results.

As many interesting cases from the nonlinear dynamics point of view were obtained, some of them will be described briefly in the following section.

11.2 DESCRIPTION OF THE MOST INTERESTING CASES

One type of interesting nonlinear behaviour was obtained for the first model with two and three articulated cylinders (N=2 and N=3), for the same h and f (h=0.2and f = 0.4) and the same other system parameters. In these cases, the route to chaos is through period-doubling bifurcations. This route takes place following a flutter instability (for N=2 model) or a divergence leading to flutter (for the N=3model). As the route for the N=3 model is richer from the nonlinear dynamics point of view, this route will be that outlined here, as follows. For $u = u_{div}$, a divergence instability occurs, which in nonlinear dynamics corresponds to a pitchfork bifurcation. Thus, for $u > u_{div}$, the origin is no longer a stable fixed point, but new stable fixed points on either side are generated. By linearizing the system in the vicinity of these new fixed points, purely imaginary eigenvalues appear for $u = u_{LC}$, and limit cycles (period-one motions) develop for this flow velocity. This is followed by a cascade of *period-doubling* bifurcations, eventually leading to chaotic motions. The Feigenbaum number was found to be in fairly good agreement to the ideal Feigenbaum number. Then, for a higher flow velocity, the chaotic motion of the system reduces suddenly to a period-one motion. Subsequently, for higher u, chaos occurs once more, but following another route: through quasiperiodicity. The motion becomes quasiperiodic, the quasiperiodicity being verified by constructing the corresponding Poincaré maps which have the form of closed curves and for which the ratios of fundamental frequencies are calculated. This is an interesting case, which displays sequentially two routes to chaos, the period-doubling and the quasiperiodic route; chaos occurs after an initial loss of stability via a pitchfork bifurcation which later gives rise to flutter; in most of the other cases, either the period-doubling or the quasiperiodic route occurs following directly a Hopf bifurcation.

Another interesting case is the one for which chaos arises through intermittency, which occurred only for the first model with N=3, h=0.5 and for two different $f\colon f=0.2$ and f=0.4. In this case, for $u=u_{div}$ a pitchfork bifurcation occurs and, as in the preceding example, new stable fixed points arise with increasing u. By linearizing the system around these points, the occurrence of unstable limit cycles could be explained by the purely imaginary eigenvalues which arise for a flow velocity u_{LC} which is impossible to detect in a bifurcation diagram, as the difference between u at which chaos through intermittency appears and u for which the motion of the system reduces to fixed points is too small, as already explained in previous chapters. Then, for a flow velocity very close to u_{LC} an unstable limit cycle develops and for large enough time τ for this u, chaos through intermittency is obtained. The behaviour of the system with increasing τ is explained in the next paragraph.

The instability is weak and, although trajectories are attracted to the vicinity of the limit cycle, the limit cycle amplitude increases gradually but continuously with time. For a longer time interval, one of the bursts of "turbulence" is captured, which are characteristic of this type of chaos; the corresponding phase-plane plots reinforce the view that, in this time period, the oscillation is chaotic. For higher τ , a quiescent, nearly steady oscillation followed by chaotic oscillations with several unsteady bursts is noticed. As shown through the construction of first and second return maps, as well as from the distribution of the lengths of laminar phases $P(\tau)$ versus τ , or from the number of laminar phases lasting longer than τ_0 , $N(\tau > \tau_0)$ versus τ_0 , the intermittency is of type III.

The third interesting case to be discussed here is the one corresponding to the first model with N=2, h=0.5 and f=0 (which corresponds to a blunt end). A limit cycle develops after a Hopf bifurcation and is followed by a periodone symmetric motion around two symmetric points with respect to the origin. Furthermore, period-two, period-three and period-four motions, followed by chaotic

motions may be observed around the same two points. For higher flow velocities u depending on the initial conditions chosen, a reverse period doubling sequence around one of the two symmetric points takes place; that means period-four, period-two, and finally period-one motion. Finally the motion reduces further from a period-one oscillation to a fixed point. Thus, this case has an interesting dynamical behaviour, as u increases: chaotic motions arise around two symmetric points with respect to the origin, through period-n motions, followed by a period-bubbling phenomenon, and finally the motion reduces to fixed points.

It is impossible to determine the behaviour of the first model with N=2 for flow velocities u between u_{div} and u_{fl} , i.e. $u_{div} < u < u_{fl}$, because of the fact that its amplitudes become too large and this model is no longer valid for this range of u. With the second model, however, no such difficulty exists. The dynamics will be discussed in the following paragraph, for the second model with N=2, h=0.2 and f=0.8.

For $u = u_{div}$ a pitchfork bifurcation occurs, so that the motion of the first cylinder reduces to a fixed point; for higher u, as for $u > u_{div}$, new fixed points occur as the flow velocity u increases: the distance away from the origin for these fixed points increases with u for a certain range of u, while it decreases with u for a second range of u, and finally increases again for a third range of u. Then, the system is stable about the origin for the fourth range of u. And finally, through a period-doubling cascade, the motion of the system becomes chaotic and for higher flow velocities reduces suddenly to a fixed point as in all cases considered when analyzed by the second model, while for the first model the amplitudes of the system become too large and solutions fail to converge.

In the cases considered until now impacting was modelled by a cubic spring. One interesting case was found with the restitution coefficient method and it is discussed next. For h = 0.5, f = 0.4 and $c_r = 0.75$, for $u = u_{fl}$ a Hopf bifurcation appears in the system. This gives rise to a symmetric period—one motion. For higher

u, the system develops a period-two motion and impacts only on one side of the external cylinder, the side being determined from the sign of the initial conditions. This period-two motion develops in fact only for a very small range of flow velocities. As u increases, a periodic motion followed by a period-eight and by chaotic motion develops, while the system then impacts on both sides of the external cylinder. For higher flow velocities, a reverse period-doubling sequence takes place: period-four, period-two and period-one motion which impacts only on one side of the external cylinder. This period-one motion modifies its shape and develops around one fixed point; it is followed at higher u by chaotic motions again. In the end, period-one motion around two symmetrical points exists and reduces to fixed point.

It should be mentioned that chaos does not always develop. In some cases the motion of the system remains periodic.

11.3 SUMMARY OF CONCLUSIONS

Two new models were constructed for the articulated cylinder system subjected to external axial flow confined by an external channel; the so-called first model was described by a linearized set of equations, apart from terms associated with impacting. In the so-called second model geometric nonlinearities, again other than those associated with impacting, were introduced mainly via Taylor expansions of the trigonometric functions of the state variables. The nonlinear behaviour of this system was studied for the first time in this thesis.

Three different models for simulating the impact of the articulated cylinder system with the external channel were considered: a cubic spring (for both the first and the second model), a trilinear spring (for the first model), and through a restitution coefficient (for the second model). The qualitative behaviour of the system (first or second model) with different impact models was found to be the same.

11.3.1 Dynamics of the N = 2 and N = 3 systems via the first model

For N=2, all motions leading to chaotic motions develop following a flutter instability, while for N=3 most of these motions (except the ones for f=0, i.e. a blunt end) occur following a divergence instability, giving birth to flutter; in this case, the new stable fixed points become unstable at higher u, and this results in a flutter instability according to linear analysis, or more precisely in the nonlinear analysis to a Hopf bifurcation, so that limit cycles develop around the new fixed points.

After performing the eigenvalue analysis of the system, the nonlinear equations were solved numerically-except for an analytical study, as summarized in section 11.3.4 here. The numerical integration was performed generally by the Runge-Kutta algorithm; some results were checked via the Runge-Kutta-Fehlberg algorithm and were found to be the same. Various sets of initial conditions were used, to check whether there are coexisting attractors, but in fact the solutions always converged to the same set.

For N=2 and h=0.2 and h=0.5 and for most values of f, the nonlinear behaviour of the system is qualitatively the same: chaos develops via the classical period-doubling route; except for f=0.8, in which case the route to chaos is through quasiperiodicity.

For N=3 and for different h, the routes to chaos are different, as follows: for h=0.2, a period-doubling cascade leads to chaos, while for h=0.5 chaotic motions occur through intermittency. There are some exceptions to this generic behaviour: (i) for f=0.8, and for f=0, h=0.5, chaotic motion is preceded by quasiperiodicity; (ii) for f=0, h=0.2, no chaotic motions at all develop, in contrast to what was obtained for the N=2 system.

In fact the dissimilarity in the results for N=2 and N=3 is not surprising

if one compares with the work of Païdoussis and Deksnis (1970) for the analogous system involving an articulated system with internal flow; in that case also, where calculations for all N from 2 to 8 as well as for the continuously flexible system $(N \to \infty)$ were conducted, the dynamics for N = 2 were particular; N = 3, however, began to display generic behaviour, typical of higher values of N.

11.3.2 Comparison of the dynamics of N = 2 system as predicted by the first and second models

It is impossible to determine the dynamics of the system with the first model for flow velocities u between the values for divergence and flutter, as predicted by linear theory, i.e. $u_{div} < u < u_{fl}$, because of the fact that its amplitudes become too large and the model is no longer valid for this range of u. In contrast, according to the second model, motion reduces to fixed points in the same range of u. The same applies for the range of flow velocities u higher than those for which the motion of the system is and remains chaotic u_{ch} , i.e. $u > u_{ch}$: the first model cannot converge, while the second one gives results.

It is of interest, however, that in the ranges of u where both models give results, notably for $u_{fl} < u < u_{ch}$, the dynamical behaviour of the system is qualitatively similar. This gives us confidence in the predictive ability of both models, at least in this crucial range of u, and suggests that the dynamics is reasonably robust and the behaviour may be structurally stable.

11.3.3 The effect of varying f and h

As the free-end form coefficient f increases, the flow velocity at which the first critical flow velocity u_{cr} occurs, decreases; or, as the end of the last cylinder has a more streamlined end, the system becomes unstable for a lower u_{cr} than for a blunt end.

As the hydraulic diameter h increases, the critical flow velocity at which the first instability u_{cr} occurs, increases. This is also known, as the diameter of the external cylinder D_{cyl} , or the hydraulic diameter $D_h = D_{cyl} - D$ increases, the system becomes unstable at higher flows; for unconfined flow $D_h \to \infty$, the critical flow velocity u_{cr} should be higher than in confined flow.

11.3.4 Analytical dynamics

The analytical part of the nonlinear study is confined to N=2, according to the first model (as described in Chapter 5). In this analytical study, centre manifold theory is used, whereby the fourth order system is reduced to one of second order (for the Hopf bifurcation). The analytical results obtained fully support the numerical ones and demonstrate the usefulness and power of centre manifold theory.

11.3.5 On the variety of nonlinear dynamical behaviour obtained

The most interesting aspect of the research described in this thesis is that it uncovered an immense richness in the dynamics of this system, surpassing that for the pipe conveying fluid.

For example for the N=3 system, as analyzed by the first model, in which only two parameters were varied h and f, three different routes to chaos were found: by a period-doubling cascade, by quasiperiodicity and via intermittency. This may not be unique, but if it is not, it is certainly rare.

In the case of type III intermittency, the critical flow velocity at which a stable limit cycle occurs cannot be pin-pointed, because of the fact that the difference between the flow velocity at which the motion of the system reduces to fixed point and the flow velocity at which the motion of the system becomes chaotic through intermittency is very small. For this reason, the intermittency phenomenon that

has been found in some of the cases considered in this thesis is quite original; to the author's knowledge this has not been encountered elsewhere.

These were the most salient conclusions reached in the work presented in this thesis. Some suggestions for extending this work follow.

11.4 SUGGESTIONS FOR FUTURE WORK

In this thesis, an original theoretical study has been made of the nonlinear dynamics of an articulated cylinder system subjected to confined axial flow. The purpose was to demonstrate that this system is capable of displaying an extremely rich behaviour, and hence — especially as it corresponds to an interesting and practically important physical system —that is deserving of further study.

The work and especially the results presented in this thesis represent a sample of a larger set. In effect, the only parameters that were varied here, other than the flow velocity u, which is the control parameter, and the number of articulations N, was the narrowness of the annulus, h, and the end-form coefficient, f; however, there are three other important parameters which might be varied in the future. These are: β , which is the nondimensional mass parameter, which is dependent on the mass of the cylinders and the mass of the displaced fluid; ϵ , which is the slenderness parameter ($\epsilon = L/D$); and γ , which is the gravitational parameter, which is related to gravity and buoyancy forces, and to the stiffnesses of the rotational springs at the articulations. As three routes to chaos were found, it would be interesting to trace how these routes transition from one to another for different ranges of parameters.

It is known that when a pitchfork and a Hopf bifurcation occur simultaneously for some parameters, a double degeneracy occurs. By using centre manifold theory and normal forms, it has been shown in some other cases that heteroclinic cycles exist in the reduced subsystem, suggesting the possible existence of chaotic behaviour (Li and Païdoussis (1994)). Unfortunately, for the ranges of parameters considered

in this thesis, no double degeneracy was found, so that no further work in this direction was done. However, the search for doubly degenerate conditions was not truly exhaustive. As another possible further work, it would be interesting to search further in the parameter space, with the aim of finding double degeneracy.

In this, the first nonlinear study of the system, several aspects of the physical system were idealized and simplified. It is clear now, after discovering the richness in the dynamical behaviour of the system, that it is definitely worth to spend the effort and time which would improve the model by bringing it closer to physical reality. One such item would be the proper, position-dependent modelling of the added mass and fluid viscous coefficients. Another is the modelling of the flow close to the articulation as it approaches the outer confining cylinder. Yet another would extend the model to cover three-dimensional motions, in which case the modelling of the impact would be much more complex-but not impossibly so (see, for example, the work of Mureithi (1993) for a different problem)). In all this, since there is a considerable range of possibilities, the choices should be guided by a real (experimental) system, which should be investigated concurrently, as discussed in the next paragraph.

An experimental investigation is recommended, in order to verify the theoretical results presented here and before further analytical work is done. A demonstration was already completed in the laboratory, for which a system of two articulated cylinders made of alderin was subjected to confined axial flow. By varying only two parameters: the external flow velocity, u, and the form coefficient of the downstream end of the last cylinder, f, one obtains critical flow velocities u_{cr} very close to those found by the theory; more exactly, the same instabilities, i.e. divergence or flutter for flow velocities relatively close to the ones predicted by linear theory. These experiments should be taken further to verify that chaotic motions of the system arise for $u > u_{cr}$, and that they are (or are not) obtained through the different routes mentioned previously.

Concerning bifurcation theory, the use of some existing software, such as the AUTO packages (Doedel 1981) would allow systematic construction of the bifurcation diagrams, and would provide more information concerning the system behaviour. A bifurcation diagram was constructed by AUTO for Case 4.1, for which the route to chaos is through period-doubling of the motions. In this case, one may find the following, in the notation of AUTO: HB (Hopf bifurcation), BP (Bifurcation point), PD (Period-doubling); as well as MP (end of branch; no convergence). The flow velocities u for HB, BP and PD were confirmed to correspond to those obtained by Runge-Kutta integration, corresponding to the Hopf, pitchfork and period-doubling bifurcations. Further work would be useful, perhaps revealing solution branches not found by our methods.

BIBLIOGRAPHY

Ashley, H. and Haviland, G. 1950, "Bending vibrations of a pipeline containing flowing fluid". Journal of Applied Mechanics, Vol. 17, pp. 229-232.

Bajaj, A.K. 1982, "Bifurcating periodic solutions in rotationally symmetric systems". SIAM Journal of Applied Mathematics, Vol. 42, pp. 1078-1098.

Bajaj, A.K. and Sethna, P.P. 1982a,b, "Bifurcations in three-dimensional motions of articulated tubes. Part 1: Linear systems and symmetry. Part 2: Non-linear analysis". *Journal of Applied Mechanics*, Vol. 49, pp. 606-618.

Benettin, G., Galgani, L., Giogilli, A. and Strelcyn, J.M. 1980, "Lyapunov characteristic exponents for smooth dynamical systems and for Hamiltonian systems. A method for computing all of them. Part 2: Numerical application". *Meccanica*, Vol. 15, pp. 21-30.

Benjamin, T.B. 1961a, "Dynamics of a system of articulated pipes conveying fluid". Proceedings Royal Society (London), Vol. 261 (A), pp. 457-486.

Benjamin, T.B. 1961b, "Dynamics of a system of articulated pipes conveying fluid". Proceedings Royal Society (London), Vol. 261 (A), pp. 487-499.

Bergé, P., Pomeau, Y. and Vidal, C. 1984, Order within chaos: Towards a deterministic approach to turbulence. New York: John Wiley and Sons.

Bourrières, F.J. 1939, "Sur un phénomène d'oscillation autoentretenue en mécanique des fluides réels". Publications Scientifiques et Techniques du Ministère de l'Air, No. 147.

Burgreen, D., Byrnes, J.J. and Benforado, D.M. 1958, "Vibration of rods induced by water in parallel flow". *Transactions ASME*, Vol. 80, pp. 991-1003.

Chen, S.S. 1977, "Flow induced vibrations of circular cylindrical structures. Part I: Stationary fluids and parallel flow". The Shock and Vibration Digest, Vol. 9 (1), pp. 25-38.

Chen, S.S. and Wambsganss, M.W. 1971, "Parallel-flow-induced vibration of fuel rods". *Nuclear Engineering and Design*, Vol. 18, pp. 253-278.

Chen, S.S., Wambsganss, M.W., Jendrzejczyk, J.A. 1976, "Added mass and damping of a vibrating rod in confined viscous fluids". *Journal of Applied Mechanics*, Vol. 98, pp. 325-329.

Doedel, E. 1981, "AUTO: A program for the automatic bifurcation analysis of autonomous systems". *Congressus Numerantium*, Vol. 30, pp. 265-284.

Dunlop Dracones 1969, The Dunlop Rubber Company Ltd., Fawley, Hants, U.K.

Feodos'ev, V.P. 1951, "Vibrations and stability of a pipe when liquid flows through it". *Inzhenernyi Sbornik*, Vol. 10, pp. 169-170.

Goldstein, S. 1938, Modern Developments in Fluid Dynamics. Oxford: Clarendon Press, p. 425.

Gregory, R.W. and Païdoussis, M.P. 1966a,b, "Unstable oscillation of tubular cantilevers conveying fluid. Part 1: Theory. Part 2: Experiments". *Proceedings of the Royal Society (London)*, Vol. 293(A), pp. 512-542.

Grotberg, J.B. and Davis, S.H. 1980, "Fluid dynamic flapping of a collapsible channel: sound generation and flow limitation". *Journal of Biomechanics*, Vol. 13, pp. 219–230.

Guckenheimer, J. and Holmes, P.J. 1983, Nonlinear Oscillations, Dynamical Systems and Bifurcations of Vector Fields. New York: Springer.

Hale, J.K. 1969, Ordinary Differential Equations. New York: Wiley - Interscience.

Hamy, N. 1971, "The Trebon Sea Chain System", Trebon Holdings Ltd., Montréal, Canada.

Hannoyer, M.J. and Païdoussis, M.P. 1979a,b, "Dynamics of slender tapered beams with internal or external axial flow. Part 1: Theory. Part 2: Experiments". Journal of Applied Mechanics, Vol. 46, pp. 45-57. Hawthorne, W.R. 1961, "The early development of the Dracone flexible barge". Proceedings of the Institution of Mechanical Engineers (London), Vol. 175, pp. 52-83.

Hennig, K., Platen, E. and Grunwald, G., 1980, "Treatment of flow-induced pendulum oscillations". Practical Experiences with Flow-Induced Vibrations (E. Naudascher and D. Rockwell, Eds). Berlin: Springer-Verlag, pp. 140-143.

Hobson, D.E. 1982, "Fluid-elastic instabilities caused by flow in annulus". Proceedings of the Third International Conference on Vibration of Nuclear Plant, pp. 440-463, Keswick, U.K.

Hoerner, S.F. 1958, Fluid-dynamic drag; practical information on aerodynamic drag and hydrodynamic resistance. New Jersey: Midland Park.

Housner, G.W. 1952, "Bending vibrations of a pipe line containing flowing fluid". *Journal of Applied Mechanics*, Vol. 19(2), pp. 205-208.

Li, G.X. and Païdoussis, M.P. 1994, "Stability, double degeneracy and chaos in cantilevered pipes conveying fluid". *International Journal of Non-Linear Mechanics*, Vol. 29(1), pp. 83-107.

Lighthill, M.J. 1960, "Note on the swimming of slender fish". *Journal of Fluid Mechanics*, Vol. 9, pp. 305-317.

Manneville, P. and Pomeau, Y. 1980, "Different ways to turbulence in dissipative dynamical systems". *Physica* 1D, Vol. 1 (2), pp. 219-226.

Mateescu, D., and Païdoussis, M.P. 1985 "The unsteady potential flow in an axially variable annulus and its effect on the dynamics of the oscillating rigid center-body". *Journal of Fluids Engineering*, Vol. 107, pp. 421-427.

Mateescu, D., and Païdoussis, M.P. 1987, "Unsteady viscous effects on the annular-flow-induced instabilities of a rigid cylindrical body in a narrow duct".

Journal of Fluids and Structures, Vol. 1, pp. 197-215.

Mateescu, D., Païdoussis, M.P. and Bélanger, F. 1988, "Unsteady pressure measurements on an oscillating cylinder in narrow annular flow". *Journal of Fluids and Structures*, Vol. 2, pp. 615-628.

McLeod, A.R. 1918, Report Memorandum Aeronautical Research Communications, London, no. 554.

Moon, F.C. 1987, Chaotic Vibrations: An Introduction for Applied Scientists and Engineers. New York: John Wiley and Sons.

Munk, M.M. 1924, NACA Report, No. 184.

Mureithi, N.W. 1993, "Nonlinear dynamics of a loosely supported cylinder in cross-flow", PhD thesis, McGill Library.

Newhouse, S., Ruelle, D., and Takens, F. 1978, "Occurrence of strange axiom-A attractors near quasiperiodic flows on T^m , m > 3". Communications in Mathematical Physics, Vol. 64, pp. 35-40.

Niordson, F.I. 1953, "Vibrations of a cylindrical tube containing flowing fluid". Kungliga Tekniska Hogskolans Handlingar, Vol. 73.

Païdoussis, M.P. 1965, "The amplitude of fluid-induced vibration of cylinders in axial flow". Atomic Energy of Canada, Report AECL-2225.

Païdoussis, M.P. 1966a,b, "Dynamics of flexible slender cylinders in axial flow. Part 1: Theory. Part 2: Experiments". *Journal of Fluid Mechanics*, Vol. 26, pp. 717-751.

Païdoussis, M.P. 1968, "Stability of towed, totally submerged flexible cylinders". *Journal of Fluid Mechanics*, Vol. 34, pp. 273-297.

Païdoussis, M.P. 1970, "Dynamics of tubular cantilevers conveying fluid".

Journal of Mechanical Engineering Science, Vol. 12, pp. 85-103.

Païdoussis, M.P. 1973, "Dynamics of cylindrical structures subjected to axial flow". Journal of Sound and Vibration, Vol. 29, pp. 365-385.

Païdoussis, M.P. 1976, "Dynamics of fuel strings in axial flow". Annals of Nuclear Energy, Vol. 3, pp. 19-30.

Païdoussis, M.P. 1979, "The dynamics of clusters of flexible cylinders in axial flow: Theory and Experiments". *Journal of Sound and Vibration*, Vol. 65, pp. 391-417.

Païdoussis, M.P. 1980, "Flow induced vibrations in nuclear reactors and heat exchangers. Practical experiences and state of knowledge", Practical Experiences with Fluid-Induced Vibrations (E. Naudascher and D. Rockwell, Eds). Berlin: Springer-Verlag, pp. 1-81.

Païdoussis, M.P. 1986, "Stability of a chain of cylinders travelling underwater".

Proceedings of the Fifth International Offshore Mechanics and Arctic Engineering

Symposium, Vol. 1, pp. 483-490.

Païdoussis, M.P. 1987, "Flow-induced instabilities of cylindrical structures". Applied Mechanics Reviews, Vol. 40(2), pp. 163-175.

Païdoussis, M.P. 1993, "Calvin Rice Lecture: Some curiosity-driven research in fluid-structure interactions and its current applications". ASME Journal of Pressure Vessel Technology, Vol. 115, pp. 2-14.

Païdoussis, M.P. and Botez, R.M. 1993, "Chaotic dynamics of articulated cylinders in confined axial flow". *Journal of Fluids and Structures*, Vol. 7, pp. 719-750.

Païdoussis, M.P., Cusumano, J.P. and Copeland, G.S. 1992, "Low-dimensional chaos in a flexible tube conveying fluid". *Journal of Applied Mechanics*, Vol. 59, pp. 196-205.

Païdoussis, M.P. and Deksnis, E.B. 1970, "Articulated models of cantilevers conveying fluid: the study of a paradox". *Journal of Mechanical Engineering Science*, Vol. 12, pp. 288-300.

Païdoussis, M.P. and Li, G.X. 1993, "Pipes conveying fluid: A model dynamical problem". Journal of Fluids and Structures, Vol. 7, pp. 137-204.

Païdoussis, M.P., Li, G.X. and Rand, R.H. 1991, "Chaotic motions of a constrained pipe conveying fluid: Comparison between simulation, analysis and experiments". *Journal of Applied Mechanics*, Vol. 58, pp. 559-565.

Païdoussis, M.P., Mateescu, D. and Sim, W.G. 1990, "Dynamics and stability of a flexible cylinder in a narrow coaxial cylindrical duct subjected to annular flow".

Journal of Applied Mechanics, Vol. 57, pp. 232-240.

Païdoussis, M.P. and Moon, F.C. 1988, "Nonlinear and chaotic fluidelastic vibrations of a flexible pipe conveying fluid". *Journal of Fluids and Structures*, Vol. 2, pp. 567-591.

Païdoussis, M.P. and Ostroja-Starzewski, M. 1981, "Dynamics of a flexible cylinder in subsonic axial flow". AIAA Journal, Vol. 19, pp. 1467-1475.

Païdoussis, M.P. and Semler, C. 1993, "Nonlinear dynamics of a fluid-conveying cantilevered pipe with an intermediate spring support". *Journal of Fluids and Structures*, Vol. 7, pp. 269-298.

Pavlica, R.T. and Marshall, R.C. 1966, "An experimental study of fuel assembly vibrations induced by coolant flow". *Nuclear Engineering Design*, Vol. 4, pp. 54-60.

Peterka, F. 1991, "Flow-induced-impact oscillation of a spherical pendulum".

Journal of Fluids and Structures, Vol. 5, pp. 627-650.

Quinn, E.P. 1962, "Vibration of fuel rods in parallel flow". U.S. Atomic Energy Commission, Report GEAP - 4059.

Quinn, E.P. 1965, "Vibration of SEFOR fuel rods in parallel flow". U.S. Atomic Energy Commission, Report GEAP - 4966.

Relf, E.F. and Powell, C.H. 1917, Reports and Memoranda of the Aeronautical Research Council, London, no. 307.

Roström, K.G. and Andersson, N. 1964a, "Boiler element for Marviken, vibration test with one rod". Ab. Atomenergi, Stockholm, Arbetsrapport RPL-724.

Roström, K.G. and Andersson, N. 1964b, "Superheater element for Marviken, vibration test with one rod". Ab. Atomenergi, Stockholm, Arbetsrapport RPL-725.

Roström, K.G. 1964c, "Seven-rod fuel element vibration tests". Ab. Atom-energi, Stockholm, Arbetsrapport RPL-726.

Roth, W. 1964, "Instabilität durchströmter Rohre". Ingenieur-Archiv, Vol. 33, pp. 236-263.

Rousselet, J. and Herrmann, G. 1977, "Flutter of articulated pipes at finite amplitude". Journal of Applied Mechanics, Vol. 44, pp. 154-158.

Sethna, P.R. and Gu, X.M. 1985, "On global motions of articulated tubes carrying fluid". International Journal of Non-Linear Mechanics, Vol. 20, pp. 453-469.

Sethna, P.R. and Shaw, S.W. 1987, "On codimension-three bifurcations in the motion of articulated tubes conveying a fluid". *Physica* 24D, pp. 305-327.

Shields, C.M., Savannah, N.S. 1960, "Fuel Pesign and Development Program -Fuel Rod Vibration". US Atomic Energy Commission Report GEAP-3583.

SOGREAH 1962, "Study of Vibrations and Load Losses in Tubular Clusters". Société Grenobloise d'Etudes et Applications Hydrauliques, Special Report No. 3, EURAEC-288.

Taylor, G.I. 1952a, "Analysis of the Swimming of Long and Narrow Animals". Proceedings of the Royal Society (London), Vol. 214 (A), pp. 158-183.

Taylor, G.I. 1952b, "The action of waving cylindrical tails in propelling microscopic organisms". *Proceedings of the Royal Society (London)*, Vol. 211 (A), pp. 225-239.

Thom, A. 1928, "The laminar boundary layer of a cylinder". ARC Report, London, nos. 1176 and 1194.

Triantafyllou, G.S. and Chryssostomidis, C. 1989, "The dynamics of towed arrays". Journal of Offshore Mechanics and Arctic Engineering, Vol. 111, pp. 208-213.

Webster, P.M., Sawatzky, R.P., Hoffstein, V., Leblanc, R., Hinchey, M.J. and Sullivan, P.A. 1985, "Wall motion in expiratory flow limitation: choke and flutter". Journal of Applied Physiology, Vol. 59, pp. 1304-1312.

Wolf, A., Swift, J.B., Swinney, H.L. and Vasano, J.A. 1985, "Determining Lyapunov exponents from a time series". *Physica* 16D, pp. 285-317.

Yeh, T.T. and Chen, S.S. 1978, "The effects of fluid viscosity on coupled tube/fluid vibrations". *Journal of Sound and Vibration*, Vol. 59, pp. 453-467.

Appendix A

Viscous Forces — Laminar

Boundary Layer

Relf and Powell (1917) gave measurements of the force on a smooth 3/8 in. diameter cylinder set at angles varying by 100 intervals from 00 to 900 to the wind direction. It was pointed out by them that F_N is nearly proportional to $\sin^2 \theta$, where θ is the angle between the axis of the cylinder and the wind direction. If U is the wind velocity, $U \sin \theta$ is the component of velocity at right angles to the cylinder, and since the drag on a cylinder placed at right angles to the wind is very nearly proportional to U^2 , Relf and Powell considered that the normal component of velocity determines the normal force, independently of the longitudinal component $U\cos\theta$. This result was to be expected on theoretical grounds, because at the Reynolds number of the Relf and Powell experiments (7.9×10^3) the boundary layer is laminar. Relf and Powell's measurements were successfully used by McLeod (1918) to calculate the shape of a flexible cable used for towing weights under an airplane. For this purpose McLeod found that sufficiently accurate results could be obtained if F_L were neglected altogether. It is not possible to apply Relf and Powell's data directly to cases in which the Reynolds number on the force acting on a cylinder placed obliquely in a stream of fluid is needed.

The component of force acting per unit length of a cylinder at right angles to its axis when placed obliquely in a fluid stream will be denoted by F_N , and F_N depends only on $U \sin \theta$, so far as variations in U and θ are concerned.

The experimental results on smooth cylinders set at right angles to a fluid stream of velocity V are represented in Figure A.1 (Goldstein 1938). In this figure the drag coefficient C_d is plotted against $\text{Re} = \rho V D/\mu$; C_d is defined by

$$F_N = \frac{1}{2}\rho V^2 DC_d,\tag{A.1}$$

where D is the diameter of the cylinder, ρ is the density of fluid and μ the viscosity. Curve a, Figure A.1, represents C_d . Curve b represents C_{dp} , the part of C_d which is due to the component of form drag normal to the surface of the cylinder and in curve c the part C_{df} due to the tangential component. Evidently

$$C_d = C_{dp} + C_{df}. (A.2)$$

It is seen in Figure A.1 that in the range $20 < \text{Re} < 10^5$, C_{dp} varies only between 0.9 and 1.1. On the other hand, C_{df} is found to be nearly equal to $4\text{Re}^{-1/2}$ in this range (Thom 1928). This applies to "smooth" surfaces, and to flows with $\text{Re} < 3 \times 10^3$, approximately. From the above equations, Taylor (1952b) obtained the empirical expression

$$F_N = \frac{1}{2}\rho DV^2 \left(C_{dp} + \frac{4}{\sqrt{\text{Re}}} \right). \tag{A.3}$$

In the case of flow with velocity U and angle of incidence θ ,

$$V = U \sin \theta$$
, Re = Re_U sin θ , (A.4)

where Re_U is the Reynolds number based on U.

Then, the component of the fluid force per unit length, acting in the direction normal to the cylinder is

$$F_N = \frac{1}{2}\rho D(U\sin\theta)^2 \left(C_{dp} + \frac{4}{\sqrt{\text{Re}_U\sin\theta}}\right), \tag{A.5}$$

O),

$$F_N = \frac{1}{2}\rho DU^2 \left(C_{dp} \sin^2 \theta + \frac{4\sin^{3/2} \theta}{\sqrt{\text{Re}_U}} \right). \tag{A.6}$$

For relatively large Re_U ,

$$F_N = \frac{1}{2}\rho DU^2 C_{dp} \sin^2 \theta. \tag{A.7}$$

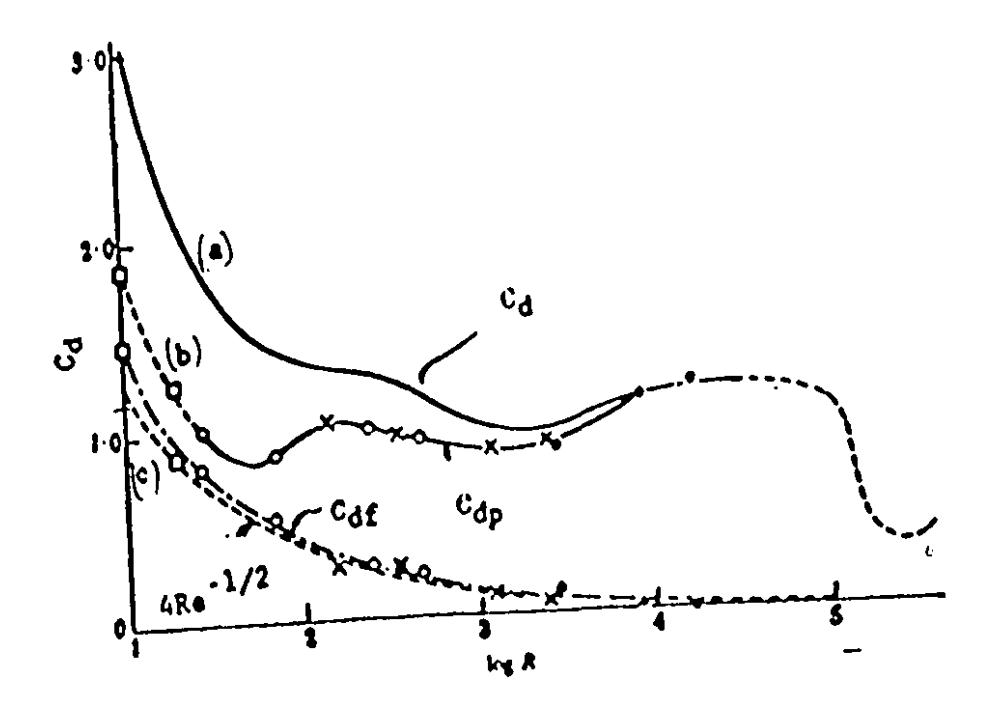


Figure A.1. Drag coefficients for lateral flow past smooth circular cylinders (Goldstein 1938): (a) C_d , the total drag coefficient; (b) the form drag coefficient, C_{dp} ; (c) the friction drag coefficient, C_{df} .

Appendix B

${f Viscous\ Forces--Turbulent}$

Boundary Layer

If the cylinder is so rough or the flow velocity high enough that the boundary layer is not laminar, the force cannot be analyzed by the method used for smooth cylinders. In general, it is not possible to make any theory of the aerodynamics of rough cylinders because the force would depend on the exact nature of roughness.

If the roughness consists of a number of long projections pointing equally in all directions, it is likely that the force on them would be in the direction opposite to that of their motion. The normal component of force F_N might be divided into portions due to the pressure and to skin friction, the friction being the resultant force on the projections. In that case, the force component formulae might be (Taylor 1952b)

$$F_N = \frac{1}{2}\rho DU^2 \left(C_{dp} \sin^2 \theta + C_f \sin \theta \right), \quad F_L = \frac{1}{2}\rho DU^2 C_f \cos \theta. \tag{B.1}$$

This case is illustrated as a in Figure B.1. In the limiting case when the diameter of the cylinder is so small that C_d is negligible compared with C_f , the "cylinder" would look like a hairy string. The force components might then be taken as

$$F_N = \frac{1}{2}\rho DU^2 C_f \sin \theta, \quad F_L = \frac{1}{2}\rho DU^2 C_f \cos \theta. \tag{B.2}$$

These formulae might also be expected to apply to a body in the form of a fine thread on which a number of equally spaced spherical beads were threaded. This case is illustrated as in the lower part of Figure B.1(c).

Another possible form of roughness might consist of thin disks or plates set at right angles to a cylinder. In this case, the roughness would make a much greater contribution to F_L than to F_N , and the appropriate formulae might be

$$F_N = \frac{1}{2}\rho DU^2 C_{dp} \sin^2 \theta, \quad F_L = \frac{1}{2}\rho DU^2 C_f \cos \theta. \tag{B.3}$$

This case is illustrated in Figure B.1(d). All these formulae are entirely speculative.

Finally, the overall normal force per unit length for an "arbitrary rough surface" is taken as a linear combination of (B.2) and (B.3), and we shall obtain the same formulae as in equation (B.1)

$$F_N = \frac{1}{2}\rho DU^2 \left(C_{dp} \sin^2 \theta + C_f \sin \theta \right). \tag{B.4}$$

The overall longitudinal force per unit length is assumed to be also of the form of (B.1), applying to both cases (B.2) and (B.3), i.e.

$$F_L = \frac{1}{2}\rho DU^2 C_f \cos \theta. \tag{B.5}$$

Additional experimental data on forces on inclined cylinders in flow, compiled by Hoerner (1958), supports equations (B.4) and (B.5). The drag and lift coefficients are given as

$$C_d = 1.1 \sin^3 \phi + 0.02$$
, and $C_l = 1.1 \sin^2 \phi \cos \phi$. (B.6)

The normal and longitudinal forces (per unit length), F_N and F_L , respectively, may be obtained from the following equations:

$$F_N = \frac{F_d}{L}\sin\phi + \frac{F_l}{L}\cos\phi \quad \text{and} \quad F_L = \frac{F_d}{L}\cos\phi - \frac{F_l}{L}\sin\phi , \qquad (B.7)$$

where F_d and F_l are the forces in the drag and lift directions, respectively, namely

$$F_d = \frac{1}{2}\rho DLU^2C_d, \quad F_l = \frac{1}{2}\rho DLU^2C_l.$$
 (B.8)

From these equations, for small ϕ ,

$$F_N \simeq \frac{1}{2}\rho DU^2(1.1\sin^2\phi + 0.02\sin\phi), \quad F_L \simeq \frac{1}{2}\rho DU^2(0.02\cos\phi).$$
 (B.9)

By inspection, equations (B.9) are of the same form as equations (B.4) and (B.5), with

$$C_{dp} = 1.1$$
, and $C_f = 0.02$. (B.10)

For a point in the jth cylinder in the system here under consideration, these expressions may be written in the form

$$(F_N)_j \simeq \frac{1}{2}\rho DU^2(1.1\sin^2\phi_j + 0.02\sin\phi_j)$$
 and $(F_L)_j \simeq \frac{1}{2}\rho DU^2(0.02\cos\phi_j)$.
(B.11)

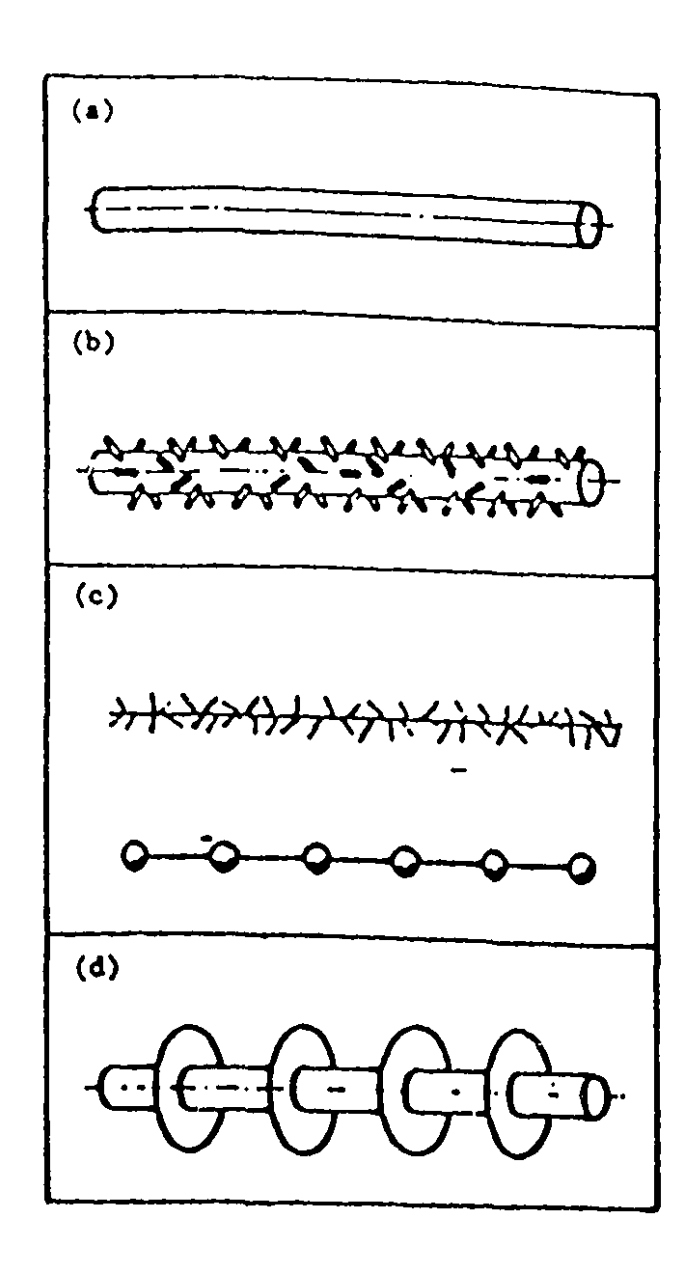


Figure B.1. Different types of roughness on the cylinders (Taylor 1952).

Appendix C

Linearization of Viscous Forces

In order to obtain the simplified linearized expressions for F_N and F_L , let us consider a (x,y)-plane cross-section of an element of cylinder (Figure C.1), where θ is the angle of incidence of the cylinder in the y-direction. By inspection of the above diagram, we can write

$$\theta = \theta_1 + \theta_2, \tag{C.1}$$

where

$$\theta_1 = \tan^{-1}[dy/dx]; \quad \theta_2 = \tan^{-1}[(1/U)(dy/dt)].$$
 (C.2)

Then, for small deformations $\theta_1 \simeq \tan \theta_1 = dy/dx$ and $\theta_2 \simeq \tan \theta_2 = (dy/dt)/U$. Therefore, $\theta = dy/dx + (dy/dt)/U$ and the normal viscous force per unit length $F_N = \frac{1}{2}\rho DU^2[C_{dp}\sin^2\theta + C_f\sin\theta] =$

$$\frac{1}{2}\rho DU^2 \left[C_{dp} \sin^2\left(dy/dx + (dy/dt)/U \right) + C_f \sin\left(dy/dx + (dy/dt)/U \right) \right].$$

For small deformations, $\sin \theta \simeq \theta$, so that the above equation reduces to:

$$F_N = \frac{1}{2}\rho DU^2 \left[C_{dp} \left(\frac{dy}{dx} + \frac{1}{U} \frac{dy}{dt} \right)^2 + C_f \left(\frac{dy}{dx} + \frac{1}{U} \frac{dy}{dt} \right) \right]. \tag{C.3}$$

To avoid powers of derivatives in the final equations of motion of the cylinders, which would make it nonlinear, the quadratic normal viscous forces have been linearized at U=0.

The linearization procedure, involving the first term of equation (C.3) is illustrated here. As $U \to 0$,

$$F_N \simeq rac{1}{2}
ho D C_{dp} \left(rac{dy}{dt}
ight)^2,$$

OΓ

$$\frac{F_N}{\frac{1}{2}\rho D} = C_{dp} \left(\frac{dy}{dt}\right)^2. \tag{C.4}$$

This expression is linearized by using the approximation

$$\frac{F_N}{\frac{1}{2}\rho D} = C_d \left(\frac{dy}{dt}\right),\tag{C.5}$$

illustrated graphically in Figure C.2, where C_d is the drag coefficient in still fluid, has dimensions L/T and is given by

$$C_d = C_{dp} \left| \frac{dy}{dt} \right| . \tag{C.6}$$

In conclusion, utilizing also the results of Appendix B, we can write equation (C.3) as follows:

$$F_N = \frac{1}{2}\rho DUC_f \left(U \frac{\partial y}{\partial x} + \frac{\partial y}{\partial t} \right) + \frac{1}{2}\rho DC_d \left(\frac{\partial y}{\partial t} \right). \tag{C.7}$$

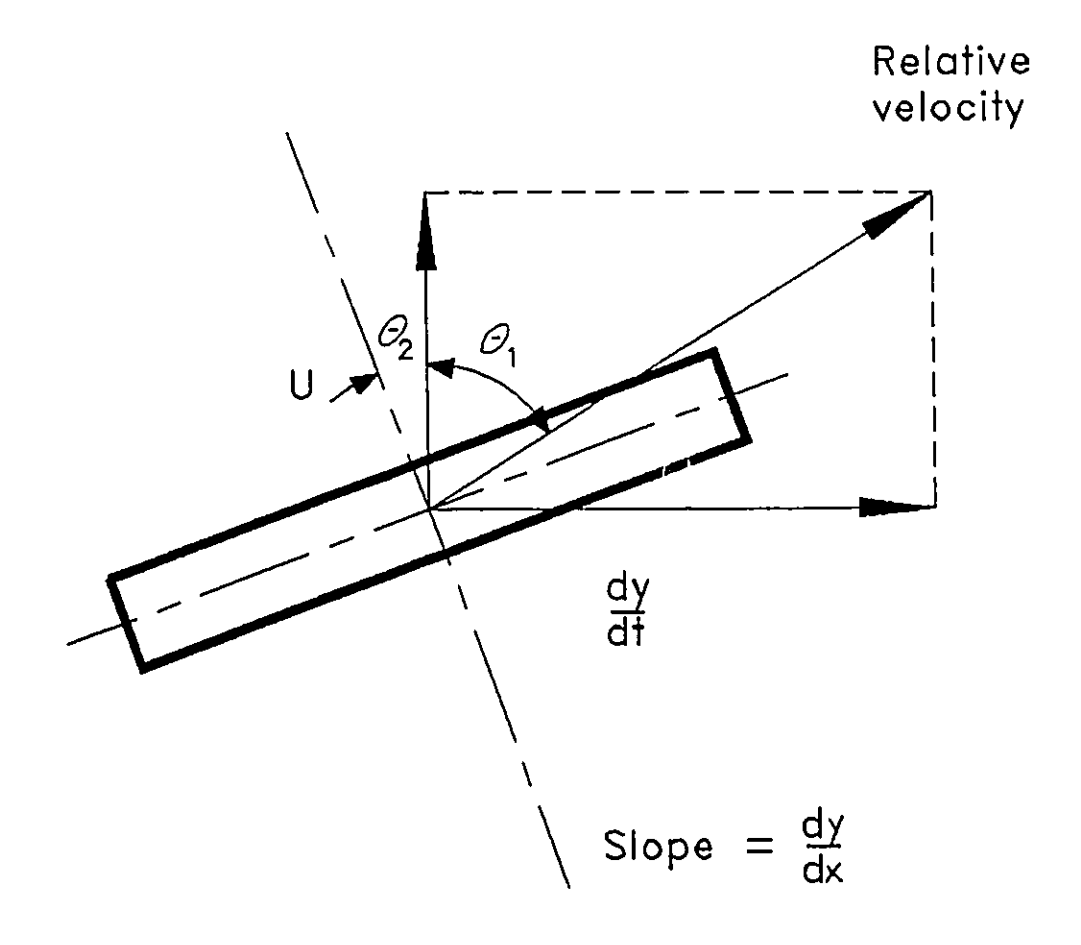


Figure C.1. Calculation of the angle of incidence θ of the cylinder, $\theta = \theta_1 + \theta_2$.

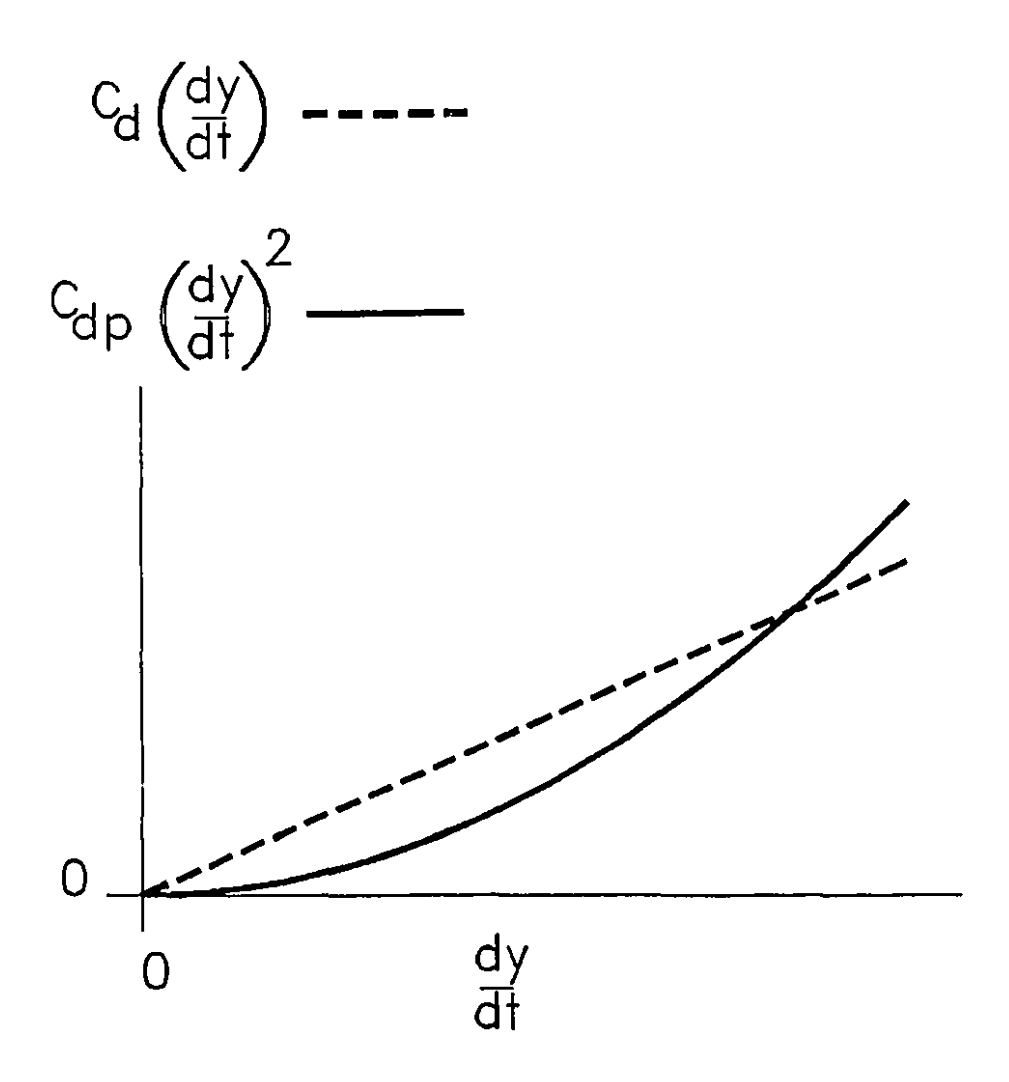


Figure C.2. Linearization procedure of normal viscous force F_N at $U \to 0$, involving the drag coefficient $C_d = C_{dp} (dy/dt)$.

Appendix D

Convergence of the Solutions of the Equations of Motion

Results for Case 1 (h = 0.5, f = 0.8, $\kappa_c = 5 \times 10^3$) and N = 2 will be analyzed in this Appendix, in order to discuss the convergence of the solutions for this system.

For any flow velocities u between 2.739 and 2.790, by taking three different time steps $\delta \tau_1 = 0.01$, $\delta \tau_2 = 0.001$ and $\delta \tau_3 = 0.0001$, we have obtained essentially the same final values for velocities and displacements of the system $\dot{\phi}_1$, $\dot{\phi}_2$, ϕ_1 and ϕ_2 . For example, for u = 2.739, 2.7397, 2.73975, 2.74 and 2.79, it was found that the velocities and displacements of the system were the same up to the fourth decimal (in Genplot, the final results on the computer screen are given to the fourth decimal).

To see more precisely the difference between the numerical results obtained with two different time steps ($\delta\tau_1=0.01$ and $\delta\tau_2=0.001$), we have taken the same system, for which the external flow velocity is u=2.77, the number of time steps being N=500 to 502. Then, for $\delta\tau_1=0.01$, we obtained $\phi_{1max}=0.0374$ 6992 6807 4892, while for $\delta\tau_2=0.001$, $\phi_{1max}=0.0374$ 7012 7821 6894. This means that the results are the same up to the fifth significant figure. More precisely, the displacement of the first cylinder ϕ_{1max} obtained with the time step $\delta\tau_2=0.001$ is 0.0005 % higher than the one obtained with $\delta\tau_1=0.01$.

Furthermore, with the same aim, we shall calculate the critical flow velocity corresponding to the symmetry-breaking pitchfork bifurcation (the first nonlinear bifurcation after the classical Hopf bifurcation), for two different time steps. Taking again as numerical example the system of Case 1, the critical flow velocities for the symmetry-breaking pitchfork bifurcation (which corresponds to the first asymmetric limit cycle), was found to be the same ($u_{cr} = 2.7944$) for both time steps, ($\delta\tau_1 = 0.001$ and $\delta\tau_2 = 0.01$), so that in this case the results are the same up to five significant figures.

For flow velocities u smaller than the one corresponding to the Hopf bifurcation, as for example, u=2.73, fewer time steps will be needed (N=400 to 410) than for u=2.7395 (N=1400 to 1410) for the system to converge to a stable solution. For u higher than the flow velocity u corresponding to the Hopf bifurcation, by taking the time step $\delta \tau=0.01$, for flow velocities 2.74 < u < 2.77, fewer time steps ($\simeq 50$ for u=2.77) will be needed than for lower flow velocities ($\simeq 80$ for u=2.74) for the solution to converge to a symmetric limit cycle.

Appendix E

Details for the Centre Manifold Calculations

E.1. Calculation of μ_1 and μ_3

In order to calculate the unfolding parameters μ_1 and μ_3 , in this Appendix will be presented the steps in the corresponding numerical calculations. In the equations of motion (5.1) for the system of Case 1, and for $u = u_{cr} = 2.7396$, their corresponding terms may be written as:

$$\mathbf{y} = \begin{bmatrix} \dot{\phi_1} \\ \dot{\phi_2} \\ \phi_1 \\ \phi_2 \end{bmatrix}$$
 (E.1)

and

$$\mathbf{A(u_{cr})} = \begin{bmatrix} -17.65 & -5.39 & -38.68 & -45.46 \\ 103.08 & 8.72 & 350.18 & 312.26 \\ 1 & 0 & 0 & 0 \\ 0 & 1 & 0 & 0 \end{bmatrix}. \tag{E.2}$$

Then, by MACSYMA, the values for the coefficients $a_0(u)$, $a_1(u)$, $a_2(u)$ and $a_3(u)$ were calculated from the equation

$$[\mathbf{A}(\mathbf{u}) - \lambda \mathbf{I}] = \lambda^4 + a_3(u)\lambda^3 + a_2(u)\lambda^2 + a_1(u)\lambda + a_0(u). \tag{E.3}$$

The flow velocity u will be taken as parameter, so that, after replacing the numerical values for our system in $[A - \lambda I]$, the coefficients will be determined as functions of u:

$$a_0(u) = 748.11u^4 - 6934.64u^2,$$

$$a_1(u) = -40.36u^3 - 94.47u^2 + 641.50u + 507.56,$$

$$a_2(u) = 2u - 75.50u^2 + 689.68,$$

$$a_3(u) = 2.72u + 1.47.$$
(E.4)

For $\lambda_{1,2} = \sigma_1 \pm i \omega_1$ (Chapter 5), and by taking into consideration equations (E.3) and (E.4), $[\mathbf{A}(\mathbf{u}) - \lambda \mathbf{I}]$ may be written as function of its real (Re₁) and imaginary (Im₁) parts as follows:

$$[\mathbf{A}(\mathbf{u}) - \lambda \mathbf{I}] = \text{Re}_1(\sigma_1, \omega_1, u) + i \, \text{Im}_1(\sigma_1, \omega_1, u) \,. \tag{E.5}$$

For $\omega_1 = 0$ in the case of a Hopf bifurcation (purely imaginary eigenvalues), the real and the imaginary parts will be functions only of σ_1 , and u, respectively. Then, one may write:

$$Re_{1}(\omega_{1}, u) = \omega_{1}^{4} - a_{2}(u)\omega_{1}^{2} + a_{0}(u),$$

$$Im_{1}(\omega_{1}, u) = -a_{3}(u)\omega_{1}^{2} + a_{1}(u),$$
(E.6)

the partial derivatives of which will be

$$\frac{\partial \operatorname{Re}_{1}}{\partial \sigma_{1}} = \frac{\partial \operatorname{Im}_{1}}{\partial \omega_{1}} = -3a_{3}\omega_{1}^{2} + a_{1} ,$$

$$\frac{\partial \operatorname{Re}_{1}}{\partial \omega_{1}} = -\frac{\partial \operatorname{Im}_{1}}{\partial \sigma_{1}} = 4\omega_{1}^{3} - 2a_{2}\omega_{1} ,$$

$$\frac{\partial \operatorname{Re}_{1}}{\partial u} = -\frac{\partial a_{2}}{\partial u}\omega_{1}^{2} + \frac{\partial a_{0}}{\partial u} ,$$

$$\frac{\partial \operatorname{Im}_{1}}{\partial u} = -\frac{\partial a_{3}}{\partial u}\omega_{1}^{3} + \frac{\partial a_{1}}{\partial u}\omega_{1} .$$
(E.7)

By replacing the corresponding values for the system considered in Section 5.1.1, $\omega_1 = 9.0176$ and $u = u_{cr} = 2.7396$, which is the critical flow velocity for the first Hopf bifurcation in the above equations, we shall obtain

$$\frac{\partial \text{Re}_{1}}{\partial \sigma_{1}} = \frac{\partial \text{Im}_{1}}{\partial \omega_{1}} = -1452.14 , \qquad \frac{\partial \text{Re}_{1}}{\partial \omega_{1}} = -\frac{\partial \text{Im}_{1}}{\partial \sigma_{1}} = 614.88 ,
\frac{\partial \text{Im}_{1}}{\partial u} = -9073.39 , \qquad \frac{\partial \text{Re}_{1}}{\partial u} = 57008.98 .$$
(E.8)

By replacing these values into the equations

$$\operatorname{Re}_{1}(\epsilon\mu_{1}, \,\omega_{0} + \epsilon\mu_{3}, \,u_{cr} + \epsilon\mu) = 0, \qquad \operatorname{Im}_{1}(\epsilon\mu_{1}, \,\omega_{0} + \epsilon\mu_{3}, \,u_{cr} + \epsilon\mu) = 0. \tag{E.9}$$

 μ_1 and μ_3 will be obtained as functions of μ only. These values will be $\mu_1=31.046517\mu$ and $\mu_3=-19.394264\mu$.

E.2. Calculation of μ_2

In this case, $\lambda_3 = \epsilon \mu_2$ is the eigenvalue for the pitchfork bifurcation, which occurs for $u = 1.694644 + \epsilon \mu$, where $u_{cr} = 1.694644$.

As the system is the same as in the foregoing section, the coefficients $a_0(u)$, $a_1(u)$, $a_2(u)$ and $a_3(u)$ will have the same form as in Section E.1 (equations (E.4)), but their numerical values will be different, because of the fact that u_{cr} is different.

By replacing λ and u from the first paragraph into equation (E.3), and by neglecting the terms in μ_2^2 , μ_2^3 and μ_2^4 , the final equation $\mu_2 = -4.919\mu$ will be obtained.

E.3. Centre manifold calculation for Hopf bifurcation

If the system of nonlinear equations is

$$m_{11}\dot{\phi}_{1} + m_{12}\dot{\phi}_{2} - m_{11}\dot{\phi}_{1} - m_{12}\dot{\phi}_{2} = 0,$$

$$m_{21}\dot{\phi}_{1} + m_{22}\dot{\phi}_{2} - m_{21}\dot{\phi}_{1} - m_{22}\dot{\phi}_{2} = 0,$$

$$m_{11}\ddot{\phi}_{1} + m_{12}\ddot{\phi}_{2} + c_{11}\dot{\phi}_{1} + c_{12}\dot{\phi}_{2} + k_{11}\phi_{1} + k_{12}\phi_{2} = -\kappa_{c}\phi_{1}^{3},$$

$$m_{21}\ddot{\phi}_{1} + m_{22}\ddot{\phi}_{2} + c_{21}\dot{\phi}_{1} + c_{22}\dot{\phi}_{2} + k_{21}\phi_{1} + k_{22}\phi_{2} = 0,$$
(E.10)

it may be written in compact form as

$$\mathbf{B}\dot{\mathbf{y}} + \mathbf{E}\mathbf{y} = \mathbf{F} \,, \tag{E.11}$$

where

$$\mathbf{B} = \begin{bmatrix} 0 & 0 & m_{11} & m_{12} \\ 0 & 0 & m_{21} & m_{22} \\ m_{11} & m_{12} & c_{11} & c_{12} \\ m_{21} & m_{22} & c_{21} & c_{22} \end{bmatrix}, \quad (E.12)$$

$$\mathbf{E} = \begin{bmatrix} -m_{11} & -m_{12} & 0 & 0 \\ -m_{21} & -m_{22} & 0 & 0 \\ 0 & 0 & k_{11} & k_{12} \\ 0 & 0 & k_{21} & k_{22} \end{bmatrix},$$
 (E.13)

$$\mathbf{F} = \begin{bmatrix} 0 \\ 0 \\ -\kappa_c \phi_1^3 \\ 0 \end{bmatrix}, \tag{E.14}$$

and y has been defined in equation (E.1).

Finally, equation (E.11) will be multiplied by \mathbf{B}^{-1} , and may be written also in the form

$$\dot{\mathbf{y}} + \mathbf{B}^{-1}\mathbf{E}\mathbf{y} = \mathbf{B}^{-1}\mathbf{F} , \qquad (E.15)$$

where $A = -B^{-1}E$, and the value of A has already been calculated for the Hopf bifurcation in equation (E.2).

The transformation of coordinates y = Px will be used. With this transformation, the following equation in x is obtained:

$$\mathbf{P}\dot{\mathbf{x}} = \mathbf{A}\mathbf{P}\mathbf{x} + \mathbf{B}^{-1}\mathbf{F} . \tag{E.16}$$

We multiply this equation by P^{-1} and we obtain

$$\dot{\mathbf{x}} = \mathbf{P}^{-1}\mathbf{A}\mathbf{P}\mathbf{x} + \mathbf{P}^{-1}\mathbf{B}^{-1}\mathbf{F},$$
 (E.17)

where **P** is the modal matrix, as already discussed in Chapter 5.

By replacing the corresponding numerical values for the system studied, equations (5.12) and (5.13) will be obtained.

Appendix F

Estimation of the End-Form Coefficient f

The downstream end is approximated by a paraboloid of the form $y^2 = 4aw$, where y is the radius of the cylinder system, w is the length of the paraboloid and a its focal distance.

Consider a specific case, in which the diameter of the cylinders is D=1.55 cm; hence, y is equal to r=1.55/2=0.775 cm. It is recalled that f=0 corresponds to a blunt end and f=1 to a streamlined end. Intermediate values of f are estimated empirically by sketching the corresponding paraboloids and drawing on the experience of Païdoussis (1973) as follows:

•
$$w = 0.19$$
; $a = 0.78$: $f \simeq 0$

•
$$w = 0.39$$
; $a = 0.39$: $f \simeq 0.2$

•
$$w = 0.78$$
; $a = 0.19$: $f \simeq 0.4$

• w = 1.16; a = 0.13 : $f \approx 0.6$

• w = 1.55; a = 0.10 : $f \approx 0.8$

Dimensional quantities (w and a) are in cm.

Appendix G

Comments on the Signs of the Various Terms appearing in $(F_N)_j$ and $(F_L)_j$

In Section 8.3.3, the viscous hydrodynamic forces $(F_N)_j$ and $(F_L)_j$ for a point in the jth cylinder for the N=2 second model were already calculated in Chapter 8, and they were given by equations (8.23) and (8.24).

Therefore, these forces may be determined for the first cylinder (j = 1), and for the second cylinder (j = 2), as follows:

$$(F_N)_1 = \frac{1}{2} \rho D C_{dp} [U \sin \phi_1 + \xi \dot{\phi_1}]^2 + \frac{1}{2} \rho D U C_f [U \sin \phi_1 + \xi \dot{\phi_1}], \qquad (G.1)$$

$$(F_N)_2 = \frac{1}{2} \rho D C_{dp} \left[l \dot{\phi}_1 \cos(\phi_2 - \phi_1) + \xi \dot{\phi}_2 + U \sin \phi_2 \right]^2 + \frac{1}{2} \rho D U C_f \left[l \dot{\phi}_1 \cos(\phi_2 - \phi_1) + \xi \dot{\phi}_2 + U \sin \phi_2 \right], \tag{G.2}$$

$$(F_L)_1 = \frac{1}{2} \rho DUC_f \left[U \cos \phi_1 \right], \tag{G.3}$$

$$(F_L)_2 = \frac{1}{2} \rho DUC_f \left[U \cos \phi_2 - l \dot{\phi}_1 \sin(\phi_2 - \phi_1) \right]. \tag{G.4}$$

We shall next calculate the Taylor expansions for the trigonometric functions appearing, in the foregoing:

$$\sin \phi_1 = \phi_1 - \frac{1}{6}\phi_1^3, \quad \sin \phi_2 = \phi_2 - \frac{1}{6}\phi_2^3,$$
 (G.5)

$$\cos \phi_1 = 1 - \frac{1}{2}\phi_1^2, \quad \cos \phi_2 = 1 - \frac{1}{2}\phi_2^2,$$
 (G.6)

$$\cos(\phi_2 - \phi_1) = 1 - \frac{1}{2}(\phi_2 - \phi_1)^2, \tag{G.7}$$

$$\sin(\phi_2 - \phi_1) = (\phi_2 - \phi_1) - \frac{1}{6}(\phi_2 - \phi_1)^3.$$
 (G.8)

By replacing these Taylor approximations in equations (G.1)-(G.4), the following expressions are obtained:

$$(F_N)_1 = \frac{1}{2}\rho DU^2 C_{dp} \left(\phi_1^2 - \frac{1}{3}\phi_1^4\right) + \rho DU C_{dp} \xi \dot{\phi}_1 \left(\phi_1 - \frac{1}{6}\phi_1^3\right) + \frac{1}{2}\rho DC_{dp} \xi^2 \dot{\phi}_1^2 + \frac{1}{2}\rho DU C_f \left[U\left(\phi_1 - \frac{1}{6}\phi_1^3\right) + \xi \dot{\phi}_1\right], \quad (G.9)$$

$$(F_{N})_{2} = \frac{1}{2}\rho DC_{dp}l^{2}\dot{\phi_{1}}^{2} \left[1 - (\phi_{2} - \phi_{1})^{2}\right] + \rho DUC_{dp}l\dot{\phi_{1}} \left[\phi_{2} - \frac{1}{6}\phi_{2}^{3} - \frac{1}{2}\phi_{2}(\phi_{2} - \phi_{1})^{2}\right] + \frac{1}{2}\rho DU^{2}C_{dp} \left(\phi_{2}^{2} - \frac{1}{3}\phi_{2}^{4}\right) + \rho DUC_{dp}\xi\dot{\phi_{2}} \left(\phi_{2} - \frac{1}{6}\phi_{2}^{3}\right) + \rho DC_{dp}l\xi\dot{\phi_{1}}\dot{\phi_{2}} \left[1 - \frac{1}{2}(\phi_{2} - \phi_{1})^{2}\right] + \frac{1}{2}\rho DC_{dp}\xi^{2}\dot{\phi_{2}}^{2} + \frac{1}{2}\rho DUC_{f} \left[\xi\dot{\phi_{2}} + U\left(\phi_{2} - \frac{1}{6}\phi_{2}^{3}\right) + l\dot{\phi_{1}}\left(1 - \frac{1}{2}(\phi_{2} - \phi_{1})^{2}\right)\right],$$
 (G.10)

$$(F_L)_1 = \frac{1}{2}\rho DU^2 C_f \left(1 - \frac{1}{2}\phi_1^2\right), \tag{G.11}$$

$$(F_L)_2 = \frac{1}{2}\rho DUC_f \left[U \left(1 - \frac{1}{2}\phi_2^2 \right) - l\dot{\phi}_1 \left(\phi_2 - \phi_1 - \frac{1}{6}(\phi_2 - \phi_1)^3 \right) \right]. \tag{G.12}$$

In equations (G.9)-(G.12), one may see that there are basically two kinds of terms: those related directly to lateral velocities, for instance $\xi \dot{\phi}_1$ (for $\dot{\phi}_1 > 0$ and $\dot{\phi}_1 < 0$ we should get F_N with opposite signs; i.e., always opposing motion); and those related to the approximating angles, such as $\sin^2 \phi_j$, the sign of which is positive or negative, as ϕ_j is positive or negative. Therefore, the signs of the terms of the viscous forces formulation, or equations (G.1) to (G.4), need to be further analyzed.

In $(F_N)_1$, i.e., in equation (G.9), we have the following terms:

- (i) $\phi_1^2 \frac{1}{3}\phi_1^4$, which will be rewritten as $|\phi_1| \phi_1 \left(1 \frac{1}{3}\phi_1^2\right)$, and we see that this changes sign as ϕ_1 does and has the desired property, as discussed above;
- (ii) $\xi^2 \dot{\phi_1}^2$, which will be rewritten as $\xi^2 \left| \dot{\phi_1} \right| \dot{\phi_1}$ for the same reason as for (i);
- (iii) $\phi_1 \frac{1}{6}\phi_1^3$, which may be written as $\phi_1 \left(1 \frac{1}{6}\phi_1^2\right)$;

(iv) $\dot{\phi}_1 \left(\phi_1 - \frac{1}{6} \phi_1^3 \right)$, which has the same sign as $\dot{\phi}_1 \phi_1$, which requires further discussion.

In the type of term as in (iv) above, the fluid force is a composite of two effects: (a) the flow due to inclination of the pipe, and (b) the flow due to the velocity of the pipe, which, in this case, is in the opposite direction. Then, the sign of the normal viscous force $(F_N)_1$ is analyzed, with respect to the sign of ϕ_1 and $\dot{\phi}_1$:

- if $\phi_1 > 0$ and $\dot{\phi}_1 > 0$, the corresponding term in $(F_N)_1$ will be positive;
- if $\phi_1 > 0$ and $\dot{\phi}_1 < 0$, the corresponding term in $(F_N)_1$ will be negative;
- if $\phi_1 < 0$ and $\dot{\phi}_1 < 0$, the corresponding term in $(F_N)_1$ will be negative;
- if $\phi_1 < 0$ and $\dot{\phi}_1 > 0$, the corresponding term in $(F_N)_1$ will be zero.

Then, the term in (iv) may be written as $\frac{1}{2} \left[\left| \dot{\phi}_1 \right| \phi_1 + \dot{\phi}_1 \left| \phi_1 \right| \right] \left(1 - \frac{1}{6} \phi_1^2 \right)$.

In the same way, the different terms of $(F_N)_2$ will be further rewritten as follows:

(v)
$$\dot{\phi_1}^2[1-(\phi_2-\phi_1)^2]$$
 will be rewritten as $\dot{\phi_1}|\dot{\phi_1}|[1-(\phi_2-\phi_1)^2]$;

(vi)
$$U^2\phi_2^2\left[1-\frac{1}{3}\phi_2^2\right]$$
 will be rewritten as $U^2\phi_2\left|\phi_2\right|\left[1-\frac{1}{3}\phi_2^2\right]$;

(vii)
$$2l\xi\dot{\phi}_1\dot{\phi}_2\left[1-\frac{1}{2}(\phi_2-\phi_1)^2\right]$$
 will be rewritten as

$$l\xi \left[\dot{\phi_1} \left| \dot{\phi_2} \right| + \left| \dot{\phi_1} \right| \dot{\phi_2} \right] \left[1 - \frac{1}{2} (\phi_2 - \phi_1)^2 \right];$$

(viii)
$$2\xi U\dot{\phi}_2\phi_2\left(1-\frac{1}{6}\phi_2^2\right)$$
 will be rewritten as $\xi U\left[\left|\dot{\phi}_2\right|\phi_2+\dot{\phi}_2\left|\phi_2\right|\right]\left(1-\frac{1}{6}\phi_2^2\right);$

(ix) $2Ul\dot{\phi_1}\phi_2\left(1-\frac{1}{6}\phi_2^2\right)\left[1-\frac{1}{2}(\phi_2-\phi_1)^2\right]$ will be rewritten in the form

$$Ul[|\dot{\phi_1}|\phi_2+\dot{\phi_1}|\phi_2|](1-\frac{1}{6}\phi_2^2)[1-\frac{1}{2}(\phi_2-\phi_1)^2];$$

 $(F_L)_1$ and $(F_L)_2$ remain unchanged.

Triantafyllou and Chryssostomidis (1988) have shown that the term of the form $\left[U\sin\phi_1+\xi\dot{\phi}_1\right]^2$, which is found in equation (G.1) for $(F_N)_1$, could be written as $\left[U\sin\phi_1+\xi\dot{\phi}_1\right]\left|U\sin\phi_1+\xi\dot{\phi}_1\right|$; in their formulation, the sign of forces changed with the model variation in time.

So that two formulations were presented for the viscous forces: the first one, which uses (i) to (ix), and the second is the one presented in the previous paragraph. These two formulations will lead to the same final viscous forces, as it will be shown in the following paragraphs, for $(F_N)_1$.

In the <u>first</u> formulation, by replacing (i) to (iv) into equation (G.9), one obtains for $(F_N)_1$ the following equation:

$$(F_{N})_{1} = \frac{1}{2}\rho DU^{2}C_{dp} |\phi_{1}| \phi_{1} \left(1 - \frac{1}{3}\phi_{1}^{2}\right)$$

$$+ \frac{1}{2}\rho DUC_{dp}\xi \left(|\phi_{1}| \dot{\phi}_{1} + \dot{\phi}_{1}|\phi_{1}|\right) \left(1 - \frac{1}{6}\phi_{1}^{2}\right)$$

$$+ \frac{1}{2}\rho DC_{dp}\xi^{2}\dot{\phi}_{1} |\dot{\phi}_{1}| + \frac{1}{2}\rho DUC_{f} \left[U\left(\phi_{1} - \frac{1}{6}\phi_{1}^{3}\right) + \xi\dot{\phi}_{1}\right]. \quad (G.13)$$

Based on the <u>second</u> formulation, from equation (G.1), one may write $(F_N)_1$ as follows:

$$(F_N)_1 = \frac{1}{2}\rho DC_{dp}[U\sin\phi_1 + \xi\dot{\phi}_1] \left| U\sin\phi_1 + \xi\dot{\phi}_1 \right| + \frac{1}{2}\rho DUC_f[U\sin\phi_1 + \xi\dot{\phi}_1], \text{ (G.14)}$$

Then, by Taylor approximations, one may write equation (G.14) as:

$$(F_{N})_{1} = \frac{1}{2}\rho DC_{dp} \left[U\left(\phi_{1} - \frac{1}{6}\phi_{1}^{3}\right) + \xi \dot{\phi}_{1} \right] \left| U\left(\phi_{1} - \frac{1}{6}\phi_{1}^{3}\right) + \xi \dot{\phi}_{1} \right| + \frac{1}{2}\rho DUC_{f} \left[U\left(\phi_{1} - \frac{1}{6}\phi_{1}^{3}\right) + \xi \dot{\phi}_{1} \right], \tag{G.15}$$

Then,

$$(F_{N})_{1} = \frac{1}{2}\rho DU^{2}C_{dp}\left(\phi_{1} - \frac{1}{6}\phi_{1}^{3}\right)\left|\phi_{1} - \frac{1}{6}\phi_{1}^{3}\right|$$

$$+ \frac{1}{2}\rho DUC_{dp}\xi\dot{\phi}_{1}\left|\phi_{1}\right|\left(1 - \frac{1}{6}\phi_{1}^{2}\right)$$

$$+ \frac{1}{2}\rho DUC_{dp}\xi\left|\dot{\phi}_{1}\right|\phi_{1}\left(1 - \frac{1}{6}\phi_{1}^{2}\right)$$

$$+ \frac{1}{2}\rho DC_{dp}\xi^{2}\dot{\phi}_{1}\left|\dot{\phi}_{1}\right| + \frac{1}{2}\rho DUC_{f}\left[U\left(\phi_{1} - \frac{1}{6}\phi_{1}^{3}\right) + \xi\dot{\phi}_{1}\right], \quad (G.16)$$

After many calculations, and retaining only terms up to third order, one may obtain the equivalence of equations (G.16), which were obtained through the second formulation, with equations (G.13), which correspond to the first formulation.

In the same way, the other viscous forces acting on the first and second cylinder for the N=2 second model, i.e., $(F_N)_2$, $(F_L)_1$ and $(F_L)_2$ were found to be the same for both, first and second formulation.

Appendix H

Calculation of Base Drag Coefficient, C_b

The pressure in the wake of a blunt-based body is reduced as a result of the tubular jet around it. Hoerner (1958) described the insulating effect of the separated boundary layer, which tends to diminish the jet-pump effect.

In our articulated cylinder system, there will be a force due to the base drag acting on the last cylinder. We already know that the last cylinder of the system has a free end, the form of which depends on the nondimensional parameter f; following Hoerner, the base drag force may be expressed as $D_b = \frac{1}{2}\rho U^2 S_b C_b$, from which the base drag coefficient will be given by

$$C_b = D_b / \left(\frac{1}{2}\rho U^2 S_b\right). \tag{H.1}$$

From (H.1), it may be concluded that C_b is inversely proportional to some measure of the boundary layer thickness at the base, which may be characterized by the drag on the forebody (D_{fore}) . Then,

$$C_b = 0.029(\frac{1}{2}\rho U^2 S_b/D_{fore})^{1/2},$$
 (H.2)

where D_{fore} is the total drag acting over the entire forebody. As $D_{fore} = \frac{1}{2}\rho U^2 S_b C_{fb}$,

where C_{fb} is the skin friction drag on the forebody, C_b will be:

$$C_b = 0.029/(C_{fb})^{1/2}.$$
 (H.3)

This formula is applicable to cases where the base area is essentially equal to the maximum cross-sectional area, which is the case for the system studied.

Hoerner proposed $C_{fb} = C_f = 0.02$ as the skin friction drag coefficient on the forebody; then, by replacing its value into equation (H.3), we obtain

$$C_b = 0.029/(0.02)^{1/2} = 0.2.$$
 (II.4)

The virtual work associated with the last cylinder (the second for a two-degree-of-freedom system) due to a virtual displacement associated with ϕ_1 , and due to the base drag force only, is given by

$$Q_1 = \frac{1}{2}\rho D^2 U^2 C_b l_1 \sin(\phi_2 - \phi_1) = \frac{1}{2}\rho D^2 U^2 C_b l \left[(\phi_2 - \phi_1) - (\phi_2 - \phi_1)^3 / 6 \right], \quad (II.5)$$

where $\sin(\phi_2 - \phi_1) = [(\phi_2 - \phi_1) - (\phi_2 - \phi_1)^3/6]$ by Taylor series expansion.

It is recognized that, despite (H.5) being a nonlinear expression, it is very approximate, since the whole reasoning leading to equation (H.3) was obtained in terms of linear concepts; thus, for example, the contributions of angular deflections of upstream cylinders to D_{fore} were not taken into account.

Appendix I

Computer Program

In this Appendix, the main computer programs for calculating the phase-plane portraits, bifurcation diagrams and Poincaré maps for two and three articulated cylinder systems are presented, with the cubic spring modelling the impact between these systems and the external cylinder. The Runge-Kutta fourth-order numerical method is used in all these programs. As this is a very well known and classical method, it needs not to be explained.

The nondimensional equations of motion for a two-degree-of-freedom (N=2) and for a three-degree-of-freedom cylinder system (N=3) using the so-called "first model" (i.e., basically linear, apart from impact-related forces) were presented in Chapter 2, in equations (2.35) and (2.36), respectively. These equations will be rewritten in the next paragraphs in a shorter form, by using the following notation: $\phi_1 = x$; $\phi_2 = y$; $\phi_3 = z$; $\dot{\phi}_1 = xx$; $\dot{\phi}_2 = yy$; $\dot{\phi}_3 = zz$; $\ddot{\phi}_1 = \dot{x}x$; $\ddot{\phi}_2 = \dot{y}y$ and $\ddot{\phi}_3 = \dot{z}z$, the dots denoting differentiation with respect to the nondimensional time, τ .

For N=2, the equations of motion (2.35) are written as follows:

$$A_1\dot{x}\dot{x} + B_1xx + C_1x + D_1\dot{y}\dot{y} + E_1yy + F_1y = \kappa_c x^3,$$

$$A_2\dot{x}\dot{x} + B_2xx + C_2x + D_2\dot{y}\dot{y} + E_2yy + F_2y = 0,$$
(I.1)

while for N=3, the equations of motion (2.36) become:

$$A_{1}\dot{x}\dot{x} + B_{1}xx + C_{1}x + D_{1}\dot{y}\dot{y} + E_{1}yy + F_{1}y + S_{1}\dot{z}z + T_{1}zz + Z_{1}z = \kappa_{c}x^{3},$$

$$A_{2}\dot{x}\dot{x} + B_{2}xx + C_{2}x + D_{2}\dot{y}\dot{y} + E_{2}yy + F_{2}y + S_{2}\dot{z}z + T_{2}zz + Z_{2}z = 0,$$

$$A_{3}\dot{x}\dot{x} + B_{3}xx + C_{3}x + D_{3}\dot{y}\dot{y} + E_{3}yy + F_{3}y + S_{3}\dot{z}z + T_{3}zz + Z_{3}z = 0,$$

$$(1.2)$$

in which the coefficients of x, y, z, xx, yy, zz, $\dot{x}x$, $\dot{y}y$ and $\dot{z}z$ are dependent on the nondimensional parameters already defined in Chapter 2, equations (2.34). These coefficients, i.e. A_1 , B_1 , C_1 , D_1 , E_1 , F_1 , S_1 , T_1 , Z_1 , A_2 , B_2 , C_2 , D_2 , E_2 , F_2 , S_2 , T_2 , Z_2 , A_3 , B_3 , C_3 , D_3 , E_3 , F_3 , S_3 , T_3 and Z_3 are found in the computer programs under their "similar" form, for the sake of simplicity, as A1, B1, C1, D1, E1, F1, S1, T1, Z1, A2, B2, C2, D2, E2, F2, S2, T2, Z2, A3, B3, C3, D3, E3, F3, S3, T3 and Z3, respectively.

In Table I.1, a description of the notation in the computer programs is given mainly for the parameters defined in equations (2.34), while in Table I.2, the notation for the results is given; furthermore, the notation for other parameters is given in Table I.3.

Mainly two writing commands exist in these computer programs. Taking, for example, the first computer program (for N=2), two sets of results are obtained, as follows. The first set gives τ , $\dot{\phi}_1(\tau)$, $\dot{\phi}_2(\tau)$, $\phi_1(\tau)$ and $\phi_2(\tau)$, which in the computer program are defined as T1, Z1, ZZ1, X1 and Y1; these are the outputs for the phase plane plots and Poincaré map construction. The second set gives u, ϕ_{1max} , which in the computer program are defined as U and X2; These are the outputs for the construction of the bifurcation diagram. These two sets of results appear at the end of the first computer program.

The graphs are constructed with Genplot software, while the programs are written, as may be seen, in Fortran.

Table I.1: Notation in computer programs for parameters defined in eqs. (2.34)

Notations in	Symbols from
computer program	theory
ВВ	β
RB	$\sqrt{\beta}$
BET1	k_c/k
CB	Сь
CC	с
ECF	ϵc_f
EE	e
EPS	E
GA	γ
HN1	h
PI	π

Table I.2: Notation in computer programs for the results

Notations in	Symbols from
computer program	theory
Z1	$\dot{\phi}_1$; Eqs. (I.1)
ZZ1	$\dot{\phi_2}$; Eqs. (I.1)
X1	ϕ_1 ; Eqs. (I.1)
Y1	ϕ_2 ; Eqs. (I.1)
X1	ϕ_1 ; Eqs. (I.2)
Y1	ϕ_2 ; Eqs. (I.2)
Z 1	ϕ_3 ; Eqs. (I.2)
XX1	$\dot{\phi_1}$; Eqs. (I.2)
YY1	$\dot{\phi_2}$; Eqs. (I.2)
ZZ1	$\dot{\phi}_3$; Eqs. (I.2)

Table I.3: Notation in computer programs for other parameters

Notations in	Symbols from
computer program	theory
DT	δt
EPP	Maximum time
EPP1	Minimum time
FF	ſ
HI	χ
HII	$1+(\chi-1)\beta$
LL	L
NN	N

```
IMPLICIT REAL*8 (A-H,O-Z)
REAL LL
REAL K1, K1P, K1S, K1T
REAL K2, K2P, K2S, K2T
REAL K3, K3P, K3S, K3T
REAL K4, K4P, K4S, K4T
REAL MM1, MM2, MM3, MM4
REAL NN1, NN2, NN3, NN4
**********
* RUNGE-KUTTA METHOD FOR SOLVING A TWO
* ARTICULATED CYLINDERS SYSTEM SUBJECTED *
* TO CONFINED AXIAL FLOW WITH IMPACTING *
* MODELLED BY A CUBIC OR A TRILINEAR
* SPRING
**********
OPEN (2, FILE='OUT', STATUS='UNKNOWN')
NUMBER PI DEFINITION
******
PI = 3.1415927
TIME STEP DT
*****
DT = 0.01
CUBIC SPRING STIFFNESS
*******
BET1 = 8662572
NUMERICAL VALUES OF PARAMETERS
*********
BB = 0.4
CB = 0.1
ECF = 0.25
EE = 0.5
EPS = 10.
FF = 0.
GA = 10.
LL = 0.155
NN = 2.
RB = SQRT(0.4)
HN1 = 0.5
CC = 0.3
HH = 1/HN1
```

```
HI = ((1+HN1)*(1+HN1)+1)/((1+HN1)*(1+HN1)-1)
HII = 1 + (HI - 1) *BB
WRITING INPUT
*****
DO 50 M = 0.200
U = 4.45 + 0.02775*M
DEFINITION OF COEFFICIENTS
*********
B1
     = U*((3*EE+1)*RB*(ECF/6)+(1-FF)*HI*RB*NN)
       + (3*EE+1) *RB*EPS*CC*4/6/PI
     = U*((2-FF)*HI*EE*NN*RB+0.25*ECF*EE*EE*RB)
E1
       +RB*EPS*CC*EE*EE/PI
     = U*(-FF*NN*HI*EE*RB+0.25*EE*EE*RB*ECF)
B2
       + (EE**2) *RB*EPS*CC/PI
E2
     = U*((1-FF)*HI*RB*NN*EE*EE+(EE**3)*RB*ECF/6)
       +(EE**3)*RB*EPS*CC*4/6/PI
     = (1/3 + EE) * HII
A1
     = (EE*EE/2)*HII
D1
     = (EE*EE/2)*HII
     = (EE*EE*EE/3)*HII
D2
     = -HI*U*U*NN*NN+NN*GA*(0.5+EE)+2*(NN**4)
C1
       + (0.25+HH/4) * (2*EE+1) *U*U*ECF*NN
       +0.5*U*U*NN*NN*CB
     = -(NN**4) - 0.5*U*U*NN*NN*CB
F1
       + (1-FF) *HI*U*U*NN*NN
     = -NN**4
C2
     = -FF*HI*U*U*NN*NN*EE+0.5*EE*EE*NN*GA
F2
       +NN**4+(EE**2)*(HH+1)*U*U*ECF*NN/4
MINIMUM TIME STEP
***********
EPP = 30
MAXIMUM TIME STEP
*****
EPP1 = 40
```

DEFINITION OF MASS APPARENT COEFFICIENTS

```
SET INITIAL CONDITIONS
******
T1
     = 0
     = 0.1
\mathbf{Z}\mathbf{1}
ZZ1
     = 0
X1
     = 0
Y1
     = 0
Z
     = Z1
     = ZZ1
ZZ
     = X1
X
Y
     = Y1
     = T1
TERM FOR CUBIC SPRING
******
   = (LL**4)*BET1*X*X*X
G1
FIRST STEP
*****
FF1
     = (D2*(B1*Z+C1*X+E1*ZZ+F1*Y+G1)
       -D1*(B2*Z+C2*X+E2*ZZ+F2*Y))
       /(A2*D1-A1*D2)
     = ((A1*B2-A2*B1)*Z+(A1*C2-A2*C1)*X
GG1
       + (A1*E2-A2*E1) *ZZ+ (A1*F2-A2*F1) *Y
       +A1*G2)/(A2*D1-A1*D2)
     = Z
MM1
NN1 = ZZ
     = DT*FF1
K1
K1P = DT*GG1
K1S = DT*MM1
K1T = DT*NN1
SECOND STEP
******
G11 = (LL**4)*BET1*(X+K1S/2)*(X+K1S/2)*(X+K1S/2)
FF2 = ((D2*B1-D1*B2)*(Z+K1/2)+(D2*C1-D1*C2)
       *(X+K1S/2)+(D2*E1-D1*E2)*(ZZ+K1P/2)
       + (D2*F1-D1*F2) * (Y+K1T/2) + (D2*G11-D1*G21))
       /(A2*D1-A1*D2)
GG2
    = ((A1*B2-A2*B1)*(Z+K)/2)+(A1*C2-A2*C1)
       *(X+K1S/2) + (A1*E2-A2*E1) *(ZZ+K1P/2)
       +(A1*F2-A2*F1)*(Y+K1T/2)+(A1*G21-A2*G11))
       /(A2*D1-A1*D2)
MM2
     = Z + K1/2
NN2 = ZZ + K1P/2
```

```
K2P = DT*GG2
K2S
    = DT*MM2
K2T = DT*NN2
THIRD STEP
******
G12 = (LL**4)*BET1*(X+K2S/2)*(X+K2S/2)*(X+K2S/2)
    = ((D2*B1-D1*B2)*(Z+K2/2)+(D2*C1-D1*C2)
FF3
       *(X+K2S/2)+(D2*E1-D1*E2)*(ZZ+K2P/2)
       +(D2*F1-D1*F2)*(Y+K2T/2)+D2*G12)
       /(A2*D1-A1*D2)
    = ((A1*B2-A2*B1)*(Z+K2/2)+(A1*C2-A2*C1)
GG3
       *(X+K2S/2)+(A1*E2-A2*E1)*(ZZ+K2P/2)
       +(A1*F2-A2*F1)*(Y+K2T/2)-A2*G12)
       /(A2*D1-A1*D2)
     = Z+K2/2
MM3
NN3 = ZZ + K2P/2
К3
     = DT*FF3
K3P = DT*GG3
K3S = DT*MM3
K3T = DT*NN3
FOURTH STEP
******
G13 = (LL**4)*BET1*(X+K3S)*(X+K3S)*(X+K3S)
FF4 = ((D2*B1-D1*B2)*(Z+K3)+(D2*C1-D1*C2)
       *(X+K3S)+(D2*E1-D1*E2)*(ZZ+K3P)
       +(D2*F1-D1*F2)*(Y+K3T)+D2*G13)
       /(A2*D1-A1*D2)
     = ((A1*B2-A2*B1)*(Z+K3)+(A1*C2-A2*C1)
GG4
       *(X+K3S)+(A1*E2-A2*E1)*(ZZ+K3P)
       +(A1*F2-A2*F1)*(Y+K3T)-A2*G13)
       /(A2*D1-A1*D2)
MM4
     = Z+K3
NN4
    = ZZ+K3P
K4
     = DT*FF4
K4P = DT*GG4
K4S
    = DT*MM4
K4T = DT*NN4
```

K2 = DT*FF2

```
BIFURCATION DIAGRAMS
******
X3 = X2
X2 = X1
FINAL VALUES CALCULATED
******
Z1 = Z + (K1+2*K2+2*K3+K4)/6
ZZ1 = ZZ + (K1P + 2 * K2P + 2 * K3P + K4P) / 6
X1
    = X + (K1S+2*K2S+2*K3S+K4S)/6
    = Y + (K1T+2*K2T+2*K3T+K4T)/6
Y1
STOP CONDITION AT THE WALL
*******
RIPI1 = (HH1+1)/EPS
RIPI = X1+Y1/2
IF (RIPI.GT.RIPI1) STOP
NEW TIME
*****
T1 = T+DT
POINCARE MAPS
*****
XA = ABS(X1)
EPS1 = 0.00001
IF (XA.LT.EP$1) THEN
IF ((T1.GT.EPP).AND.(T1.LT.EPP1)) THEN
WRITING FOR BIFURCATION DIAGRAMS STUDY
*************
IF ((X2.GT.X3).AND.(X2.GT.X1)) THEN
WRITE (2,12) U,X2
WRITE (*,12) U,X2
ENDIF
WRITING FOR THE PHASE PLOTS AND POINCARE MAP
**************
WRITE (*,12) T1,Z1,ZZ1,X1,Y1
```

WRITE (2,12) T1, Z1, ZZ1, X1, Y1

```
12 FORMAT (10X,4(F10.4,2X))

ENDIF
ENDIF

IF (T1.LT.EPP1) THEN
GO TO 11
ENDIF

50 CONTINUE
STOP
```

END

```
IMPLICIT REAL*8 (A-H,O-Z)
REAL LL
REAL II1, LL1, MM1, II2, LL2, MM2
REAL II3, LL3, MM3, II4, LL4, MM4
REAL K1P, K1S, K1, K1T, K1F, K1V
REAL K2P, K2S, K2, K2T, K2F, K2V
REAL K3P, K3S, K3, K3T, K3F, K3V
REAL K4P, K4S, K4, K4T, K4F, K4V
***********
* RUNGE-KUTTA METHOD FOR SOLVING A THREE *
* ARTICULATED CYLINDERS SYSTEM SUBJECTED *
* TO CONFINED AXIAL FLOW WITH IMPACTING
* MODELLED BY A CUBIC OR A TRILINEAR
* SPRING
***********
OPEN (2, FILE='OUT', STATUS='UNKNOWN')
NUMBER PI DEFINITION
******
PI = 3.1415927
TIME STEP DT
*******
DT = 0.01
CUBIC SPRING STIFFNESS
******
BET1 = 5775000
NUMERICAL VALUES OF PARAMETERS
********
BB = 0.4
CB = 0.1
ECF = 0.25
EE = 0.5
EPS = 10.
FF = 0.
GA = 10.
LL = 0.155
NN
   = 3.
RB = SQRT(0.4)
HN1 = 0.5
CC = 0.3
HH = 1/HN1
```

```
DEFINITION OF MASS APPARENT COEFFICIENTS
***********
HI = ((1+HN1)*(1+HN1)+1)/((1+HN1)*(1+HN1)-1)
HII = 1 + (HI - 1) *BB
WRITING INPUT
********
DO 50 M = 0.200
U = 4.45 + 0.02775*M
DEFINITION OF COEFFICIENTS
*******
    = (RB*(3*EE+4)*ECF/6+(1.-FF)*HI*NN*RB)*U
B1
       + (3*EE+4) *RB*EPS*CC*4/6/PI
    = (1+2*EE)*RB*(0.25*U*ECF+EPS*CC/PI)
E1
       +(2-FF)*HI*U*NN*RB
    = 0.25 \times EE \times EE \times RB \times (U \times ECF + EPS \times CC \times 4/PI)
T1
       +U*NN*RB*HI*EE*(2-FF)
B2
    \approx (1+2*EE)*0.25*RB*(U*ECF+EPS*CC*4/PI)
       -FF*HI*U*NN*RB
E2
    = 0.5*RB*(1/3+EE)*(U*ECF+EPS*CC*4/PI)
       +(1-FF)*HI*U*NN*RB
    = 0.25 \times EE \times EE \times RB \times (U \times ECF + EPS \times CC \times 4/PI)
T2
       +(2-FF)*EE*HI*U*NN*RB
    = EE*EE*0.25*RB*(U*ECF+EPS*CC*4/PI)
B3
       -HI*U*NN*EE*FF*RB
E3
    \approx 0.25 \times EE \times EE \times RB \times (U \times ECF + EPS \times CC \times 4/PI)
       -HI*U*NN*EE*FF*RB
T3
    = (EE**3)*RB*(U*ECF+EPS*CC*4/PI)/6
       +(1-FF)*HI*RB*U*NN*EE*EE
   = (4+3*EE)*HII/3
A1
D1
    = (2*EE+1)*HII/2
Sı
   \approx EE*EE*HII/2
A2 = (2*EE+1)*HII/2
    \approx (1+3*EE)*HII/3
D2
S2
    = EE*EE*HII/2
A3
    = EE*EE*HII/2
D3
    = EE*EE*HII/2
S3
    = EE*EE*EE*HII/3
C1 = (3+2*EE)*(0.5*NN*GA+U*U*0.25*NN*ECF*(HH+1))
       +2*(NN**4)-HI*(U*U)*(NN*NN)+(U*U)*(NN*NN)*CB/2
F1 = -NN**4
U1 = -U*U*NN*NN*CB/2+(1-FF)*HI*U*U*NN*NN
```

```
C2 = -NN**4.
    F2
       = -HI*U*U*NN*NN+NN*GA/2+NN*GA*EE+2*(NN**4)
          +ECF*NN*(U*U)*(HH+1)*(2*EE+1)/4
          +(U**2)*(NN**2)*CB/2
        = -NN**4. - (U*U)*(NN*NN)*CB/2+HI*(U*U)*(NN*NN)
    U2
          -FF* HI*(U**2)*(NN**2)
    C3
       = 0
    F3
       = -NN**4
        = NN**4+(EE**2)*ECF*(U*U)*NN*(HH+1)/4
    U3
          -HI*(U**2)*(NN**2)*EE*FF+NN*GA*(EE**2)/2
    SET INITIAL CONDITIONS
    ******
    TE1 = 0
    X1 = 0
    Y1
       = 0
    Z1 = 0
    XX1 = 0.1
    YY1 = 0
    ZZ1 = 0
    X = X1
11
    Y = Y1
    Z = Z1
    XX = XX1
    YY = YY1
    ZZ = ZZ1
    TE = TE1
    TERM FOR CUBIC SPRING
     ******
    G1 = (LL**4)*BET1*X*X*X
    FIRST STEP
     ******
     FL1 = G1+B1*XX+C1*X+E1*YY+F1*Y+T1*ZZ+U1*Z
     FL2 = B2*XX+C2*X+E2*YY+F2*Y+T2*ZZ+U2*Z
    FL3 = B3*XX+C3*X+E3*YY+F3*Y+T3*ZZ+U3*Z
    FF1 = ((A2*FL1-A1*FL2)*(A3*S2-A2*S3)
          +(A2*FL3-A3*FL2)*(A2*S1-A1*S2))
          /((A1*D2-A2*D1)*(A3*S2-A2*S3)
          +(A3*D2-A2*D3)*(A2*S1-A1*S2))
```

```
GG1 = ((A2*FL1-A1*FL2)*(A3*D2-A2*D3)
      +(A2*FL3-A3*FL2)*(A2*D1-A1*D2))
      /((A1*S2-A2*S1)*(A3*D2-A2*D3)
      +(A3*S2-A2*S3)*(A2*D1-A1*D2))
HH1 = -(FL1+D1*FF1+S1*GG1)/A1
II1 = XX
LL1 = YY
MM1 = ZZ
K1 = DT*FF1
K1P = DT*GG1
K1S = DT*HH1
K1T = DT*II1
K1F = DT*LL1
K1V = DT*MM1
SECOND STEP
*****
SIA = X+K1T/2
G11 = (LL**4)*BET1*(X+K1T/2)*(X+K1T/2)*(X+K1T/2)
FL11 = G11+B1*(XX+K1S/2)+C1*(X+K1T/2)
       +E1*(YY+K1/2)+F1*(Y+K1F/2)+T1*(ZZ+K1P/2)
       +U1*(Z+K1V/2)
FL21 = B2*(XX+K1S/2)+C2*(X+K1T/2)
       +E2*(YY+K1/2)+F2*(Y+K1F/2)+T2*(ZZ+K1P/2)
       +U2*(Z+K1V/2)
FL31 = B3*(XX+K1S/2)+C3*(X+K1T/2)
       +E3*(YY+K1/2)+F3*(Y+K1F/2)+T3*(ZZ+K1P/2)
       +U3*(Z+K1V/2)
FF2 = ((A2*FL11-A1*FL21)*(A3*S2-A2*S3)
      +(A2*FL31-A3*FL21)*(A2*S1-A1*S2))
      /((A1*D2-A2*D1)*(A3*S2-A2*S3)
      +(A3*D2-A2*D3)*(A2*S1-A1*S2))
GG2 = ((A2*FL11-A1*FL21)*(A3*D2-A2*D3)
      +(A2*FL31-A3*FL21)*(A2*D1-A1*D2))
      /((A1*S2-A2*S1)*(A3*D2-A2*D3)
      +(A3*S2-A2*S3)*(A2*D1-A1*D2))
HH2 = -(FL11+D1*FF2+S1*GG2)/A1
II2 = XX+K1S/2
LL2 = YY+K1/2
MM2 = ZZ + K1P/2
```

```
K2 = DT*FF2
K2P = DT*GG2
K2S = DT*HH2
K2T = DT*II2
K2F = DT*LL2
K2V = DT*MM2
THIRD STEP
******
SIB = X + K2T/2
G12 = (LL**4)*BET1*(X+K2T/2)*(X+K2T/2)*(X+K2T/2)
FL12 = G12+B1*(XX+K2S/2)+C1*(X+K2T/2)
       +E1*(YY+K2/2)+F1*(Y+K2F/2)+T1*(ZZ+K2P/2)
       +U1*(Z+K2V/2)
FL22 = B2*(XX+K2S/2)+C2*(X+K2T/2)
       +E2*(YY+K2/2)+F2*(Y+K2F/2)+T2*(ZZ+K2P/2)
       +U2*(Z+K2V/2)
FL32 = B3*(XX+K2S/2)+C3*(X+K2T/2)
       +E3*(YY+K2/2)+F3*(Y+K2F/2)+T3*(ZZ+K2P/2)
       +U3*(Z+K2V/2)
FF3 = ((A2*FL12-A1*FL22)*(A3*S2-A2*S3))
      + (A2*FL32-A3*FL22) * (A2*S1-A1*S2))
      /((A1*D2-A2*D1)*(A3*S2-A2*S3)+(A3*D2-A2*D3)
      *(A2*S1-A1*S2))
GG3 = ((A2*FL12-A1*FL22)*(A3*D2-A2*D3)
      +(A2*FL32-A3*FL22)*(A2*D1-A1*D2))
      /((A1*S2-A2*S1)*(A3*D2-A2*D3)+(A3*S2-A2*S3)
      *(A2*D1-A1*D2))
HH3 = -(FL12+D1*FF3+S1*GG3)/A1
II3 = XX+K2S/2
LL3 = YY+K2/2
MM3 = ZZ + K2P/2
K3 = DT*FF3
K3P = DT*GG3
K3S = DT*HH3
K3T = DT*II3
K3F = DT*LL3
K3V = DT*MM3
```

```
FOURTH STEP
******
SID = X + K3T
G13 = (LL**4)*BET1*(X+K3T)*(X+K3T)*(X+K3T)
FL13 = G13+B1*(XX+K3S)+C1*(X+K3T)
       +E1*(YY+K3)+F1*(Y+K3F)+T1*(ZZ+K3P)
       +U1*(Z+K3V)
FL23 = B2*(XX+K3S)+C2*(X+K3T)
       +E2*(YY+K3)+F2*(Y+K3F)+T2*(ZZ+K3P)
       +U2*(Z+K3V)
FL33 = B3*(XX+K3S)+C3*(X+K3T)
       +E3*(YY+K3)+F3*(Y+K3F)+T3*(ZZ+K3P)
       +U3*(Z+K3V)
FF4 = ((A2*FL13-A1*FL23)*(A3*S2-A2*S3)
      + (A2*FL33-A3*FL23) * (A2*S1-A1*S2))
      /((A1*D2-A2*D1)*(A3*S2-A2*S3)+(A3*D2-A2*D3)
      *(A2*S1-A1*S2))
GG4 = ((A2*FL13-A1*FL23)*(A3*D2-A2*D3)
      +(A2*FL33-A3*FL23)*(A2*D1-A1*D2))
      /((A1*S2-A2*S1)*(A3*D2-A2*D3)+(A3*S2-A2*S3)
      *(A2*D1-A1*D2))
HH4 = -(FL13+D1*FF4+S1*GG4)/A1
II4 = XX+K3S
LL4 = YY+K3
MM4 = ZZ + K3P
K4 = DT*FF4
K4P = DT*GG4
K4S = DT*HH4
K4T = DT*II4
K4F = DT*LL4
K4V = DT*MM4
MINIMUM TIME
*****
EPP = 30
MAXIMUM TIME
*****
EPP1 = 40
```

```
POINCARE MAP
  *****
  EPL = 0.001
  EPL1 = 0.0301
  EPL2 = 0.03015
  BIFURCATION DIAGRAM
  X3 = X2
  X2 = X1
  STOP CONDITION AT THE WALL
  ******
  RIPI = EPS*(X1+Y1+EE*Z1)
  RIPI1 = 3.*(HN1+1)/2
  IF (RIPI.GT.RIPI1) STOP
  FINAL VALUES CALCULATED BY R-K METHOD
  ***********
  X1 = X + (K1T+2*K2T+2*K3T+K4T)/6
  Y1 = Y + (K1F+2*K2F+2*K3F+K4F)/6
  Z1 = Z + (K1V + 2 * K2V + 2 * K3V + K4V) / 6
  XX1 = XX + (K1S+2*K2S+2*K3S+K4S)/6
  YY1 = YY + (K1+2*K2+2*K3+K4)/6
  ZZ1 = ZZ + (K1P + 2 * K2P + 2 * K3P + K4P) / 6
  TE1 = TE + DT
  XA = ABS(XX1)
  WRITING CONDITIONS
  *****
  FOR PHASE PLANE PORTRAITS
  **************
  IF (TE1.GT.EPP.AND.TE1.LT.EPP1) THEN
  FOR POINCARE MAPS
  ******
  IF (XA.LT.EPL) THEN
  WRITE (2,17) YY1,Y1
  WRITE (*,17) YY1,Y1
17 FORMAT (2(F20.10,3X))
```

```
WRITE (2,12) TE1,XX1,YY1,X1,Y1
  WRITE (*,12) TE1,XX1,YY1,X1,Y1
  ENDIF
  ENDIF
  WRITING CONDITION FOR BIFURCATION DIAGRAM
  ***********
  IF ((X2.GT.X3).AND.(X2.GT.X1)) THEN
  WRITE (*,12) U,X2
  WRITE (2,12) U,X2
  ENDIF
12 FORMAT (10X,4(F10.4,2X))
  STOP CONDITION
  *****
  IF (TE1.LT.EPP1) THEN
  GO TO 11
  ENDIF
50 CONTINUE
```

STOP END

τ	$\dot{\phi}_1$	$\dot{\phi}_2$	ϕ_1	ϕ_2
30.0100	0.0031	0.0010	-0.0015	-0.0015
30.0200	0.0032	0.0011	-0.0014	-0.0015
30.0300	0.0033	0.0012	-0.0014	-0.0015
30.0400	0.0033	0.0013 ·	-0.0014	-0.0014
30.0500	0.0034	0.0014	-0.0013	-0.0014
30.0600	0.0035	0.0015	-0.0013	-0.0014
30.0700	0.0035	0.0015	-0.0013	-0.0014
30.0800	0.0036	0.0016	-0.0012	-0.0014
30.0900	0.0037	0.0017	-0.0012	-0.0014
30.1000		0.0018	-0.0012	-0.0014
30.1100	0.0038	0.0018	-0.0011	-0.0013
30.1200	0.0038	0.0019	-0.0011	-0.0013
30.1300	0.0039	0.0020	-0.0010	-0.0013
30.1400	0.0040	0.0021	-0.0010	-0.0013
30.1500	0.0040	0.0021	-0.0010	-0.0013
30.1600	0.0041	0.0022	-0.0009	-0.0012
30.1700	0.0041	0.0023	-0.0009	-0.0012
30.1800 30.1900	0.0041 0.0042	0.0023	-0.0008 -0.0008	-0.0012
30.2000	0.0042	,0.0024	-0.0008	-0.0012 -0.0011
30.2100	0.0043	0.0025	-0.0007	-0.0011
30.2200	0.0043	0.0026	-0.0007	-0.0011
30.2300	0.0043	0.0026	-0.0006	-0.0011
30.2400	0.0044	0.0027	-0.0006	-0.0010
30.2500	0.0044	0.0027	-0.0005	-0.0010
30.2600	0.0044	0.0028	-0.0005	-0.0010
30.2700 30.2800	0.0044 0.0045	0.0028 0.0029	-0.0004	-0.0010
30.2900	0.0045	0.0029	-0.0004 -0.0004	-0.0009 -0.0009
30.3000	0.0045	0.0030	-0.0003	-0.0009
30.3100	0.0045	0.0030	-0.0003	-0.0008
30.3200	0.0045	0.0031	-0.0002	-0.0008
30.3300	0.0045	0.0031	-0.0002	-0.0008
30.3400	0.0045	0.0032	-0.0001	-0.0007
30.3500	0.0045	0.0032	-0.0001	-0.0007
30.3600 30.3700	0.0045 0.0045	0.0032 0.0033	0.0000	-0.0007
30.3800	0.0045	0.0033	0.0000	-0.0006 -0.0006
30.3900	0.0045	0.0033	0.0001	-0.0006
30.4000	0.0045	0.0034	0.0001	-0.0005
30.4100	0.0045	0.0034	0.0002	-0.0005
30.4200	0.0044	0.0034	0.0002	-0.0005
30.4300	0.0044	0.0034	0.0003	-0.0004
30.4400	0.0044	0.0034	0.0003	-0.0004
30.4500 30.4600	0.0044 0.0044	0.0035 0.0035	0.0004	-0.0004
30.4700	0.0043	0.0035	0.0004 0.0004	-0.0003 -0.0003
30.4800	0.0043	0.0035	0.0005	-0.0003
30.4900	0.0043	0.0035	0.0005	-0.0002
30.5000	0.0042	0.0035	0.0006	-0.0002

•

au	$\dot{\phi_1}$	$\dot{\phi}_2$	ϕ_1	ϕ_2
30.5100 30.5200 30.5300 30.55000 30.55000 30.55000 30.59000 30.62000 30.62000 30.64000 30.65000 30.65000 30.67000 30.720	0.0042 0.0041 0.0041 0.0040 0.0039 0.0039 0.0037 0.0037 0.0035 0.0035 0.0035 0.0033 0.0033 0.0033 0.0030 0.0030 0.0029 0.0029 0.0025 0.0025 0.0025 0.0025 0.0025 0.0021 0.0020 0.0019 0.0019 0.0015 0.0010 0.0010 0.0010	0.0035 0.0035 0.0035 0.0035 0.0035 0.0035 0.0035 0.0035 0.0035 0.0035 0.0034 0.0034 0.0034 0.0034 0.0033 0.0033 0.0033 0.0032 0.0032 0.0031 0.0031 0.0031 0.0031 0.0031 0.0031 0.0031 0.0039 0.0029 0.0029 0.0029 0.0029 0.0025 0.0025 0.0025 0.0024 0.0023 0.0022 0.0022 0.0022	0.0006 0.0007 0.0007 0.0008 0.0008 0.0009 0.0009 0.0010 0.0011 0.0011 0.0012 0.0012 0.0013 0.0013 0.0013 0.0013 0.0014 0.0014 0.0014 0.0015 0.0015 0.0015 0.0016 0.0016 0.0016 0.0017 0.0017 0.0017 0.0017 0.0017 0.0017 0.0018 0.0018	-0.0002 -0.0001 -0.0001 -0.0000 0.0000 0.0000 0.0001 0.0002 0.0002 0.0003 0.0003 0.0003 0.0003 0.0004 0.0004 0.0004 0.0005 0.0005 0.0005 0.0006 0.0006 0.0007 0.0007 0.0007 0.0007 0.0007 0.0008 0.0008 0.0009 0.0009 0.0009 0.0010 0.0011 0.0011 0.0011
30.9000 30.9100 30.9200	0.0012 0.0011 0.0010	0.0023 0.0022 0.0022	0.0017 0.0018 0.0018	0.0011 0.0011 0.0011
31.0000	0.0002	0.0016	0.0018	0.0012

4.4500	0.0018
4.4500	0.0016
4.4500	0.0013
4.4500	0.0011
4.4777	0.0185
4.4777	0.0187
4.4777	0.0189
4.4777	0.0190
4.5055	0.0366
4.5055	0.0367
4.5055	0.0367
4.5055	0.0367
4.5055	0.0367
4.5055	0.0367
4.5332	0.0479
4.5332	0.0479
4.5332	0.0479
4.5332	0.0479
4.5332	0.0479
4.5610	0.0569
4.5610	0.0539
4.5610	0.0569
4.5610	0.0569
4.5610	0.0569
4.5887	0.0647
4.5887	0.0647
4.5887	0.0647 0.0646
4.5887	0.0647
4.5887	0.0647
4.5887	0.0646
4.6165	0.0716
4.6165	0.0716
4.6165	0.0716
4.6165	0.0716
4.6165	0.0716
4.6165	0.0716
4.6442	0.0780
4.6442	0.0780
4.6442	0.0779
4.6442	0.0780
4.6442	0.0780
4.6442	0.0780
4.6720	0.0839
4.6720	0.0839
4.6720	0.0839
4.6720	0.0839
4.6720	0.0839
4.6720	0.0839
4.6720	0.0839
	·